UNCLASSIFIED

AD NUMBER:	AD0843629

LIMITATION CHANGES

TO:

Approved for public release; distribution is unlimited.

FROM:

Distribution authorized to DoD Components only; Export Controlled; 1 Sep 1967. Other requests shall be referred to Space and Missile Systems Organization, Air Force Systems Command, Norton AFB, CA 90045.

AUTHORITY

USAF ltr dtd 30 Jun 1980

THIS PAGE IS UNCLASSIFIED

THIS REPORT HAS BEEN DELIMITED
AND CLEARED FOR PUBLIC RELEASE
UNDER DOD DIRECTIVE 5200.20 AND
NO RESTRICTIONS ARE IMPOSED UPON
ITS USE AND DISCLOSURE.

DISTRIBUTION STATEMENT A

APPROVED FOR PUBLIC RELEASE;
DISTRIBUTION UNLIMITED.

SAMSO TR 67-121

L

AD843629

RADIATION DAMAGE STUDY - PHASE II (RADS II)
FINAL REPORT

VOLUME VI--SHOCK PROPAGATION IN HETEROGENEOUS MATERIALS
BOOK TWO OF TWO BOOKS

Prepared under
Contract AF04(694)-990

by

Shock Hydrodynamics, Inc.
Sherman Oaks, California

Under Subcontract 182378

to

AVCO GOVERNMENT PRODUCTS GROUP
MISSILE SYSTEMS DIVISION
201 Lowell Street
Wilmington, Massachusetts 01887

AVMSD-0852-67-RR Volume VI

September, 1967

EACH TRANSMITTAL OF THIS DOCUMENT OUTSIDE THE DEPARTMENT OF DEFENSE MUST HAVE PRIOR APPROVAL OF HEADQUARTERS, SPACE AND MISSILE SYSTEMS ORGANIZATION, N[redacted]
CA[redacted]

Attn: SMSP
Los Angeles AFS, Calif. 90045

Prepared for

SPACE AND MISSILE SYSTEMS ORGANIZATION
AIR FORCE SYSTEMS COMMAND
Norton Air Force Base, California 92409

FOR OFFICIAL USE ONLY

SAMSO TR 67-121

This document consists of 188 pages,
200 copies, Series A

RADIATION DAMAGE STUDY - PHASE II (RADS II)
FINAL REPORT

VOLUME VI--SHOCK PROPAGATION IN HETEROGENEOUS MATERIALS
BOOK TWO OF TWO BOOKS

Prepared under
Contract AF04(694)-990

by

R. L. Bjork, M. H. Wagner and H. A. Lang

Shock Hydrodynamics, Inc.
Sherman Oaks, California

Under Subcontract 182378

to

AVCO GOVERNMENT PRODUCTS GROUP
MISSILE SYSTEMS DIVISION
201 Lowell Street
Wilmington, Massachusetts 01887

AVMSD-0852-67-RR Volume VI

September, 1967

APPROVED

J. T. Olson,
RADS Program Manager

EACH TRANSMITTAL OF THIS DOCUMENT OUTSIDE THE DEPARTMENT OF DEFENSE MUST HAVE PRIOR APPROVAL OF HEADQUARTERS, SPACE AND MISSILE SYSTEMS ORGANIZATION, [redacted]
C[redacted]

Prepared for

SPACE AND MISSILE SYSTEMS ORGANIZATION
AIR FORCE SYSTEMS COMMAND
Norton Air Force Base, California 92409

FOREWORD

This volume was prepared by Shock Hydrodynamics, Inc., under subcontract to the Avco Corporation as part of the Radiation Damage Study (RADS) Program, Contract AF04(694)-990, sponsored by the Air Force Space and Missile Systems Organization.

The complete RADS II Final Report consists of the following volumes:

I. Summary

II. Supplement to Phenomenology Survey

III. Atmospheric Transport and Energy Deposition

IV. Material Response Studies and XIP II

V. Comparison of Code Predictions with Test Results

VI. Shock Propagation in Heterogeneous Materials

VII. Recent Advances in Reentry Vehicle Hardening Technology

VIII. Conceptual Design of Advanced Vehicles (CCN-1 results)

IX. Simulation

X. Material Property Determinations

XI. Advanced Techniques for Material Characterization

Additional volumes are now being planned.

ABSTRACT

Numerical studies of shock propagation in anisotropic and in heterogeneous materials are reported. This work was performed by Shock Hydrodynamics, Inc., using the SHAN and SHEP computer codes.

EDITED BY:
EDITORIAL SERVICES SECTION
P. S. FALCEY

CONTENTS

Chapter

CONTENTS (Concl'd)

ILLUSTRATIONS

ILLUSTRATIONS (Concl'd)

TABLES

CHAPTER I

INTRODUCTION

This report describes investigations conducted by Shock Hydrodynamics, Inc., in support of the RADS II program, under subcontract to Avco Corporation. Studies performed on two separate topics are covered in this report: Chapter II-formulation and application of a one-dimensional characteristic code (SHAN) that treats wave propagation in anisotropic materials; Chapter III-two-dimensional analyses of wave propagation in heterogeneous materials.

CHAPTER II

SHAN FORMULATION AND RESULTS*

2.1 OBJECTIVES OF STUDY

The most markedly anisotropic property of many laminated ablatives is that of failure. For example, carbon phenolic, MX 4926(1), can sustain 18,000 psi of tension in the plane of the weave, but only 900 psi of tension normal to that plane. Similarly, it can support 14,700 psi of pure shear stress in the weave plane, but only 2,900 psi of pure shear, which tends to cause slip between adjacent layers.

In contrast to these order of magnitude variations in the failure properties, the constitutive relations are not extremely anisotropic, in that no element of the stiffness matrix is significantly different from the corresponding element of the isotropic equivalent matrix. However, in view of the sensitivity of the material to certain stress components, it becomes important to include the anisotropy to provide an accurate computation of all stress components.

The one-dimensional characteristics code described in Section 2.2 was developed by Shock Hydrodynamics, Inc., to provide a useful and inexpensive tool for studying the effects of anisotropy. A particular objective of the present study was to determine the stress fields produced by the impact of an aluminum flyer plate on anisotropic targets comprised of laminated quartz phenolic at various layup angles.

A second objective of the study was to provide stress fields for comparison with experiments undertaken by Avco Corporation(2), in order to identify criteria that may lead to failure of the anisotropic composite.

A third objective was to include a capability for simulating initial X-ray loadings in order to obtain stress fields that can be compared with those obtained from flyer plate impacts.

These three objectives constitute essential steps in determining the response of ablative-bond-substrate structures to X-ray loadings for a variety of layup angles. The ultimate goal of the overall effort is to determine the effect of layup angle on failure of anisotropic composites under X-ray loading based on the failure criteria identified from the flyer plate experiments.

2.2 DESCRIPTION OF SHAN CODE

The one-dimensional characteristic code developed under this contract is described below.**

---

*Written by H. A. Lang and R. L. Bjork

**The SHAN Code (Shock Hydrodynamics Anisotropic) was developed by R. L. Bjork and M. Rosenblatt of Shock Hydrodynamics, Inc.

2.2.1 Assumptions

2.2.1.1 The Material

Most laminates and composites consist of a fiber or woven matrix intended to impart additional strength in one direction (the direction corresponds to the warp in textiles). The direction transverse to this in the plane of the weave (corresponding to the woof) and the direction normal to the plane of weave constitute, together with the warp direction, three material axes which are also usually the axes of reference for determining material behavior. Designating these material axes as 1, 2, 3 in the sense:

1 - parallel to weave or warp,

2 - transverse to weave or woof, and

3 - perpendicular to weave; defined by $(\vec{1}) \times (\vec{2})$

generates a right-handed cartesian coordinate system, and three mutually orthogonal planes of elastic symmetry.

Such materials are specified by nine stiffnesses or compliances corresponding to the degree of anisotropy commonly labelled as "orthotropic".

2.2.1.2 The Coordinate System

Only right-handed cartesian frames of reference will be used. In particular, Lagrangian spatial coordinates x, y, z and Eulerian variables X, Y, Z are introduced. The only independent variables of the one dimensional program are the time t and the spatial coordinate z. The x-axis must coincide with one of the material axes (material axis 1), but the other material axes may make any desired layup angle. As a matter of terminology, this is called the ability to rotate the material about the x-axis (material axis 1).

2.2.1.3 The Loading

The dependent variables may be arbitrarily set at $t = 0$. Thus, impact loadings and instantaneous X-ray energy depositions can be treated.

2.2.2 The Constitutive Relations and the Differential Equations

The assumptions discussed in 2.2.1.1 and 2.2.1.2 lead to the following constitutive relations for such an anisotropic material (Ref. 3, p. 18; Ref. 4, p. 160):

$$\begin{bmatrix} \sigma_x \\ \sigma_y \\ \sigma_z \\ \sigma_{zy} \\ \sigma_{zx} \\ \sigma_{xy} \end{bmatrix} = \begin{bmatrix} E_{11} & E_{12} & E_{13} & E_{14} & 0 & 0 \\ E_{12} & E_{22} & E_{23} & E_{24} & 0 & 0 \\ E_{13} & E_{23} & E_{33} & E_{34} & 0 & 0 \\ E_{14} & E_{24} & E_{34} & E_{44} & 0 & 0 \\ 0 & 0 & 0 & 0 & E_{55} & E_{56} \\ 0 & 0 & 0 & 0 & E_{56} & E_{66} \end{bmatrix} \text{X} \begin{bmatrix} \epsilon_x \\ \epsilon_y \\ \epsilon_z \\ \epsilon_{zy} \\ \epsilon_{zx} \\ \epsilon_{xy} \end{bmatrix} \quad (2.1)$$

Here, σ, ϵ, and E are the stresses, strains, and stiffnesses.

Since the displacement (u, v, and w) are functions of z only, ϵ_z, ϵ_{zy}, ϵ_{zx} are the only non-zero strain components. Consequently, the strain displacement equations are:

$$\epsilon_z = \frac{\partial w}{\partial z} = \frac{\partial Z}{\partial z} - 1 \quad (2.2a)$$

$$\epsilon_{zy} = \frac{\partial v}{\partial z} = \frac{\partial Y}{\partial z} \quad (2.2b)$$

$$\epsilon_{zx} = \frac{\partial u}{\partial z} = \frac{\partial X}{\partial z} \quad (2.2c)$$

Since the particle velocities U, V, and W in the X, Y, and Z directions, respectively, are the time derivatives of the Lagrangian coordinates, we have

$$\frac{\partial \epsilon_z}{\partial t} = \frac{\partial W}{\partial z} \quad (2.3a)$$

$$\frac{\partial \epsilon_{zy}}{\partial t} = \frac{\partial V}{\partial z} \quad (2.3b)$$

$$\frac{\partial \epsilon_{zx}}{\partial t} = \frac{\partial U}{\partial z} \quad (2.3c)$$

Euler's equations in Lagrangian coordinates are:

$$\rho_o \frac{\partial W}{\partial t} = \frac{\partial \sigma_z}{\partial z} \tag{2.4a}$$

$$\rho_o \frac{\partial V}{\partial t} = \frac{\partial \sigma_{zy}}{\partial z} \tag{2.4b}$$

$$\rho_o \frac{\partial U}{\partial t} = \frac{\partial \sigma_{zx}}{\partial z} \tag{2.4c}$$

Equations (2.4) show that even though there exist, in general, six non-zero stress components, only three are directly involved in the wave propagation aspects of this problem. Equations (2.5) give the three stress components in terms of the three non-zero strain components:

$$\sigma_z = E_{33}\,\epsilon_z + E_{34}\epsilon_{zy} \tag{2.5a}$$

$$\sigma_{zy} = E_{34}\,\epsilon_z + E_{44}\,\epsilon_{zy} \tag{2.5b}$$

$$\sigma_{zx} = E_{55}\,\epsilon_{zx} \tag{2.5c}$$

Equations (2.3), (2.4) and (2.5) represent a complete set of equations for the nine dependent variables, W, V, U, σ_z, σ_{zy}, σ_{zx}, ϵ_z, ϵ_{zy}, and ϵ_{zx}.

These nine equations may be reduced to six by eliminating either the three stresses or the three strains in the equations. For purposes of matching boundary conditions on free surfaces and interfaces, it is more convenient to work with the stresses and velocities as the dependent variables. Thus, the strains will be eliminated in the equations. For this purpose Equations (2.5) must be inverted and the strains must be expressed in terms of the stresses, leading to:

$$\epsilon_z = A_{33}\,\sigma_z + A_{34}\,\sigma_{yz} \tag{2.6a}$$

$$\epsilon_{yz} = A_{34}\,\sigma_z + A_{44}\,\sigma_{yz} \tag{2.6b}$$

$$\epsilon_{zx} = A_{55}\,\sigma_{zx} \tag{2.6c}$$

where

$$A_{33} = \frac{E_{44}}{\Delta_o}, \quad A_{34} = \frac{-E_{34}}{\Delta_o}, \quad A_{44} = \frac{E_{33}}{\Delta_o}, \quad A_{55} = \frac{1}{E_{55}}$$

and

$$\Delta_o \equiv E_{33} E_{44} - E_{34}^2$$

After elimination of the strains, the complete set of six equations is:

$$A_{33} \frac{\partial \sigma_z}{\partial t} + A_{34} \frac{\partial \sigma_{zy}}{\partial t} - \frac{\partial W}{\partial z} = 0 \qquad (2.7a)$$

$$A_{34} \frac{\partial \sigma_z}{\partial t} + A_{44} \frac{\partial \sigma_{zy}}{\partial t} - \frac{\partial V}{\partial z} = 0 \qquad (2.7b)$$

$$\frac{\partial \sigma_z}{\partial z} - \rho_o \frac{\partial W}{\partial t} = 0 \qquad (2.7c)$$

$$\frac{\partial \sigma_{zy}}{\partial z} - \rho_o \frac{\partial V}{\partial t} = 0 \qquad (2.7d)$$

$$A_{55} \frac{\partial \sigma_{zx}}{\partial t} - \frac{\partial U}{\partial z} = 0 \qquad (2.7e)$$

$$\frac{\partial \sigma_{zx}}{\partial z} - \rho_o \frac{\partial U}{\partial t} = 0 \qquad (2.7f)$$

It is to be noted that Eq. (2.7e) and Eq. (2.7f) form a decoupled set in the dependent variables U and σ_{zx}. This arises from the fact that the x-axis was chosen to be a principal axis.

2.2.3 A Solution by the Method of Characteristics

The method of characteristics, when applied to Equations (2.7a) through (2.7d), determines the characteristic directions dz/dt = C, given by $\pm C_{\pm}$ where

$$C_{\pm}^{2} = \frac{A_{33} + A_{44} \pm \sqrt{(A_{33} - A_{44})^{2} + 4A_{34}^{2}}}{2\,\rho_o\,(A_{33}\,A_{44} - A_{34}^{2})} =$$

$$\frac{E_{33} + E_{44} \pm \sqrt{(E_{33} - E_{44})^{2} + 4E_{34}^{2}}}{2\,\rho_o}$$

$$\pm C_{\pm} \equiv \pm\sqrt{C_{\pm}^{2}} \tag{2.8}$$

$$C_1 = +C_+$$

$$C_2 = -C+$$

$$C_3 = +C-$$

$$C_4 = -C-$$

Equation (2.8) shows that there are four characteristic directions at every (z, t) point. These characteristic directions are constants throughout one material and the characteristics are straight lines. The four characteristic directions are indicated in Figure 2-1. Along the ith characteristic the following equation is valid:

$$\rho_o C_i A_{34} W - A_{34}\,\sigma_z + \frac{(1 - \rho_o C_i^{2} A_{33})\,V}{C_i} + (\rho_o C_i^{2}\left[A_{33}A_{44} - A_{34}^{2}\right] - A_{44})\sigma_{zy} = K_i \tag{2.9}$$

The K_i are constant along any given characteristic; the subscript i labels the type of characteristic and the sound speed formula to be used.

For impact problems, $U = \sigma_{zx} = 0$. However, in some problems of X-ray deposition, U and σ_{zx} are not zero and a solution to Equations (2.7e) and (2.7f) must be obtained. Applying the method of characteristics to these equations yields the following results:

$$C_5 = \sqrt{\frac{1}{\rho_o\,A_{55}}} = +\sqrt{\frac{E_{55}}{\rho_o}}\,,\quad C_6 = -\,C_5 \tag{2.10}$$

$$\rho_o\,C_5\,U - \sigma_{zx} = K_5,\quad \rho_o C_6\,U - \sigma_{zx} = K_6$$

2.2.4 Application to the SHAN Code

The SHAN code uses six characteristics to solve for the six variables, W, σ_z, V, σ_{zy}, U, and σ_{zx}. U and σ_{zx} are included, since for X-ray loading σ_{zx} may not be zero.

For convenience in writing the solution to the characteristic equations, we introduce the definitions indicated in Figure 2-2. These definitions lead to a solution of the characteristic equations in matrix notation. A matrix $\underline{\underline{a}}$ is associated with each material. The material matrix $\underline{\underline{a}}$ is related to the dependent variable $\underline{X}$ and the characteristic constants $\underline{K}$ by Equation (2.11):

$$\underline{\underline{a}}\,\underline{X} = \underline{K} \tag{2.11}$$

The matrix $\underline{\underline{b}}$ is defined for each material as the inverse to $\underline{\underline{a}}$. This implies that the solution for the dependent variables in any material is given by Equation (2.12):

$$\underline{X} = \underline{\underline{b}}\;\underline{K} \tag{2.12}$$

2.2.4.1 Special Case - Interfaces

The X^i are considered to be continuous across an interface. Figure 2-3 shows the six characteristics involved in finding the dependent variables, X^i, on an interface. The odd numbered characteristics refer to the left materials and the even numbered characteristics refer to the right materials. We can define a new matrix, $\underline{\underline{a}}^1$, which enables us to solve for the dependent variables on an interface. The method of forming $\underline{\underline{a}}^1$ from $\underline{\underline{a}}^{\text{left}}$ and $\underline{\underline{a}}^{\text{right}}$ is indicated in Figure 2-3.

2.2.4.2 Special Case - Free Surfaces

The condition on a free surface is indicated in Equation (2.13):

$$\sigma_{i\alpha}\,\nu^{\alpha} = 0 \tag{2.13}$$

In the present case, this implies:

$$X^2 = X^4 = X^6 = 0 \tag{2.14}$$

For a left free surface, the only characteristics are 2, 4 and 6. For a right free surface, the only characteristics are 1, 3 and 5. The matrix for a free surface thus degenerates to a 3 x 3 matrix formed from 3 rows and 3 columns of the matrix (see Figure 2-4).

2.2.4.3 Special Case - $A_{34} = E_{34} = 0$

One special case must be considered, namely, $E_{34} = 0$. This case leads to the result that the material matrix is singular so that the previous approach fails. However, if E_{34} is in fact zero, the differential equations decouple, and a matrix of a different form can be obtained. The material matrix and the sound speed formulas for this special case are given below in Equation (2.15):

$$C_1 = \sqrt{\frac{1}{\rho_o A_{33}}} = \sqrt{\frac{E_{33}}{\rho_o}}, \quad C_2 = -C_1$$

$$C_3 = \sqrt{\frac{1}{\rho_o A_{44}}} = \sqrt{\frac{E_{44}}{\rho_o}}, \quad C_4 = -C_3$$

$$C_5 = \sqrt{\frac{1}{\rho_o A_{55}}} = \sqrt{\frac{E_{55}}{\rho_o}}, \quad C_6 = -C_5$$

$$\underline{\underline{a}} = a^i_j = \begin{bmatrix} \rho_o C_1 & -1 & 0 & 0 & 0 & 0 \\ \rho_o C_2 & -1 & 0 & 0 & 0 & 0 \\ 0 & 0 & \rho_o C_3 & -1 & 0 & 0 \\ 0 & 0 & \rho_o C_4 & -1 & 0 & 0 \\ 0 & 0 & 0 & 0 & \rho_o C_5 & -1 \\ 0 & 0 & 0 & 0 & \rho_o C_6 & -1 \end{bmatrix} \qquad (2.15)$$

2.3 PROBLEM SPECIFICATIONS

Laminated quartz phenolic (LQP) was selected as a representative material for the SHAN cases run in this study. Experimental tests in tension and torsion were conducted by personnel at Avco to determine the appropriate material properties. These properties, initially expressed in terms of engineering constants, were converted to the stiffness and compliance matrixes listed below:

$$\left[C_{ij}\right] = \begin{bmatrix} 4.116 & 0.701 & 0.656 & 0 & 0 & 0 \\ & 3.714 & 0.617 & 0 & 0 & 0 \\ & & 1.848 & 0 & 0 & 0 \\ & & & 0.89 & 0 & 0 \\ & & & & 0.91 & 0 \\ & & & & & 0.82 \end{bmatrix} \times 10^{6} \text{ psi} \qquad (2.16)$$

$$\left[S_{ij}\right] = \begin{bmatrix} .262 & -.036 & -.081 & 0 & 0 & 0 \\ & .290 & -.084 & 0 & 0 & 0 \\ & & .598 & 0 & 0 & 0 \\ & & & 1.1236 & 0 & 0 \\ & & & & 1.0989 & 0 \\ & & & & & 1.2195 \end{bmatrix} \times \frac{1}{10^{6}} \text{ psi}^{-1} \qquad (2.17)$$

Since these matrixes are symmetric, elements below a main diagonal are omitted. The density of LQP is $\rho_o = 1.71 \text{ gm/cm}^3$. Stress fields produced in flyer plate impacts were initiated using an aluminum flyer plate assumed to be of type 6061-T6 with properties derived from the Metals Handbook. The values used are:

$\rho_o = 2.7 \text{ gm/cm}^3$

$\lambda = 0.503$ Mb   Aluminum Flyer Plate

$\mu = 0.259$ Mb

The material axes of LQP are shown in Figure 2-5.

Separate Shock Hydrodynamics programs are applied to convert material matrixes (C_{ij}) and (S_{ij}) to the spatial frame required for specific geometries. These programs convert results to megabar units and provide the elements for the matrixes (A_{ij}) and (E_{ij}) of the SHAN program.

Specific geometries are simulated by introducing the layup angle, α, which represents rotation about the x-axis. The layup angle is defined to be positive for a rotation about the x-axis in the sense indicated in Figure 2-6.

2.3.1 Geometric Considerations in Impact Loading

The aluminum flyer plate is roughly 1/8 the thickness of the LQP plate. The geometric dimensions suggested by Avco and some additional inputs are summarized in Figure 2-7.

The flyer plate always impacts with an initial velocity of 0.002 cm/μsec. To assess the influence of layup angle, values of α = 0, 20, 40, 65 and 90 degrees were chosen.

2.3.2 Material Matrix for an Equivalent Isotropic Plate

In order to assess the influence of anisotropy, it is a common practice to compare the results of an anisotropic problem with an isotropic problem under comparable boundary and initial conditions. Keeping in mind the fact that anisotropic and isotropic wave propagation exhibit some distinctly different physical features, a reasonable isotropic model for comparison can be generated by averaging stiffnesses or compliances. There are numerous methods of averaging or, equally, constraining the elements of a given anisotropic material matrix to obtain a simpler matrix, representing a lesser degree of anisotropy.

To provide a basis of comparison, the isotropic model used is based upon a zero layup angle. The stiffness matrix (C_{ij}) then suggests an average shear modulus $\mu = 0.06$ Mb and an average value of $\lambda = 0.045$ Mb*. The two Lame constants are then used to determine the diagonal element given by $\lambda + 2\mu = 0.166$ Mb. The resulting (equivalent) isotropic matrix for Case 6 is:

$$\left[E_{ij} \right]_{\text{isotropic}} = \begin{bmatrix} .16577 & .04535 & .04535 & 0 & 0 & 0 \\ & .16577 & .04535 & 0 & 0 & 0 \\ & & .16577 & 0 & 0 & 0 \\ & & & .06021 & 0 & 0 \\ & & & & .06021 & 0 \\ & & & & & .06021 \end{bmatrix} \tag{2.18}$$

---

* Engineering judgment suggests that averaging elements of comparable magnitude is preferable to averaging elements that differ widely. To illustrate, averaging C_{ii} yields $\lambda + 2\mu = 0.222$ and, hence $\lambda = 0.102$, more than twice the value obtained by the method used above.

2.3.3 Determination of Stresses in Plane of Weave

Experimental evidence on some laminated ablatives suggest that these materials exhibit the lowest tensile strength and lowest pure shearing strength in the plane of the weave. For this reason, we monitor the plane of weave stresses σ and τ (shown in Figure 2-8) which are related to these two simple failure modes. It is readily seen that for sufficiently great tensile stress σ, separation can occur between contiguous layers of the weave. Similarly, a large value of shear stress τ suggests slippage between two or more adjacent bonded layers.

It appeared desirable to extend the usefulness of the SHAN code by adding a separate subroutine which would generate values of σ and τ from the well-known equations:

$$\begin{aligned} \sigma &= \tfrac{1}{2}(\sigma_z + \sigma_y) + \tfrac{1}{2}(\sigma_z - \sigma_y)\cos 2\alpha - \sigma_{zy}\sin 2\alpha \\ \tau &= \tfrac{1}{2}(\sigma_z - \sigma_y)\sin 2\alpha + \sigma_{zy}\cos 2\alpha \end{aligned} \tag{2.19}$$

Figure 2-8 shows the stresses σ_z, σ_y and σ_{zy} in the positive sense*.

2.3.4 X-ray Deposition

X-ray deposition is introduced into the SHAN code by first generating the energy profile shown in Figure 2-9. In the absence of sufficient material properties for LQP plate, material properties were obtained from a type X6200 quartz phenolic. Using representative values for the specific heat and for coefficients of thermal expansion, a separate computer code was used to determine the temperature and initial stress field corresponding to the energy profile of Figure 2-9.

The stress profiles are determined by applying compressive stresses σ_i along the material axes to balance the thermal expansion $\alpha_i \Delta T$ produced by the X-ray depositions. The coefficients of thermal expansion used for X6200 quartz phenolic were:

$$\alpha = 3.852 \times 10^{-6}\ (^{\circ}C)^{-1} \text{ in warp direction}$$

$$\alpha = 0.99 \times 10^{-6}\ (^{\circ}C)^{-1} \text{ in plane normal to warp direction}$$

The temperature rise is generated by dividing the energy by the specific heat, C = 0.206 gram-calories per gram per °C. The profiles of energy, temperature and stress are based on 129 increments of distance z. Rotation from the material to the spatial axes then generates initial profiles for the non-vanishing stresses designated by σ_z', σ_{xy}', σ_y' and σ_x'. However, one further adjustment is required because the SHAN formulation can accept only the stresses σ_z' and σ_{zy}' initially (as noted earlier in the discussion following Equations 2.5). While the SHAN code is designed to generate values of σ_x, σ_y, these two stresses are determined only from the three non-vanishing strains ϵ_z, ϵ_{zy},

---

*The sign convention corresponds to that used on Page 3 of Reference 4.

ϵ_{zy} and are not directly involved in the wave propagation aspects of the problem. The values of these stresses generated by the SHAN code will not agree with the initial stress profiles for σ_x' and σ_y' generated from the energy curve.

To adjust for this fact, the known initial differences between the thermally determined stresses σ_x' and σ_y' and the SHAN-computed stresses σ_x and σ_y is added (at each location) at subsequent times to the SHAN-computed stresses. The adjusted stresses may be represented by the equations

$$\begin{aligned} \sigma_x(z,t)_{\text{adjusted}} &= \sigma_x(z,t) + D_x(z) \\ \sigma_y(z,t)_{\text{adjusted}} &= \sigma_y(z,t) + D_y(z) \end{aligned} \qquad (2.20)$$

where

$$\begin{aligned} D_x(z) &= \sigma_x'(z,o) - \sigma_x(z,o) \\ D_y(z) &= \sigma_y'(z,o) - \sigma_y(z,o) \end{aligned} \qquad (2.21)$$

The procedure discussed here may be summarized as follows:

1. The only non-vanishing initial variables are σ_z' and σ_{zy}'.

2. The X-ray loading initialization determines D_x and D_y from Equation (2.21) where σ_x', σ_y' are known initially and σ_x and σ_y are determined by the SHAN code at $t = 0$.

3. The X-ray loading option then adds D_x and D_y to the SHAN code stresses $\sigma_x(z, t)$ and $\sigma_y(z, t)$ to obtain the adjusted stresses of Equation (2.20).

4. The adjusted stress $\sigma_y(z, t)$ is required for accurately determining the plane of weave stresses σ and τ .

5. The thermal expansion does not influence the stresses σ_{zx} and σ_{zy}. Since these stresses and the corresponding strains are not excited initially, they vanish at all times as a consequence of the decoupling of the equations of motion.

2.4 DISCUSSION OF RESULTS

2.4.1 Wave Speeds and Characteristics

Seven computer runs at different layup angles were completed. A summary of the wave speeds and the transit times for each case is listed in Table 2-I.

Cases 1 to 5 constitute the principal impact-flyer plate runs made at increasing layup angles. Using the material matrix for Case 2, Case 7 was run with the energy profile shown in Figure 2-9. Case 6 represents the "equivalent isotropic" run described by the isotropic material matrix exhibited in the previous section.

In all cases, the aluminum flyer has the wave speeds and transit times listed in Table 2-I. The transit time always represents the time interval in μsec for a wave of any type to traverse the thickness of material it is traveling in.

TABLE 2-I WAVE SPEEDS AND TRANSIT TIME FOR LQP

Case No.	Layup Angle (deg)	Wave Speed C_1 (cm/μsec)	Transit Time (μsec)	Wave Speed C_2 (cm/μsec)	Transit Time (μsec)
1	0	.273	2.34	.189	3.38
2	20	.286	2.24	.194	3.31
3	40	.321	1.99	.196	3.76
4	65	.368	1.74	.192	3.33
5	90	.387	1.65	.189	3.38
7 (X-ray Loading)	20	.286	2.24	.194	3.31
6 (Isotropic)		.311	2.06	.188	3.41
(Aluminum Flyer Plate)		.615	.13	.310	.258

For Cases 1, 5, and 6, the anisotropic material matrix contains elements such that $A_{34} = E_{34} = 0$. This corresponds to the special case mentioned earlier, and implies that the equations for the axial stress and axial displacement (σ_z, W) are uncoupled from the transverse shear stress and displacement (σ_{zy}, V). Since σ_{zy} and V are not excited initially, they vanish for all times in these three cases.

The duration of a run was 6.5 μsec. The greater wave speed C_1 is such that, for this time interval, there are two traverses of the target plate for layup angles of 0 and 20 degrees and three traverses for the higher layup angles through the 0.64 cm thick LQP plate. The lower wave speed, C_2, corresponds to one reflection only at the right free edge. During the same time interval, the two waves in the thinner aluminum flyer plate reflect back and forth 50 times and 25 times, respectively. The numerous reflections in the flyer plate initiate new characteristics at the interface with the anisotropic material and thus tend to smooth out sharp fronts.

The wave speeds as functions of layup angle are shown in Figure 2-10. The "equivalent isotropic" speeds are shown by dashed lines. The higher wave speed, C_1, increases approximately 50 percent as the layup angle increases from 0 to 90 degrees, but the lower wave speed, C_2, remains relatively constant.

The wave speeds and transit times may be used to construct a typical characteristics graph as suggested by Figure 2-11. However, the identification of states on such a diagram is not feasible because of the multiplicity of reflections in the flyer plate.

The progress of the initial compression wave can be traced readily from the SHAN code print out. Table 2-II, corresponding to a 20 degree layup angle (Case 2), shows the time and location of the maximum axial stress σ_z. In addition the corresponding values of σ_{zy}, σ_y, σ_z are listed. Both the reflection at the right edge and the progression of the wave throughout the LQP plate, arriving again at the interface at about 4.45 μsec, are easily noted.

Since a major objective is to assess failure, the discussion of stresses is emphasized. The SHAN code determines the velocity field as well as the stress field, but the former is of lesser interest than the latter.

The displacement, U, and stress, σ_{zx}, which are not initially excited, vanish. Hence, those quantities and the associated uncoupled equations may be disregarded, as mentioned earlier. This corresponds to disregarding Equation (2.7e) and Equation (2.7f) and eliminates one wave speed and two characteristics.

The general features of the stress field for all layup angles are reflected in the typical results exhibited in Table 2-II. The normal stresses perpendicular to the direction of impact velocity, σ_y and σ_x, are approximately equal to each other. Both stresses are roughly 1/3 the normal stress, σ_z, and agree in sign with σ_z, so that the three stresses σ_x, σ_y, σ_z are either all tensile or all compressive. The shear stress, σ_{zy}, has an approximate value between 10 and 20 percent that of σ_z. This stress will also vanish (together with the velocity, V) when A_{34} and E_{34} vanish, since there is a decoupling of the four equations of motion. The dominant stress is σ_z, corresponding to the direction of impact.

TABLE 2-II PROGRESSION OF WAVE (CASE 2, 20° LAY UP ANGLE)

Time (μsec)	Location From Interface (cm)	Stresses (kb)				
		σ_z	σ_{zy}	σ_y	σ_x	
.05	.096	-.747	-.033	-.247	-.251	
1.00	.256	-.726	-.141	-.277	-.238	
1.5	.400	-.726	-.141	-.277	-.238	
2.0	.544	-.726	-.141	-.277	-.238	Reflection
2.5	.576	.374	.072	.143	.122	
2.5	.576	.374	.072	.143	.122	
3.0	.432	.686	.175	.276	.222	
3.5	.288	.722	.145	.277	.236	
4.0	.144	.726	.142	.277	.237	
4.5	0	1.12	.187	.416	.238	Interface
5.0	.112	.501	.094	.112	.164	
5.5	.256	.417	-.025	.256	.143	
6.0	.4	.391	.0631	.400	.129	

2.4.2 The Initial Compressive Pulse

The progression of the initial compressive pulse across the LQP target plate is summarized in Table 2-III. In each case, the stress σ_z is given for locations corresponding to the plate quarter thicknesses. The numbers in parenthesis denote the time in μsec corresponding to the arrival of the stress σ_z.

Comparing the flyer plate runs to the equivalent isotropic results of Case 6 emphasizes that the process of averaging properties appears reasonable, but no sharp or unusual features are suggested by the transition from isotropic to anisotropic material (beyond the implications this change has in the number of speeds and characteristics).

2.4.3 Peak Tensile Stress

In all flyer plate cases, the compressive pulse progresses (at the higher wave speed, C_1, of Table 2-I) to the right in the LQP plate and reflects as a tensile unloading wave. The tensile unloading wave progresses along the incoming characteristic at the same speed, C_1. The existing SHAN code implies a welded interface across which the basic six variables are continuous. Since failure and spallation phenomena are related to the tensile unloading wave, the stresses that arise after the tensile unloading wave reaches the interface between the target and flyer plate are ignored. Physically, the flyer plate would rebound, but the existing SHAN code was not designed to take this phenomenon into account. The rough edit used in establishing Table 2-III also leads to Table 2-IV, which lists the maximum tensile stress, σ_z, at the plate quarter thicknesses.

The flyer plate cases were run with a fine edit option over regions centered upon the unloading characteristics, in order to locate peak tensile stresses, σ_z and σ.

The peak tensile stresses, σ_z and σ, are shown as functions of position in Figures 2-12 and 2-13. The peak in-plane shear stress, τ, is exhibited in Figure 2-13 only for Cases 2, 3 and 4. In Cases 1, 5 and 6, decoupling of the equations of motion is such that the shear stress, τ, vanishes.

Figure 2-12 shows that as the layup angle, α, increases, the peak stress, σ_z, also increases. For layup angles from 0 to 40 degrees, the differences in peak stress, σ_z, are small. The mean position of the equivalent isotropic case is evident.

In contrast, Figure 2-13 shows that the transition from isotropy to anisotropy reduces the peak value of the plane of weave tensile stress σ. Thus, there is in this case a small compensating effect for the weakness to σ concomitant with the introduction of anisotropy. The stress decreases further as the layup angle increases, reaching its minimum value for a 90-degree layup.

Peak values of the plane of weave shear stress, τ, when this stress is appreciable, occur only for layup angles other than 0 and 90 degrees. Figure 2-14 exhibits the maximum value for this stress as obtained in the neighborhood of the incoming characteristic associated with the tensile unloading wave.

TABLE 2-III MAXIMUM COMPRESSIVE STRESS, σ_z (KILOBARS)

Case No.	Initial Pulse	LOCATION IN LQP PLATE z = . 16 cm		z = .32 cm		z = .48 cm		
1	.728	.728	(.75)	.728	(1. 25)	.623	(2.)	
2	.747	.726	(.75)	.726	(1. 25)	.726	(1. 75)	
3	.803	.758	(.5)	.758	(1. 0)	.758	(1. 5)	
4	.898	.876	(.5)	.876	(1. 0)	.876	(1. 5)	
5	.946	.946	(.5)	.946	(1. 0)	.946	(1. 25)	
6	.805	.694	(.75)	.737	(1. 25)	.780	(1. 75)	Isotropic
7	1.19 *	.313	(.5)	1.88	(1.0)	2.13	(1.6)	X-Ray Loading

(*Initial pulse at z = . 005 cm)

TABLE 2-IV MAXIMUM TENSILE STRESS, σ_z (KILOBARS)

Case No.	LOCATION IN LQP PLATE								
	$z = 0$(1)		$z = .16$ cm		$z = .32$ cm		$z = .48$ cm		
1	1.13	(4.75)	.728	(4.25)	.638	(3.75)	.663	(3.)	
2	1.12	(4.5)	.725	(4.)	.721	(3.5)	.647	(3.)	
3	1.13	(4.0)	.756	(3.5)	.746	(3.)	.628	(2.5)	
4	1.267	(3.5)	.843	(3.25)	.867	(2.75)	.798	(2.25)	
5	1.35	(3.5)	.946	(3.)	.600(2)	(2.75)	.886	(2.25)	
6	1.221	(4.25)	.806	(3.75)	.802	(3.25)	.763	(2.75)	Isotropic
7	0		.244	(.6)	.321	(3.3)	.208	(1.8)	X-Ray Loading

(1) Values in this column correspond to a tensile wave after reflection at the interface.

(2) Edit misses peak stress of .818 located at $z = .304$ cm when $t = 2.75$ μsec.

Comparison of peak values of σ and τ in Cases 2, 3 and 4 indicate that generally the normal stress, σ, is greater than the shear stress, τ. The two peak stresses are roughly comparable, however, in Cases 3 and 4 in the right half of the LQP target plate.

In all flyer impact runs (Cases 1 to 6), there is no isolated relative maximum value of σ_z or σ near the right free edge of the target plate. The search, based on fine edits in domains of z-t space along the characteristic corresponding to the tensile unloading wave, leads to the conclusion that, in every case, the maximum value of σ_z and σ increases steadily as the wave approaches the interface. Since the lack of anisotropy as exhibited by Case 6 does not alter this conclusion, the steady increase in peak values of σ_z and σ can presumably be attributed to the effect of the numerous reflections that the thin flyer plate generates at the interface.

2.4.4 Results of X-ray Loading

The procedure discussed in Section 2.3.4 was incorporated as a separate option in the original SHAN code. A representative run (designated as Case 7) was completed. The material matrix for the anisotropic target plate was identical to that used in Case 2 of the flyer plate runs (corresponding to a 20-degree layup angle).

It is necessary to initiate the X-ray pulse at a location just inside the stress-free left face. The value $z = 0.005$ cm corresponds to this initial location. In the first few time steps, the pulse decays rapidly. The decay of the initial stress, σ_z, in the first two time steps is shown in Figure 2-15.

2.5 DISCUSSION OF STRESS PROFILES

In Section 2.7 are exhibited profiles of the dominant stress, σ_z, generated by the SHAN code for a 20-degree layup angle. Profiles of σ_z as functions of both time and distance are shown for the flyer plate impact and the X-ray loading for the same material matrix in order to facilitate comparison of the wave shapes in these two cases.

The progression of each wave can be traced readily. The two wave speeds are $C_1 = 0.286$ cm/μsec and $C_2 = 0.194$ cm/μsec. The transit times to traverse one fourth the distance of the target plate are $t_1 = 0.56$ and $t_2 = 0.83$ μsec, respectively. The curves of stress σ_z versus time t for the flyer plate run (Case 2) exhibit a sharp pulse followed by an unloading wave. The width of this pulse on the curves is about 0.27 μsec corresponding to the time difference $(t_1 - t_2)$. The progression of the pulse is readily traced by comparing profiles at successive locations corresponding to $z = 0.16$, 0.32 and 0.48 cm. Each profile exhibits the outgoing compressive pulse and the tensile pulse reflected from the right edge of the target plate. For example, the profile corresponding to $z = 0.16$ cm reflects a time difference of 3.25 μsecs between these two pulses, which may be compared with the computed time interval $6t_1 = 3.36$ μsecs.

It should be recalled that interface reflections occur after 4.48 μsecs, so events beyond this time interval do not correspond to a rebounding flyer plate.

An analysis, similar to that of Case 2, may be made for the X-ray loading of Case 7. Here, the initial profile corresponds to two waves: a compressive pulse moving to the right from the initial location z = 0.005 cm, and a similar pulse moving to the left, which reflects as a tensile pulse at the location z = 0 cm. The latter pulse travels a distance 0.01 cm further than the compressive pulse in reaching a particular station. However, this difference is negligible in analyzing the stress profiles, both because it is less than a cell width in z, and because it corresponds to a time interval of only about 0.035 μsecs.

Hence, the X-ray loading profiles exhibit a sharp peak extending from compression at the leading edge to tension at the trailing edge. The pulse progresses across the plate and is reversed by reflection at the right free edge with a pulse width again of order 0.24 to 0.27 μsec. The progression of the pulse peaks can be traced through the successive profiles corresponding to z = 0.16, 0.32 and 0.48 cm., as discussed above for the flyer plate case. However, the wave shape is more dispersed spatially, as a consequence of the initial loading, than in the comparable flyer plate run.

The influence of layup angle is reflected primarily by the peak stresses plotted in Figures 2-12 through 2-14. For the material matrix used in this report, the axial stress, σ_z, reaches an increasingly higher tensile peak as the layup angle increases. However, the peak tensile stress normal to the plane of weave decreases with increasing layup angle and reaches a minimum at 90 degrees. Since the selection of a layup angle for a typical nose tip model probably depends on many design factors and fabrication considerations, it does not appear justifiable to recommend an optimum angle based on the limited runs of the current SHAN code.

Since the peak tensile stress normal to the plane of weave is less for an anisotropic material than for an isotropic material, it is tentatively concluded that anisotropy tends to reduce peak stresses in layered woven composites. This is inferred from the comparison of stress, σ, for the isotropic material (Case 6) with the anisotropic material (Case 1, zero layup angle) in Figure 2-13.

2.6 FUTURE APPLICATIONS OF THE SHAN CODE

The preceding discussion has emphasized the stress fields generated by the current version of the SHAN code as applied to thin flyer plate impacts upon a laminated quartz phenolic target plate for five different layup angles. It was originally expected that X-ray energy deposition profiles generating stress fields of about the order of magnitude of those resulting from the assumed impact velocity of 0.002 cm/μsec would be available as inputs. In the absence of such profiles, the single X-ray loading of Case 7 constitutes a representative sample. The linearity of the equations implies that doubling the initial velocity will double the stress. Consequently, differences in peak stresses between, for example, Cases 2 and 7 can be easily scaled. A comparison of the wave shapes in these two cases reveals significant differences in the waveforms.

In order to exhibit typical outputs, plots of axial stress, σ_z, as a function of time and of distance are included in Section 2.7. All representative printouts were selected from Case 2 and Case 7, corresponding to a 20-degree layup angle, in order to facilitate a comparison of wave shapes for the two types of loading. Plots of stress σ_z against time, t, are included for locations corresponding to one-fourth the thickness of the LQP plate. Stress profiles throughout the plate are shown for times of 2, 4 and 6 μsec.

The initial version of the SHAN code is a relatively inexpensive exploratory tool; many more geometries and initial velocities can be introduced, not only for LQP plate, but for other laminates and composites found in nose tip construction. Indeed, a useful parametric study can be conceived based on changing the elements of the material matrix of the anisotropic material in order to minimize a stress or to satisfy some other selected design criterion.

The most markedly anisotropic property of many laminated ablatives is that of failure. For example, carbon phenolic (MX4926) can sustain 18,000 psi of tension in the plane of the weave, but only 900 psi of tension normal to that plane. Similarly it can support 14,700 psi of pure shear stress in the weave plane, but only 2,900 psi of pure shear which tends to cause slip between adjacent layers.

In contrast to these order of magnitude variations in the failure properties, the constitutive relations are not extremely anisotropic, in that no element of the stiffness matrix is significantly different from the corresponding element of the isotropic equivalent matrix.

The utility of the SHAN code has been extended to include the option of determining maximum stresses associated with the plane of weave. Further runs using this option should be made and assessed relative to the two modes of failure described. This assessment requires a close correlation with the experimental effort being conducted by Avco(2).

In summary, it appears desirable to extend the SHAN code in one or more of the directions suggested while retaining its one-dimensional character. It would also be desirable to more fully explore the effect of changes in the material matrix and in geometries. Additional X-ray loadings and problems possessing initial conditions which excite all six stresses should be examined more fully.

2.7 APPENDIX TO CHAPTER II

The following describes the various SHAN printouts included in this section:

1. Stress σ_z versus time t for 20-degree layup angle (Flyer plate impact - 4 locations) - Figures 2-16 through 2-19.

2. Stress σ_z versus time t for 20-degree layup angle (X-ray loading - 3 locations) - Figures 2-20 through 2-22.

3. Stress σ_z versus location z in LQP plate for 20-degree layup angle (flyer plate impact - time, t = 2, 4, 6 μsecs) - Figures 2-23 through 2-25.

4. Stress σ_z versus location z in LQP plate for 20-degree layup angle (X-ray loading - time, t = 2, 4, 6 μ secs) - Figures 2-26 through 2-28.

NOTE:

Difficulties in edit procedures are reflected in the numbering of the profiles in the Appendix. Case 3 above is Case 2 of text.

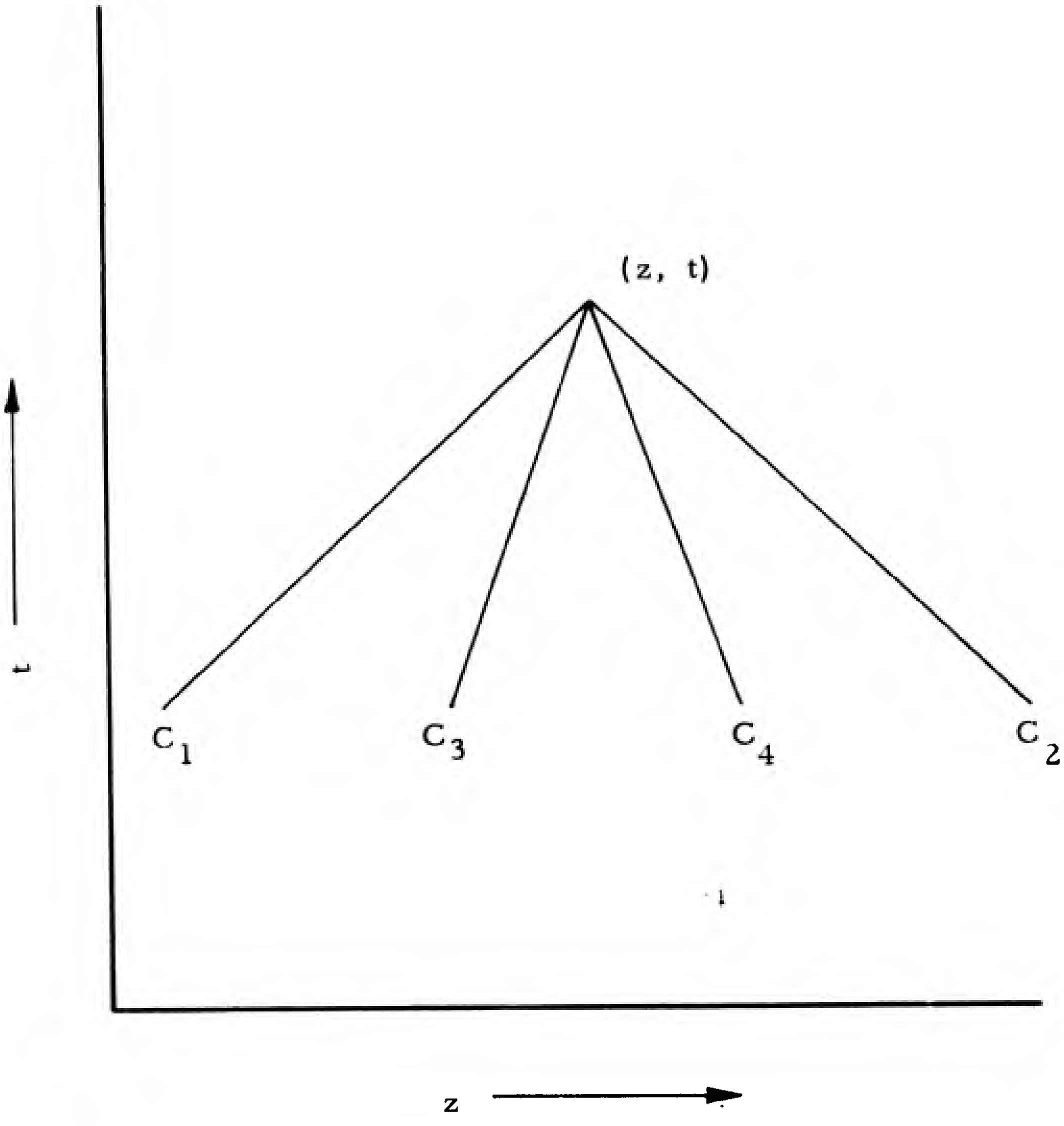

Figure 2.1 CHARACTERISTIC DIRECTIONS

DEFINITIONS

$$\underline{\underline{a}} = \begin{bmatrix} \rho_o C_1 A_{34} & -A_{34} & \dfrac{1-\rho_o C_1^2 A_{33}}{C_1} & \rho_o C_1^2 \Delta - A_{44} & 0 & 0 \\ \rho_o C_2 A_{34} & -A_{34} & \dfrac{1-\rho_o C_2^2 A_{33}}{C_2} & \rho_o C_2^2 \Delta - A_{44} & 0 & 0 \\ \rho_o C_3 A_{34} & -A_{34} & \dfrac{1-\rho_o C_3^2 A_{33}}{C_3} & \rho_o C_3^2 \Delta - A_{44} & 0 & 0 \\ \rho_o C_4 A_{34} & -A_{34} & \dfrac{1-\rho_o C_4^2 A_{33}}{C_4} & \rho_o C_4^2 \Delta - A_{44} & 0 & 0 \\ 0 & 0 & 0 & 0 & \rho_o C_5 & -1 \\ 0 & 0 & 0 & 0 & \rho_o C_6 & -1 \end{bmatrix}$$

$$\Delta = A_{33} \; A_{44} - A_{34}^2$$

$$\underline{X} = \begin{bmatrix} X^1 \\ X^2 \\ X^3 \\ X^4 \\ X^5 \\ X^6 \end{bmatrix} = \begin{bmatrix} W \\ \sigma_z \\ V \\ \sigma_{zy} \\ V \\ \sigma_{zx} \end{bmatrix}, \quad \underline{K} = \begin{bmatrix} K^1 \\ K^2 \\ K^3 \\ K^4 \\ K^5 \\ K^6 \end{bmatrix}, \quad \underline{\underline{b}}\;\underline{\underline{a}} = \underline{\underline{a}}\;\underline{\underline{b}} = 1$$

$$\underline{\underline{a}}\;\underline{X} = \underline{K} \qquad \underline{X} = \underline{\underline{b}}\;\underline{K}$$

Figure 2.2 MATRIX DEFINITIONS

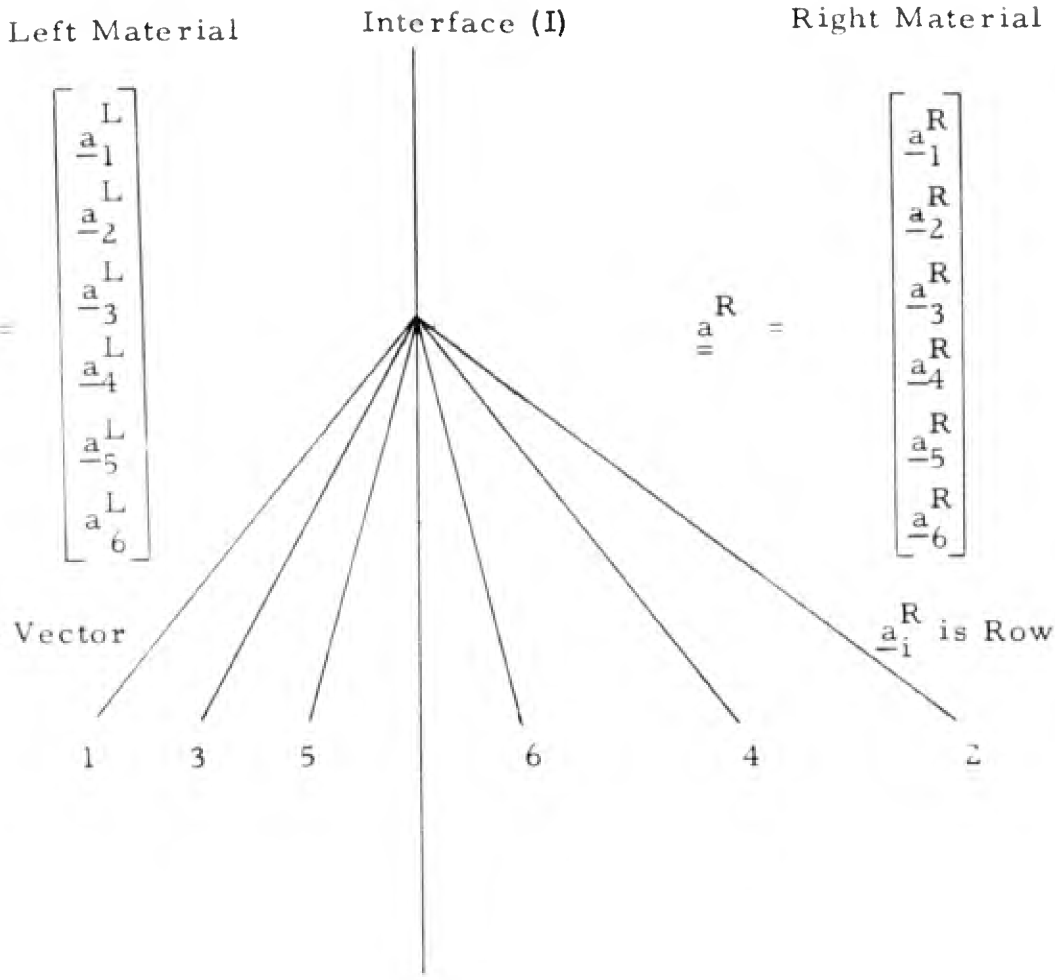

$$\underline{\underline{a}}^{L} = \begin{bmatrix} \underline{a}_1^{L} \\ \underline{a}_2^{L} \\ \underline{a}_3^{L} \\ \underline{a}_4^{L} \\ \underline{a}_5^{L} \\ a_6^{L} \end{bmatrix} \qquad \underline{\underline{a}}^{R} = \begin{bmatrix} \underline{a}_1^{R} \\ \underline{a}_2^{R} \\ \underline{a}_3^{R} \\ \underline{a}_4^{R} \\ \underline{a}_5^{R} \\ \underline{a}_6^{R} \end{bmatrix}$$

$\underline{a}_i^{L}$ is Row Vector

$\underline{a}_i^{R}$ is Row Vector

$$\underline{\underline{a}}^{I} = \begin{bmatrix} \underline{a}_1^{L} \\ \underline{a}_2^{R} \\ \underline{a}_3^{L} \\ \underline{a}_4^{R} \\ \underline{a}_5^{L} \\ \underline{a}_6^{R} \end{bmatrix}$$

Interface Matrix Where:

$$\underline{\underline{a}}^{I}\,\underline{x} = \underline{K}$$

$$\underline{x} = \underline{\underline{b}}^{I}\,K$$

Where:

$$\underline{\underline{b}}^{I}\,\underline{\underline{a}}^{I} = \underline{\underline{a}}^{I}\,\underline{\underline{b}}^{I} = \underline{\underline{1}}$$

Figure 2.3 INTERFACE MATRIX

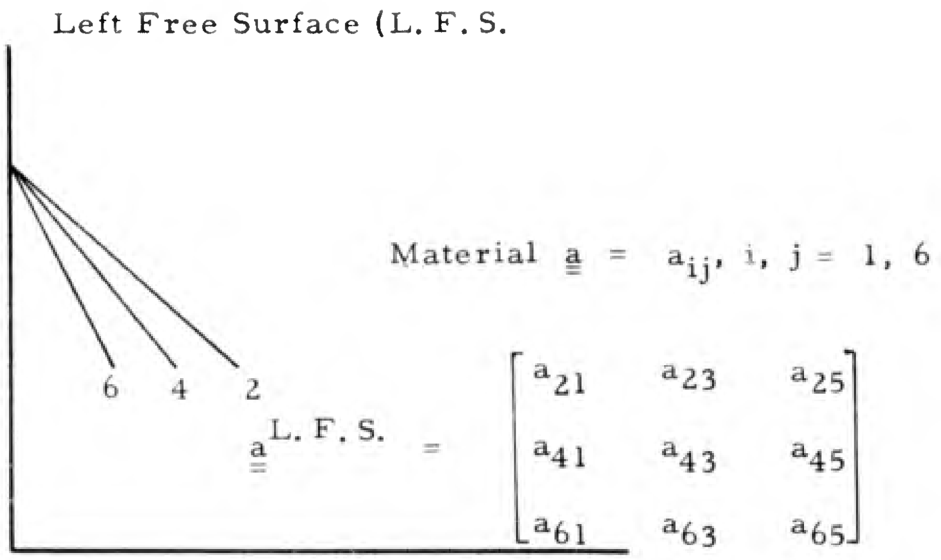

Material $\underline{\underline{a}} = a_{ij}, \; i, j = 1, 6$

$$\underline{\underline{a}}^{L.F.S.} = \begin{bmatrix} a_{21} & a_{23} & a_{25} \\ a_{41} & a_{43} & a_{45} \\ a_{61} & a_{63} & a_{65} \end{bmatrix}$$

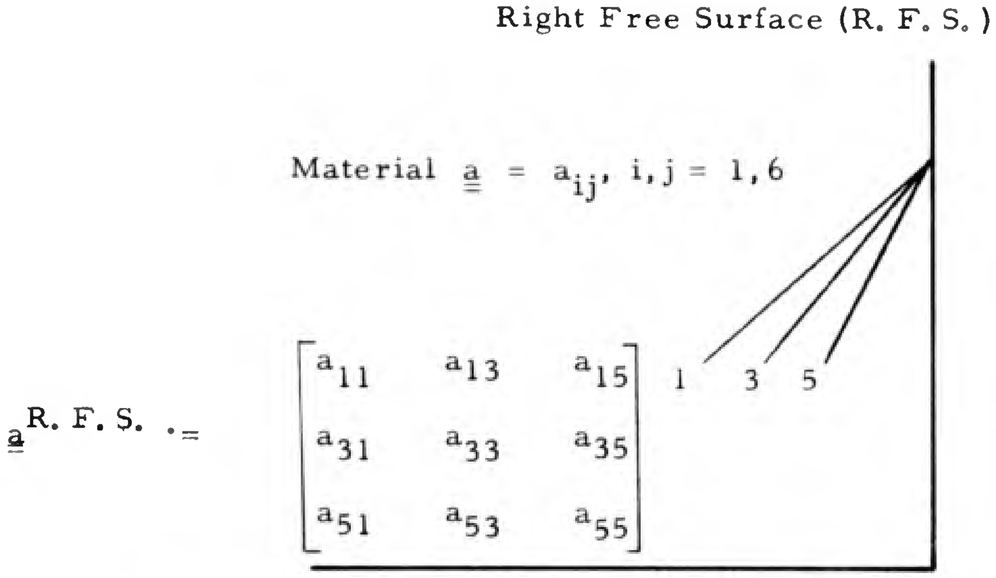

Material $\underline{\underline{a}} = a_{ij}, \; i,j = 1,6$

$$\underline{\underline{a}}^{R.F.S.} = \begin{bmatrix} a_{11} & a_{13} & a_{15} \\ a_{31} & a_{33} & a_{35} \\ a_{51} & a_{53} & a_{55} \end{bmatrix}$$

$$\left[\underline{\underline{a}}^{L.F.S.}\right] \begin{bmatrix} x^1 \\ x^3 \\ x^5 \end{bmatrix} = \begin{bmatrix} K^2 \\ K^4 \\ K^6 \end{bmatrix} \qquad \left[\underline{\underline{a}}^{R.F.S.}\right] \begin{bmatrix} x^1 \\ x^3 \\ x^5 \end{bmatrix} = \begin{bmatrix} K^1 \\ K^3 \\ K^5 \end{bmatrix}$$

Figure 2.4 FREE SURFACE

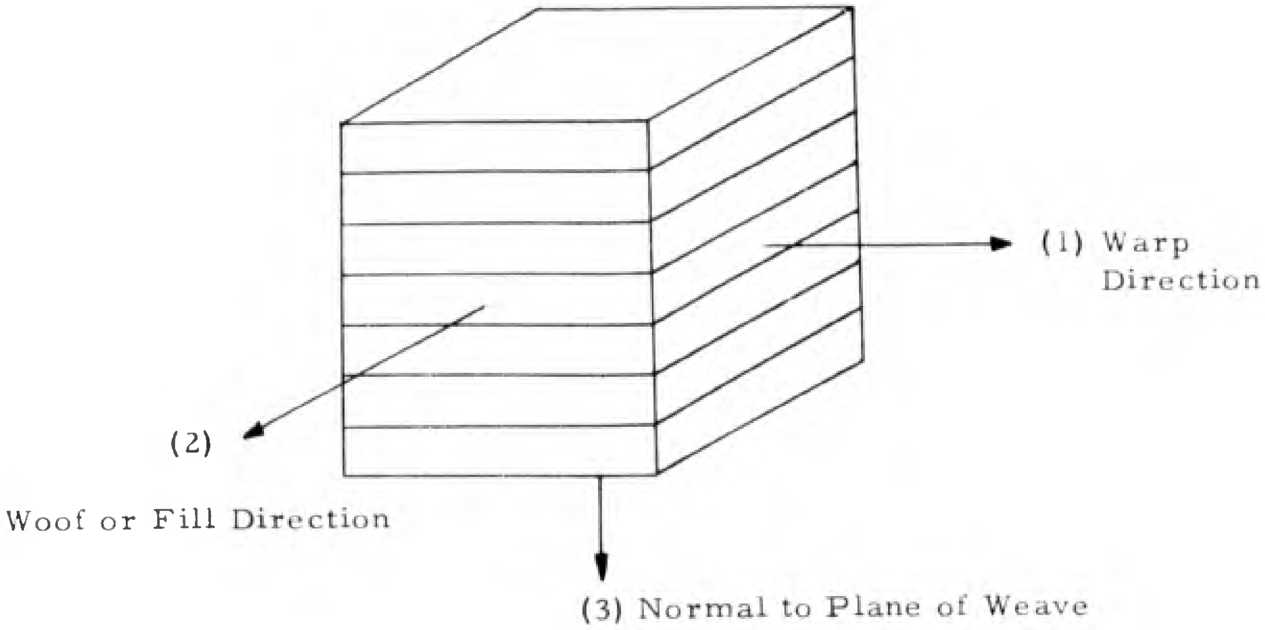

Figure 2.5 MATERIAL AXES FOR LQP (PLANE 1-2 IS PLANE OF WEAVE)

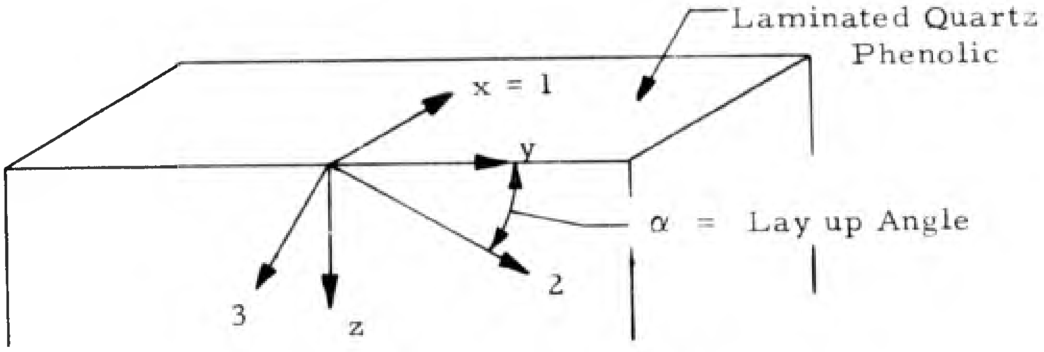

Figure 2.6 SPATIAL AXES FOR LQP (PLANE 1-2 IS PLANE OF WEAVE)

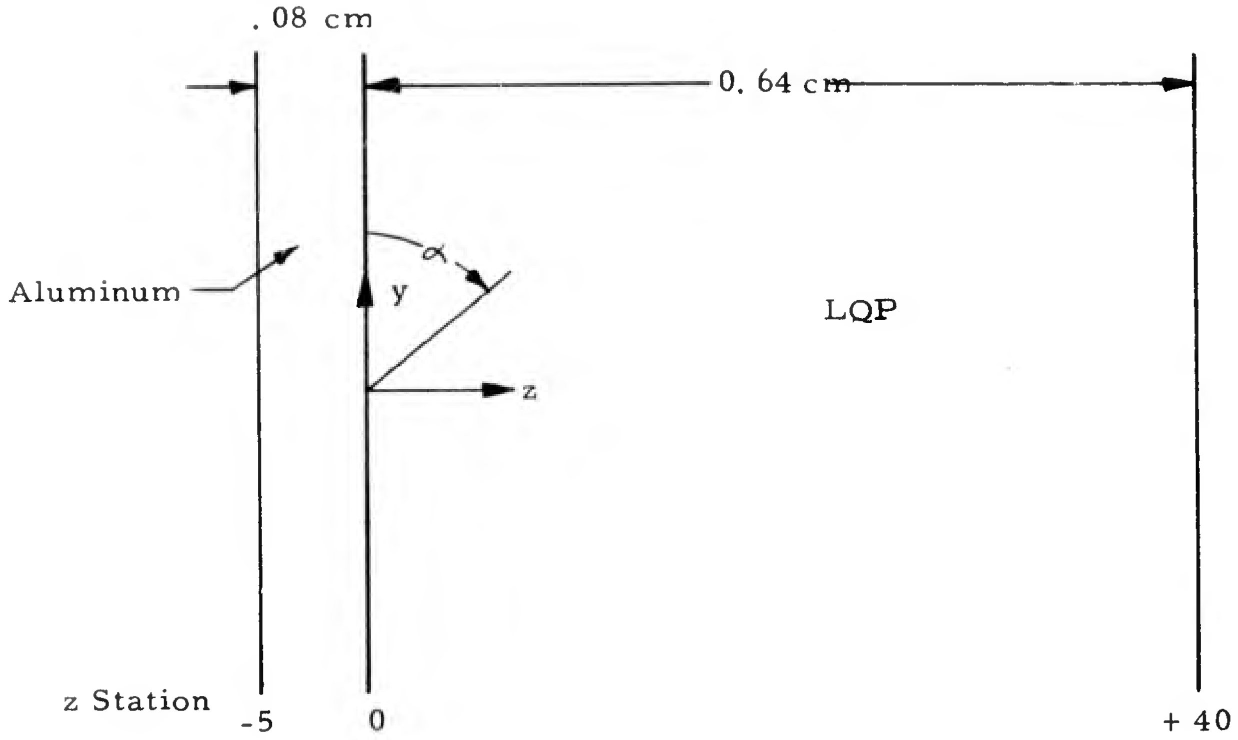

Spatial Increment, Δz = . 016 cm

Time Increment, Δt = . 05 μsec

Figure 2.7 GEOMETRIC DIMENSIONS FOR FLYER PLATE IMPACTS

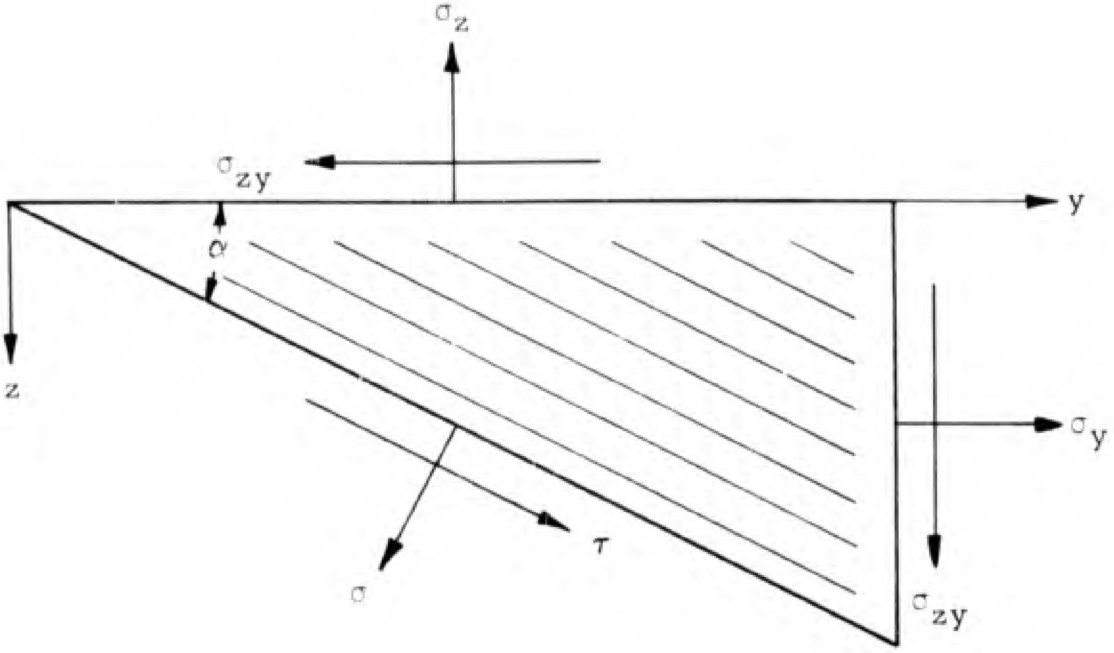

Figure 2.8 NORMAL AND SHEAR STRESSES ON PLANE OF WEAVE

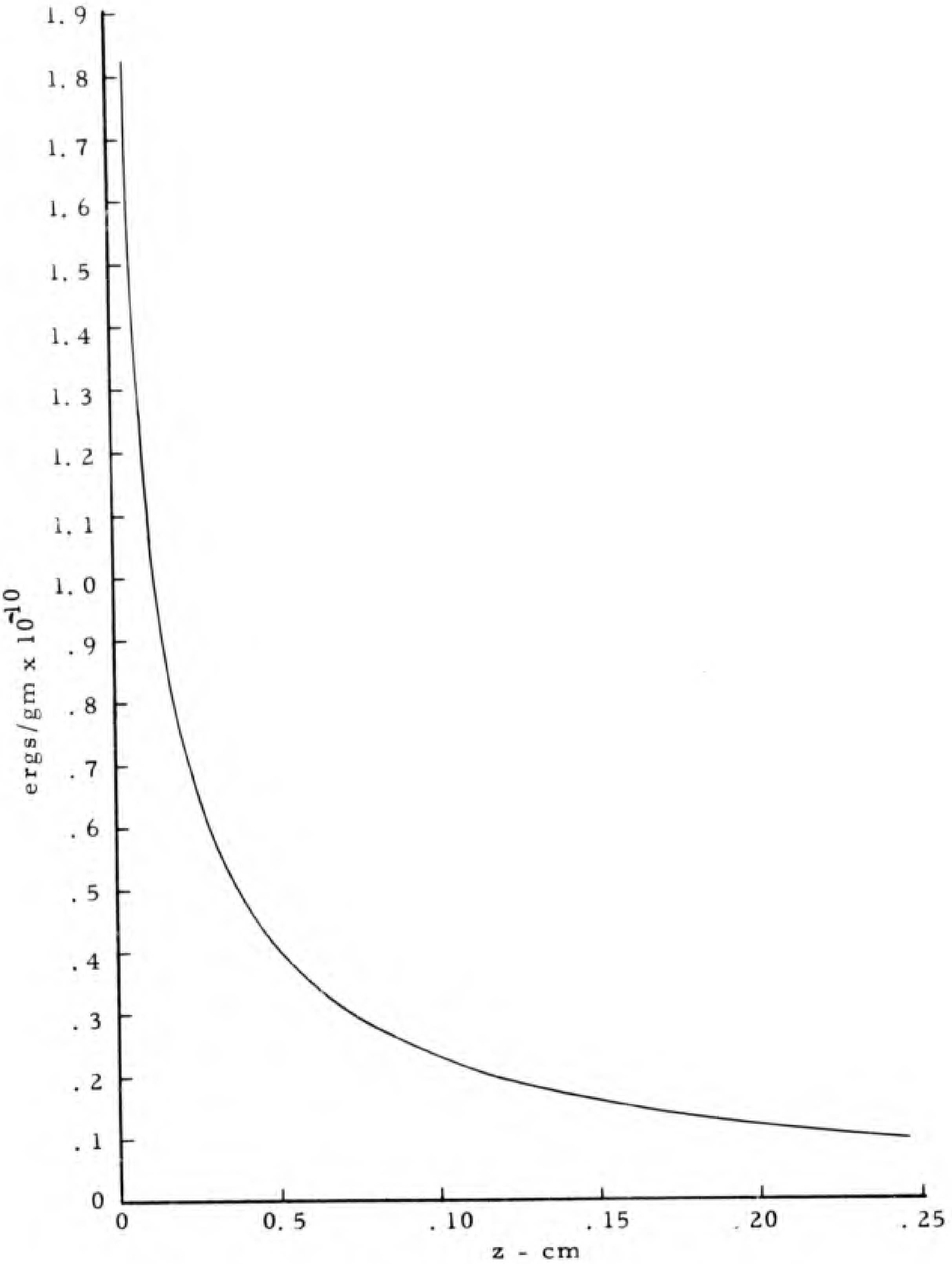

Figure 2.9 REPRESENTATIVE X-RAY PROFILE

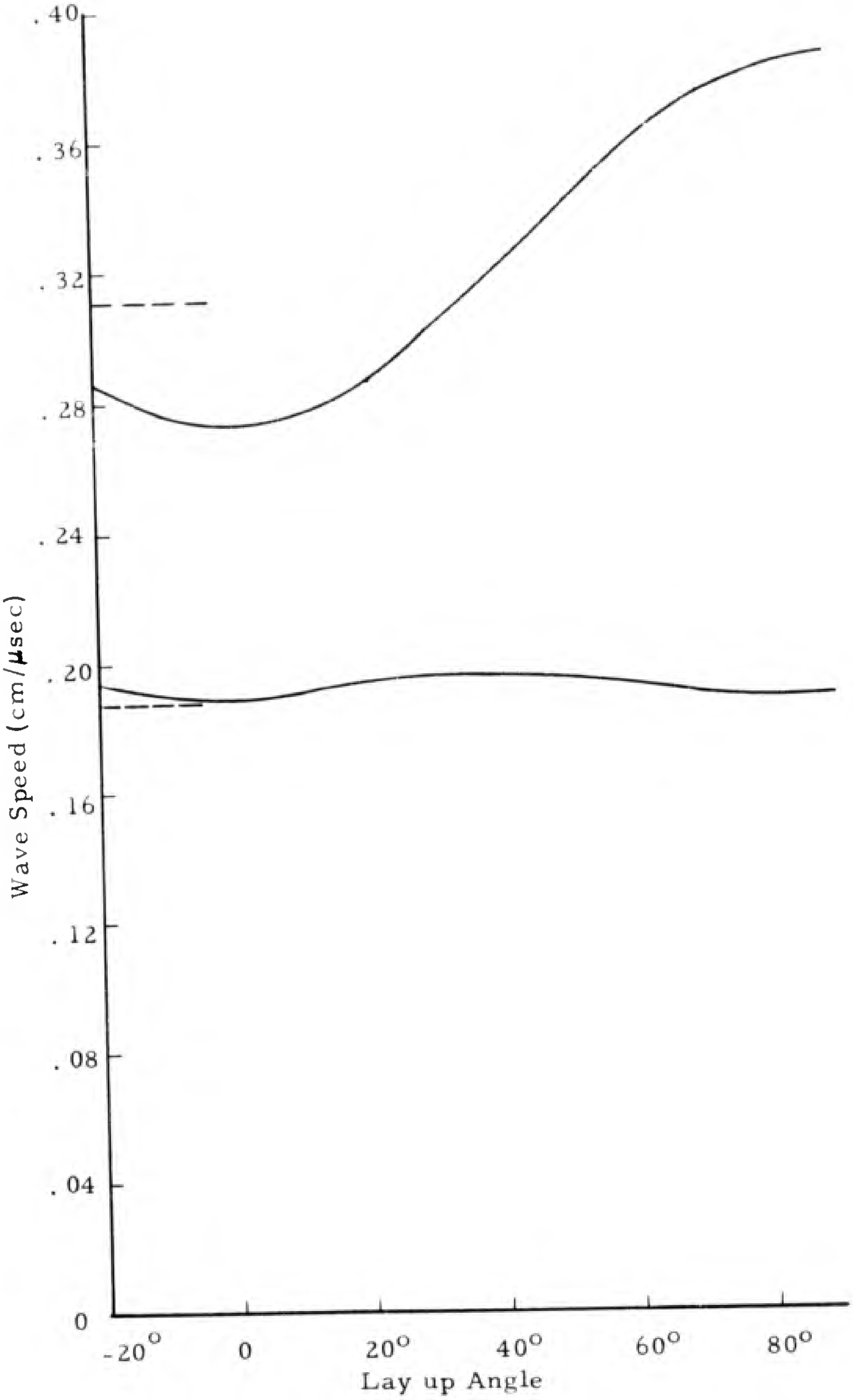

Figure 2.10 WAVE SPEED AS A FUNCTION OF LAYUP ANGLE

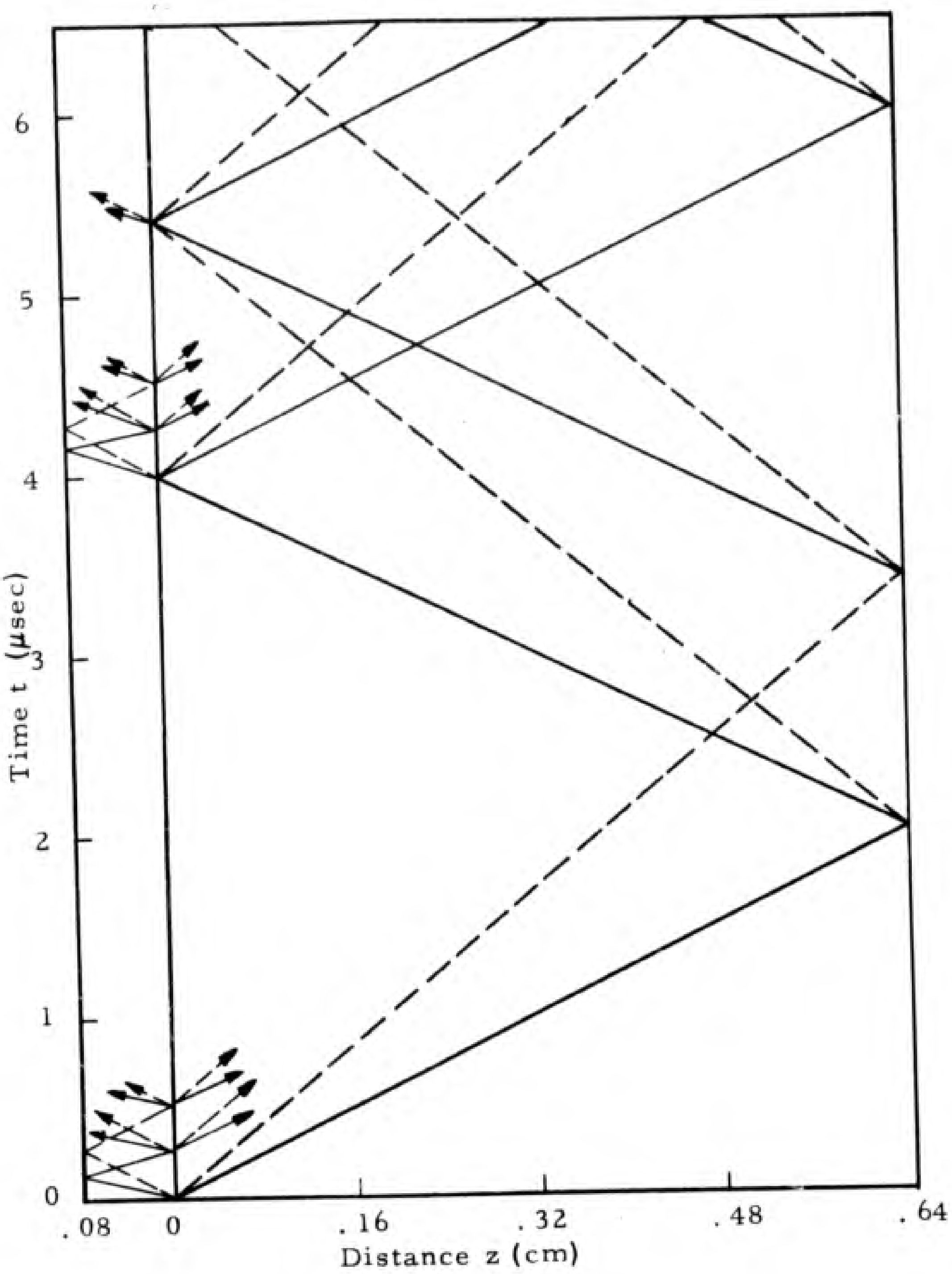

Figure 2.11 CHARACTERISTICS GRAPH

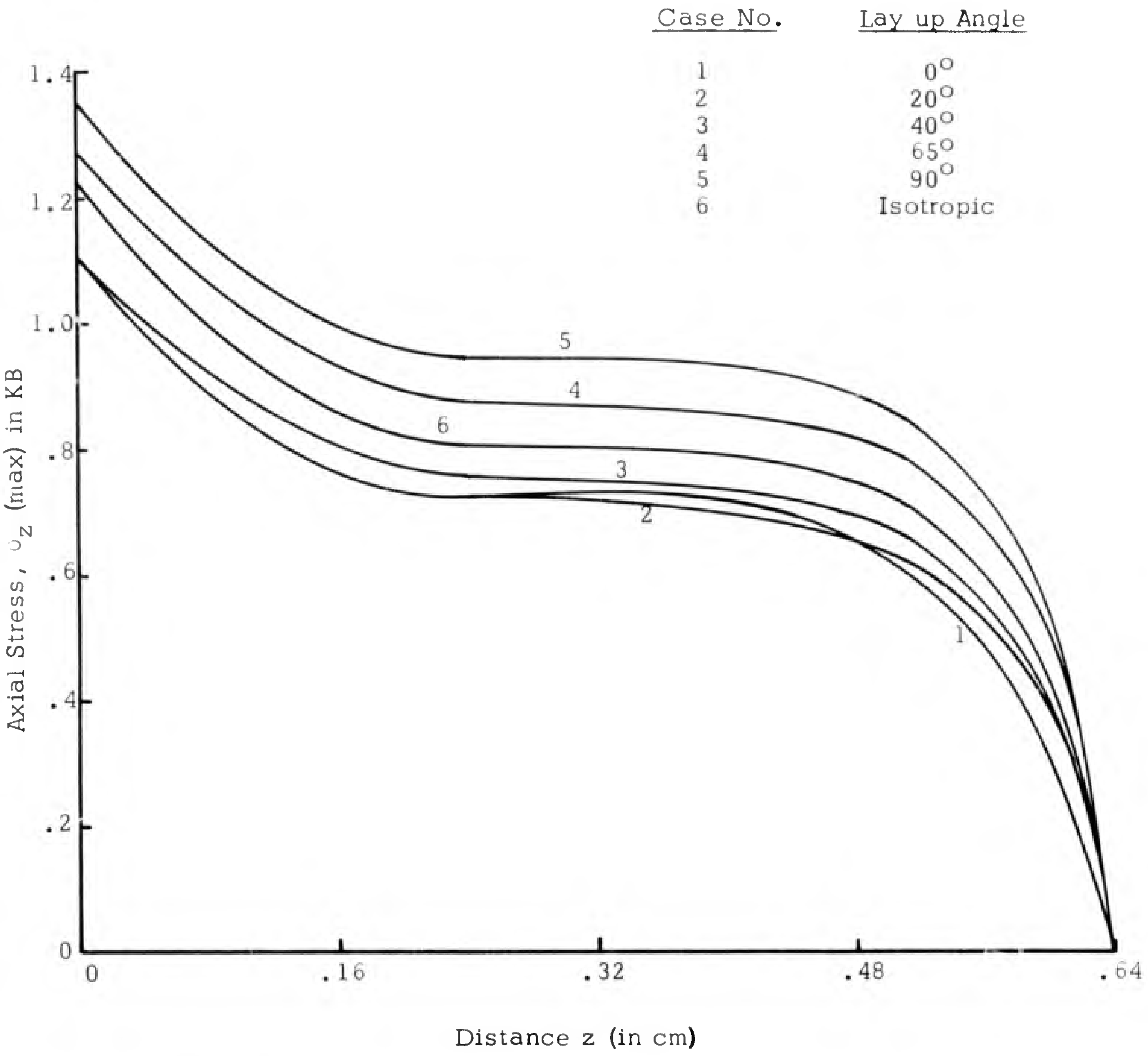

Figure 2.12 MAXIMUM AXIAL STRESS IN LAMINATED QUARTZ PHENOLIC TARGET

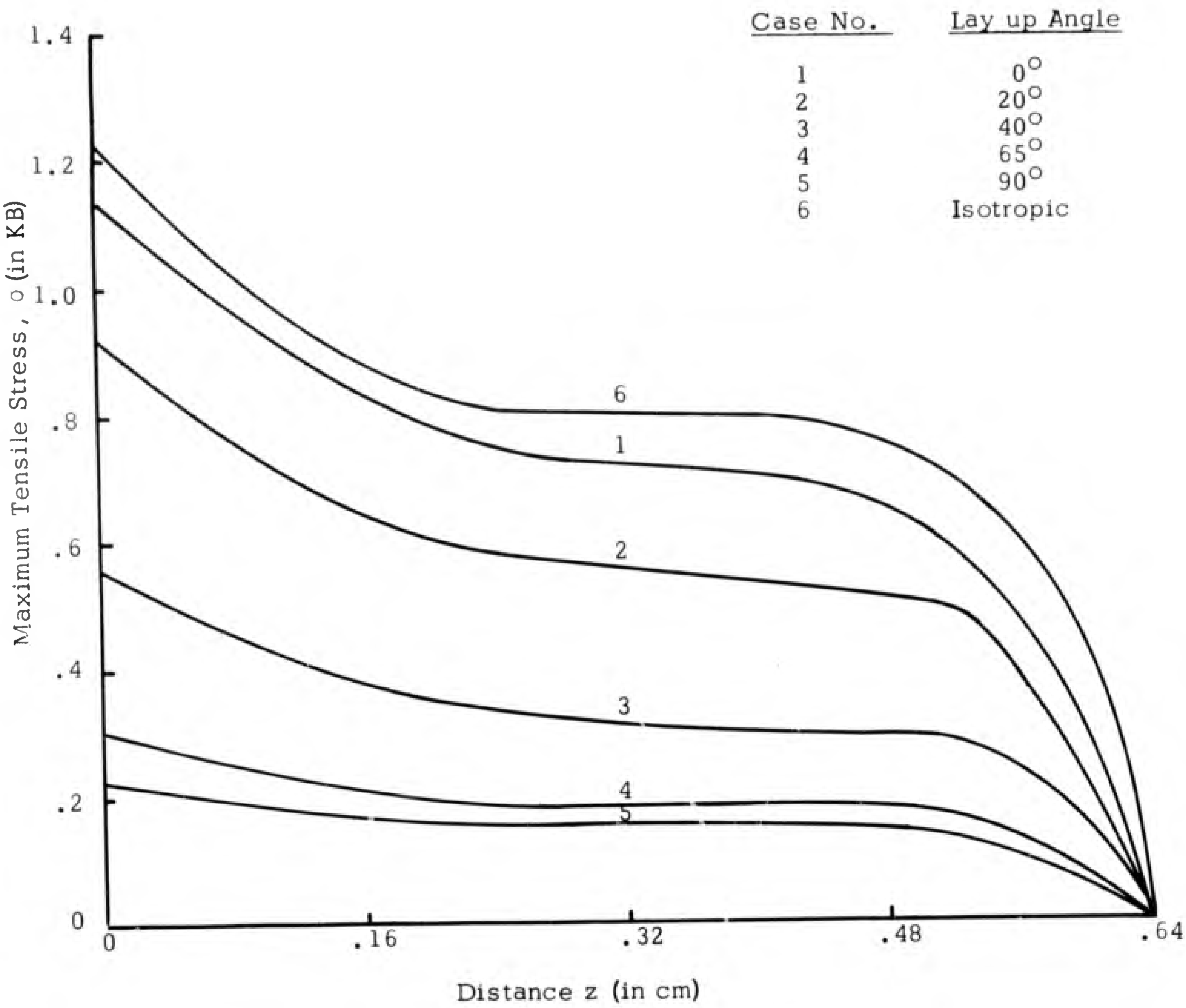

Figure 2.13 PEAK TENSILE STRESS NORMAL TO THE PLANE OF WEAVE

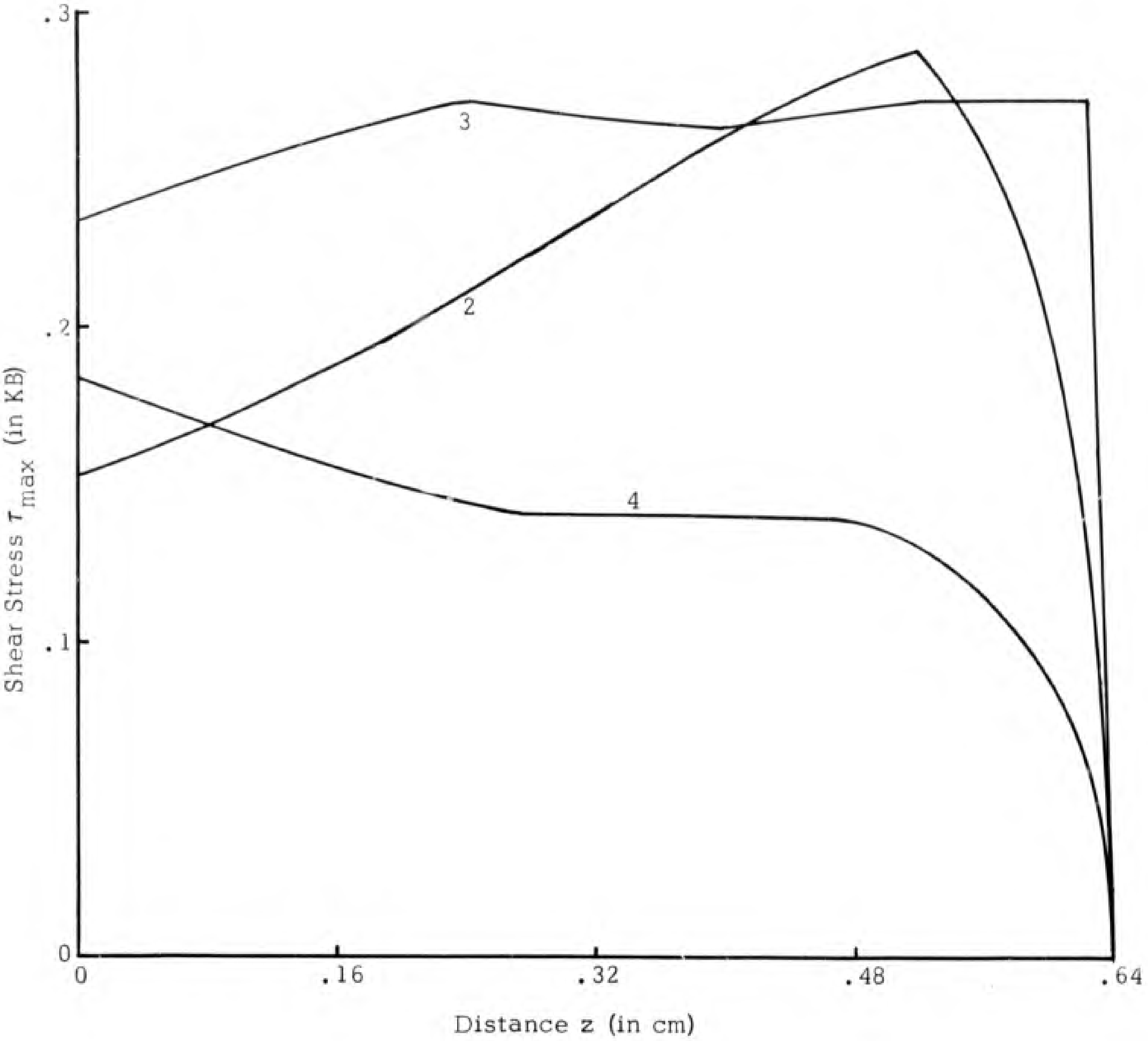

Figure 2.14 PEAK SHEAR STRESS, τ, IN PLANE OF WEAVE
(Based on fine edits used for determining σ_{max})

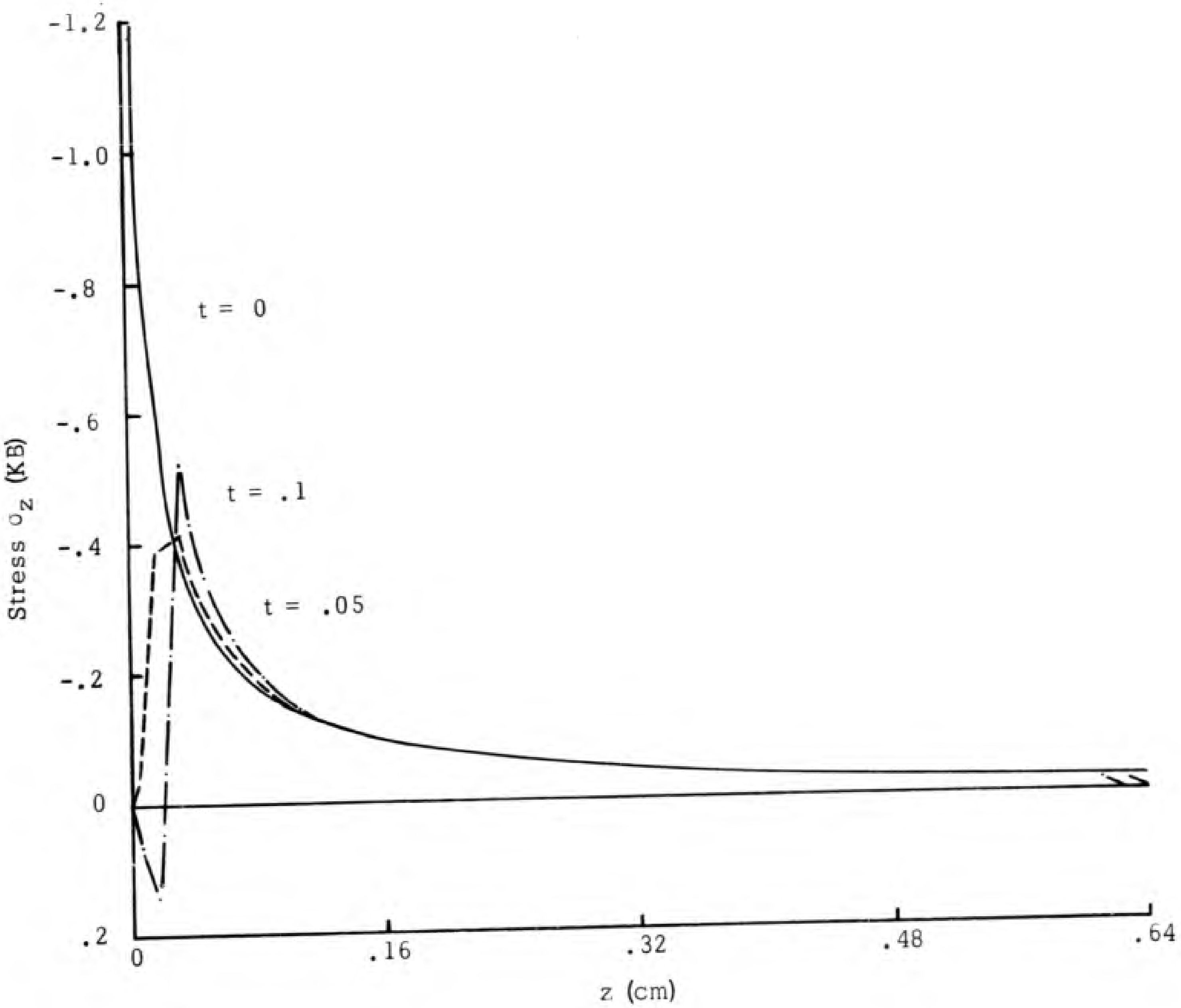

Figure 2.15 STRESS DECAY FOR X-RAY LOADING (Case 7)

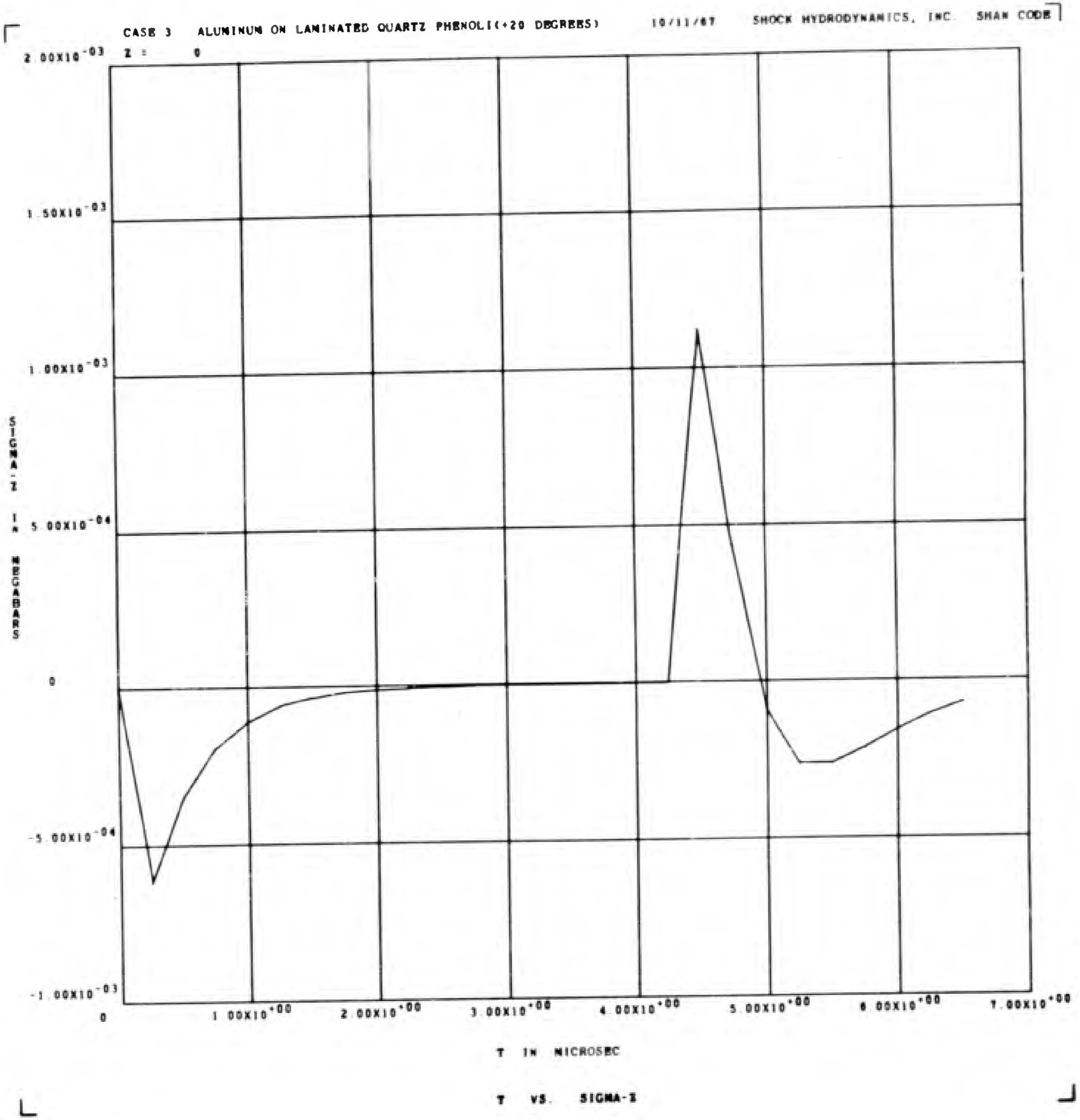
CASE 3 ALUMINUM ON LAMINATED QUARTZ PHENOLI(+20 DEGREES) 10/11/87 SHOCK HYDRODYNAMICS, INC. SHAN CODE
Z = 0
2.00X10^-03
1.50X10^-03
1.00X10^-03
5.00X10^-04
0
-5.00X10^-04
-1.00X10^-03
SIGMA-Z IN MEGABARS
0
1.00X10^+00
2.00X10^+00
3.00X10^+00
4.00X10^+00
5.00X10^+00
6.00X10^+00
7.00X10^+00
T IN MICROSEC
T VS. SIGMA-Z

Figure 2.16

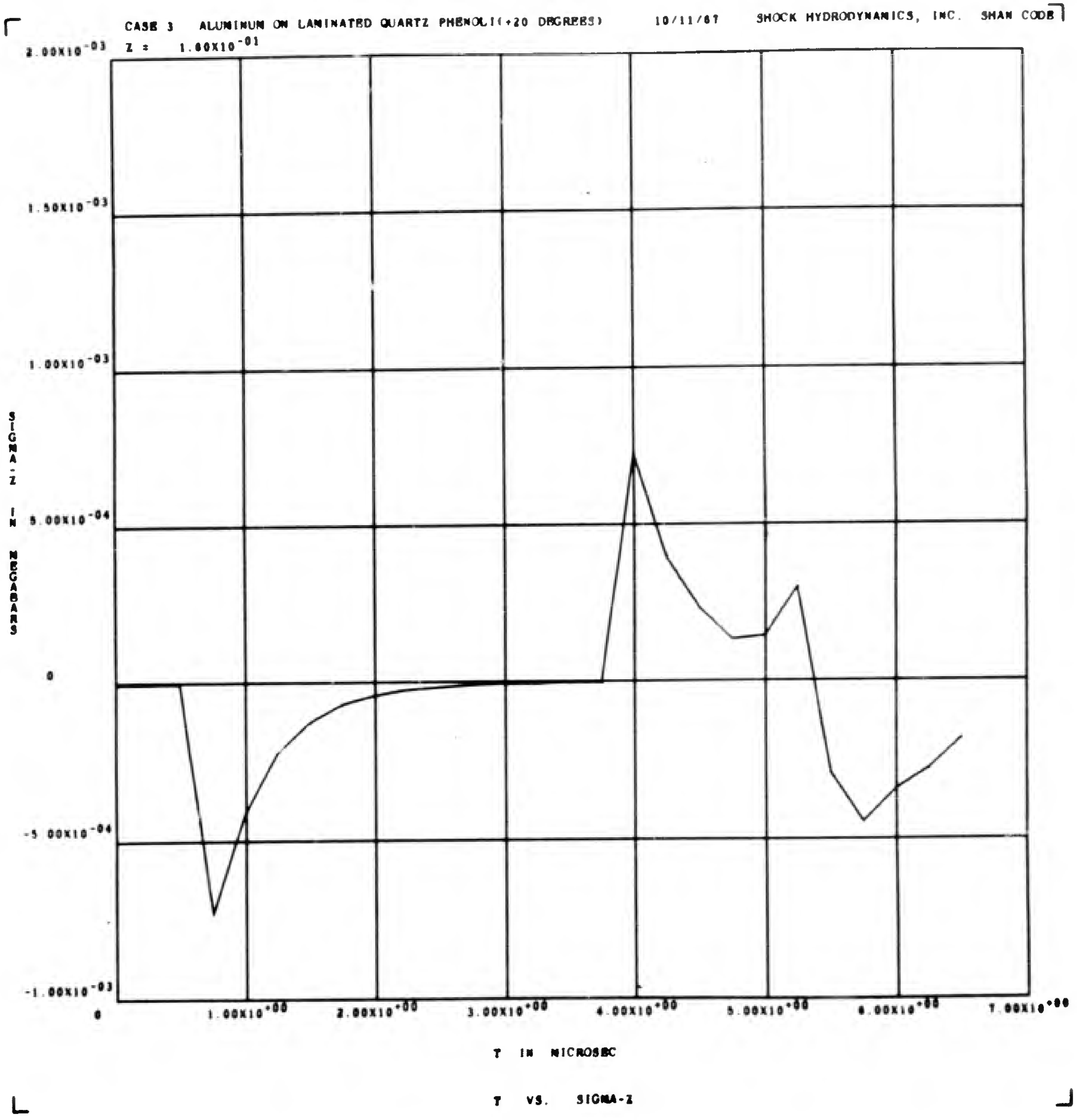
CASE 3 ALUMINUM ON LAMINATED QUARTZ PHENOLI(+20 DEGREES) 10/11/67 SHOCK HYDRODYNAMICS, INC. SHAN CODE
Z = 1.60X10^-01
2.00X10^-03
1.50X10^-03
1.00X10^-03
5.00X10^-04
0
-5.00X10^-04
-1.00X10^-03
SIGMA-Z IN MEGABARS
0
1.00X10^+00
2.00X10^+00
3.00X10^+00
4.00X10^+00
5.00X10^+00
6.00X10^+00
7.00X10^+00
T IN MICROSEC
T VS. SIGMA-Z

Figure 2.17

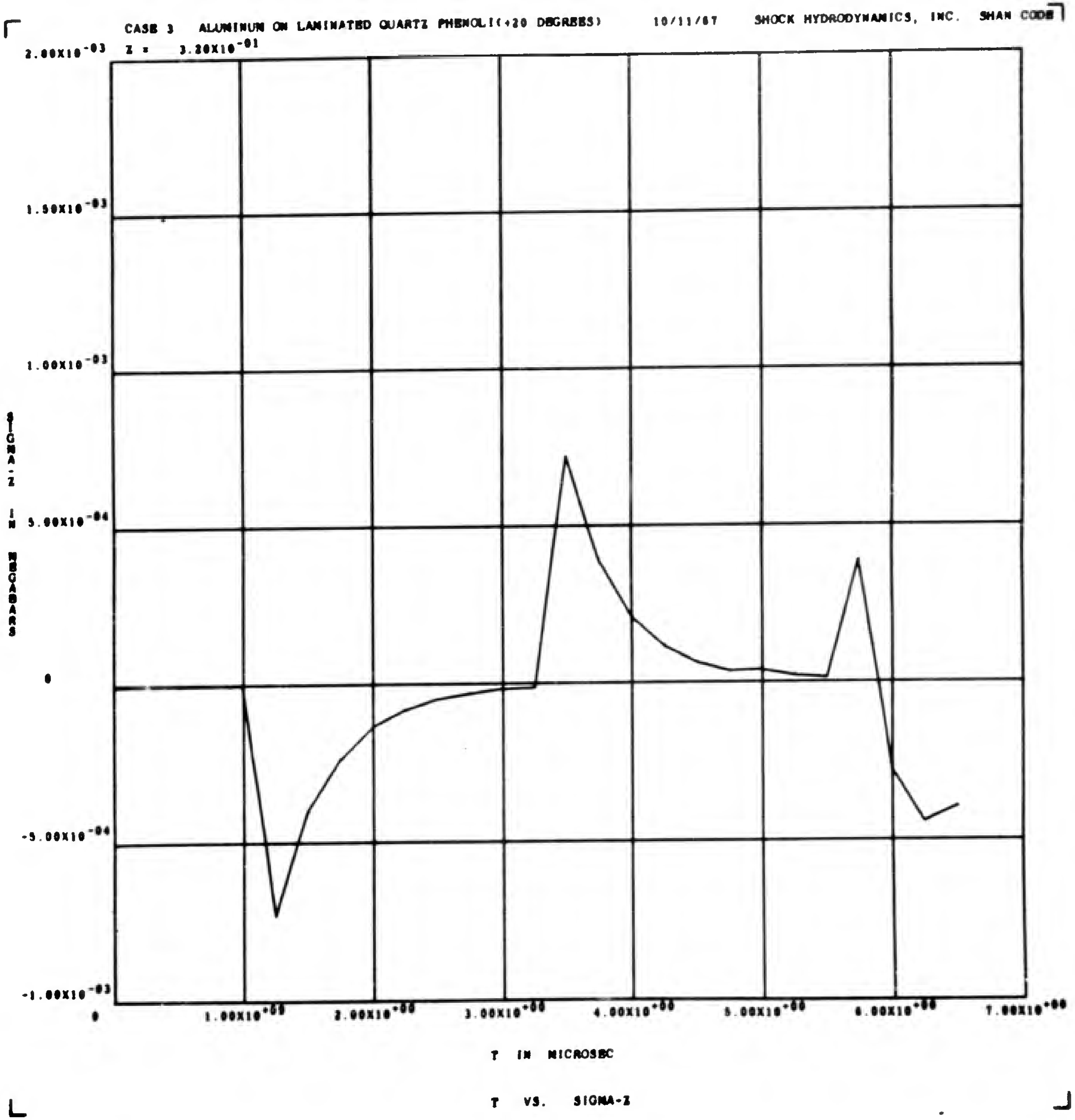
CASE 3 ALUMINUM ON LAMINATED QUARTZ PHENOLI(+20 DEGREES) 10/11/87 SHOCK HYDRODYNAMICS, INC. SHAN CODE
Z = 3.20X10^{-01}
2.00X10^{-03}
1.50X10^{-03}
1.00X10^{-03}
5.00X10^{-04}
0
-5.00X10^{-04}
-1.00X10^{-03}
SIGMA-Z IN MEGABARS
0
1.00X10^{+00}
2.00X10^{+00}
3.00X10^{+00}
4.00X10^{+00}
5.00X10^{+00}
6.00X10^{+00}
7.00X10^{+00}
T IN MICROSEC
T VS. SIGMA-Z

Figure 2.18

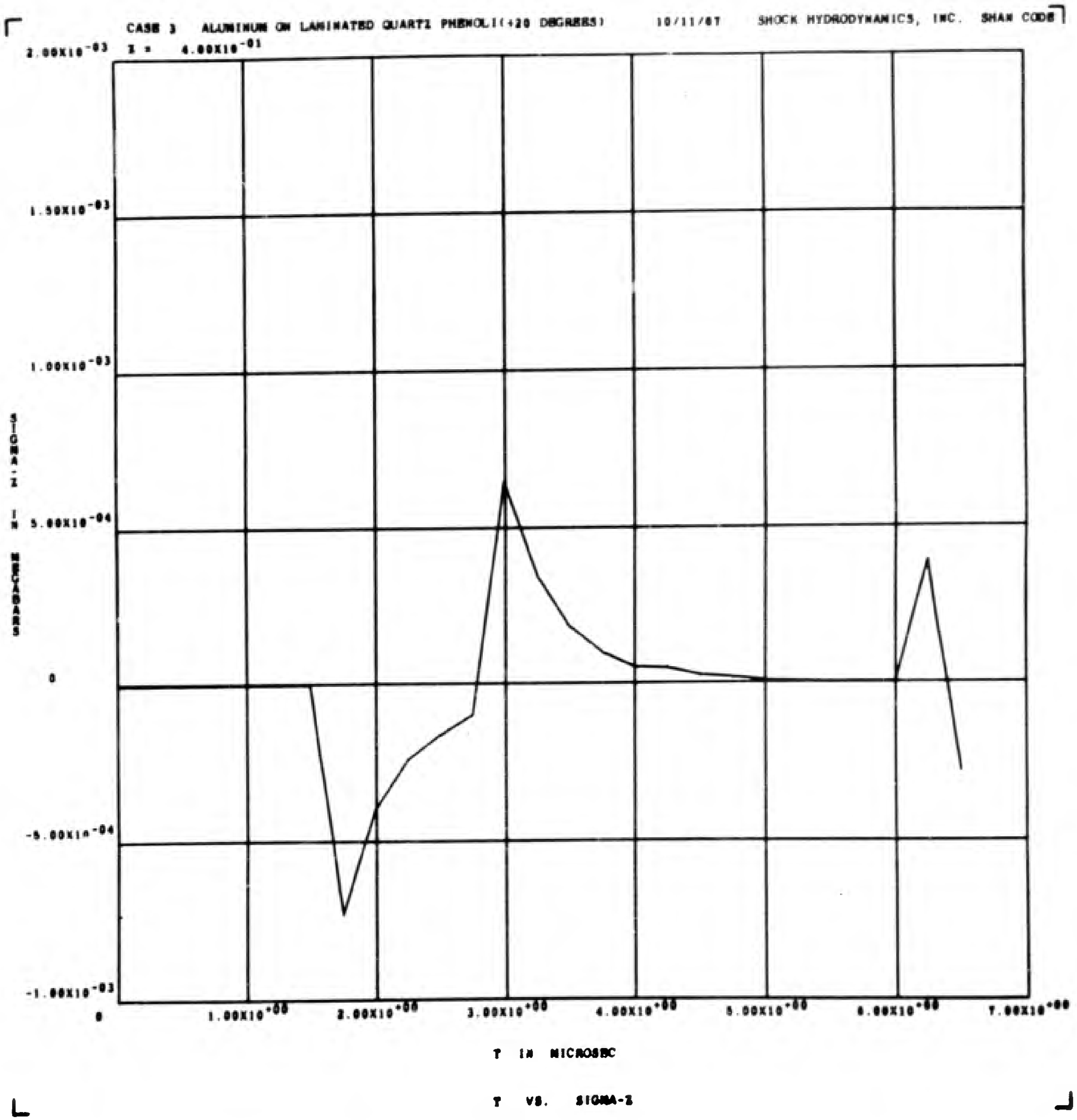
CASE 3 ALUMINUM ON LAMINATED QUARTZ PHENOLI(+20 DEGREES) 10/11/87 SHOCK HYDRODYNAMICS, INC. SHAN CODE
Z = 4.00X10^{-01}
2.00X10^{-03}
1.50X10^{-03}
1.00X10^{-03}
5.00X10^{-04}
0
-5.00X10^{-04}
-1.00X10^{-03}
SIGMA-Z IN MEGABARS
0
1.00X10^{+00}
2.00X10^{+00}
3.00X10^{+00}
4.00X10^{+00}
5.00X10^{+00}
6.00X10^{+00}
7.00X10^{+00}
T IN MICROSEC
T VS. SIGMA-Z

Figure 2.19

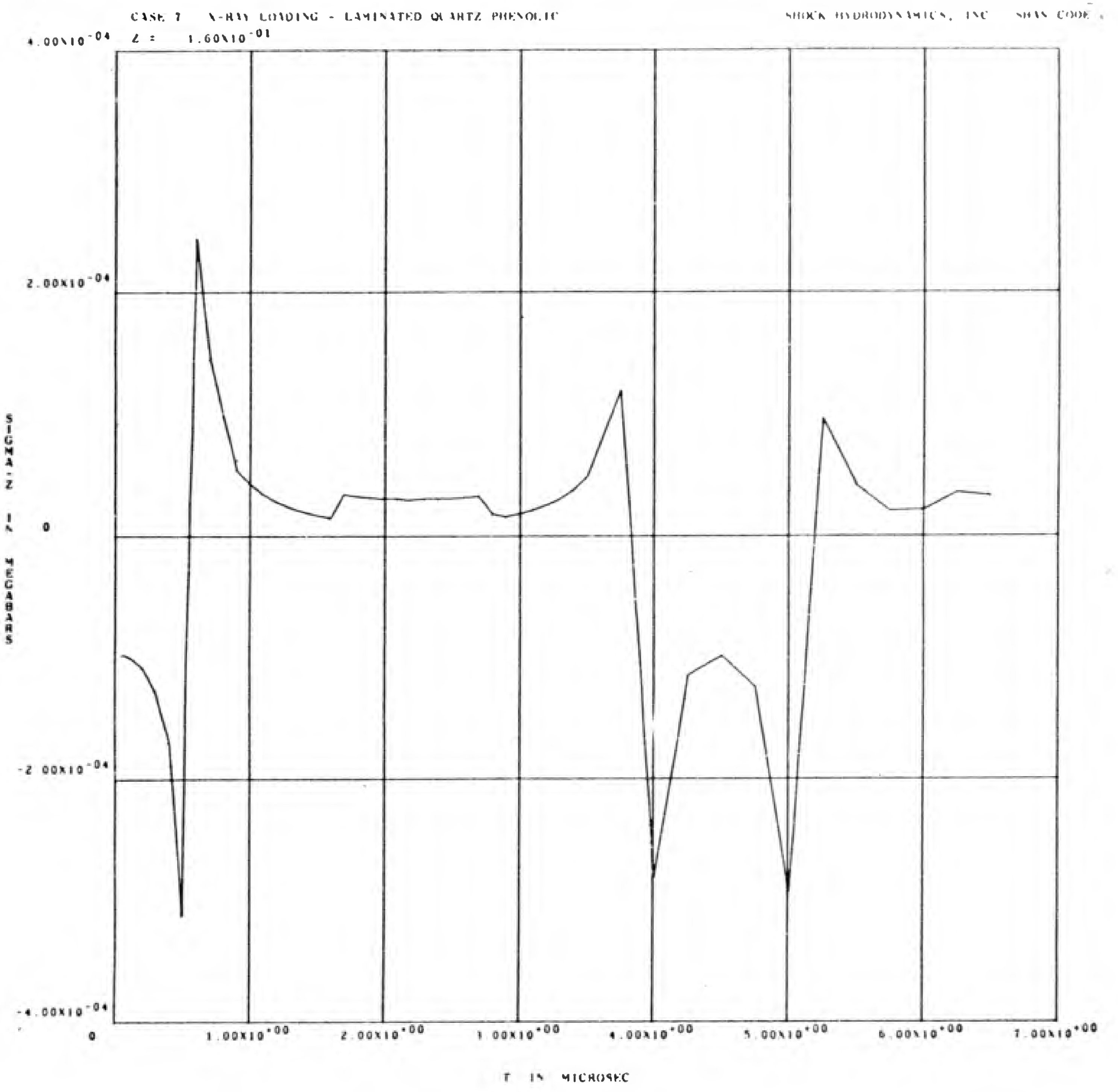

T VS. SIGMA-Z

Figure 2.20

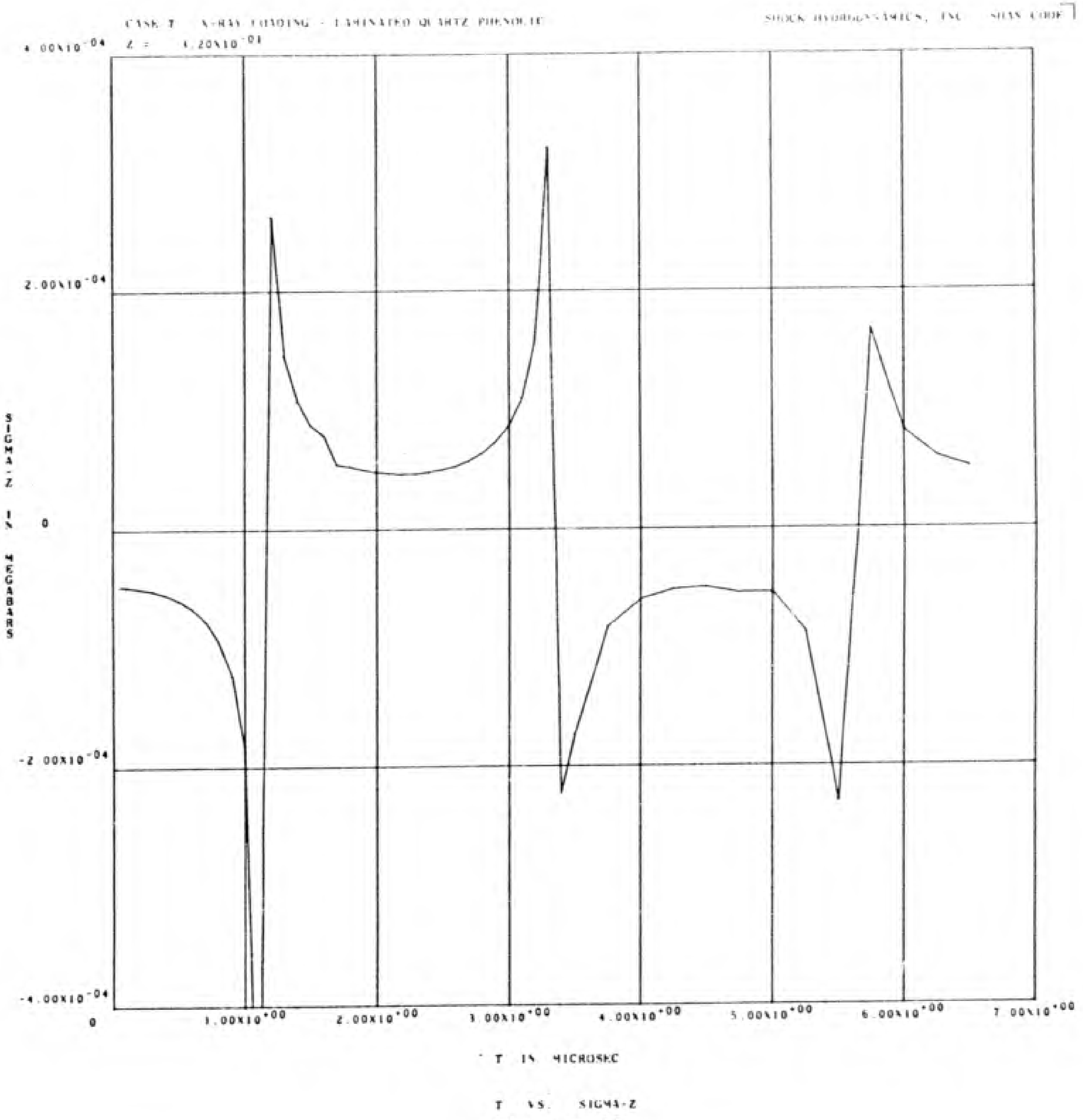
CASE 7 X-RAY LOADING - LAMINATED QUARTZ PHENOLIC
SHOCK HYDRODYNAMICS, INC. SHAN CODE
Z = 1.20X10^-01
4.00X10^-04
2.00X10^-04
0
-2.00X10^-04
-4.00X10^-04
SIGMA-Z IN MEGABARS
0
1.00X10^+00
2.00X10^+00
3.00X10^+00
4.00X10^+00
5.00X10^+00
6.00X10^+00
7.00X10^+00
T IN MICROSEC
T VS. SIGMA-Z

Figure 2.21

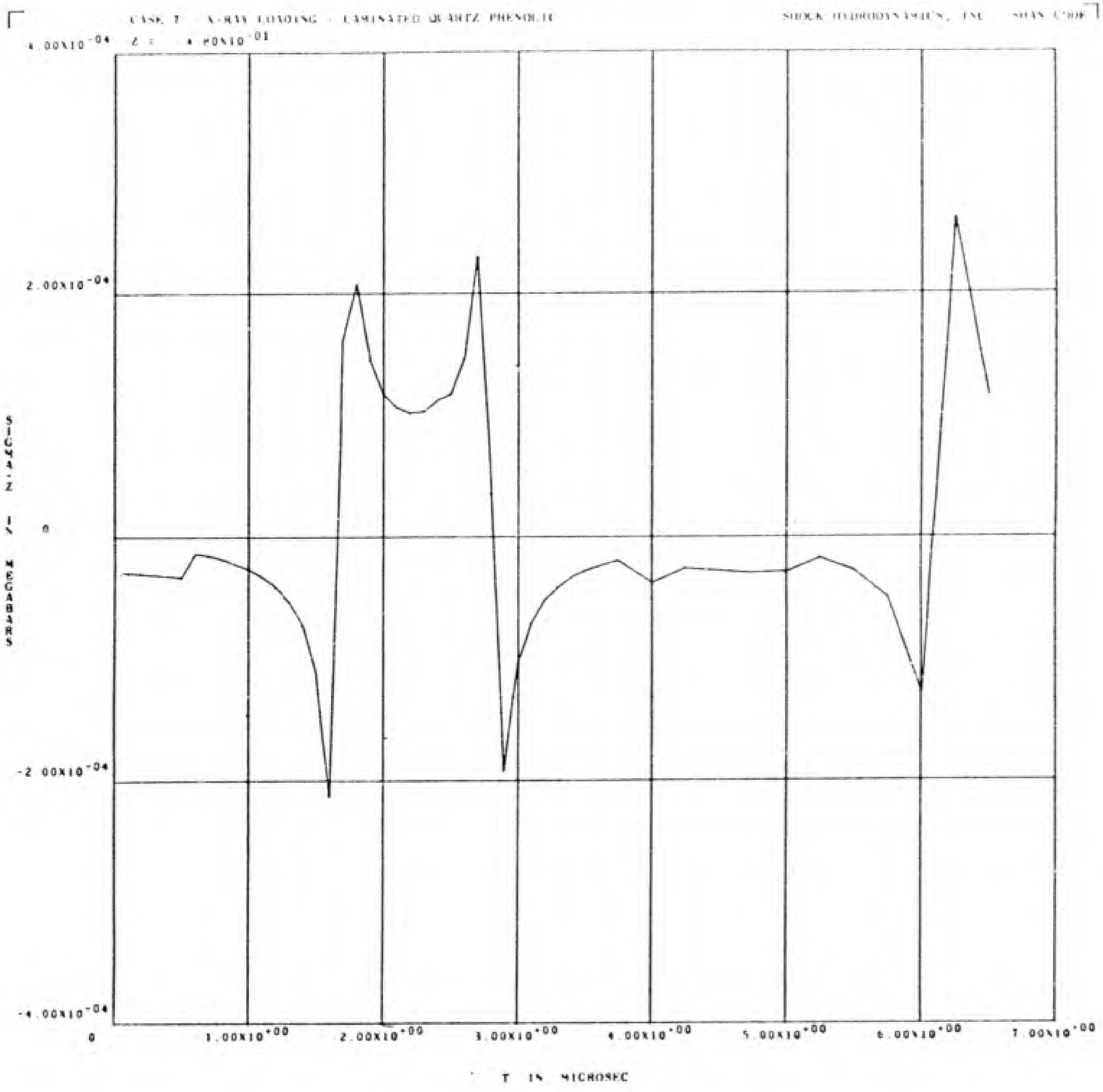

T VS. SIGMA-Z

Figure 2.22

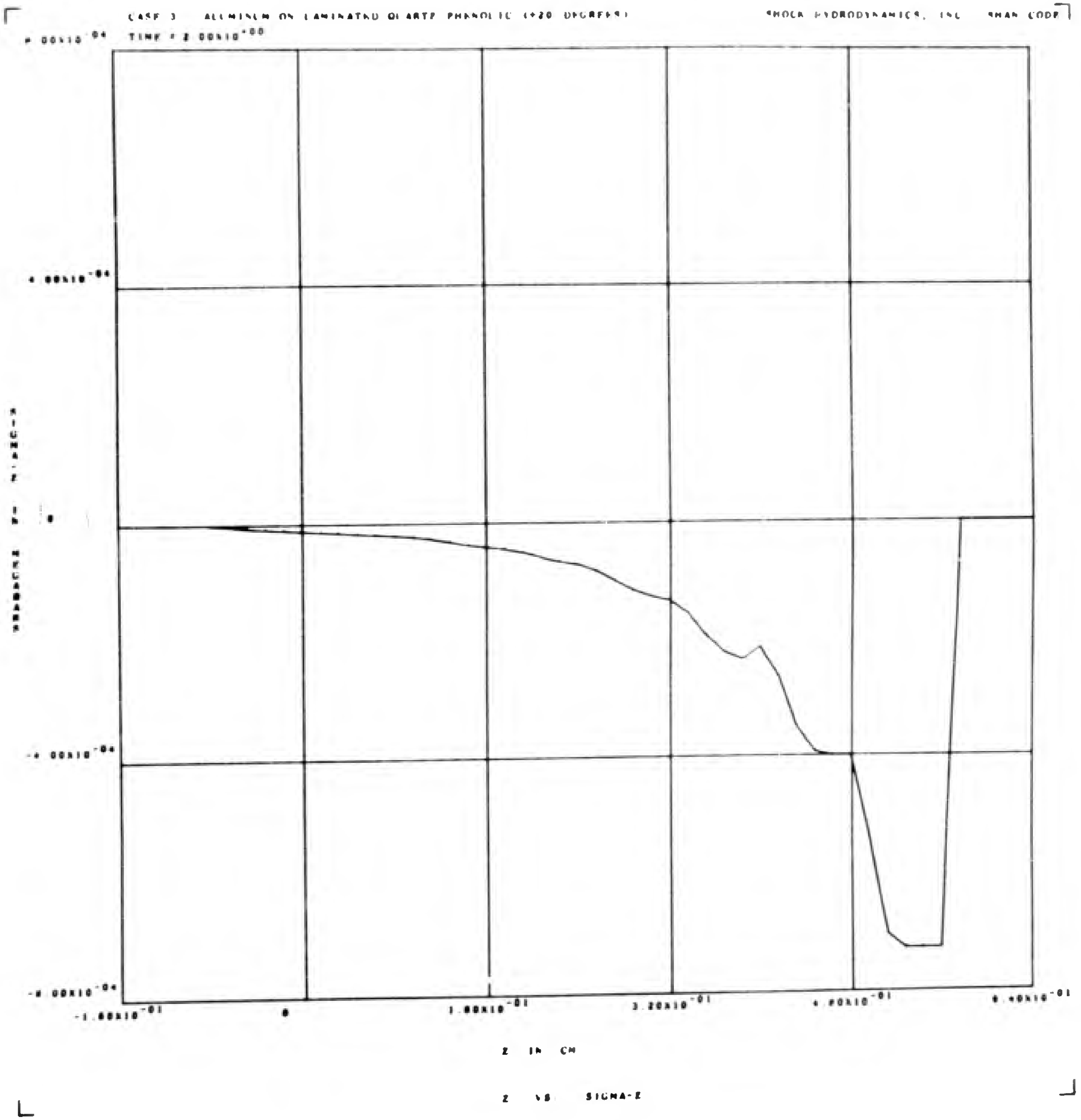
CASE 3 ALUMINUM ON LAMINATED QUARTZ PHENOLIC (+20 DEGREES)
SHOCK HYDRODYNAMICS, INC. SHAN CODE
TIME = 2.00x10^+00
8.00x10^-04
4.00x10^-04
0
-4.00x10^-04
-8.00x10^-04
SIGMA-Z IN MEGABARS
-1.60x10^-01
0
1.60x10^-01
3.20x10^-01
4.80x10^-01
6.40x10^-01
Z IN CM
Z VS SIGMA-Z

Figure 2.23

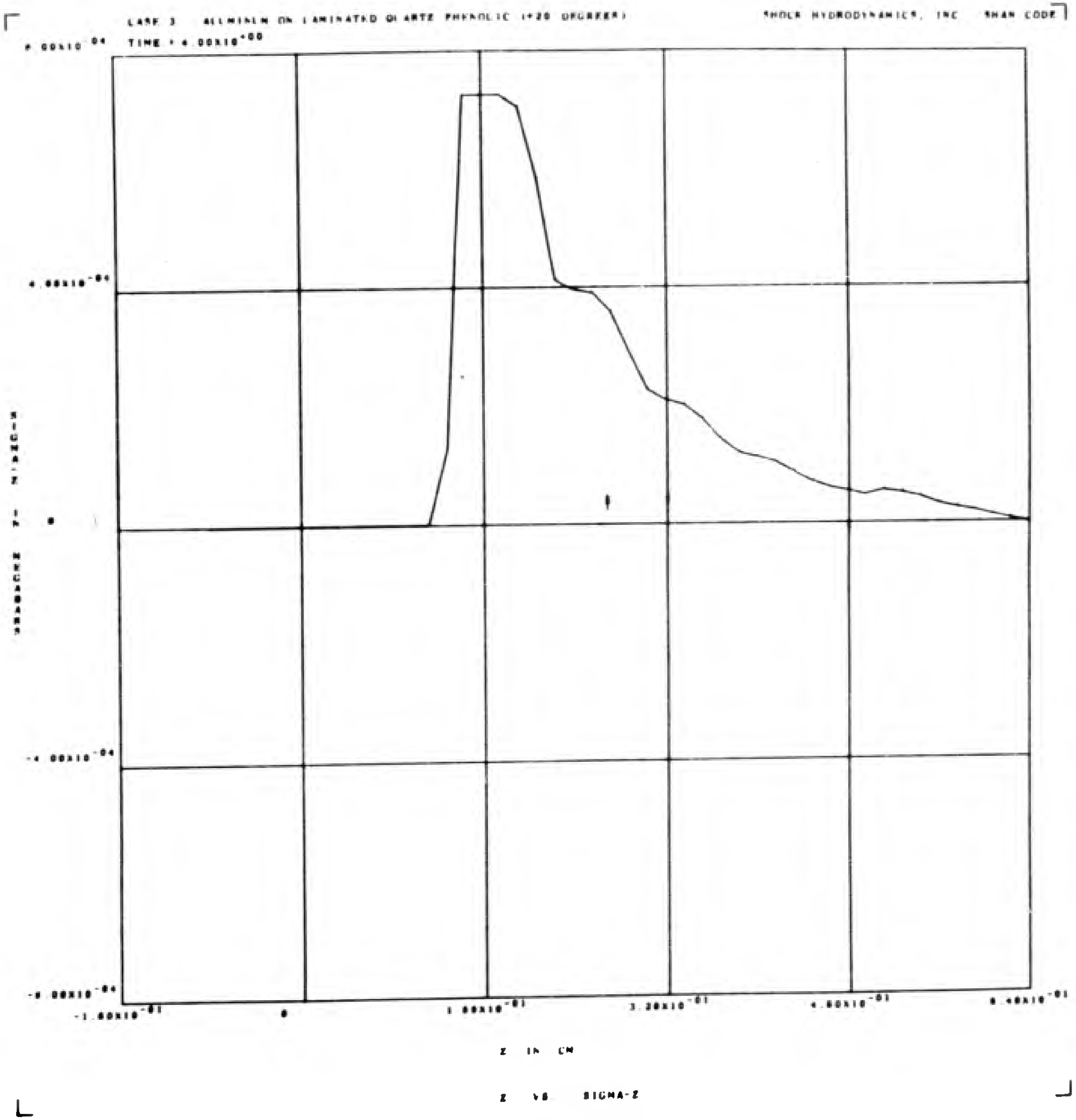
CASE 3 ALUMINUM ON LAMINATED QUARTZ PHENOLIC (+20 DEGREES)
SHOCK HYDRODYNAMICS, INC SHAN CODE
TIME = 4.00x10^+00
8.00x10^-04
4.00x10^-04
0
-4.00x10^-04
-8.00x10^-04
SIGMA-Z IN MEGABARS
-1.60x10^-01
0
1.60x10^-01
3.20x10^-01
4.80x10^-01
6.40x10^-01
Z IN CM
Z VS SIGMA-Z

Figure 2.24

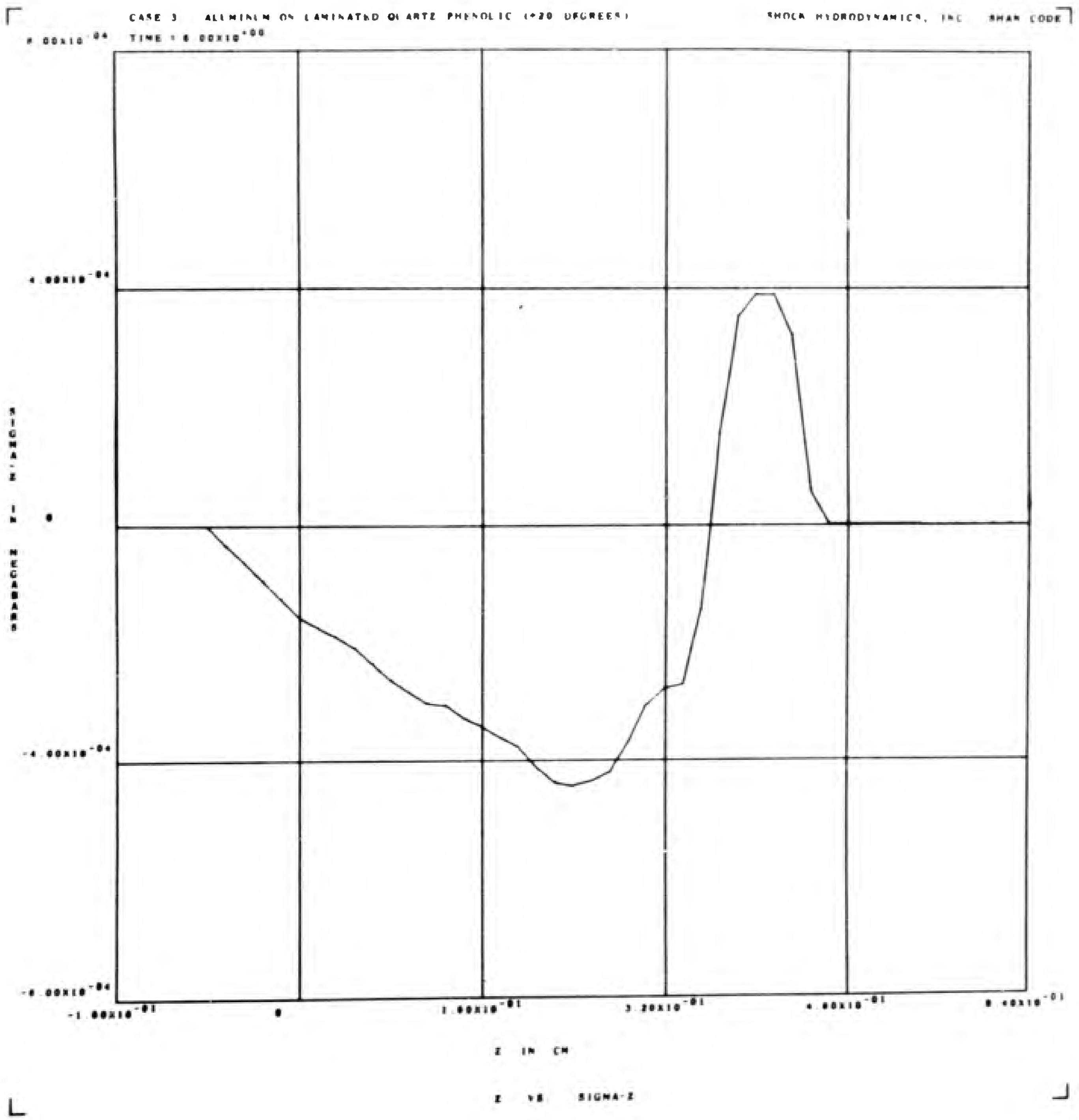
CASE 3   ALUMINUM ON LAMINATED QUARTZ PHENOLIC (+20 DEGREES)
SHOCK HYDRODYNAMICS, INC.   SHAR CODE
TIME = 8.00X10^+00
8.00X10^-04
4.00X10^-04
0
-4.00X10^-04
-8.00X10^-04
SIGMA-Z IN MEGABARS
-1.60X10^-01
0
1.60X10^-01
3.20X10^-01
4.80X10^-01
6.40X10^-01
Z IN CM
Z VS SIGMA-Z

Figure 2.25

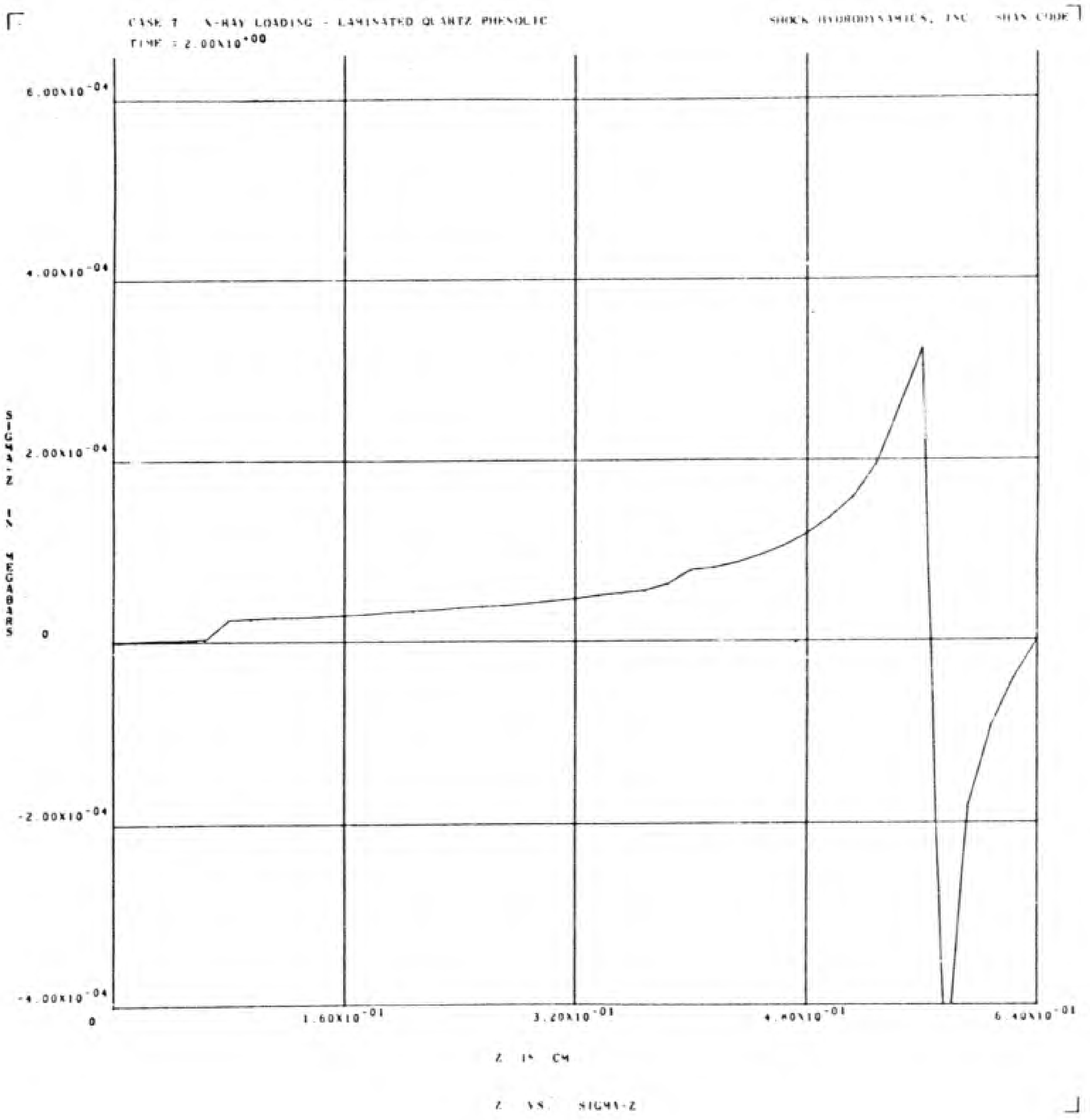
CASE 7 X-RAY LOADING - LAMINATED QUARTZ PHENOLIC
TIME = 2.00X10^+00
SHOCK HYDRODYNAMICS, INC. SHYS CODE
6.00X10^-04
4.00X10^-04
2.00X10^-04
0
-2.00X10^-04
-4.00X10^-04
SIGMA-Z IN MEGABARS
0
1.60X10^-01
3.20X10^-01
4.80X10^-01
6.40X10^-01
Z IN CM
Z VS. SIGMA-Z

Figure 2.26

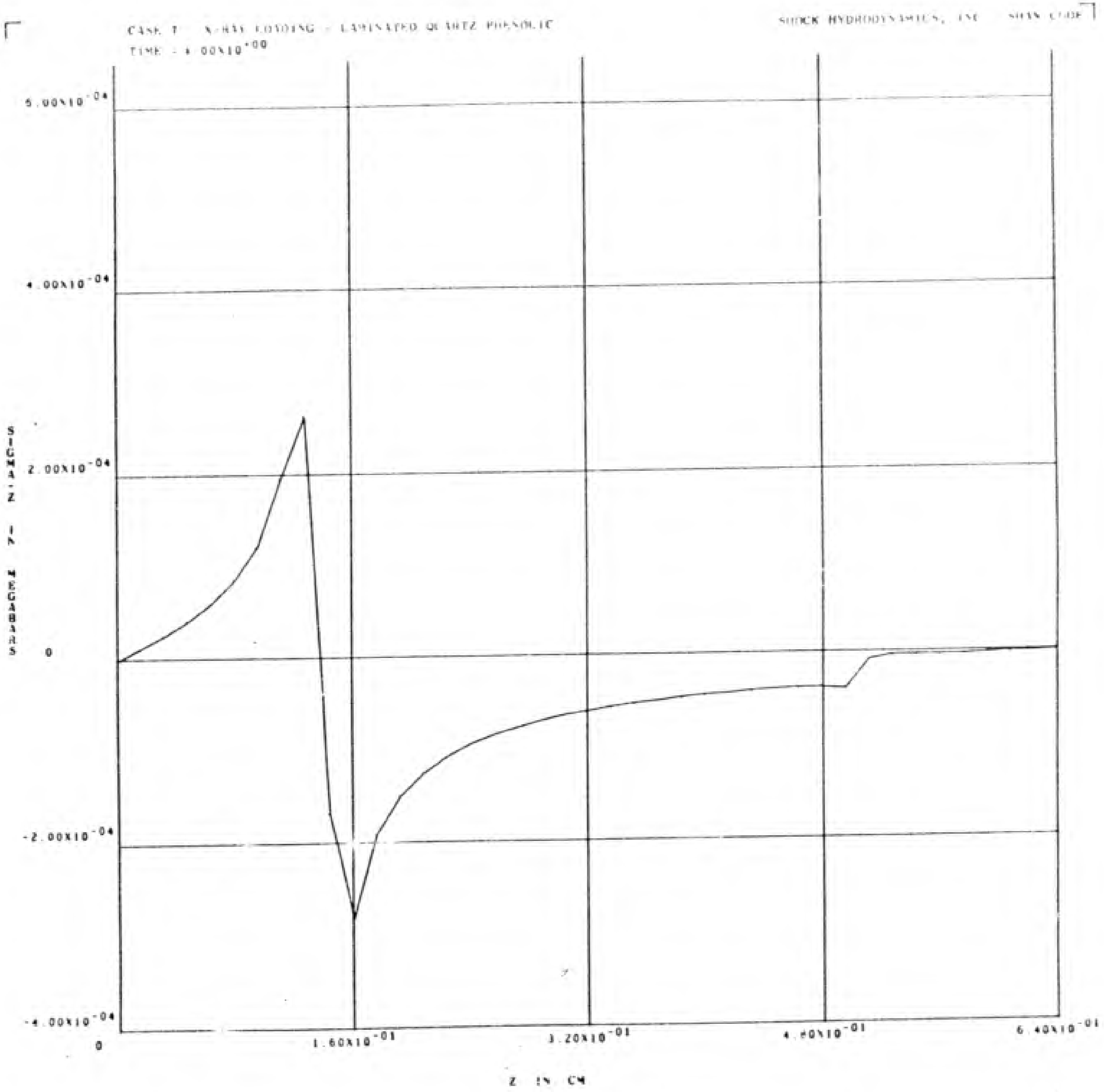

Z VS. SIGMA-Z

Figure 2.27

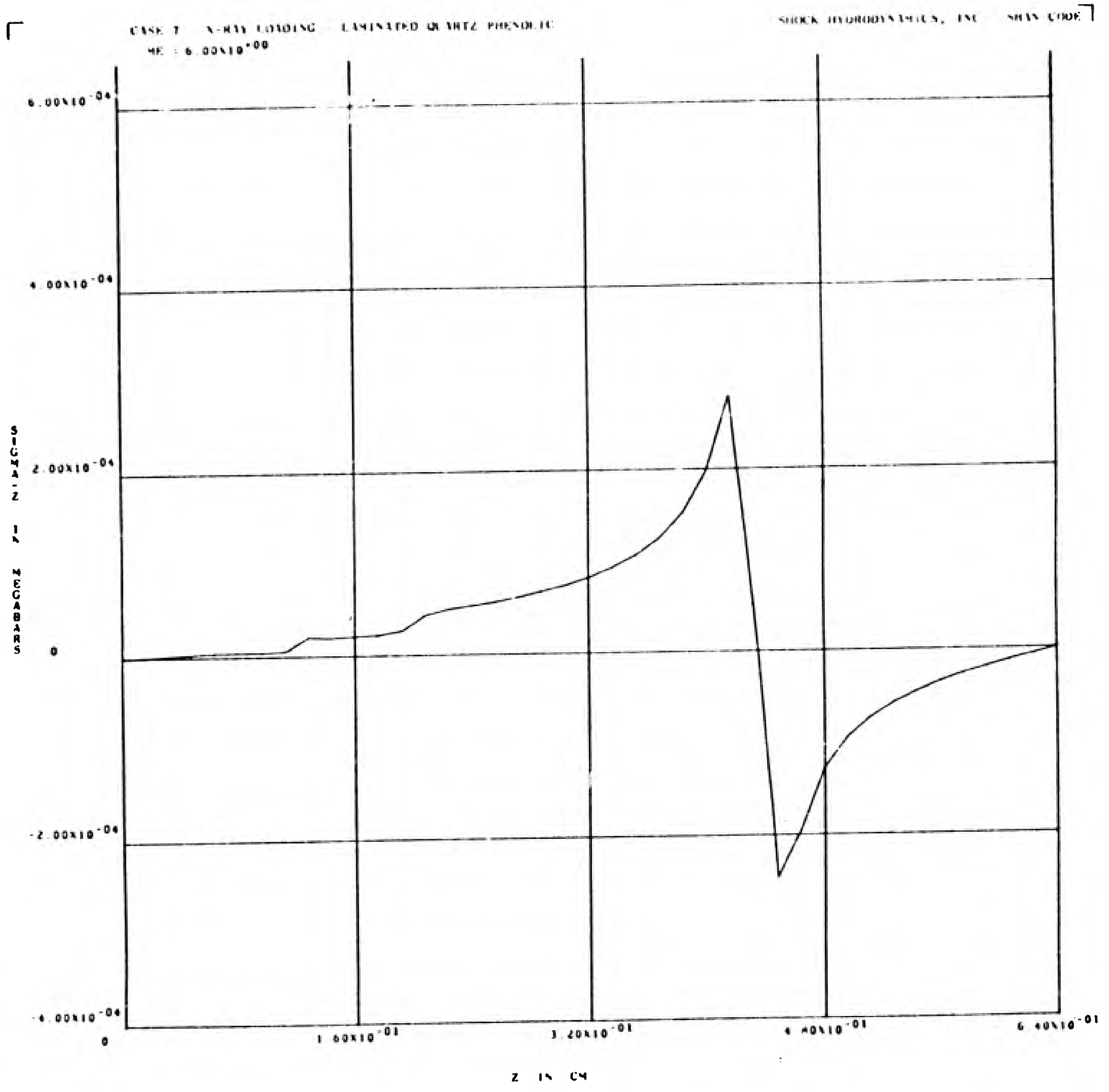
CASE 7 X-RAY LOADING LAMINATED QUARTZ PHENOLIC
ME : 6.00x10^{+00}
SHOCK HYDRODYNAMICS, INC SHAY CODE
SIGMA-Z IN MEGABARS
6.00x10^{-04}
4.00x10^{-04}
2.00x10^{-04}
0
-2.00x10^{-04}
-4.00x10^{-04}
0
1.60x10^{-01}
3.20x10^{-01}
4.80x10^{-01}
6.40x10^{-01}
Z IN CM
Z VS. SIGMA-Z

Figure 2.28

CHAPTER III. SHOCK PROPAGATION THROUGH HETEROGENEOUS STRUCTURES*

3.1 OBJECTIVE OF STUDY

The wave shape and amplitude of a shock which propagates through an ablative structure determines the extent of spallation and/or destructive interactions with interfaces. The objective of this task was to examine the effect of relatively gross heterogeneities in an ablative material upon the shock front and the pulse shape. These studies were conducted by performing a number of two-dimensional SHEP code solutions of wave propagation through targets containing arrays of cylindrical or spherical inclusions. One-dimensional SHEP code solutions of wave propagation through homogeneous targets were performed to provide a basis for comparing the shock attenuation and broadening occurring with and without the presence of inclusions.

3.2 COMPUTATIONAL METHOD

The numerical solutions were obtained with the SHEP code, a two-dimensional Lagrangian program employing a hydrodynamic-elastic-plastic behavioral model (Reference 5). Either cartesian or cylindrical coordinate systems were used, as dictated by the problem. The loading for each case was a specified step-function of pressure applied uniformly along the target face; both square-wave and constant loadings were considered. For the cases having homogeneous targets, the one-dimensional version of the SHEP code was employed.

3.3 PROBLEM SPECIFICATIONS

The cases selected for study comprised two basic types of target configurations: two inclusion materials plus void spaces, and finite and constant in time pressure loadings.

The following target configurations were considered:

a. Matrix of cylindrical inclusions. This geometry is shown in Figure 3-1a. If the upper and lower horizontal boundaries are treated as planes of symmetry, this configuration represents a regular array of parallel, cylindrical inclusions. Assuming that the target will be strain free in the z direction (normal to the cross section shown), the problem can be treated with the two-dimensional code, using plane x-y coordinates.

b. Stacked Spherical Inclusions. This geometry is shown in Figure 3-1b. The lower boundary is an axis of symmetry and the upper boundary is a fixed cylindrical shell. The problem is treated in the cylindrical coordinates option of the code. This configuration represents a two-dimensional approximation of an array of spherical inclusions.

c. Homogeneous Target. These one-dimensional targets are single material slabs of the same thickness as the corresponding 2-D targets, and are used for the comparative solutions.

---

*Written by M. H. Wagner

A total of nine cases were considered, as listed in Table 3-I. In this table, the pulse length of the external pressure loading is given as $c_o t_d/\text{dia}$, where c_o is the normal sound speed in the epoxy, t_d is the duration of application, and dia is the inclusion diameter. The behavior of just the shock front was investigated in the Group 1 problems. For these solutions, the applied pressure was constant in time. A target with spherical tungsten inclusions was selected. Targets with cylindrical inclusions were studied in the Group 2 problems. Two inclusion materials, tungsten and quartz, and two pulse lengths for the pressure function were considered. The Group 3 problems dealt with square wave loadings of targets having spherical inclusions. The inclusion materials were tungsten and void spaces. Epoxy was used as the filler material for all of the cases.

The following listed material properties were used in the calculations. The noted references were used in compiling these data.

Epoxy (Reference 6)

Normal Density: 1.19 gm/cm^3

Yield Strength: 0.005 Mb

Shear Modulus: 0.03 Mb

Equation of State:

$$P = (A\mu + B\mu^2 + C\mu^3)\left(1 - \frac{G\mu}{2}\right) + G\rho e$$

$A = 0.078$ $\quad C = 0.1441$

$B = 0.1647$ $\quad G = 0.79$

These properties were used for epoxy in the Group 2 and Group 3 problems. For Case 1B, a normal density of 1.22 gm/cm^3 and the following equation of state constants were specified for the epoxy (Reference 6):

$A = 0.11$ $\quad C = 1.0$

$B = -0.20$ $\quad G = 0.79$

This equation of state has the property that the shock velocity along the Hugoniot decreases with increasing pressure, in the low pressure regime; this characteristic prevents the build up of a sharp shock front. The first listed equation of state was used therefore for subsequent solutions.

Epoxy (Modified)

Normal Density: 2.402
Yield Strength: 0.0009 Mb
Shear Modulus: 0.03 Mb
Equation of State:

$$P = (A\mu + B\mu^2 + C\mu^3)\left(1 - \frac{G\mu}{2}\right) + G\rho e$$

A total of nine cases were considered, as listed in Table 3-I. In this table, the pulse length of the external pressure loading is given as $c_o t_d/\text{dia}$, where c_o is the normal sound speed in the epoxy, t_d is the duration of application, and dia is the inclusion diameter. The behavior of just the shock front was investigated in the Group 1 problems. For these solutions, the applied pressure was constant in time. A target with spherical tungsten inclusions was selected. Targets with cylindrical inclusions were studied in the Group 2 problems. Two inclusion materials, tungsten and quartz, and two pulse lengths for the pressure function were considered. The Group 3 problems dealt with square wave loadings of targets having spherical inclusions. The inclusion materials were tungsten and void spaces. Epoxy was used as the filler material for all of the cases.

The following listed material properties were used in the calculations. The noted references were used in compiling these data.

Epoxy (Reference 6)

Normal Density: 1.19 gm/cm^3

Yield Strength: 0.005 Mb

Shear Modulus: 0.03 Mb

Equation of State:

$$P = (A\mu + B\mu^2 + C\mu^3)\left(1 - \frac{G\mu}{2}\right) + G\rho e$$

$A = 0.078$ $C = 0.1441$

$B = 0.1647$ $G = 0.79$

These properties were used for epoxy in the Group 2 and Group 3 problems. For Case 1B, a normal density of 1.22 gm/cm^3 and the following equation of state constants were specified for the epoxy (Reference 6):

$A = 0.11$ $C = 1.0$

$B = -0.20$ $G = 0.79$

This equation of state has the property that the shock velocity along the Hugoniot decreases with increasing pressure, in the low pressure regime; this characteristic prevents the build up of a sharp shock front. The first listed equation of state was used therefore for subsequent solutions.

Epoxy (Modified)

Normal Density: 2.402
Yield Strength: 0.0009 Mb
Shear Modulus: 0.03 Mb
Equation of State:

$$P = (A\mu + B\mu^2 + C\mu^3)\left(1 - \frac{G\mu}{2}\right) + G\rho e$$

TABLE 3-1 DESCRIPTION OF CASES

Case	Inclusion Geometry	Materials		Spacing (c. to c.) / Inclusion Diameter	External Pressure Loading		No. of Inclusions Considered (in x direction)
		Filler	Inclusion		Amplitude (kb)	Pulse Length $\left(\frac{c_o t_d}{dia}\right)$	
1B	Spheres	Epoxy	Tungsten	2	5	∞	4
1C	None (1-D Case)	Epoxy (Modified)	---	---	5	∞	-
2A	Cylinders	Epoxy	Tungsten	1.75	5	1.2	4
2B	Cylinders	Epoxy	Quartz	1.75	5	1.2	4
2C	None (1-D Case)	Epoxy	---	---	5	Same as 2A & 2B	-
2D	Cylinders	Epoxy	Quartz	1.75	5	0.3	4
3A	Spheres	Epoxy	Tungsten	1.5	5	1.2	6
3B	Spheres	Epoxy	Void	1.5	5	1.2	6
3C	None (1-D Case)	Epoxy	---	---	5	Same as 3A & 3B	-

$A = 0.306$ $C = 1.128$

$B = 0.0585$ $G = 0.84$

These properties were used in Case 1C, and represents composite properties for a homogeneous mixture of the epoxy filler material and the tungsten inclusions in Case 1B, which had a volume fraction of 6.54 percent for the inclusions. Hugoniot points for the composite were established by weighting the Hugoniot pressures at given compression ratios according to the relation:

$$P_C^H = P_E^H + \frac{\rho_C^o - \rho_E^o}{\rho_W^o - \rho_E^o} (P_W^H - P_E^H)$$

where the subscripts C, E, and W refer to the composite, epoxy, and tungsten. This formula is equivalent to

$$P_C = \epsilon P_W^H + (1 - \epsilon) P_E^H$$

where ϵ is the volume fraction of the tungsten.

Tungsten (Reference 7)

Normal Density: 19.3 gm/cm^3

Yield Strength: 0.007 Mb

Shear Modulus: 1.57 Mb

Equation of State:

$$P = k_1 \eta^{2/3} \exp(-B\eta^{-1/3}) - k_2 \eta^{4/3} + \frac{\rho}{2b}\left(\left[a^2 + 4b\left\{e + e_o + \frac{3k_2}{\rho_o}(\eta^{1/3} - 1) - \frac{3k_1}{\rho_o B}\left[\exp(-B\eta^{-1/3}) - \exp(-B)\right]\right\}\right]^{1/2} - a\right)$$

$B = 6.08$ $k_1 = 994.6$

$a = 0.64935$ $k_2 = 2.276$

$b = -2.7$ $e_o = 6.04 \times 10^{-6}$

Quartz: (Reference 8)

Normal Density: $2.204\ \mathrm{gm/cm^3}$

Yield Strength: 0.0525 Mb

Shear Modulus: 0.153 Mb

Equation of State:

$$P = -A\left(\frac{1}{\eta} - 1\right)$$

$$A = 0.4$$

An elastic equation of state for quartz was sufficient, due to the low stress levels experienced in these problems.

In the above listed equations of state, the symbols are defined as:

P = pressure (Mb)

$\dot{e}$ = specific internal energy (10^{12}) ergs/gm)

ρ = density ($\mathrm{gm/cm^3}$)

ρ_o = normal density ($\mathrm{gm/cm^3}$)

η = ρ/ρ_o

μ = $\eta - 1$

3.4 SUMMARY OF RESULTS

The amounts of attenuation and broadening of the pulse shapes occurring after transit of the stress pulses through the various targets are listed in Table 3-II. Comparisons of the peak stress and pulse width with their initial values and with the results of 1-D runs (no inclusions) are tabulated. The latter comparisons are more significant, since they isolate the effects due solely to the presence of the inclusions. The values for the 2-D runs were taken along the upper target boundary (corresponding to the planes of symmetry midway between the inclusion rows, for the cylindrical inclusion cases). σ_{xo} was 5 kb for all the cases. $\lambda_o = c_o t_d$, where c_o is the normal sound speed in the epoxy and t_d is the duration of the pressure loading.

The Case 1 results refer to the broadening of the plastic shock front only, as there was no elastic precursor in the 1-D case, due to the modified equation of state used.

The Case 2 problems show that, as expected, the higher impedance tungsten inclusions produce greater pulse attenuation and broadening than do the quartz inclusions.

TABLE 3-II SUMMARY OF RESULTS

CASE	LAST VALUE OF WIDTH OF WAVEFRONT λ (cm)	$\frac{\lambda \text{ (with inclusions)}}{\lambda \text{ (without inclusions)}}$ (%)
1 B	.0024	200.
1 C	.0012	---

CASE	LAST VALUE OF PEAK STRESS σ_x (kb)	$\frac{\sigma_x}{\sigma_{xo}}$ (%)	$\frac{\sigma_x \text{ (with inclusions)}}{\sigma_x \text{ (without inclusions)}}$	LAST VALUE OF PULSELENGTH λ (cm)	$\frac{\lambda}{\lambda_o}$ (%)	$\frac{\lambda \text{ (with inclusions)}}{\lambda \text{ (without inclusions)}}$ (%)
2A	-1.24	25.	36.	.20	415.	202.
2B	-2.04	41.	59.	.16	332.	162.
2C	-3.43	69.	--	.099	205.	---
2D	-0.74	15.	--	.063	524.	---
3A	-2.38	48.	85.	4.0	329.	121.
3B	-0.77	15.	28.	2.3	189.	70.
3C	-2.80	56.	--	3.3	272.	---

The Case 3 problems compare the effect of spherical inclusions with a large and a small (zero) impedance, relative to that of the epoxy. In Case 3B, it should be noted that there is a subsequent long-pulse length wave having stress comparable to that in the leading pulse.

3.5 NUMERICAL SOLUTIONS

To illustrate the results of the numerical solutions, several types of SC 4020 edits were obtained at selected times during the course of the solutions:

a. Lagrangian computing mesh.

b. Principal stress field.

c. Particle velocity field.

d. Stress (σ_x) versus x for given y positions.

e. Particle velocity ($\dot{x}$) versus x for given y positions.

For the stress field plots, the principal components of the stress tensor for each cell are shown, using the conventions described below. The two principal directions in the x-y plane are identified, being always orthogonal to each other. In each principal direction, the magnitude of the corresponding principal stress is plotted. As a sign convention, compressive components are plotted with positive x-components and tensile components are plotted with negative x-components. If one principal direction has no x-component (is parallel with the y-axis), compressive stress is plotted downward. The third principal direction is always in the z-direction (or azimuthal (ϕ) for cylindrical coordinates); the magnitude of that principal stress is plotted along the line bisecting the principal directions in the x-y plane. The same sign convention is used for it, a positive x-component or straight down denoting compressive stress. If the two principal components in the x-y plane are equal, there are no preferred principal directions in the x-y plane; in this case the principal directions are arbitrarily selected as the x and y directions. The length of the vectors are scaled to the unit length indicated at the top of the plot (in Mb) equal to 1 cm on the scale shown, i.e., vector magnitude (Mb) = [vector length plotted (in cm, using the scale shown)] x [unit length (Mb/cm)] .

The edits of the velocity vector field plot the direction and magnitude of the velocity of each lattice point in the computing grid. The vector lengths are scaled to the unit length indicated on the plot (in cm/μsec) equal to 1 cm on the scale shown.

In the plots of σ_x versus x the usual convention that negative values of stress are compressive is adopted.

3.5.1 Solution of Case 1B

The Lagrangian computing mesh employed for this case is shown in Figure 3-2. The inclusions were tungsten spheres, with a ratio of center-to-center spacing to inclusion diameter of 2. A single row of 4 inclusions was considered. The inclusion diameter was arbitrarily set at 0.004 cm. The epoxy filler material occupies the remainder of the computing region, which is a 0.008 cm radius cylinder. The periphery of the cylinder was fixed, except for the ends, which were free surfaces. A uniform pressure loading of 5 kilobars was applied to the left end of the cylinder, starting at time zero. The pressure was constant in time so that the behavior of just the shock front could be studied.

The principal stress and particle velocity fields occurring at times of 0.0010, 0.0093, 0.0160, 0.0262, 0.0364, 0.0533, 0.0584, 0.0686, and 0.0733 μsec are shown in Figure 3-3 through 3-16.

At t = 0.001 μsec (Figure 3-3), the shock front has advanced a short distance into the epoxy and the behavior is seen, as expected, to be purely one-dimensional. The succeeding figures show the effect of the inclusions on the velocity field.

The further advance (in the x-direction) of the wave in the vicinity of the inclusions is due to the relatively higher wave speeds in the tungsten. Note also how the flow in the epoxy is diverted around the periphery of the relatively stiff spherical inclusions. The reflected shock off the inclusion is also seen to decelerate the material between the left boundary and the inclusion, leading to a bulged surface whose apex is on the axis of symmetry, in line with the inclusions. At late times, the flow is nearly stable in time behind the front. The velocity of the flow increases with radius and the radial components of velocity have been nearly damped out.

At time sequence of profiles of the stress (σ_x) versus x for several radial positions is shown in Figure 3-17. The development of an elastic precursor in the epoxy is clearly seen in these graphs. An edit of σ_x for x for all the radial mesh positions at t = 0.0733 μsec is shown in Figure 3-18. The shock front at radii comparable with or less than the radius of the inclusions is persistently different than the others, and would not be expected to conform to the shape of the outer radius profiles upon traversal of the shock through an additional depth of the target.

A time sequence of plots of the particle velocity ($\dot{x}$) versus x at five different radial positions is shown in Figure 3-19. Note the reduced forward velocity along constant radius lines passing through the inclusions. This deceleration is caused by the shocks reflected from the higher impedance inclusions.

3.5.2 Solution of Case 1C

To help assess the amount of broadening of a shock front passing through a heterogeneous structure, it is useful to obtain a solution of the response of a homogeneous medium to the same loading. This was done for Case 1B, using the composite equation of state described previously for the homogeneous material.

For a constant loading, as in this case, the wave characteristics are soon established, and remain stable in time thereafter, consisting merely of a shock front passing through the material, with a region of constant state behind the front. Representative stress and velocity profiles are shown in Figure 3-20. The broadening of the shock front is due solely to the artificial viscosity used in the machine solution.

The two-dimensional solution (Case 1B), in this case, showed that there was no uniform stress profile established across the material (radially); however, the broadening of the front in the epoxy at large radii can be compared with the homogeneous case. Since there was no elastic precursor in the 1-D case, due to the modified equation of state, comparisons were made of the broadening of just the plastic wave. The shock front was spread over approximately 0.0024 cm in Case 1B, compared with 0.0012 cm in the case with no inclusions.

3.5.3 Solution of Case 2A

This problem considered the propagation of a shock wave due to a square-wave external pressure loading through a target containing a regular array of cylindrical inclusions. The inclusions were tungsten, imbedded in an epoxy target. The Lagrangian computing grid used for this solution is shown in Figure 3-21. The horizontal boundaries are treated as planes of symmetry, so that the solution will represent the response of an infinitely long heterogeneous medium in the y direction, as well as the z direction. The ratio of inclusion spacing to diameter was 1.75. The inclusion diameter was arbitrarily set at 0.04 cm. A uniform pressure loading of 5 kb was applied to the left face of the structure for 0.153 μsec, corresponding to a pulse length in the epoxy of 1.2 times the inclusion diameter and to approximately twice the transit time of a sound wave in the tungsten across the diameter of an inclusion.

The principal stress and particle velocity fields occurring in the structure at times of 0.0103, 0.0728, 0.1405, 0.1744, 0.2422, 0.4122, 0.5459, and 0.7343 are shown in Figures 3-22 through 3-31. Figures 3-22 through 3-24 show the wave propagation resulting from the pressure loading on the left face. At t = 0.1744 μsec (Figure 3-25), the rarefaction wave set up upon release of the pressure (at t = 0.153 μsec) is seen moving into the structure. This wave overtakes and attenuates the shock front at subsequent times. The configuration of the Lagrangian mesh at the end of the solution is shown in Figure 3-32. Plots of the stress (σ_x) along the symmetry planes and midway between them for the same times are shown in Figure 3-33. After traversing four rows of inclusions, the stress profiles of the waves are not yet uniform in the lateral (y) direction, due to the reverberations of the tungsten inclusions. This may be seen in Figure 3-34, which shows the stress along each row of cells (σ_x versus x) at t = 0.7343 μsec.

The peak compressive stress ($-\sigma_x$) in the wave at t = 0.7343 μsec along the midplane between the inclusion rows (upper boundary of computing region) was 1.24 kb, or 25 percent of the loading pressure. The pulse length was 0.20 cm, or 4.15 times the pulse length of the pressure loading.

3.5.4 Solution of Case 2B

The specifications of this case were identical to those of Case 2A, except that the inclusion material was quartz. The same pressure loading function was used, giving, thereby, a pulse length equivalent to twice the transit time of a sound wave in the quartz across the diameter of an inclusion.

The Lagrangian computing mesh appears the same as in Case 2A (Figure 3-21). The principal stress and particle velocity fields occurring in the structure at times of 0.0133, 0.0762, 0.1439, 0.1778, 0.2117, 0.2456, 0.3811, 0.5166, and 0.6522

μsec are presented in Figures 3-35 to 3-46. The first three figures show the loading of the material and the advance of the wave during the period of pressure application. The subsequent figures show the effect of the pressure release, producing a rarefaction wave which eventually overtakes and attenuates the shock front. At late times the lateral (y direction) velocity components have been nearly damped out, due to the wave reverberations across the material between the symmetry planes. There was relatively small material distortion in this case compared with Case 2A, due to the smaller difference in shock impedance of the filler and inclusion materials.

Profiles of the stress (σ_x) versus x along the symmetry planes and midway between them are shown in Figure 3-47. Note that the profiles tend to become more uniform as time progresses, even for the profile passing through the inclusions. Stress profiles along each computing row at t = 0.6522, μsec are shown in Figure 3-48. Particle velocity profiles ($\dot{x}$ versus x) at several times are shown in Figure 3-49. These plots confirm the tendency toward the laterally uniform distribution indicated in the stress plots.

The peak compressive stress ($-\sigma_x$) in the wave at t = 0.6522 μsec along the midplane between the inclusions was 2.04 kb, or 41 percent of the loading pressure. The pulse length was 0.16 cm, or 3.32 times the pulse length of the pressure loading. The reduced pulse attenuation and broadening in this case compared with Case 2A can be attributed to the closer impedance match between the epoxy and quartz as opposed to epoxy and tungsten.

3.5.5 Solution of Case 2C

This problem consisted of a 1-D solution o. the response of a homogeneous epoxy target to the pressure loading used in Cases 2A and 2B. All specifications of the problem were as in these cases, except that there were no inclusions imbedded in the epoxy.

The results of the solution are shown in Figures 3-50 and 3-51, which plot the stress and particle velocity profiles occurring at times of 0.1451, 0.1906, 0.5089 and 0.8045 μsec.

The last value of the peak compressive stress ($-\sigma_x$) was 3.43 kb, or 69 percent of the loading pressure. The pulse length had broadened to 0.099 cm, or 2.05 times the pulse length of the pressure loading. Comparisons of Cases 2A and 2B with this case are tabulated in Table 3-II. These comparisons indicate the large degree of shock dispersion which takes place during wave propagation through even a relatively few number of inclusions.

3.5.6 Solution of Case 2D

The specifications of this problem were the same as for Case 2B, except that the duration of the pressure application was 0.0382 μsec, corresponding to a pulse length in the epoxy of 0.3 times the inclusion diameter and to one-half the transit time of a sound wave in the quartz across the diameter of an inclusion.

The material response up to a time of 0.0382 μsec is the same as in Case 2B. For subsequent times, at t = 0.0423, 0.0762, 0.1101, 0.1609, 0.2286, 0.3642, 0.4997, and 0.6352 μsec, the principal stress and particle velocity fields in the target appear as shown in Figures 3-52 through 3-62. Associated stress profiles (σ_x versus x) along the symmetry planes and midway between them are shown in Figure 3.63. Stress profiles along each row of cells for the last time 0.6352 μsec) are shown in Figure 3-64. Particle velocity profiles ($\dot{x}$ versus x) are shown in Figure 3-65.

The peak compressive stress ($-\sigma_x$) in the wave at t = 0.6352 μsec along the midplane between the inclusion rows was 0.74 kb, or 15 percent of the loading pressure. The pulse length was broadened to 0.063 cm or 5.24 times the pulse length of the pressure loading, at this time. The results of Cases 2B and 2D indicate the amount of increased dispersion to be expected as the ratio of initial pulse width to inclusion size decreases.

3.5.7 Solution of Case 3A

The Lagrangian computing mesh employed for this case is shown in Figure 3-66. The inclusions were tungsten spheres, with a ratio of center-to-center spacing to inclusion diameter of 1.5. A single row of 6 inclusions was considered. The inclusion diameter was arbitrarily set at 1 cm. The inclusions were imbedded in a 1.5 cm radius epoxy cylinder. The periphery of the cylinder was fixed, except for the ends, which were free surfaces. A uniform pressure loading of 5 kb was applied to the left face of the structure for 3.857 μsec, corresponding to a pulse length in the epoxy of 1.2 times the inclusion diameter, and to twice the transit time of a sound wave in the tungsten across the diameter of an inclusion.

The principal stress and particle velocity fields occurring in the structure at times of 1.165, 4.967, 6.131, 7.295, 12.42, 17.07, and 26.39 μsec are shown in Figures 3-67 through 3-76. Note how passage of the wave through the material sets up a relatively long-lasting ringing of the spherical inclusions. Profiles of the stress (σ_x versus x) along the axis of symmetry, the sides of the cylinder, and the midplane are shown in Figure 3-77. Stress profiles along each computing row for the final time are plotted in Figure 3-78. This graph shows that a uniform wave in the radial direction has not been established after transit of the wave past six inclusions. This may also be seen in Figure 3-76, which indicates that there are still significant radial components of particle velocity present in the wave system.

The peak compressive stress ($-\sigma_x$) in the wave at t = 26.39 μsec along the cylinder periphery was 2.38 kb, or 48 percent of the loading pressure. The pulse length at this time was 4.0 cm, or 3.29 times the pulse length of the pressure loading.

3.5.8 Solution of Case 3B

The specifications of this problem were identical to Case 3A, except that the tungsten inclusions were replaced by spherical void spaces. The Lagrangian computing grid employed is shown in Figure 3-79.

The principal stress and particle velocity fields occurring in the structure at times of 2.173, 5.558, 6.886, 8.241, 10.27, 17.03, 23.65, and 27.12 μsec are shown in Figures 3-80 through 3-90. Note that in this case, there are reflected rarefaction waves off the "inclusions," instead of reflected shocks, as in the other cases. The 5 kb loading was of sufficient intensity to cause a collapse of the first void space. This action caused considerable distortion of the Lagrangian net, and certain cells around the periphery of the first void space had to be removed in order to continue the solution. Note also how the left end of the cylinder is depressed, as opposed to being bulged out in the case of high impedance inclusions.

Stress profiles (σ_x versus x) along the axis of symmetry, the cylinder periphery, and the midplane between them are shown in Figure 3-91. The profiles along the axis of symmetry ($y = 0$) may be identified as the non-continuous curves, due to their passing through void material. Stress profiles along each computing row at $t = 27.12$ μsec are shown in Figure 3-92.

The peak compressive stress ($-\sigma_x$) in the leading wave at $t = 27.12$ μsec along the cylinder periphery was 0.77 kb, or 15 percent of the loading pressure. The pulse length of the leading wave at this time was 2.3 cm, or 1.89 times the pulse length of the pressure loading. However, as may be seen in Figures 3-91 and 3-92, there is a subsequent long-pulselength wave having stress comparable to that in the leading pulse.

3.5.9 Solution of Case 3C

This problem consisted of a 1-D solution of the response of a homogeneous epoxy target to the pressure loading used in Cases 3A and 3B.

The results of the solution are shown in Figures 3-93 and 3-94, which plot the stress and particle velocity profiles occurring at times of 3.822, 5.556, 15.965, and 28.628 μsec. The last value of the peak compressive stress ($-\sigma_x$) was 2.80 kb, or 56 percent of the loading pressure. The pulse length had broadened to 3.3 cm, or 2.72 times the pulse length of the pressure loading, at this time. Comparisons of Cases 3A and 3B with this case are tabulated in Table 3-II. For the combinations of pulse width and inclusion spacing and diameter of the Group 3 problems, it is seen that the tungsten spheres effect relatively little pulse dispersion, whereas the void spheres are very effective.

3.6 CONCLUDING REMARKS

These solutions demonstrate the type of quantitative analysis that can be obtained of wave propagation through heterogeneous structures. If it were desired to determine the dependence of pulse dispersion on parameters such as inclusion material properties, pulse width/inclusion diameter ratios, inclusion spacing/diameter ratios, a parametric series of solutions similar to those performed in this program would be recommended. Studies involving other loadings, such as X-ray deposition, would also be of interest.

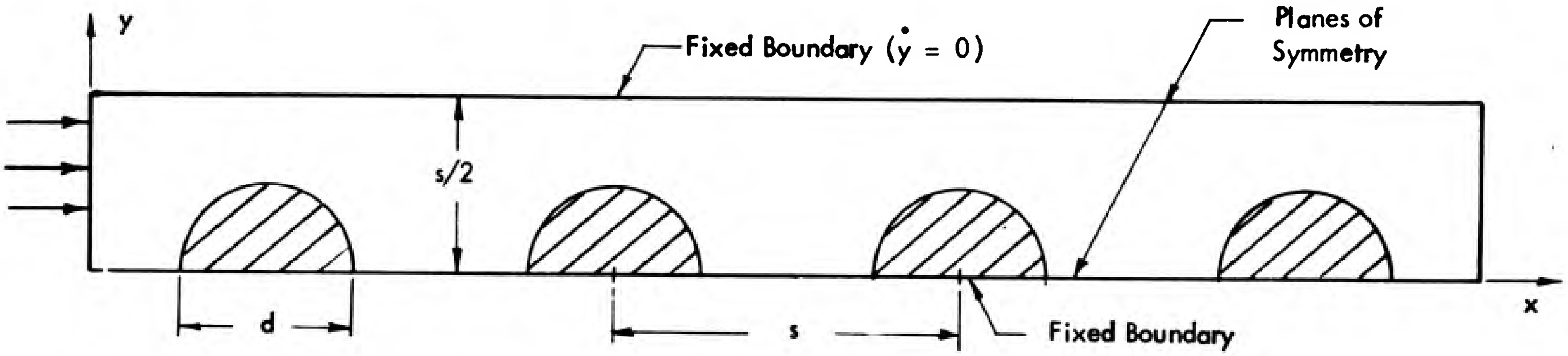

(a) CYLINDRICAL INCLUSIONS, PLANE GEOMETRY

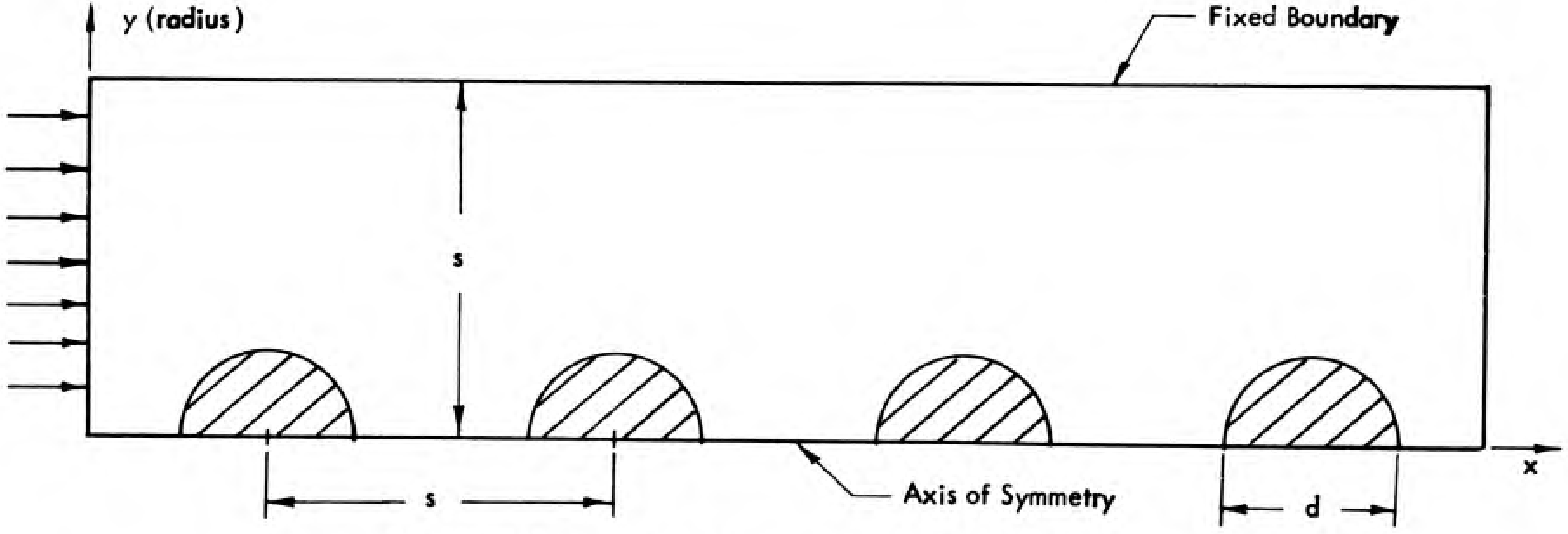

(b) SPHERICAL INCLUSIONS, CYLINDRICAL GEOMETRY

FIGURE 3-1. HETEROGENEOUS TARGET CONFIGURATIONS.

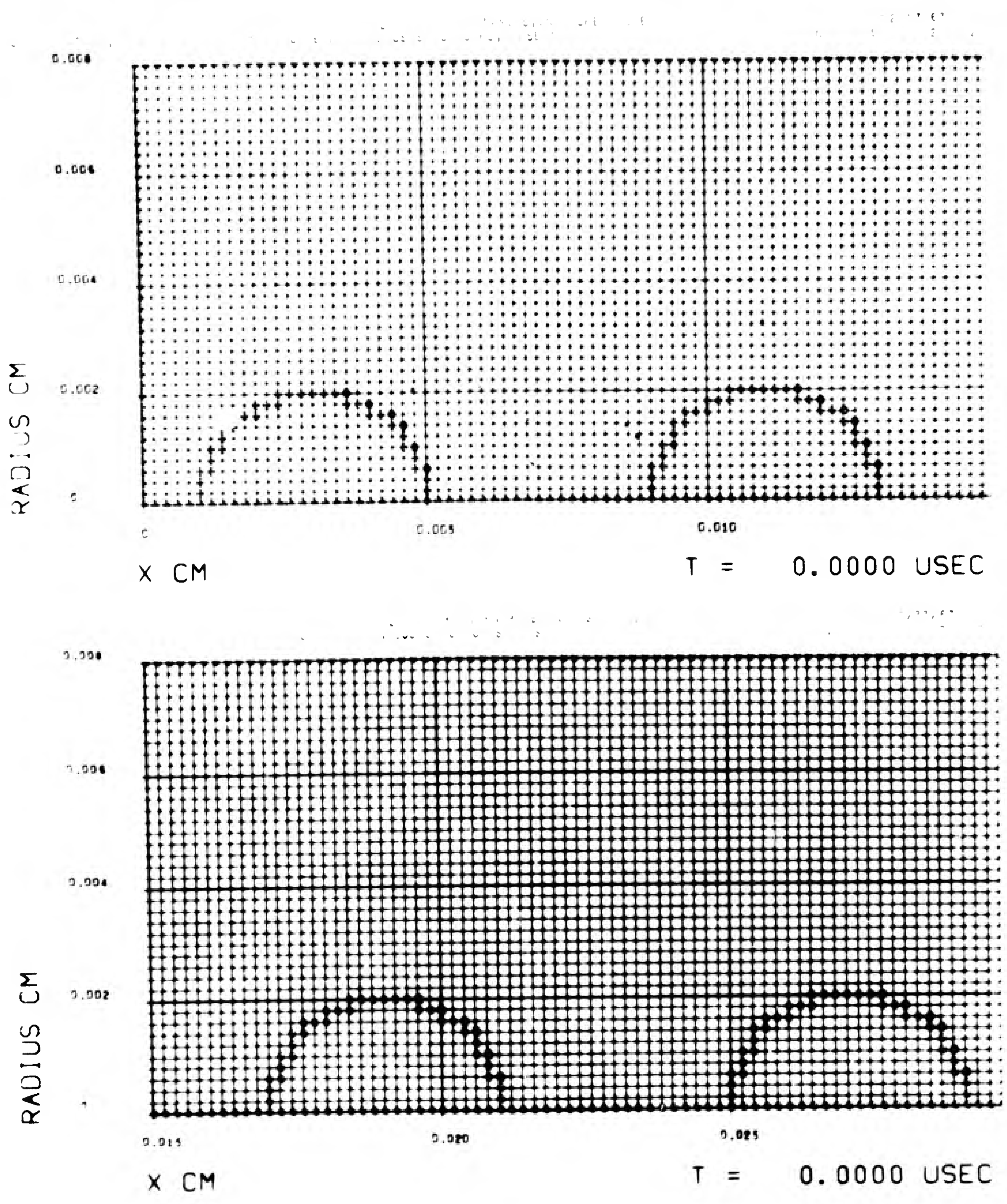

FIGURE 3-2. LAGRANGIAN MESH, CASE 1B

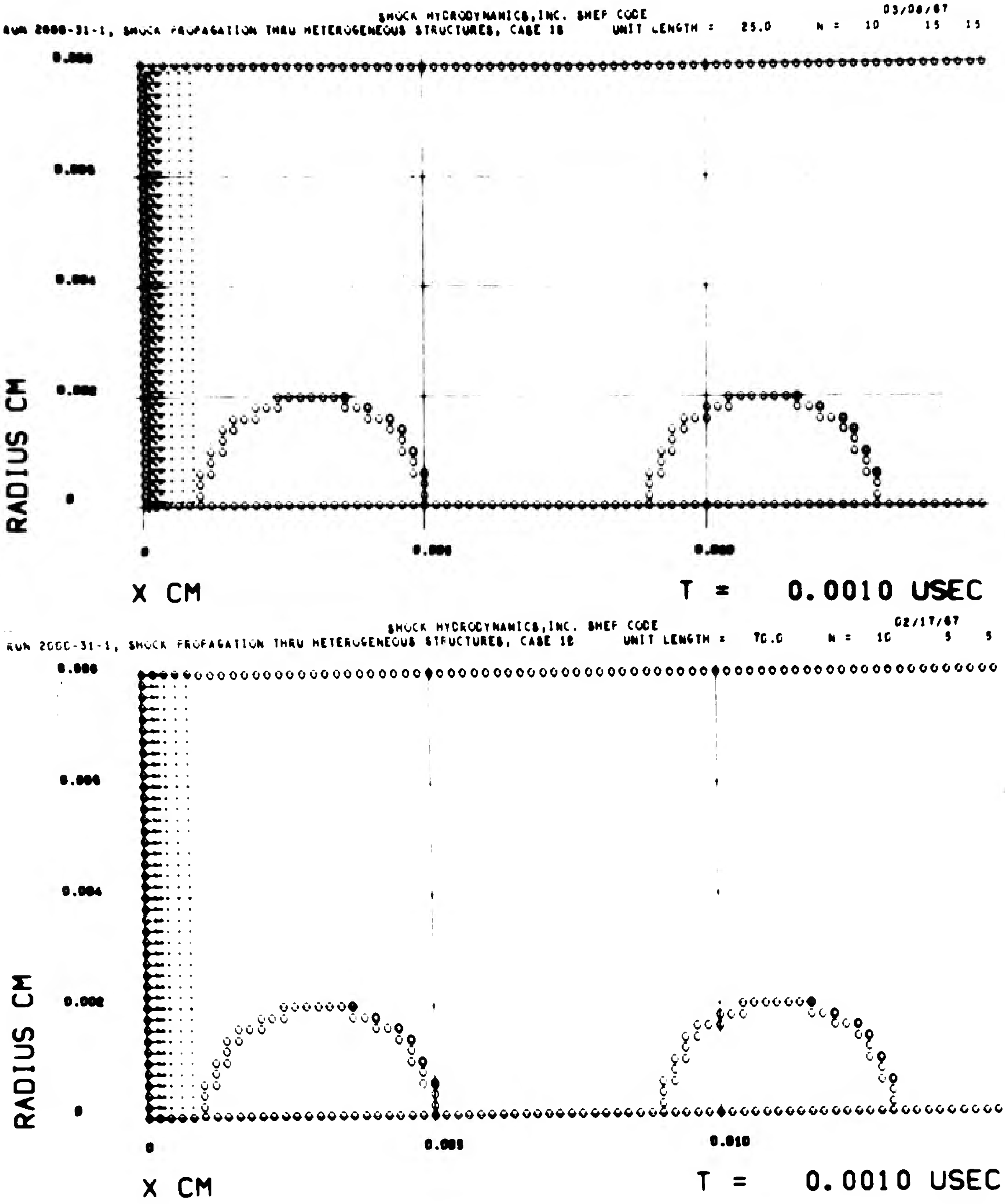

FIGURE 3-3. PRINCIPAL STRESS AND PARTICLE VELOCITY FIELDS, CASE 1B, $t = .0010\ \mu sec$.

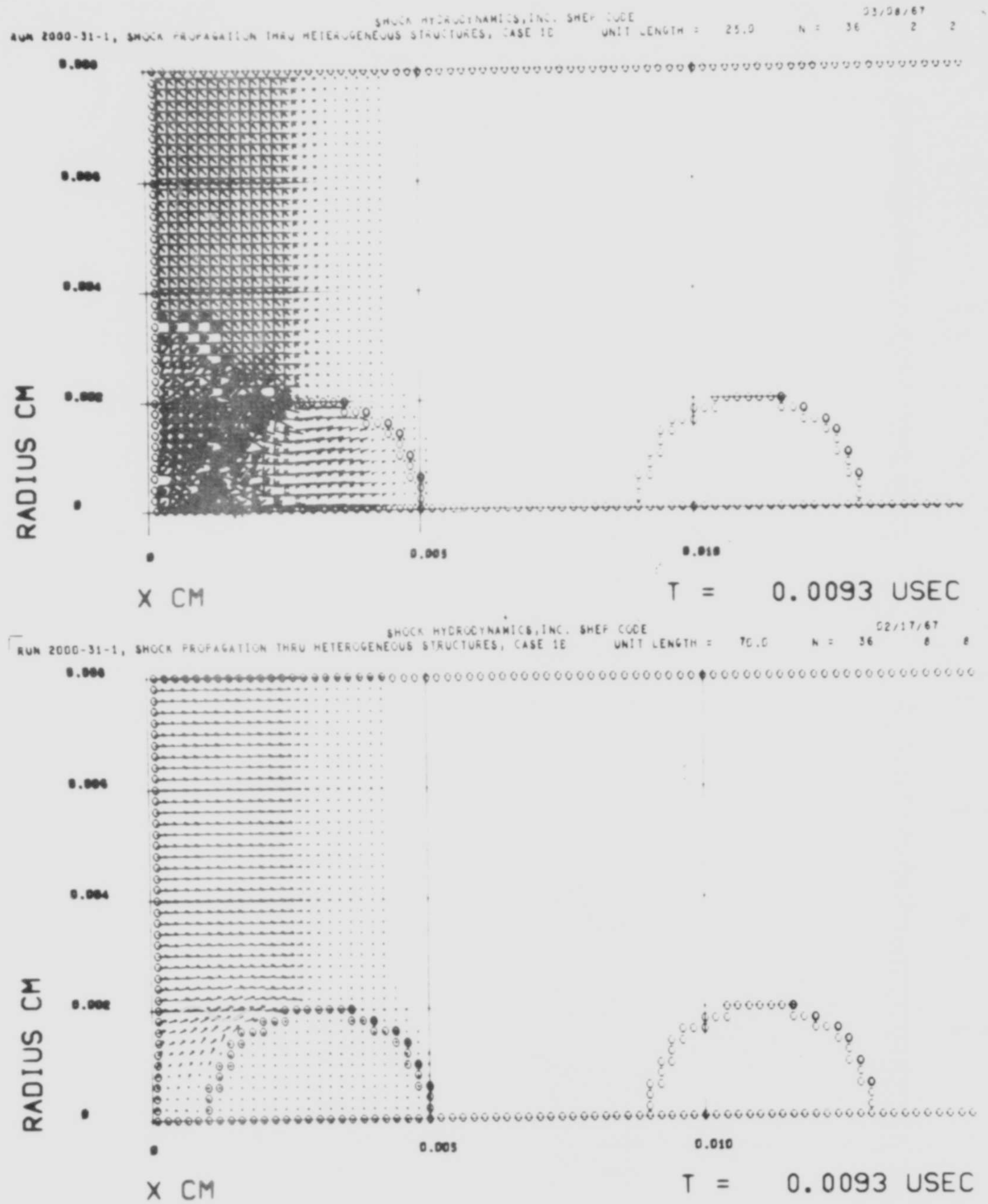

FIGURE 3-4. PRINCIPAL STRESS AND PARTICLE VELOCITY FIELDS, CASE 1B, t = .0093 μsec.

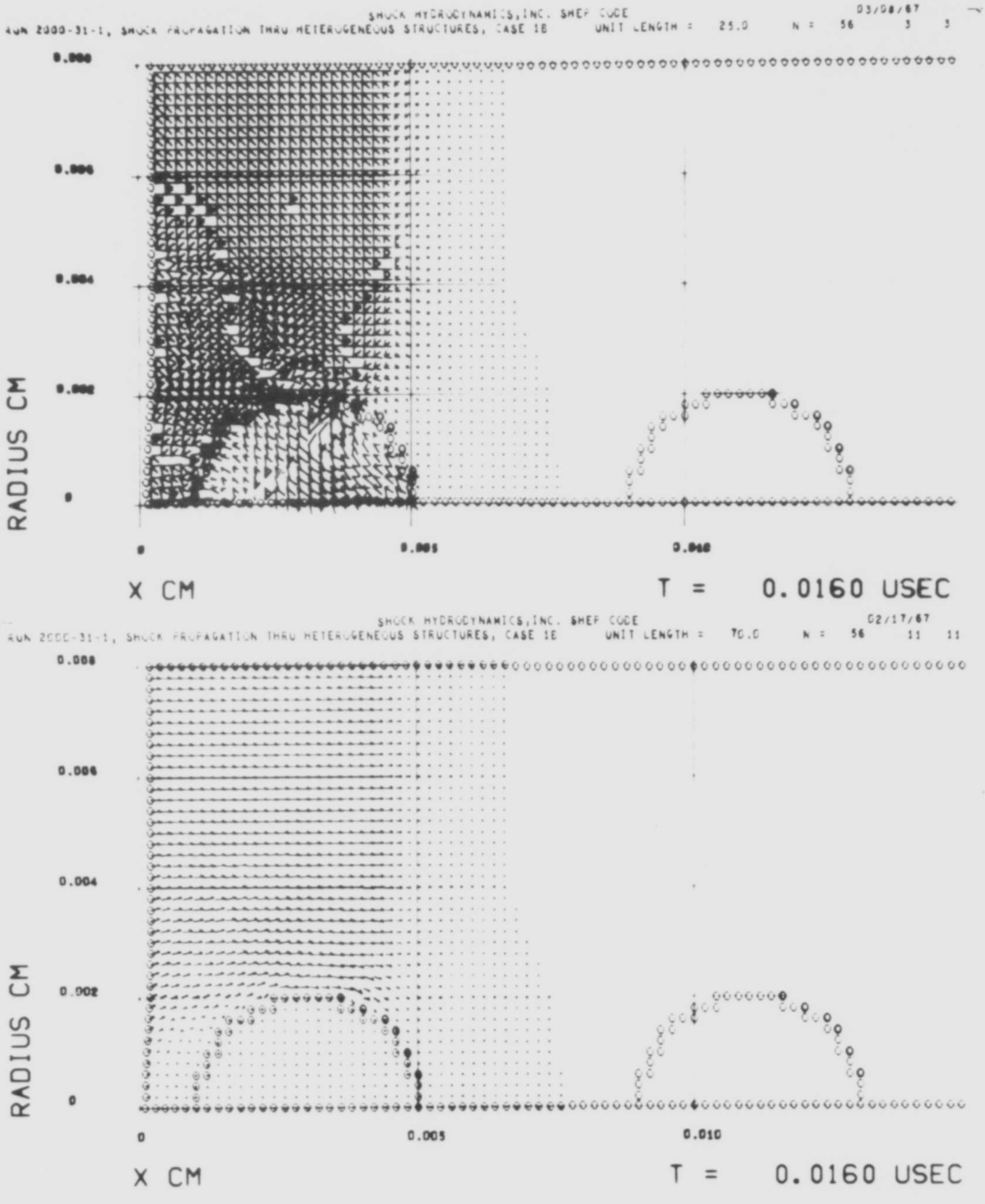

FIGURE 3-5. PRINCIPAL STRESS AND PARTICLE VELOCITY FIELDS, CASE 1B, t = .0160 μ sec.

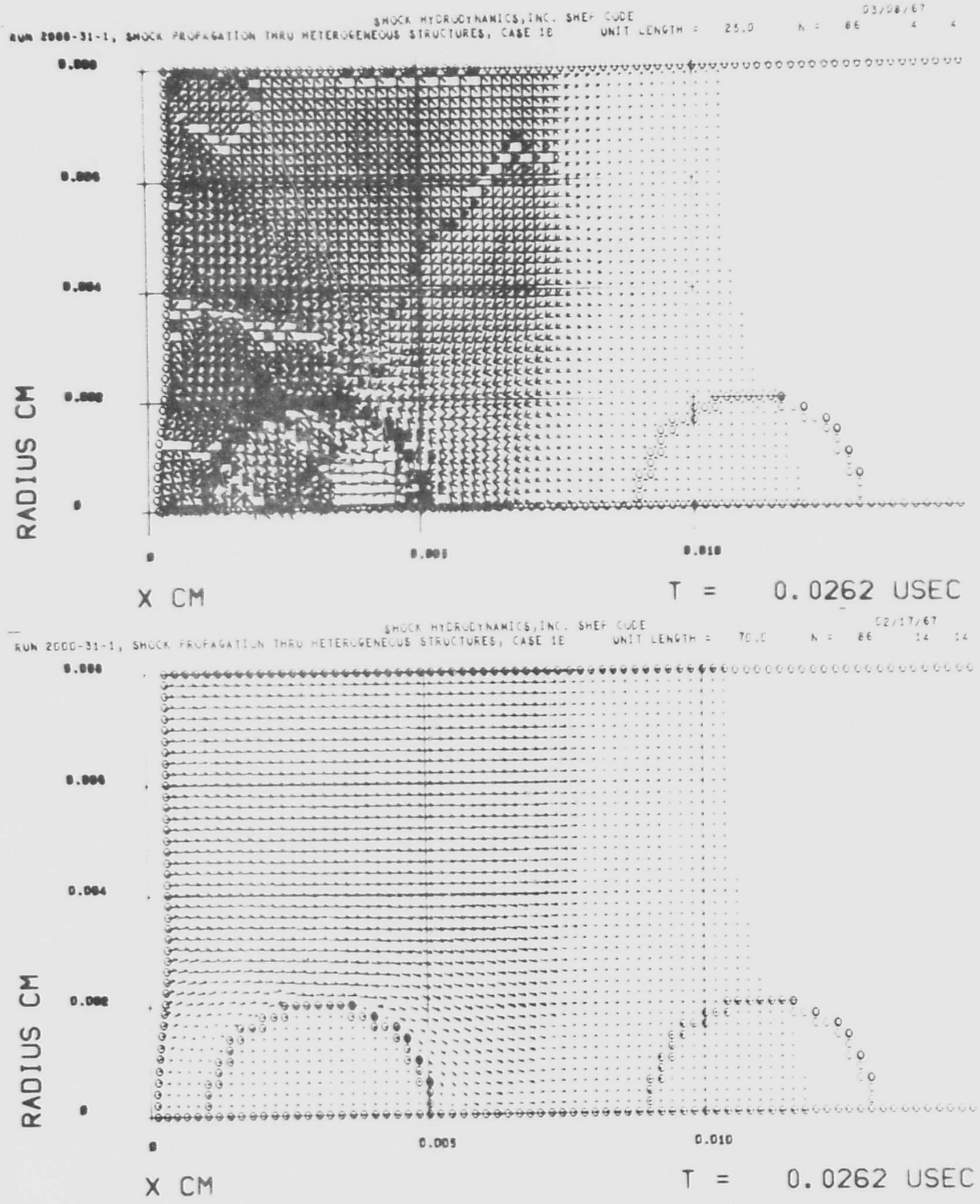

FIGURE 3-6, PRINCIPAL STRESS AND PARTICLE VELOCITY FIELDS, CASE 1B, t = .0262 μsec.

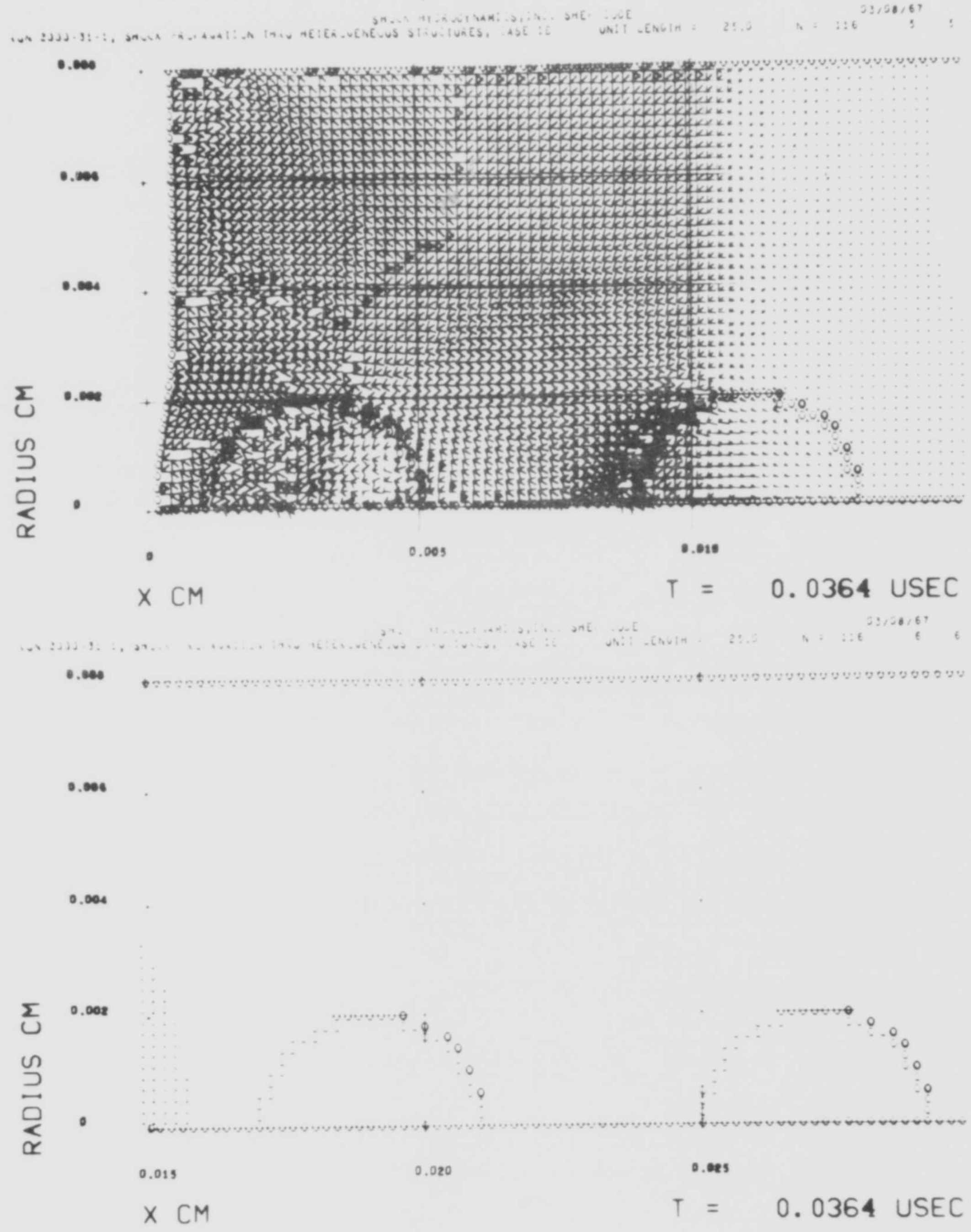

FIGURE 3-7. PRINCIPAL STRESS FIELD, CASE 1B, t = .0364 μsec.

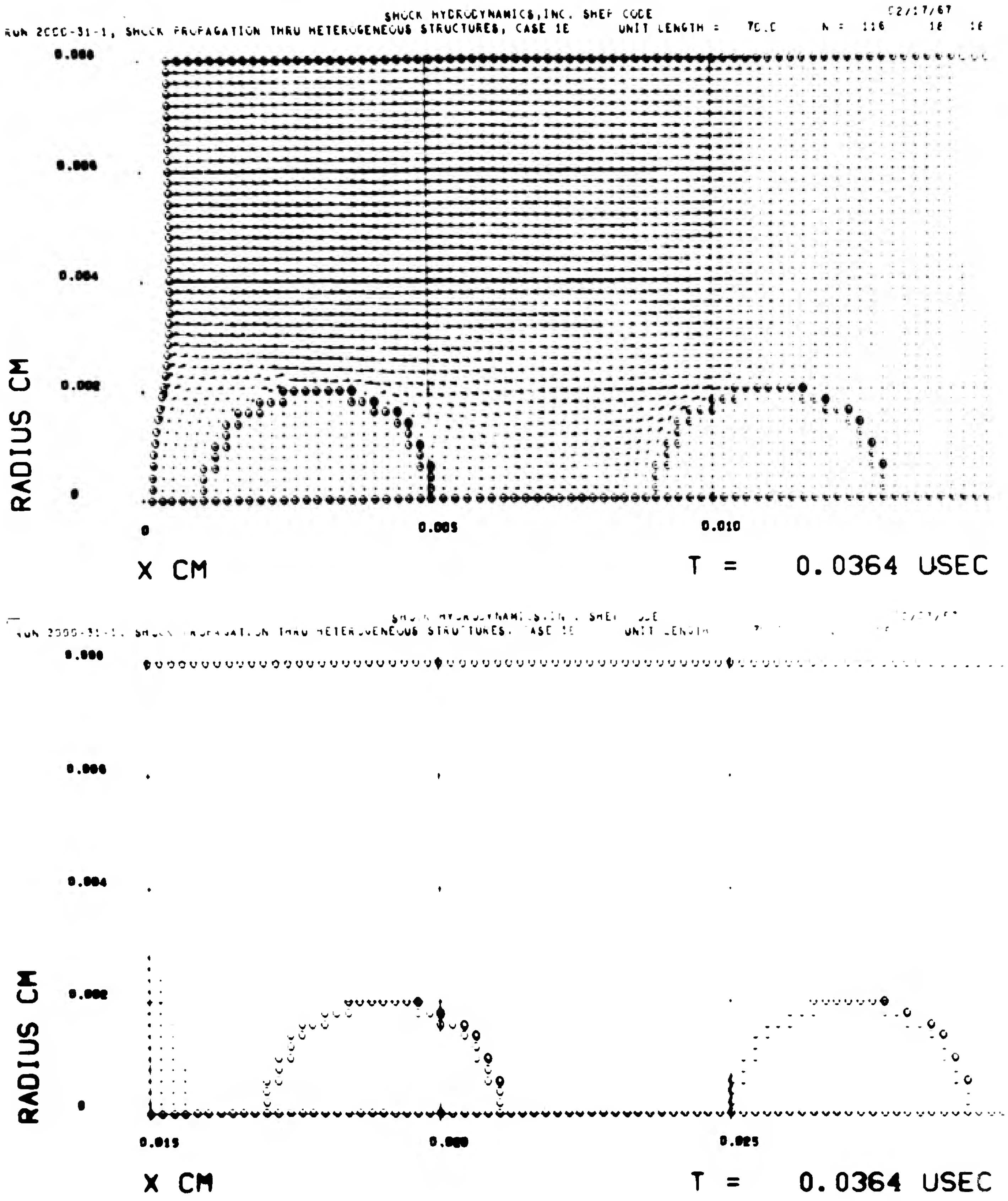

FIGURE 3-8. PARTICLE VELOCITY FIELD, CASE 1B, t = .0364 μsec.

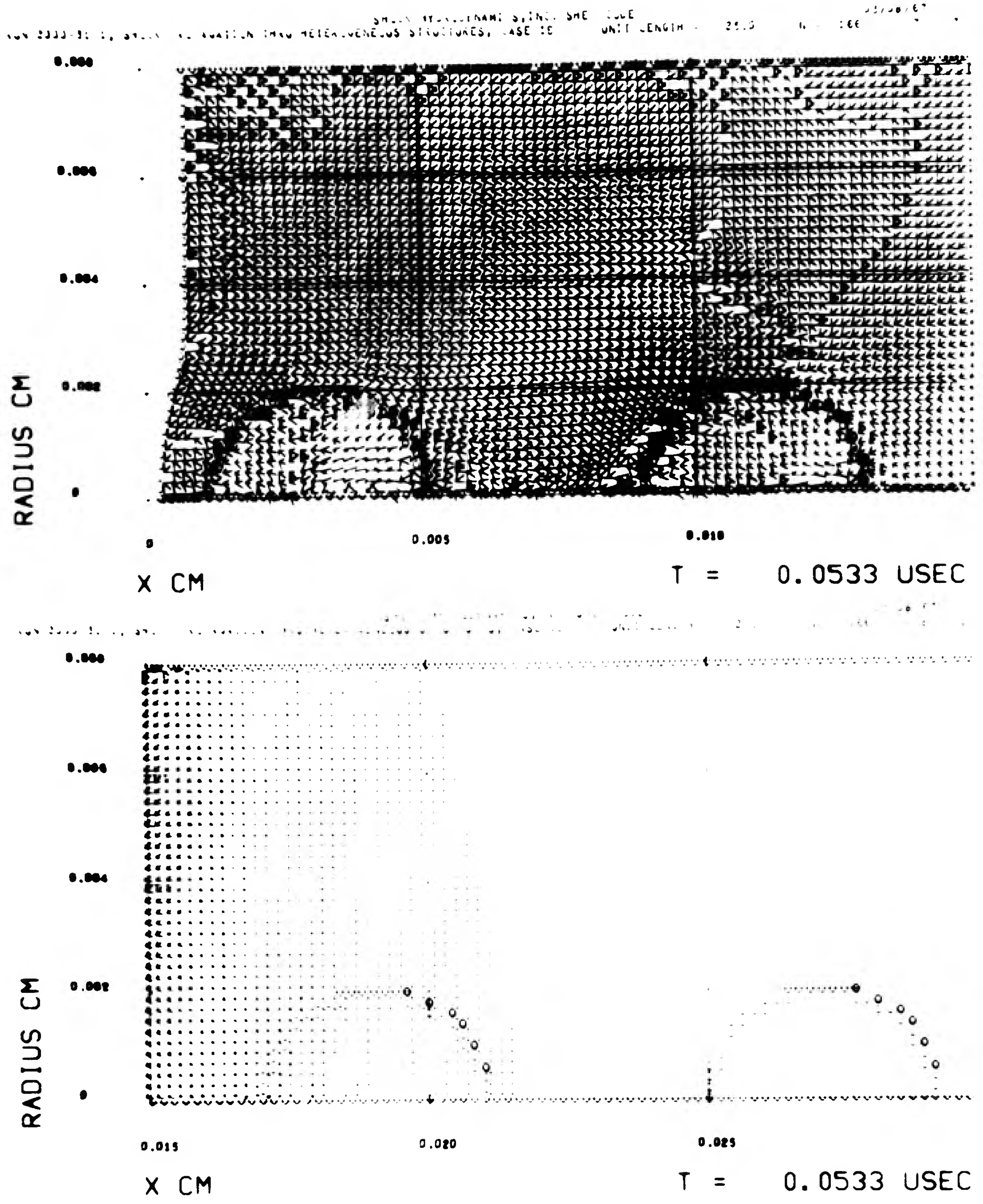

FIGURE 3-9. PRINCIPAL STRESS FIELD, CASE 1B, t = .0533 μsec.

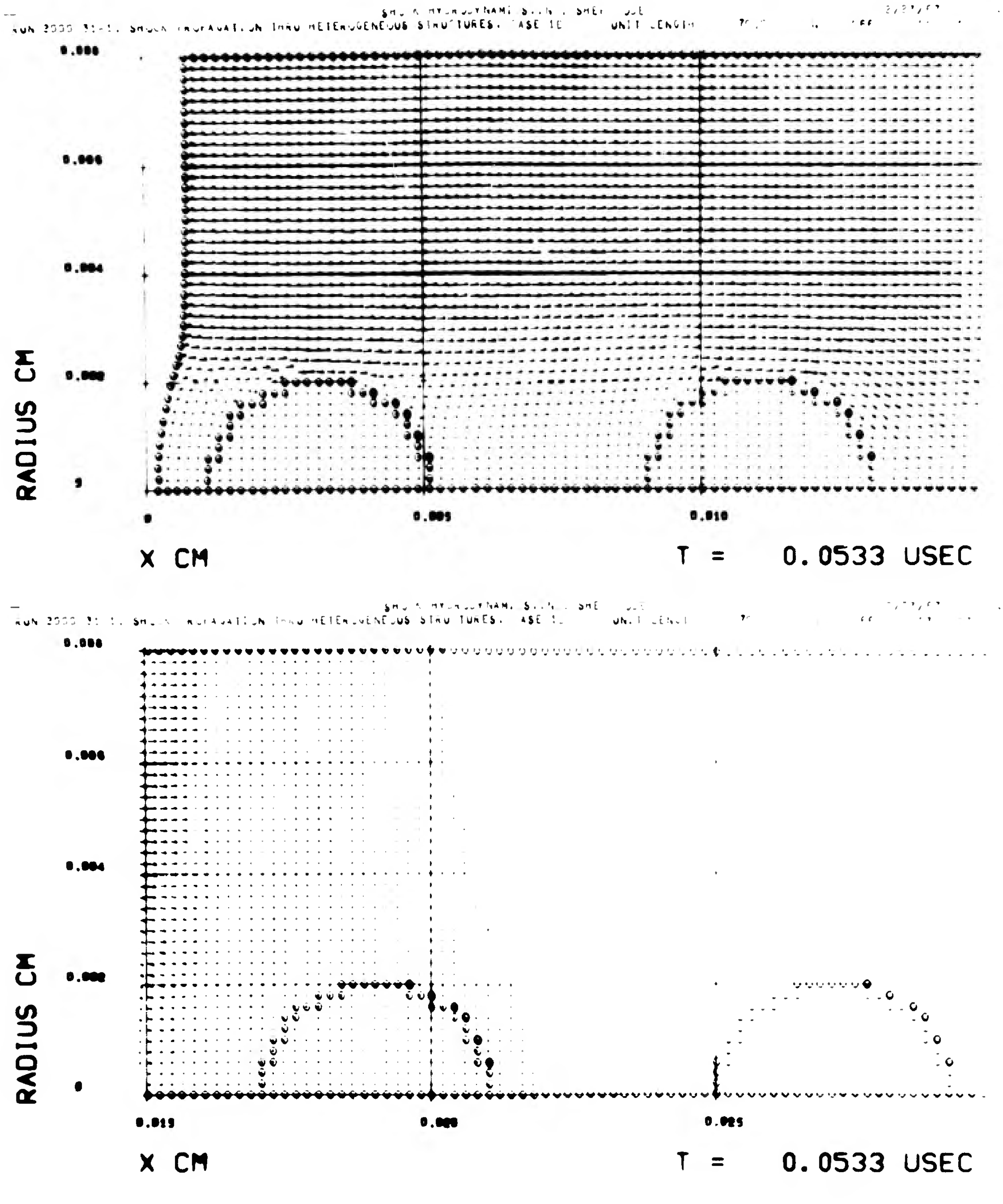

FIGURE 3-12. PARTICLE VELOCITY FIELD, CASE 1B, t = .0533 μ sec.

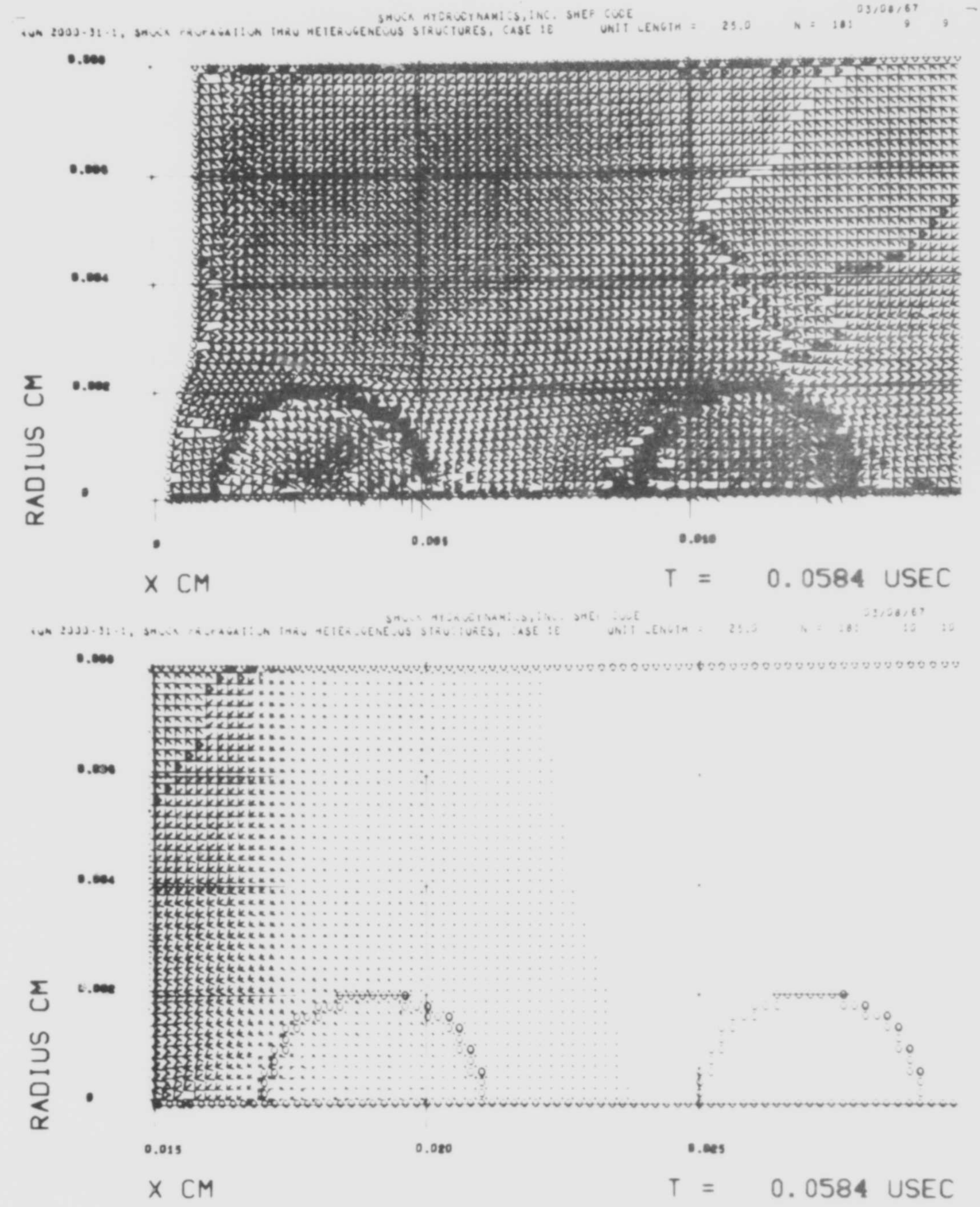

FIGURE 3-11. PRINCIPAL STRESS FIELD, CASE 1B, t = .0584 μsec.

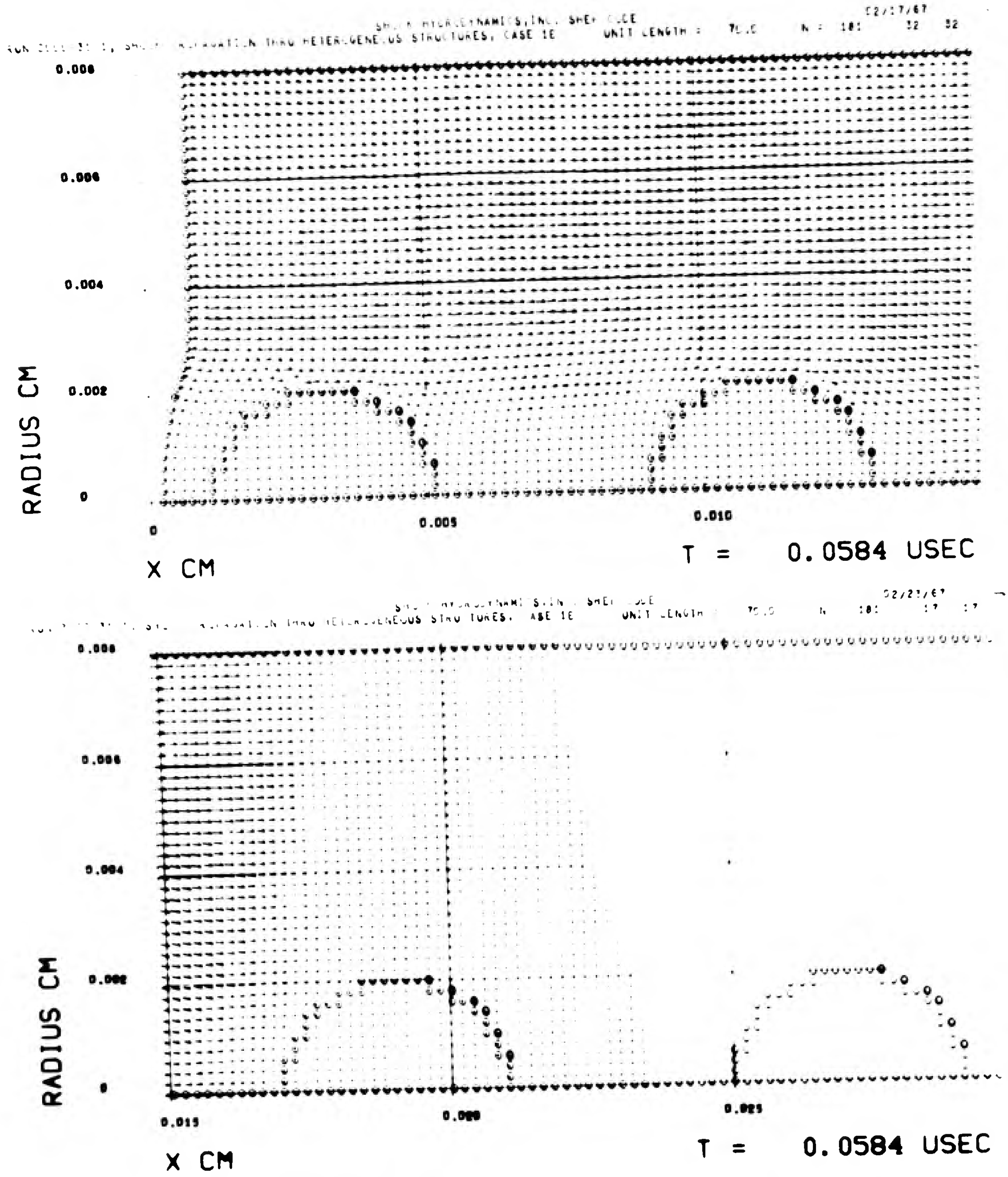

FIGURE 3-12. PARTICLE VELOCITY FIELD, CASE 1 B, t = .0584 μsec.

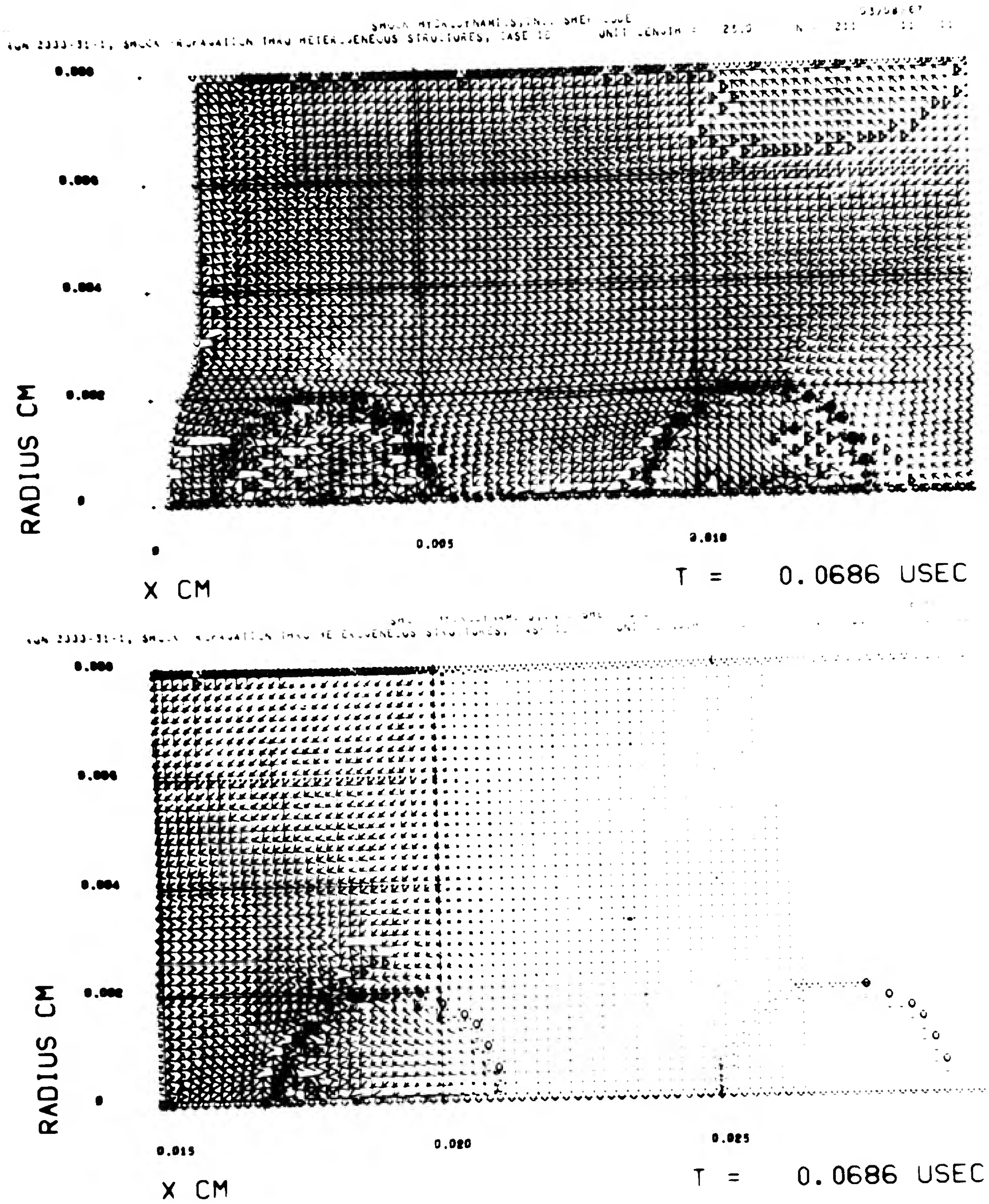

FIGURE 3-13. PRINCIPAL STRESS FIELD, CASE 1B, t = .0686 u sec.

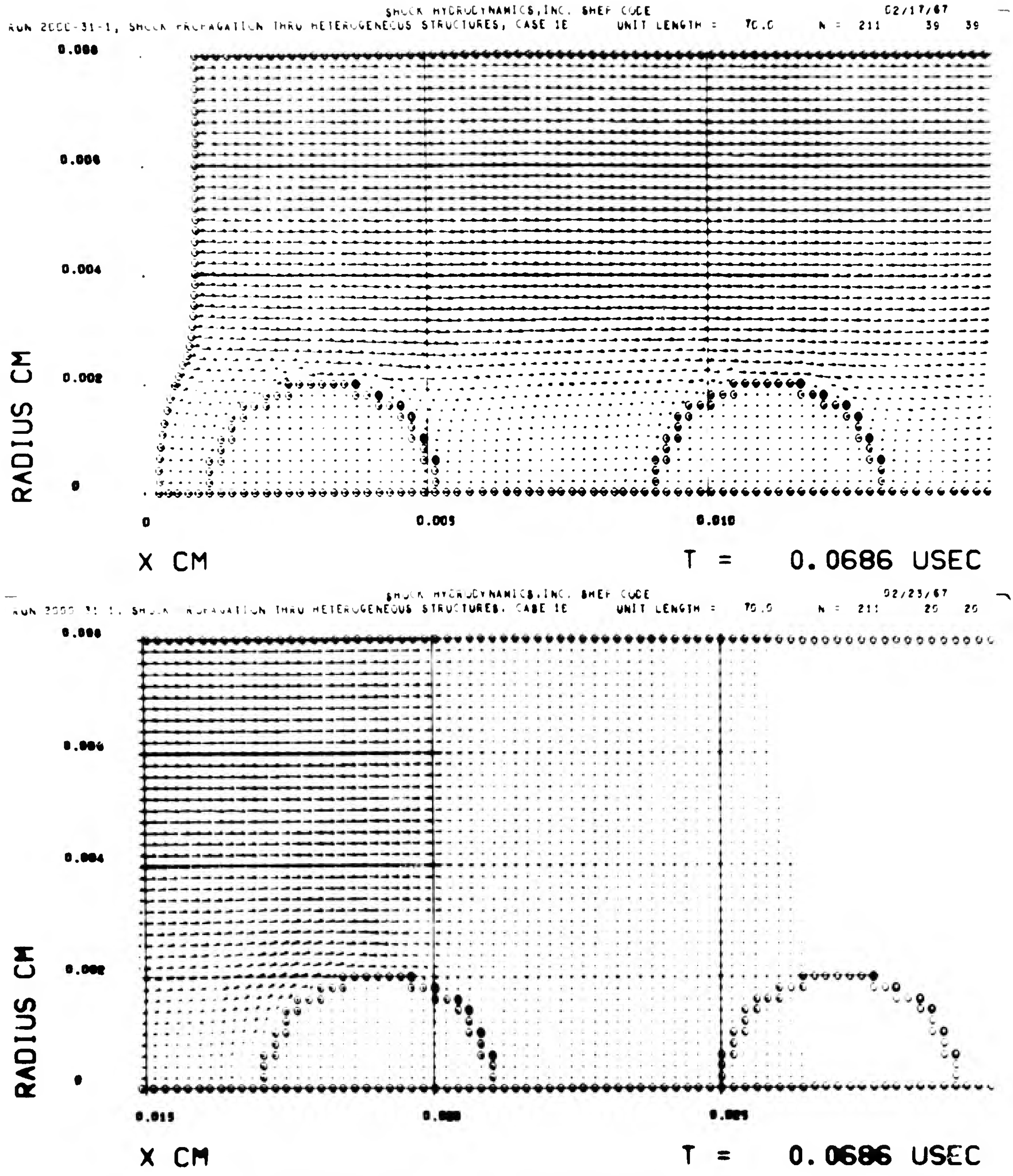

FIGURE 3-14. PARTICLE VELOCITY FIELD, CASE 1 B, t = .0686 μ sec.

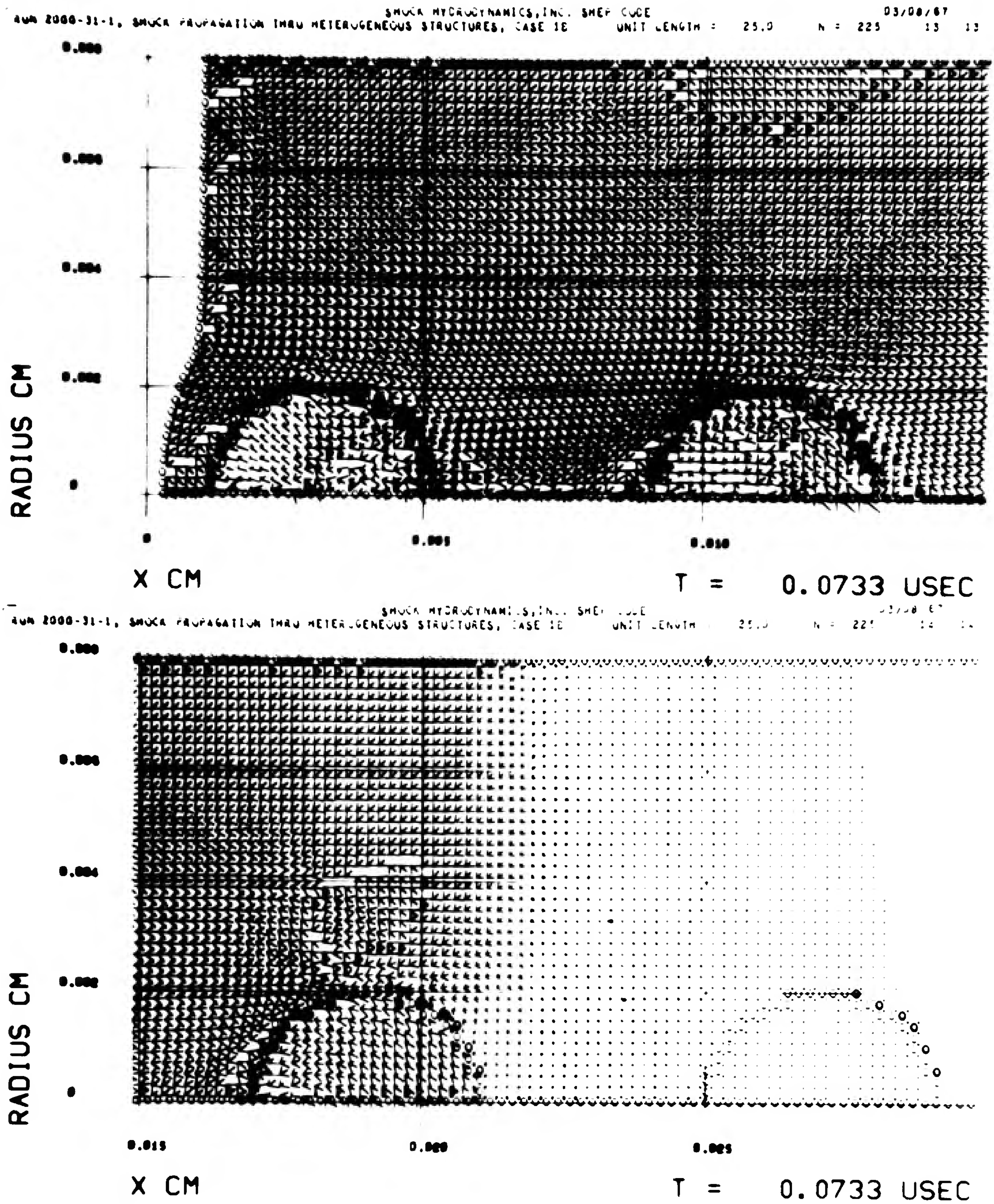

FIGURE 3-15. PRINCIPAL STRESS FIELD, CASE 1 B, t = .0733 u sec.

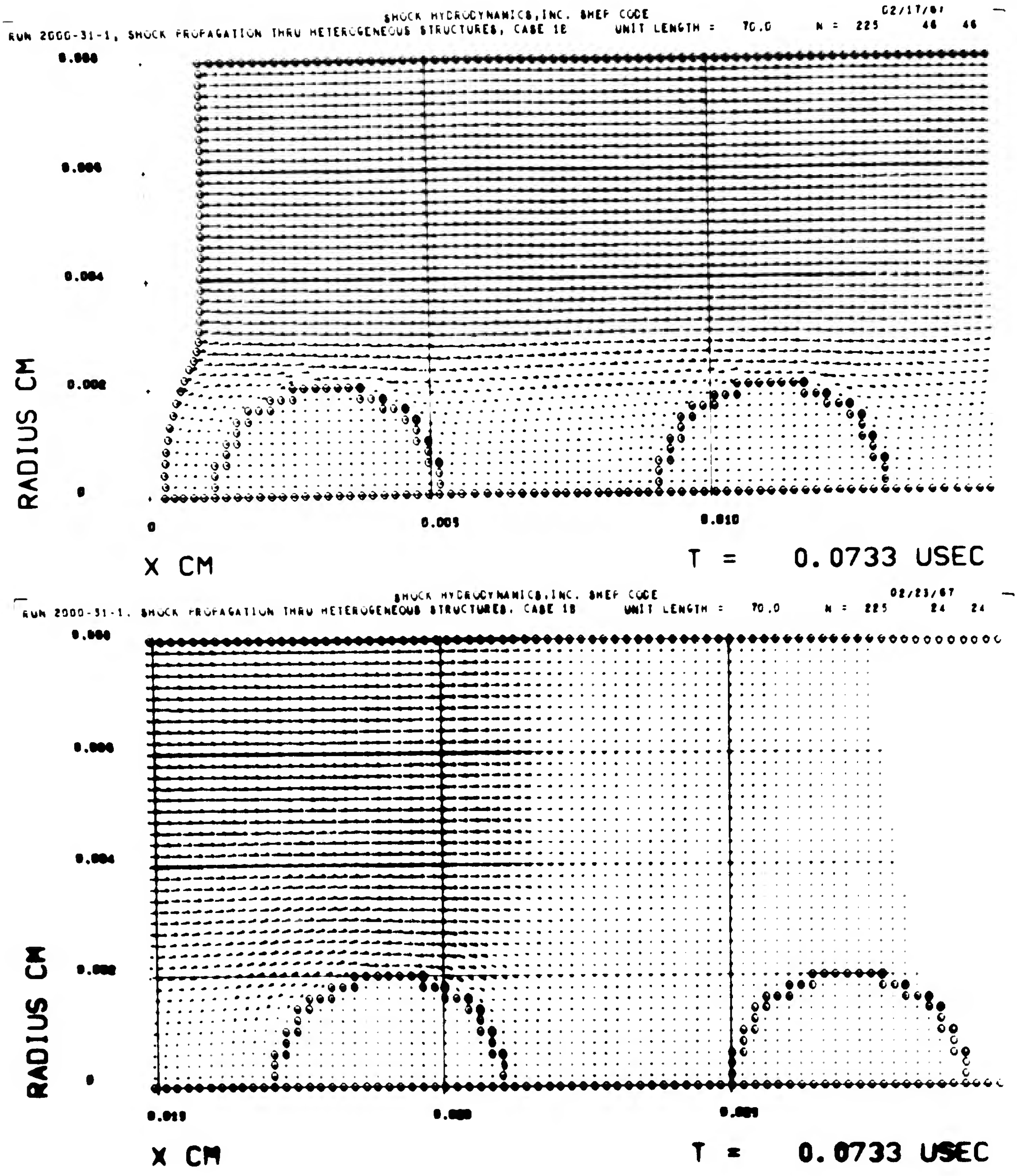

FIGURE 3-16. PARTICLE VELOCITY FIELD, CASE 1B, t = .0733 μsec.

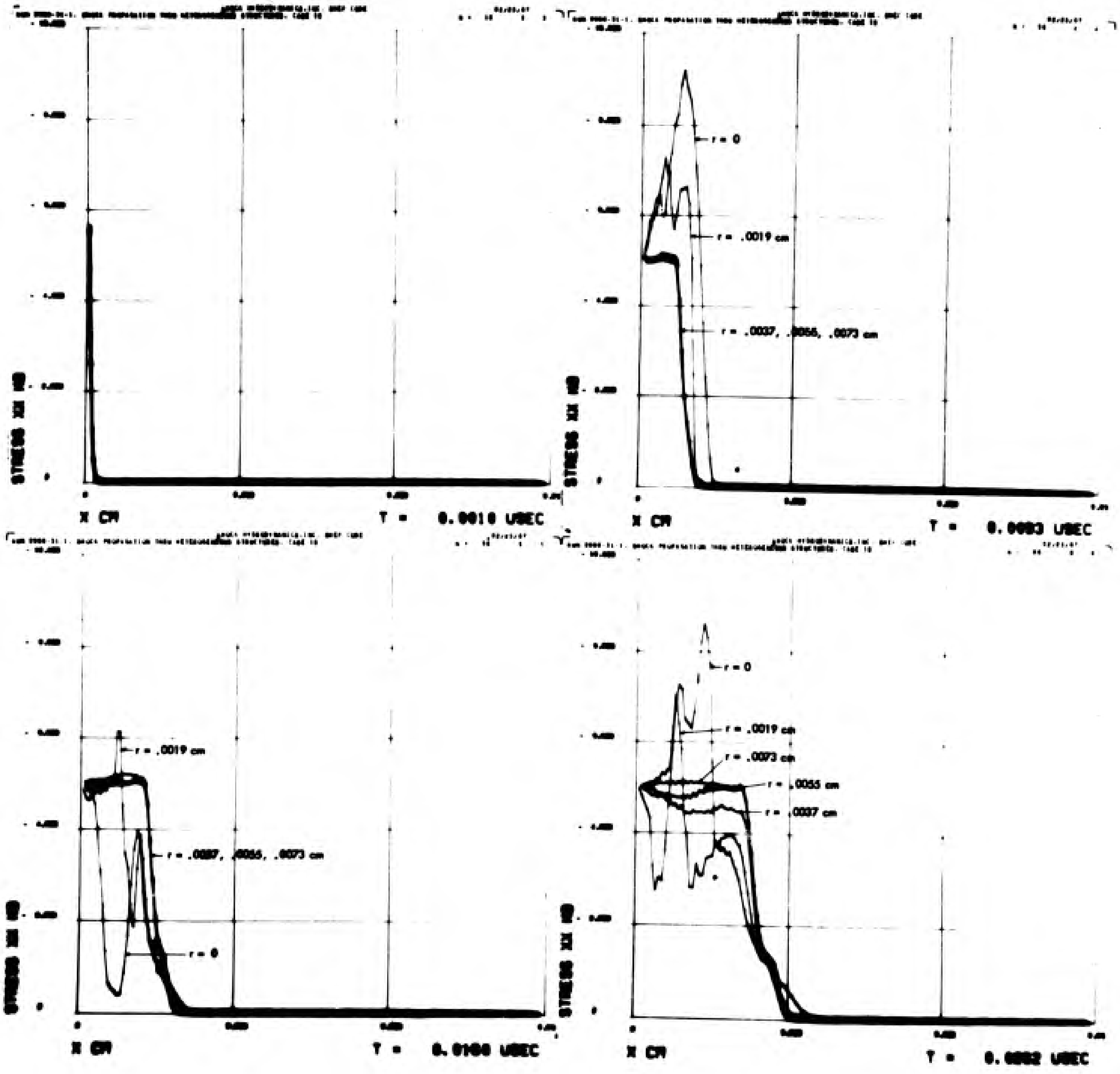

FIGURE 3-17. σ_x vs x AT SEVERAL RADIAL POSITIONS, CASE 1 B.

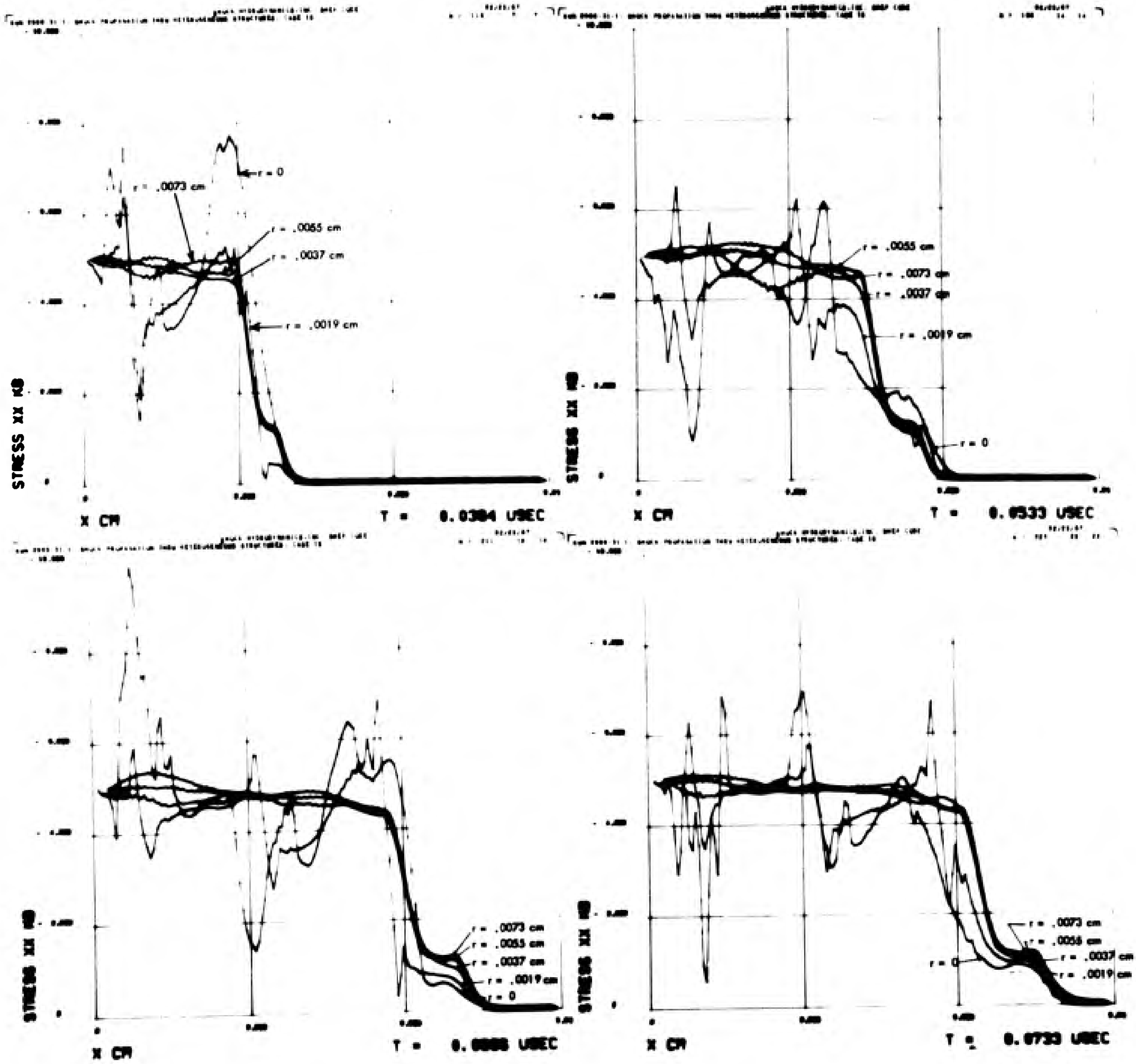

FIGURE 3-17 (cont'd) σ_x vs x AT SEVERAL RADIAL POSITIONS, CASE 1B.

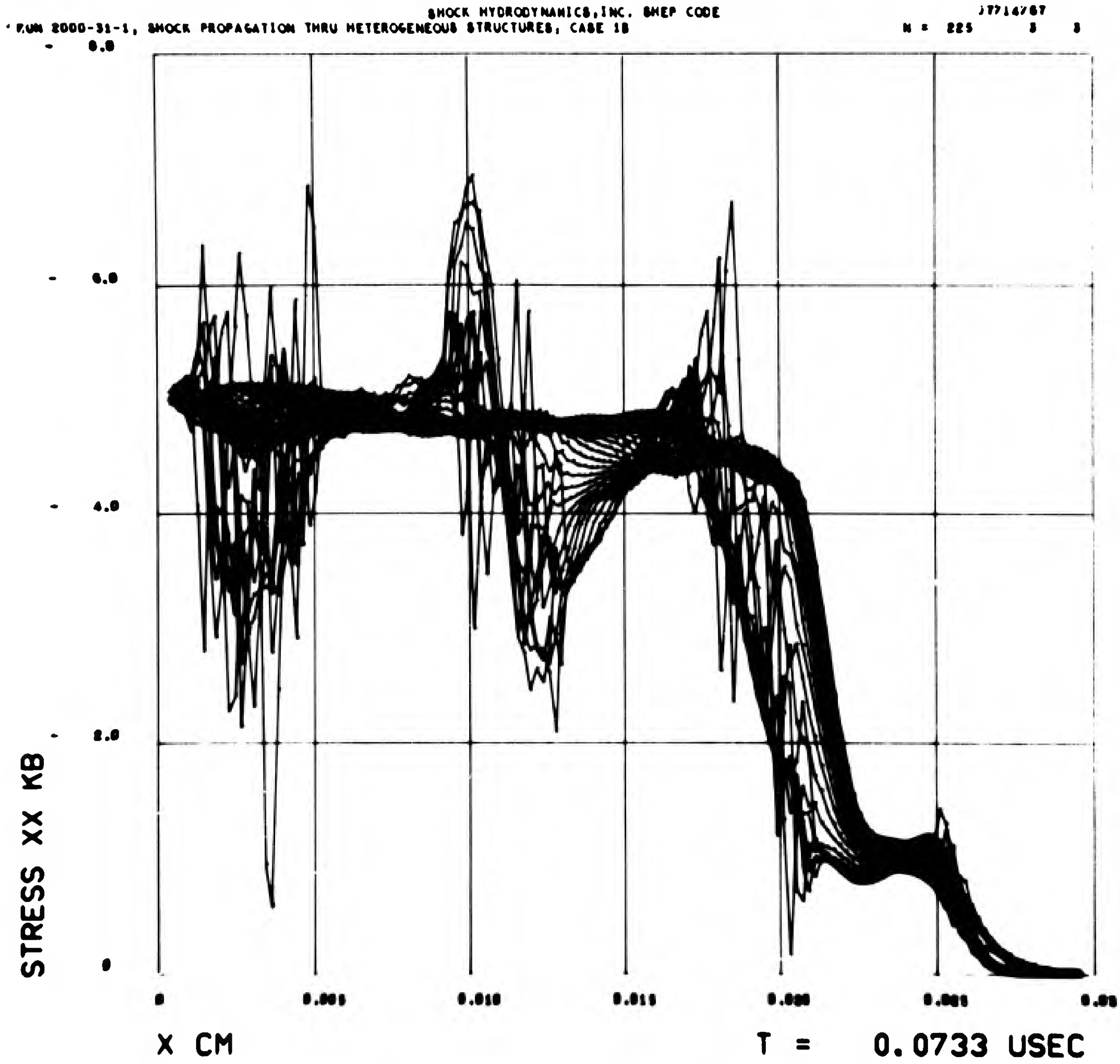

FIGURE 3-18. σ_x vs x at all Radial Mesh Positions, t = .0733 μ sec.

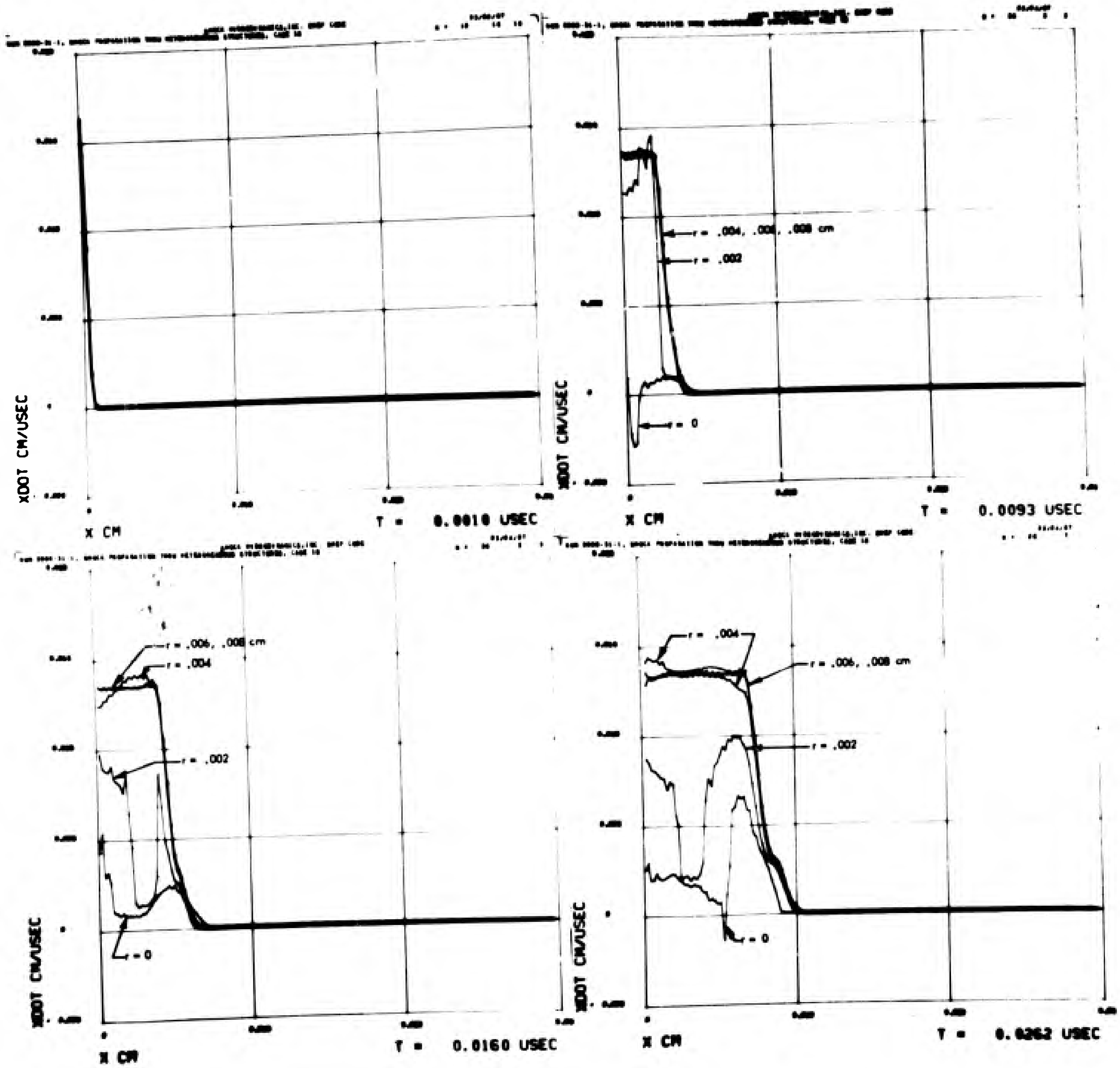

FIGURE 3-19. $\dot{x}$ vs x AT SEVERAL RADIAL POSITIONS, CASE 1 B.

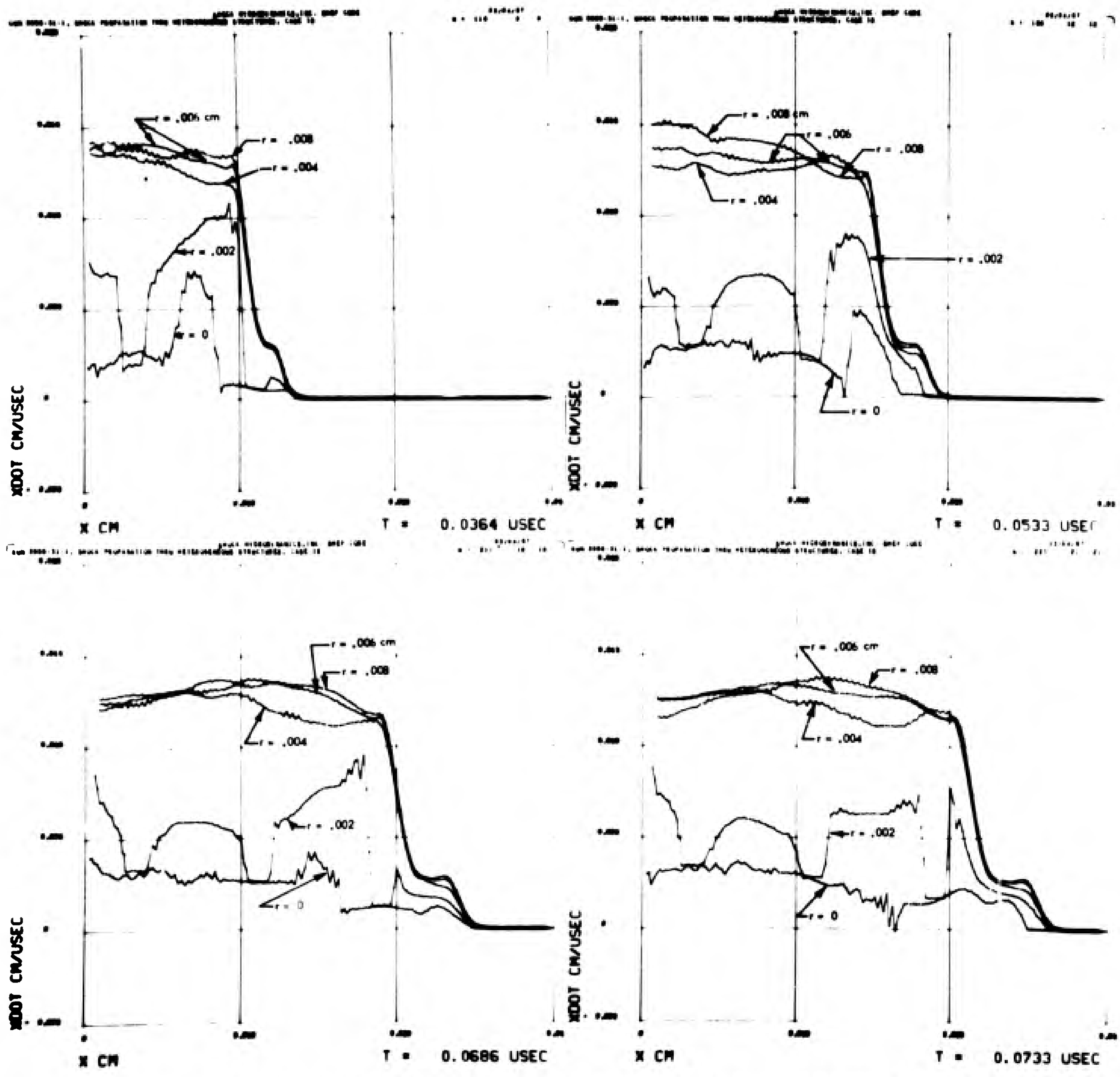

FIGURE 3-19 (cont'd). $\dot{x}$ vs x AT SEVERAL RADIAL POSITIONS, CASE 1B.

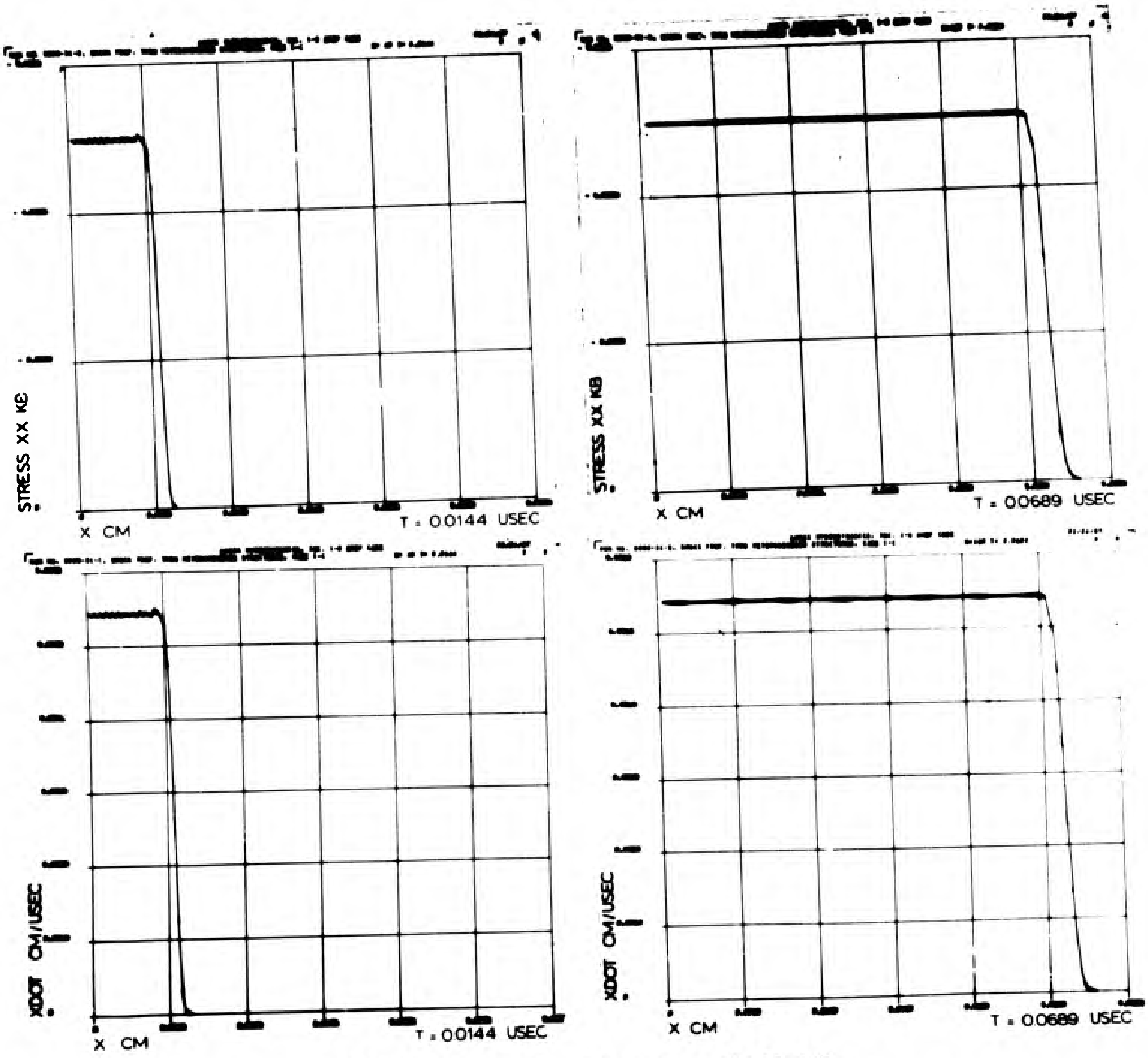

FIGURE 3-20. σ_x and x vs x, CASE 1C.

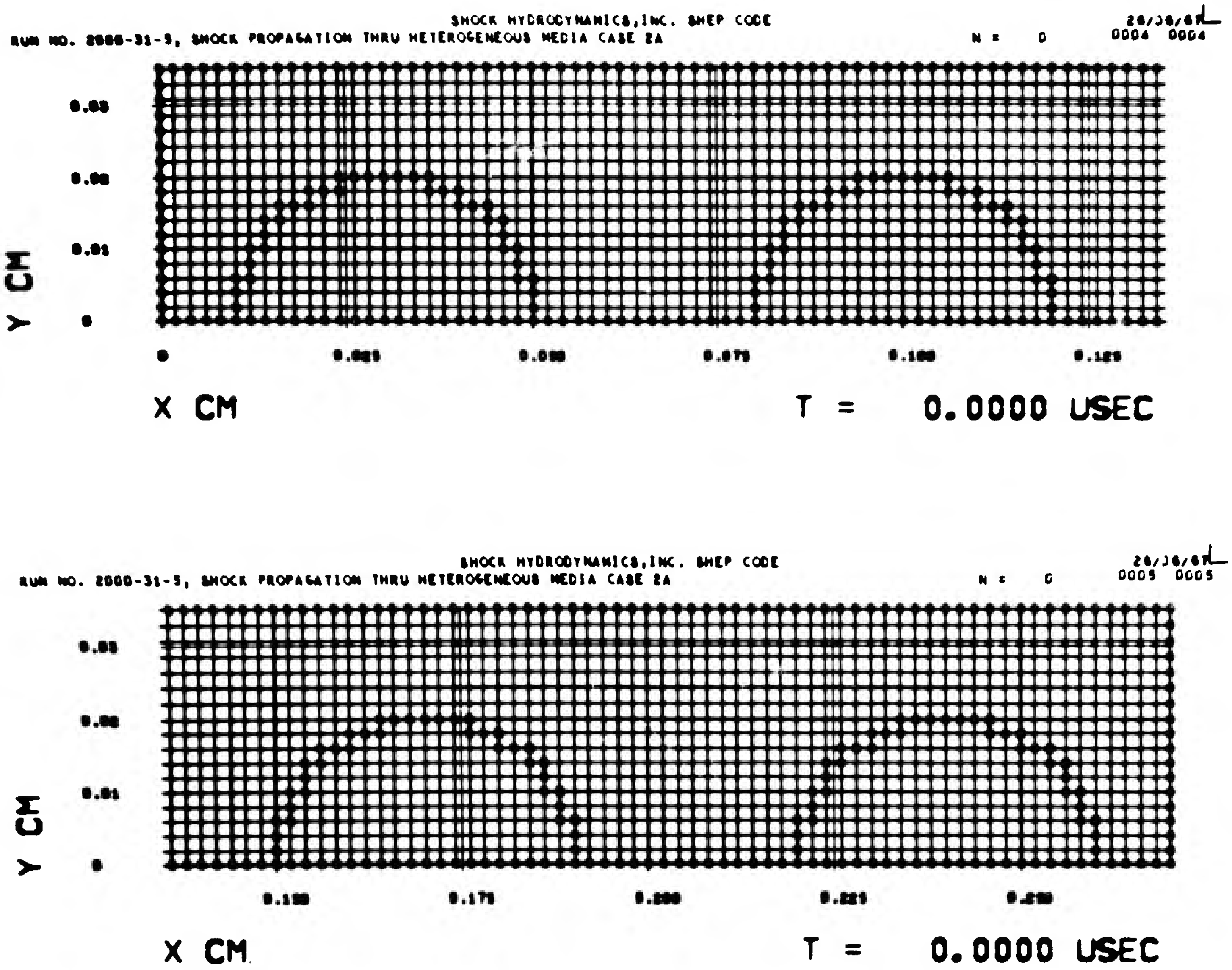

FIGURE 3-21. LAGRANGIAN MESH, CASE 2A.

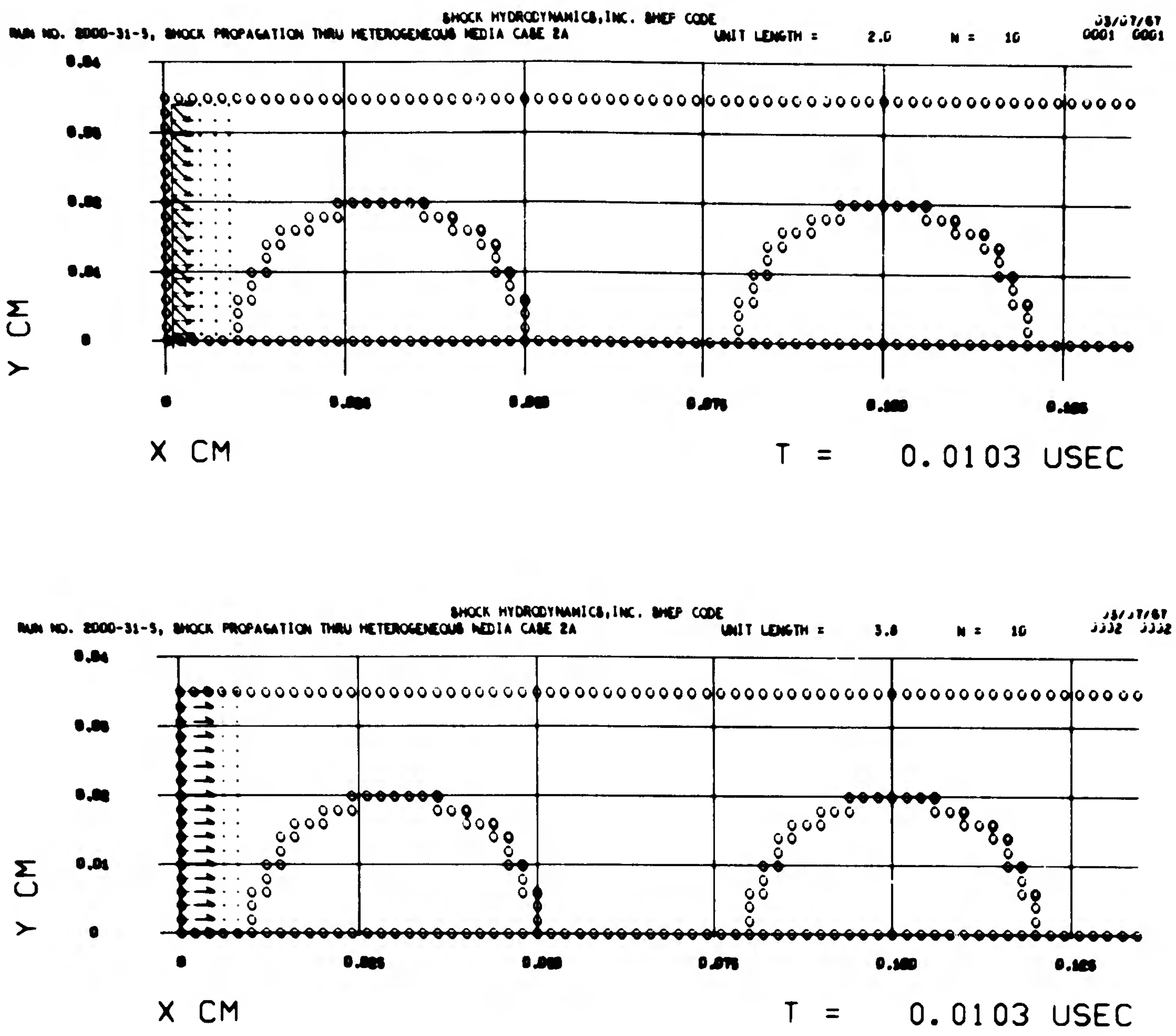

FIGURE 3-22. PRINCIPAL STRESS AND PARTICLE VELOCITY FIELDS, CASE 2A, t = .0103μ sec.

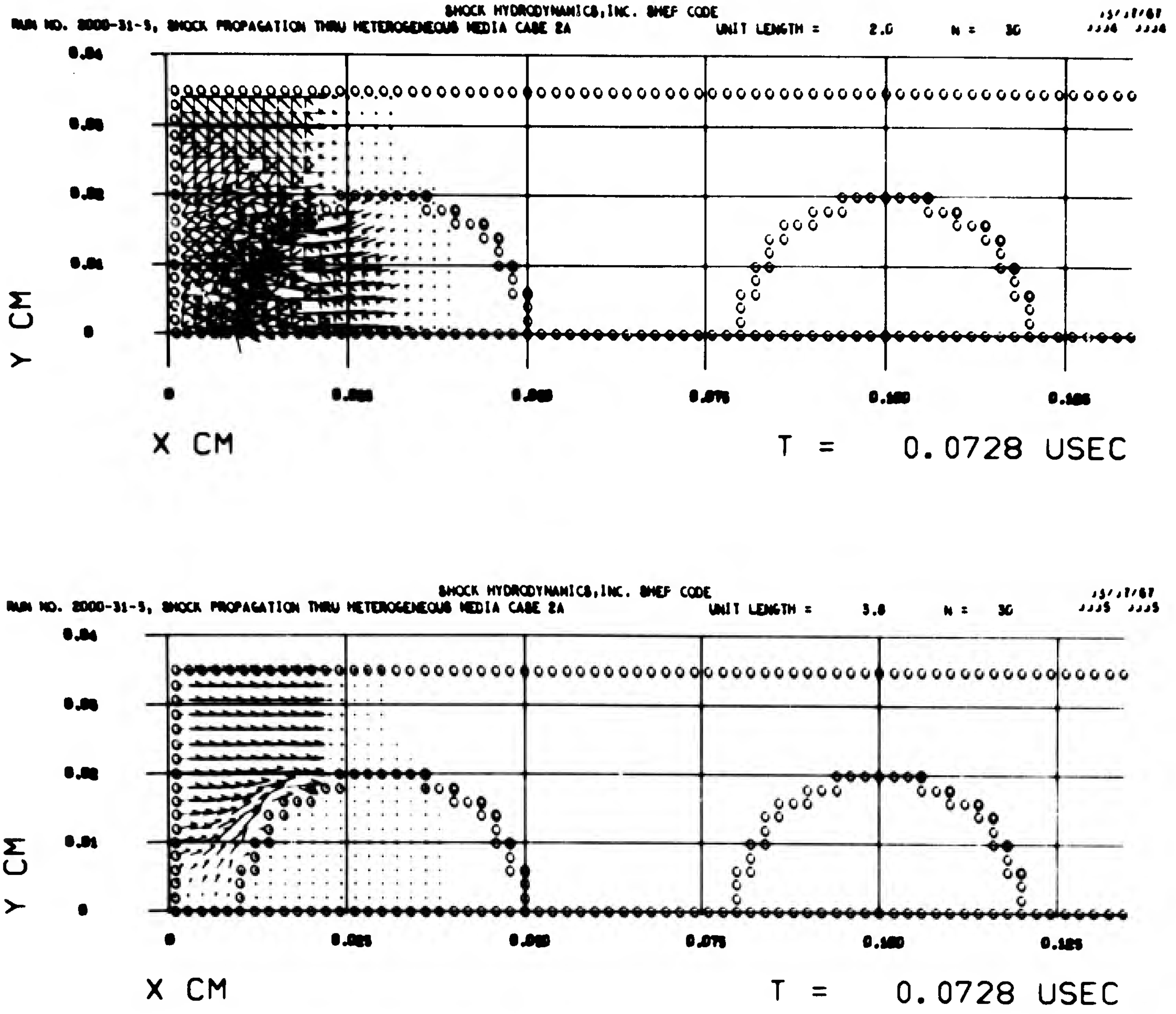

FIGURE 3-23. PRINCIPAL STRESS AND PARTICLE VELOCITY FIELDS, CASE 2A, t = .0728 μsec.

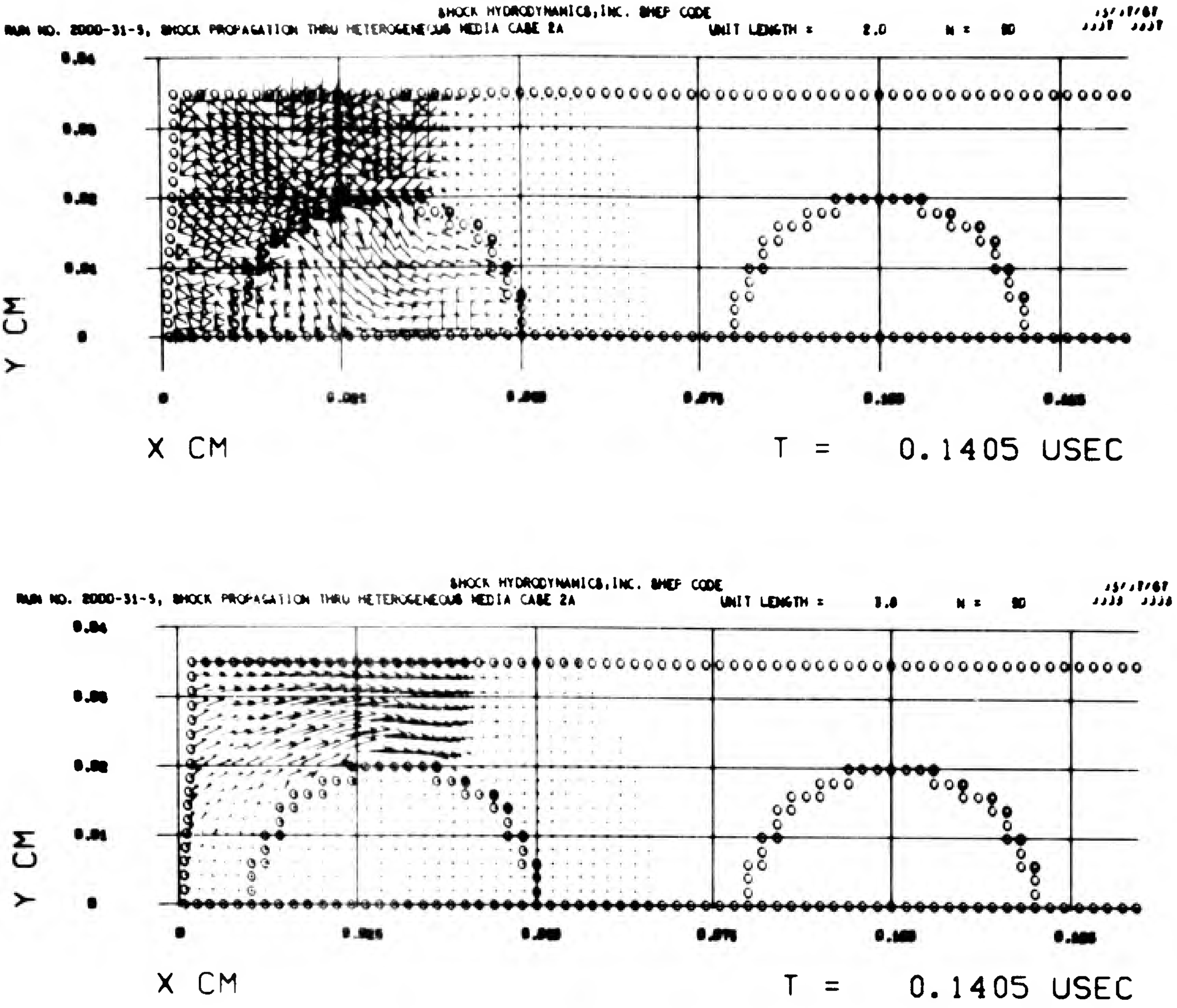

FIGURE 3-24. PRINCIPAL STRESS AND PARTICLE VELOCITY FIELDS, CASE 2A, t = .1405μsec.

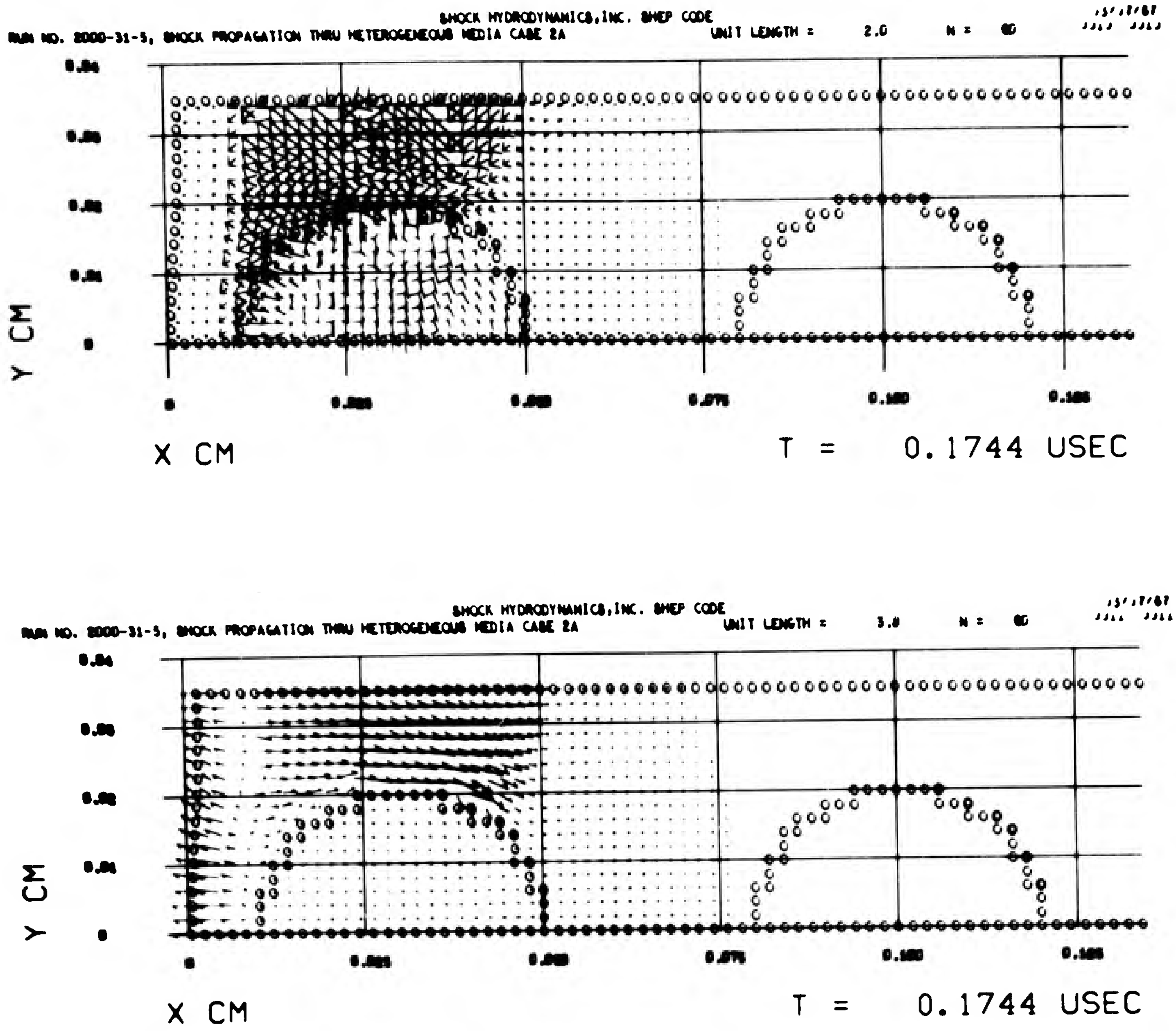

FIGURE 3-25. PRINCIPAL STRESS AND PARTICLE VELOCITY FIELDS, CASE 2A, t = .1744 μsec.

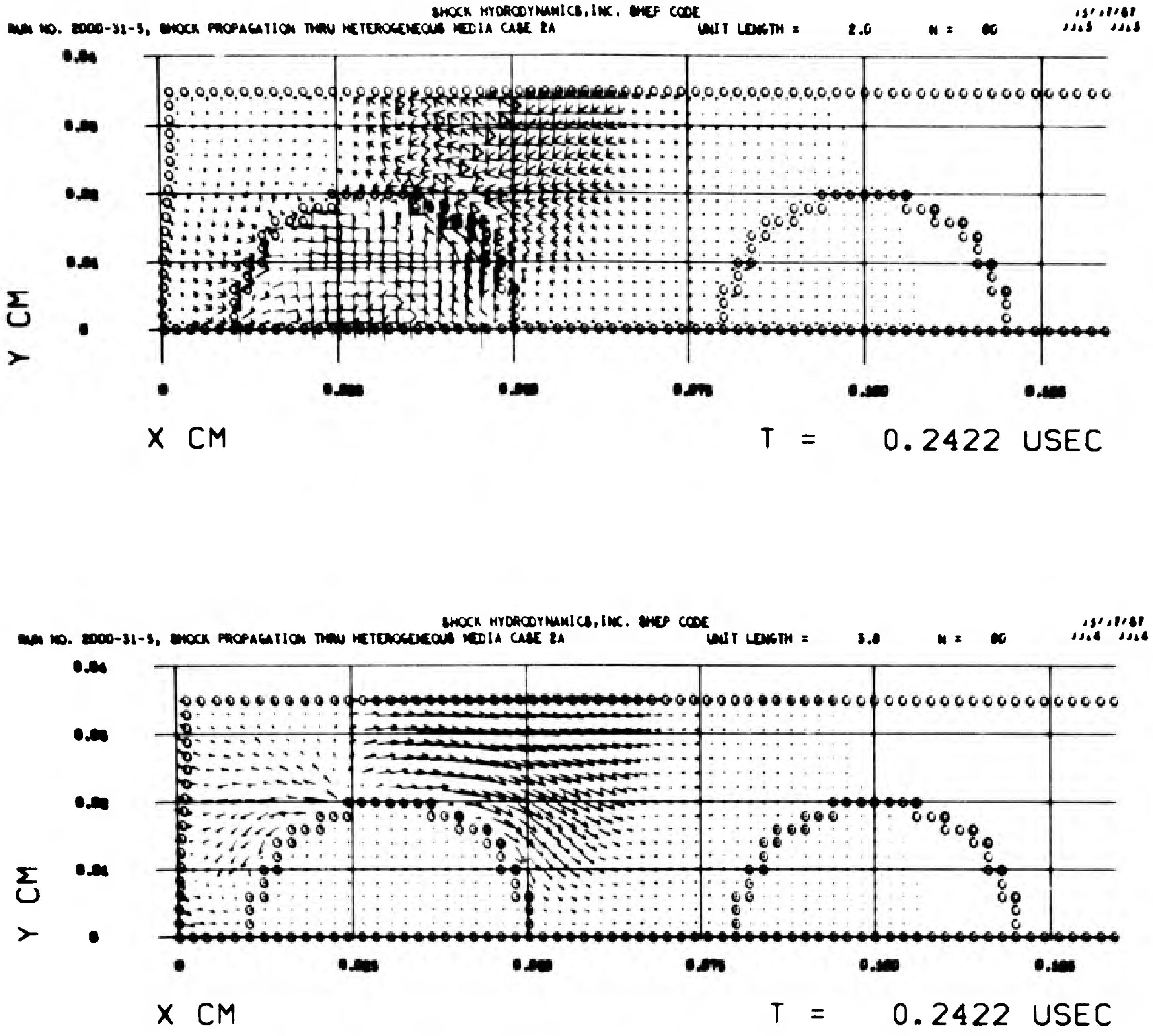

FIGURE 3-26. PRINCIPAL STRESS AND PARTICLE VELOCITY FIELDS, CASE 2A, t = .2422 μsec.

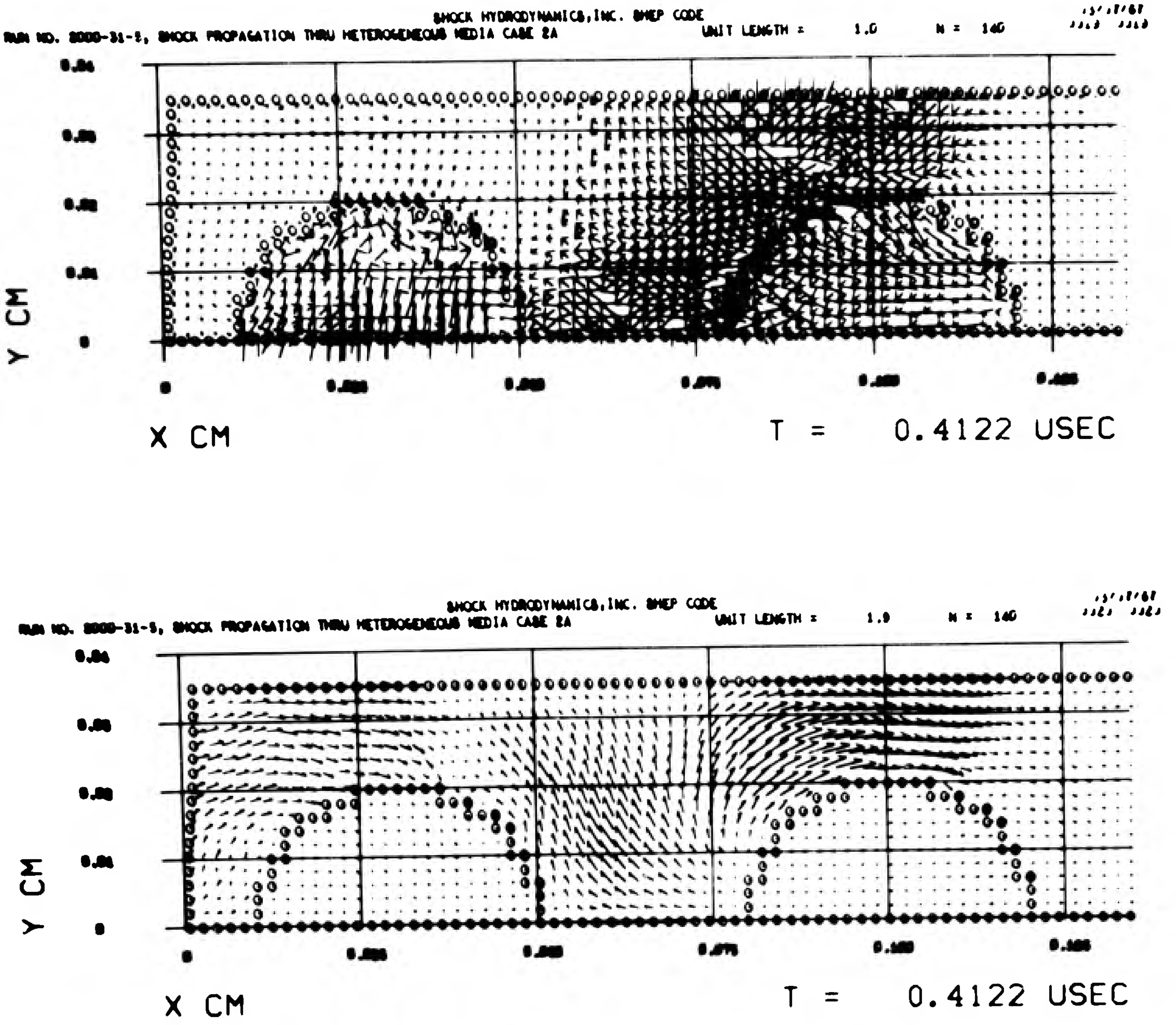

FIGURE 3-27. PRINCIPAL STRESS AND PARTICLE VELOCITY FIELDS, CASE 2A, t = .4122 μsec.

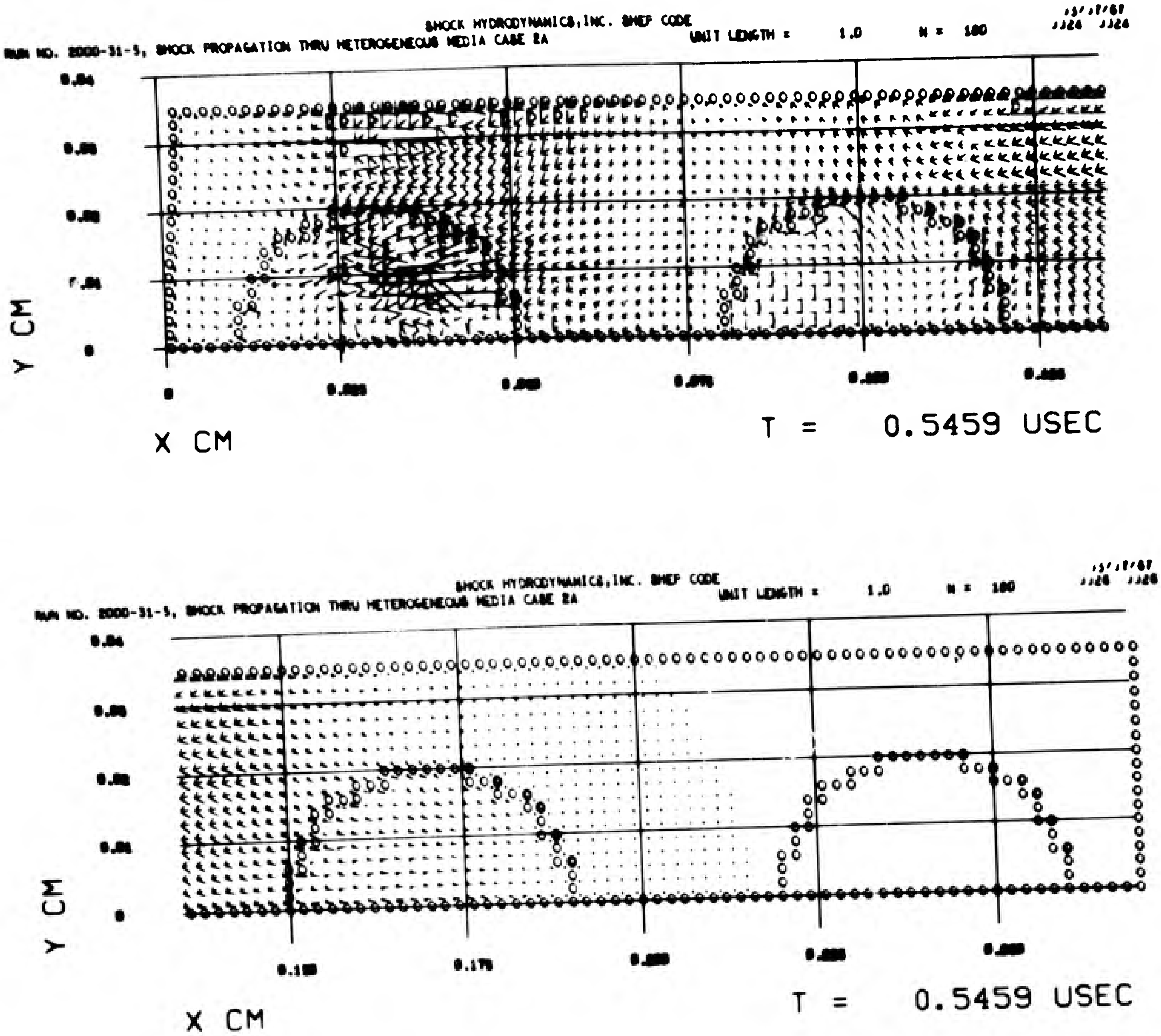

FIGURE 3-28. PRINCIPAL STRESS FIELD, CASE 2A, $t = .5459 \mu$ sec.

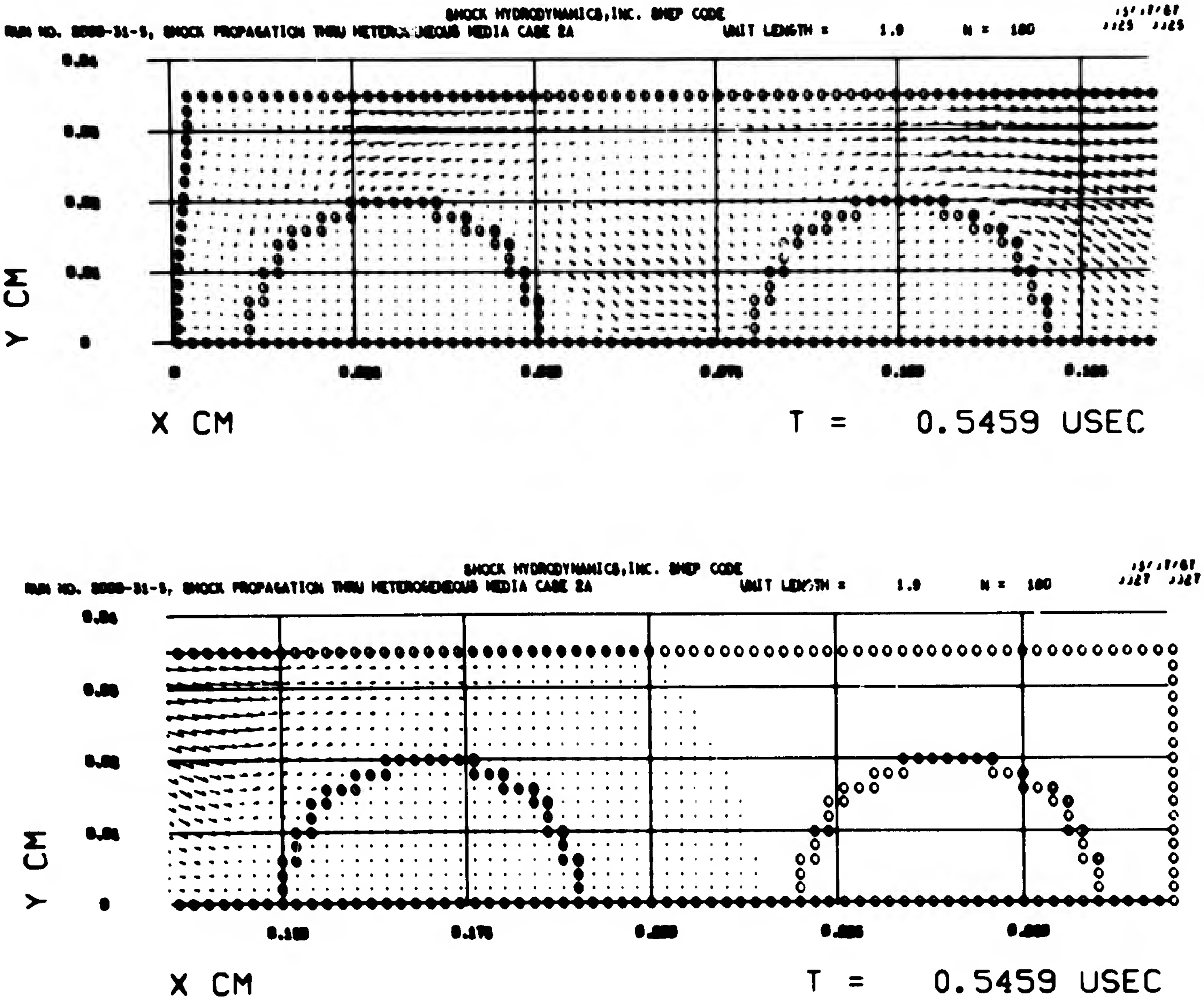

FIGURE 3-29. PARTICLE VELOCITY FIELD, CASE 2A, t = .5459μ sec.

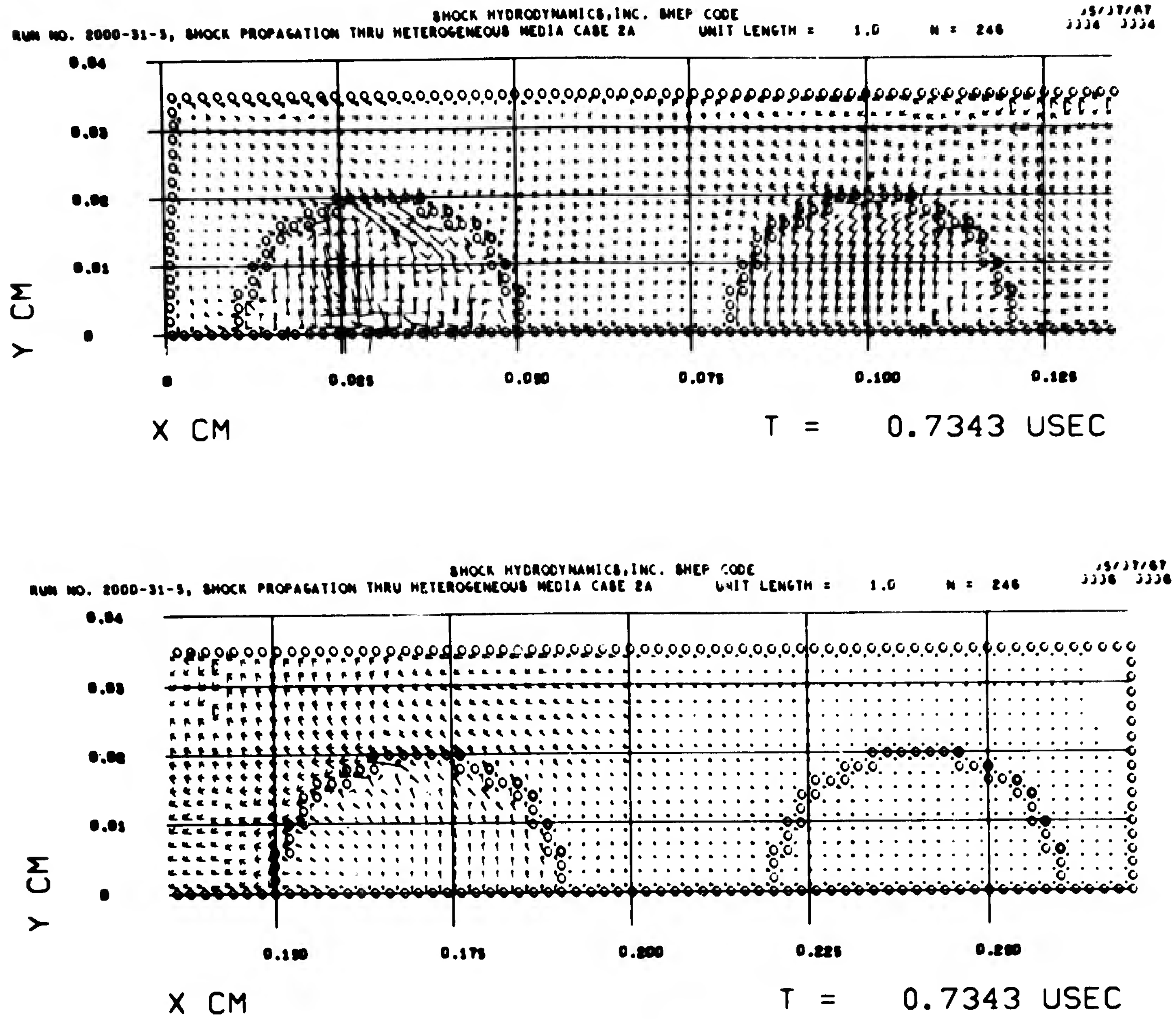

FIGURE 3-30. PRINCIPAL STRESS FIELD, CASE 2A, t = .7343 μ sec.

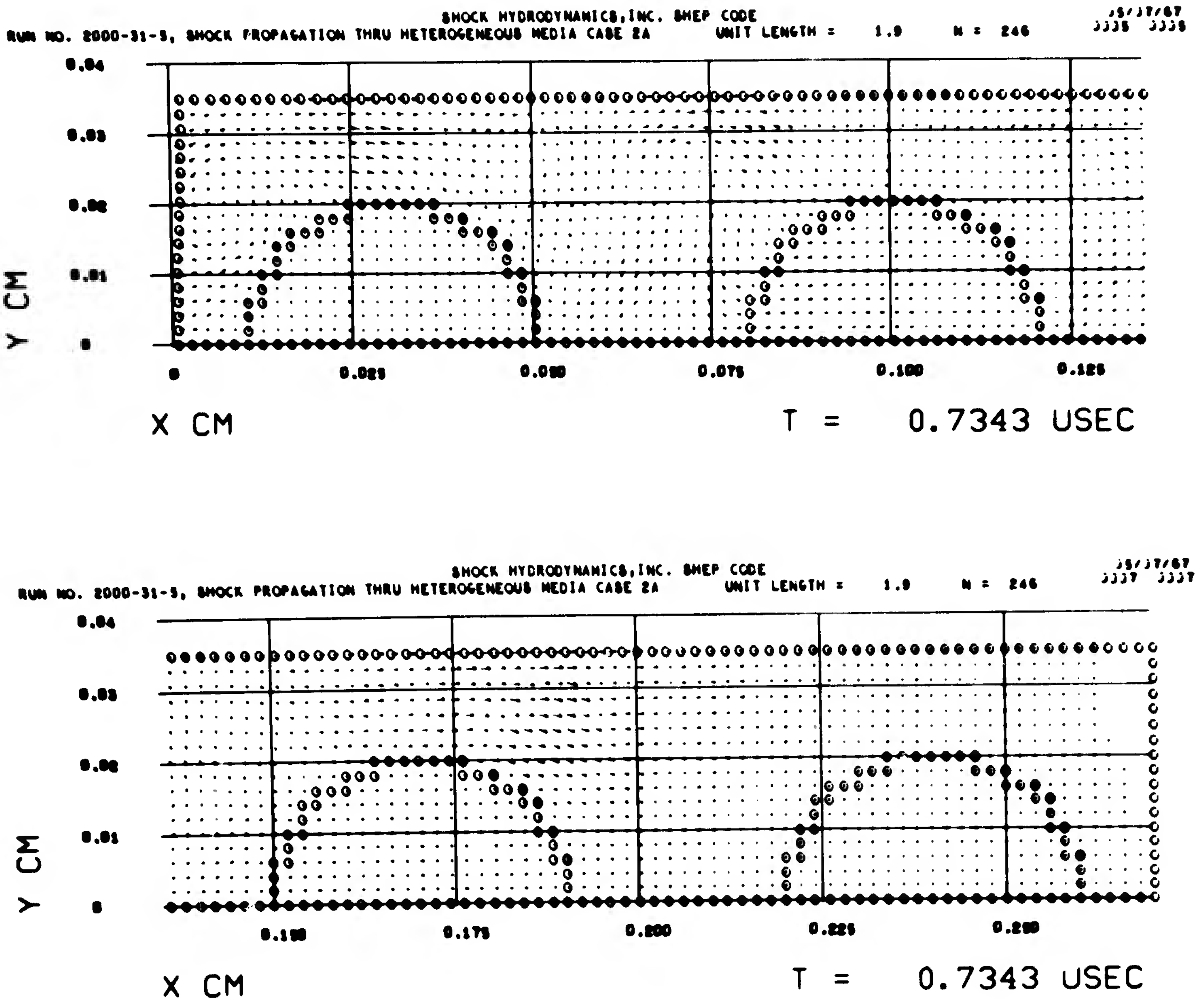

FIGURE 3-31. PARTICLE VELOCITY FIELD, CASE 2A, $t = .7343\ \mu$ sec.

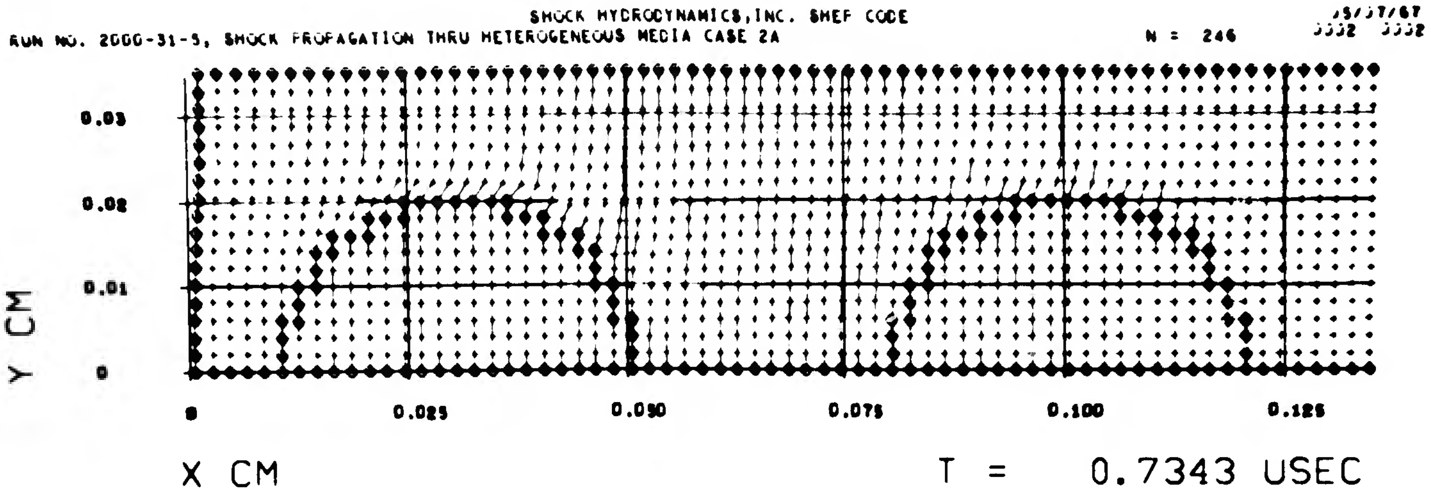

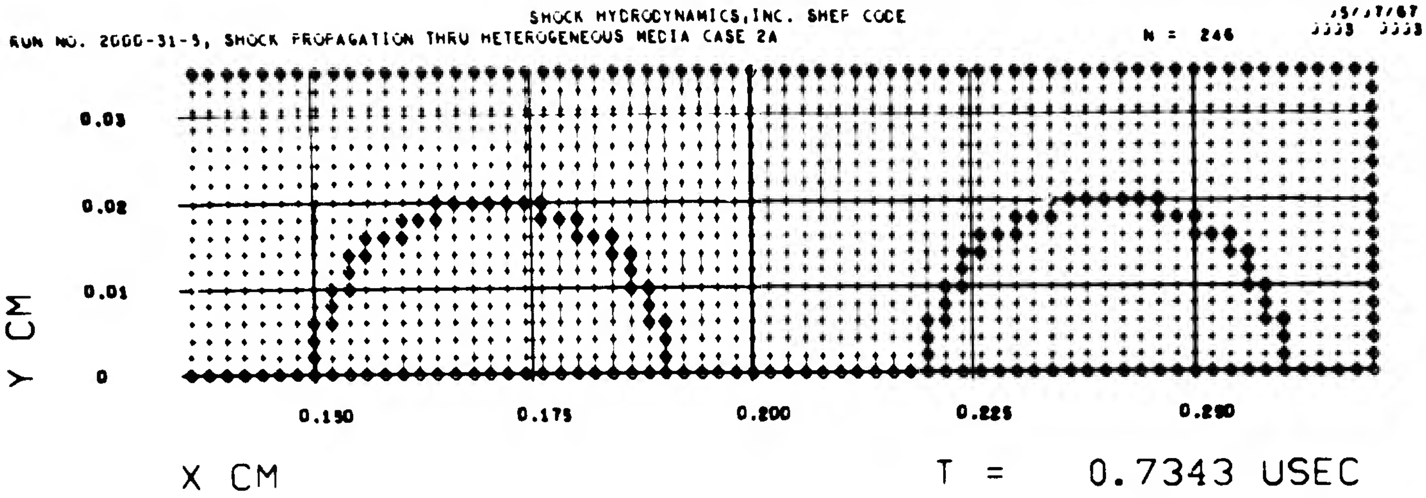

FIGURE 3-32. LAGRANGIAN MESH, CASE 2A, t = .7343 μsec.

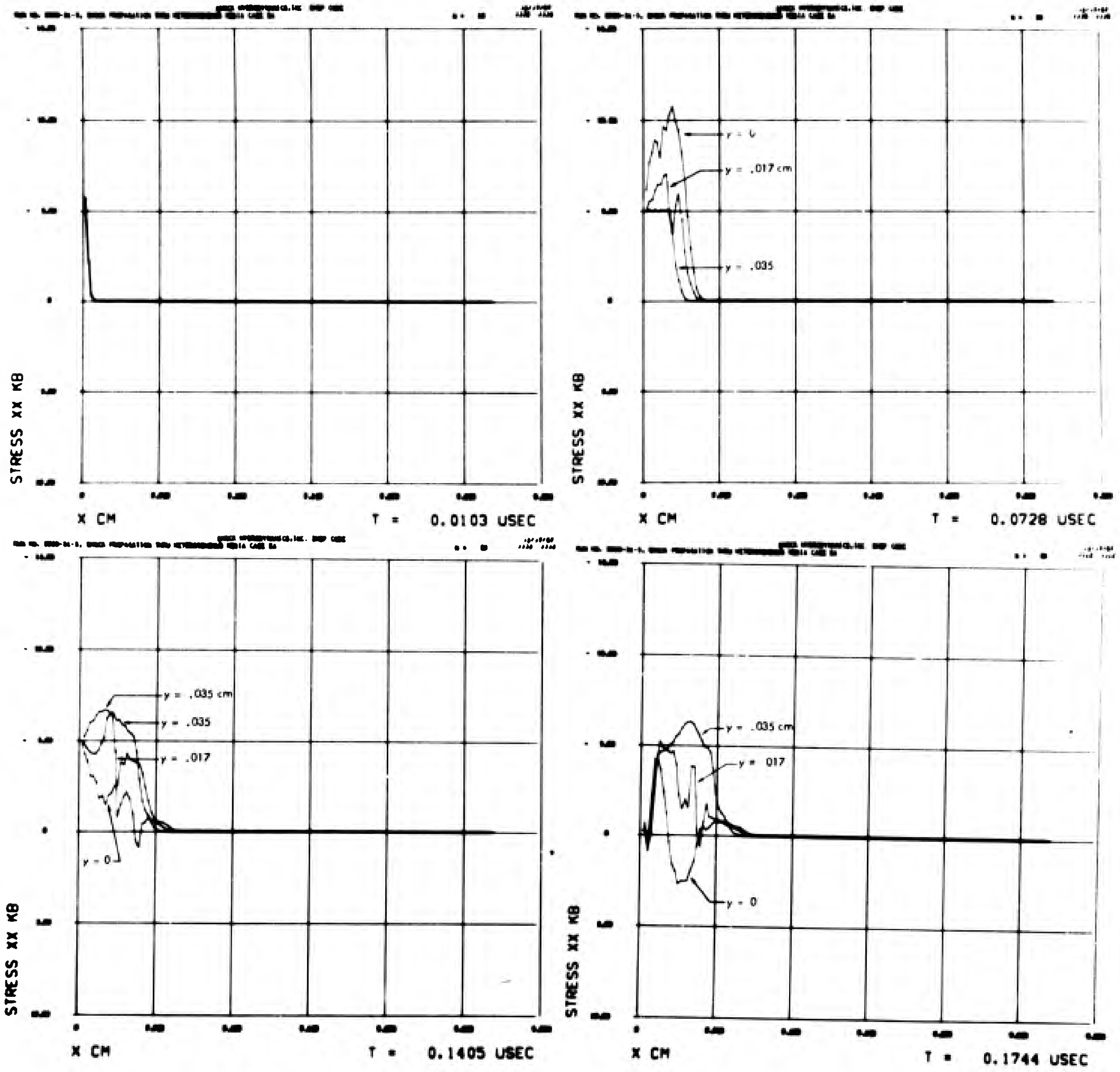

FIGURE 3-33. σ_x vs x AT THREE LATERAL POSITIONS, CASE 2A.

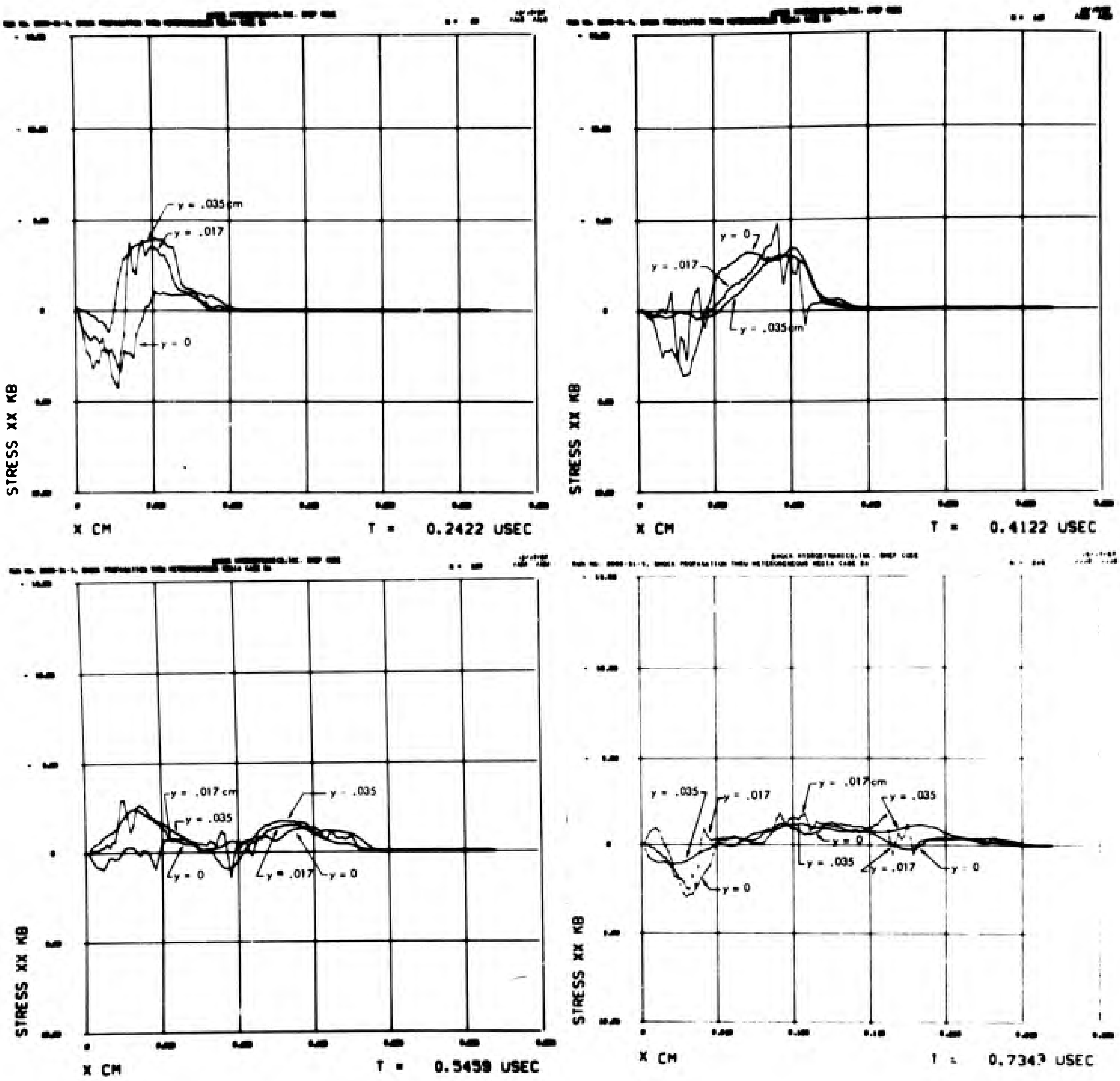

FIGURE 3-33 (cont'd). σ_x vs x AT THREE LATERAL POSITIONS, CASE 2A.

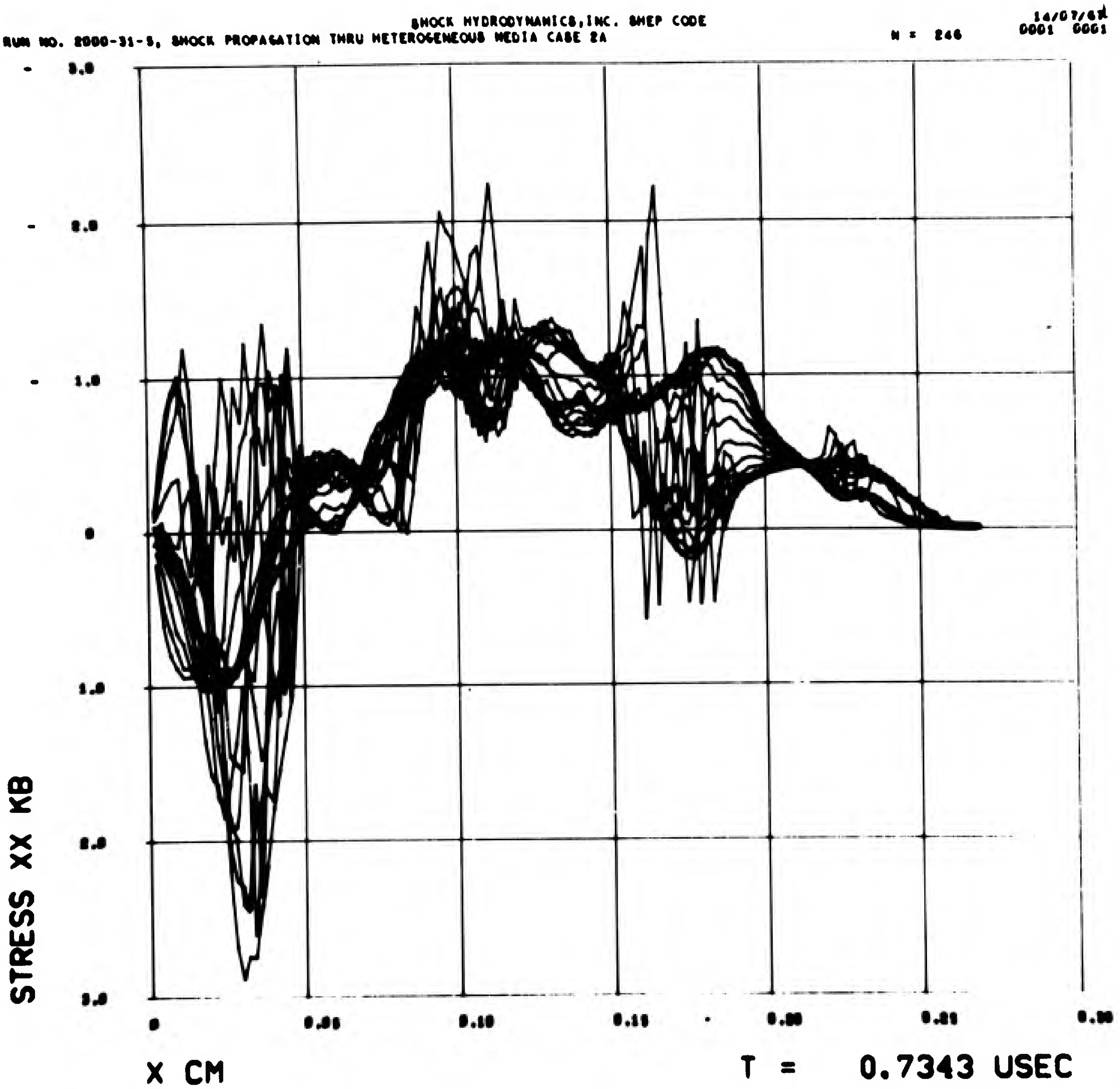

FIGURE 3-34. σ_x vs x AT ALL LATERAL MESH POSITIONS, CASE 2A.

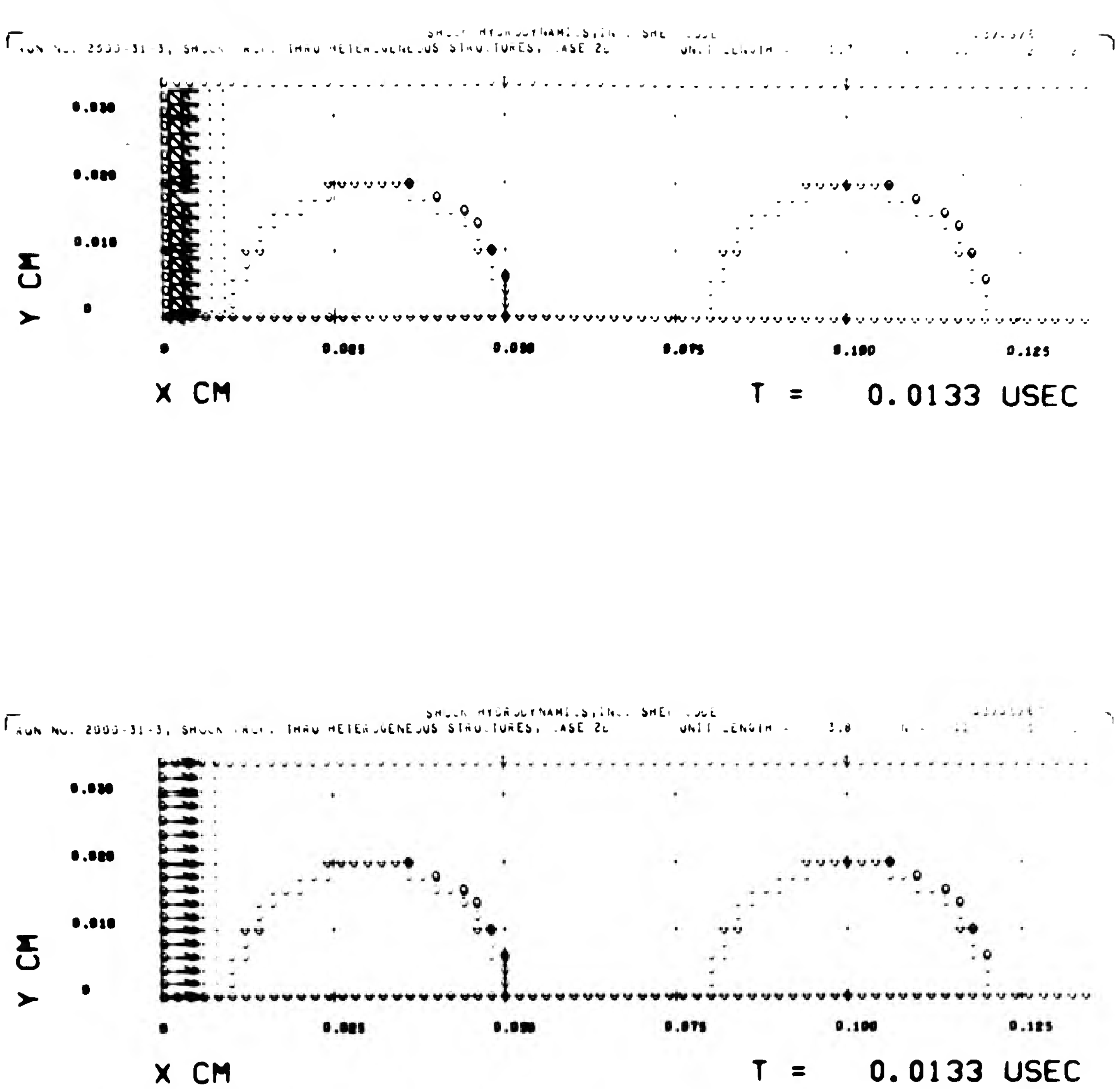

FIGURE 3-35. PRINCIPAL STRESS AND PARTICLE VELOCITY FIELDS, CASE 2B, t = .0133μ sec.

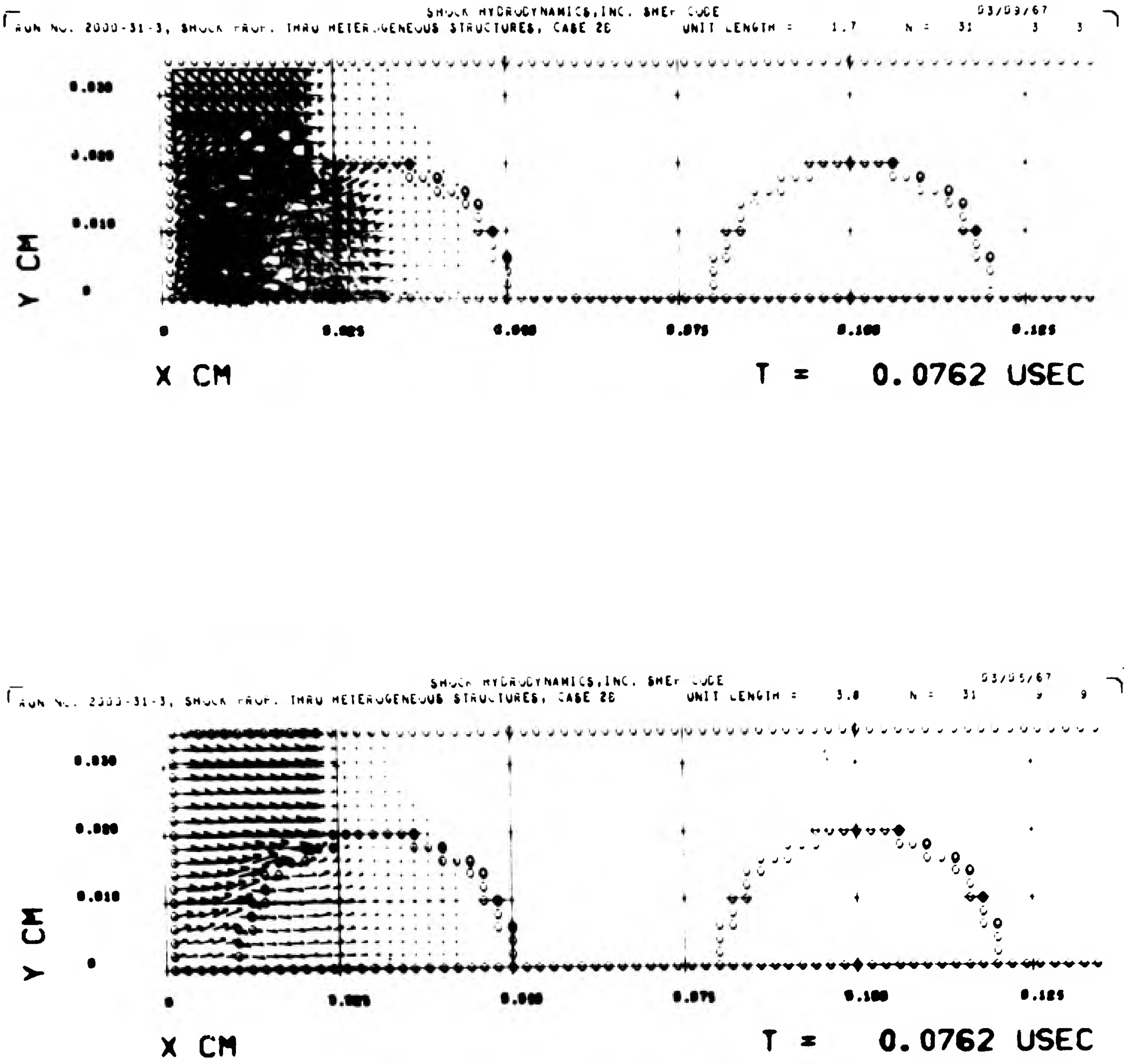

FIGURE 3-36. PRINCIPAL STRESS AND PARTICLE VELOCITY FIELDS, CASE 2B, t = .0762μ sec.

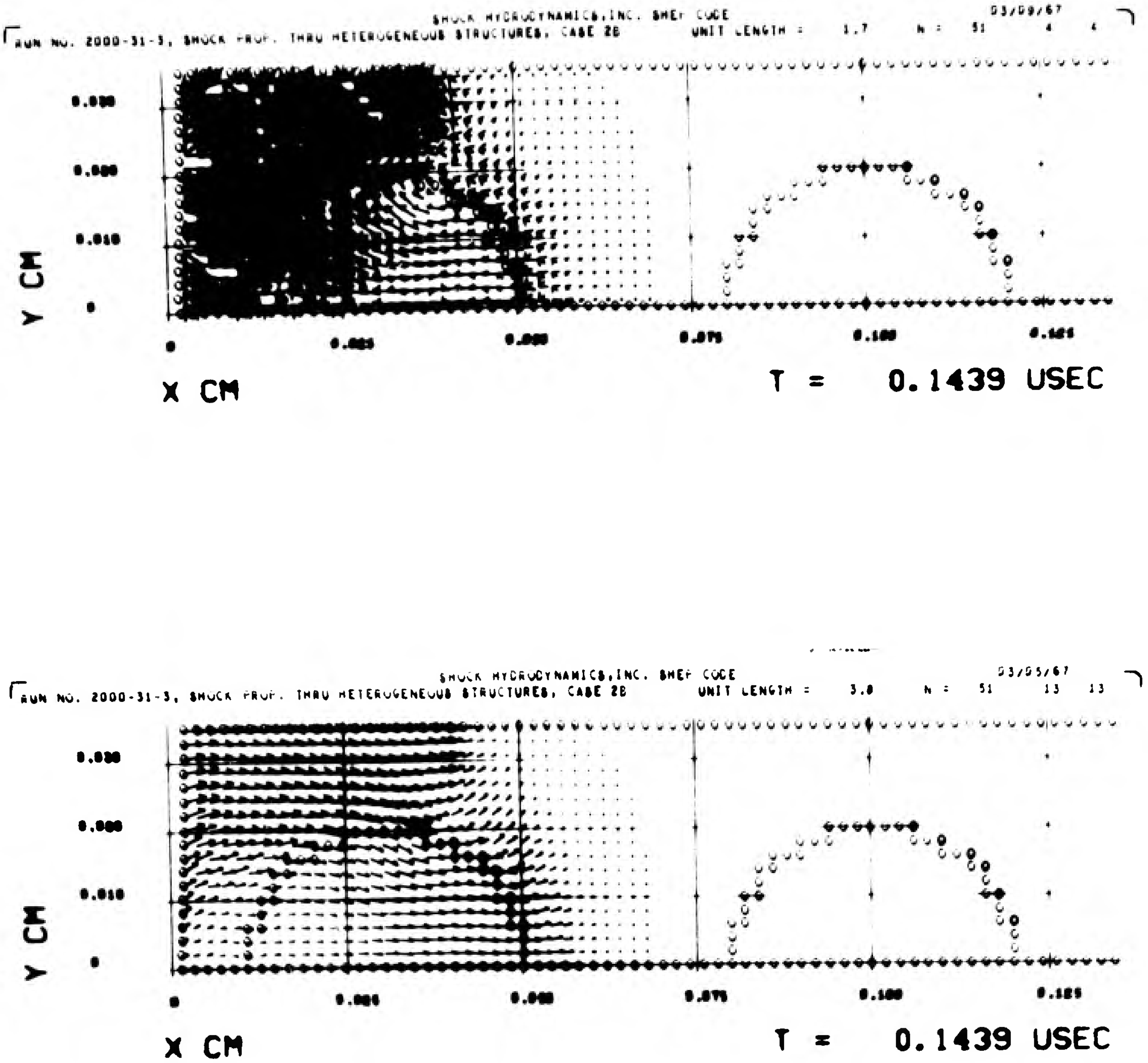

FIGURE 3-37. PRINCIPAL STRESS AND PARTICLE VELOCITY FIELDS, CASE 2B, $t = .1439 \mu$ sec.

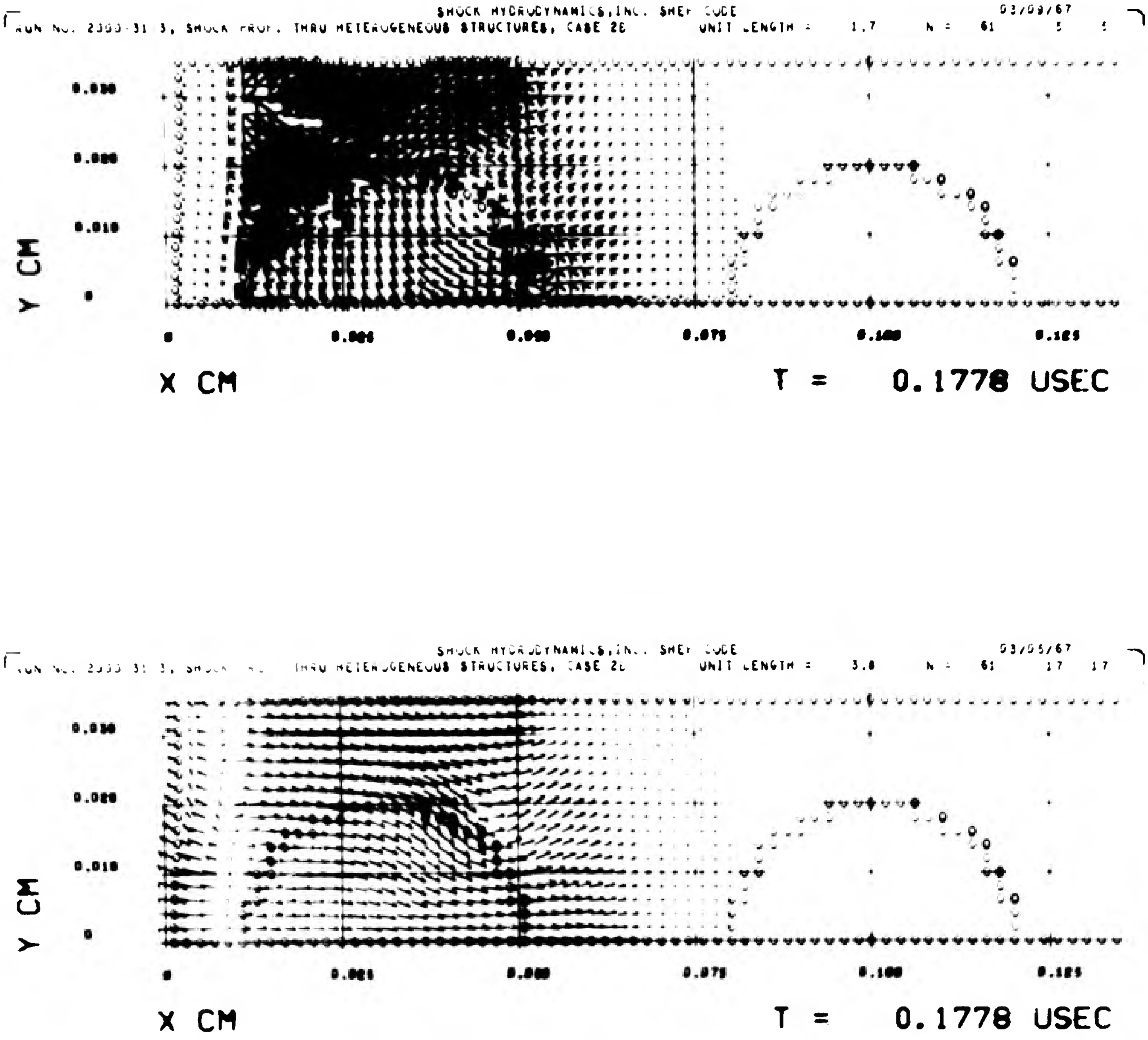

FIGURE 3-38. PRINCIPAL STRESS AND PARTICLE VELOCITY FIELDS, CASE 2B, t = .1778 μ sec.

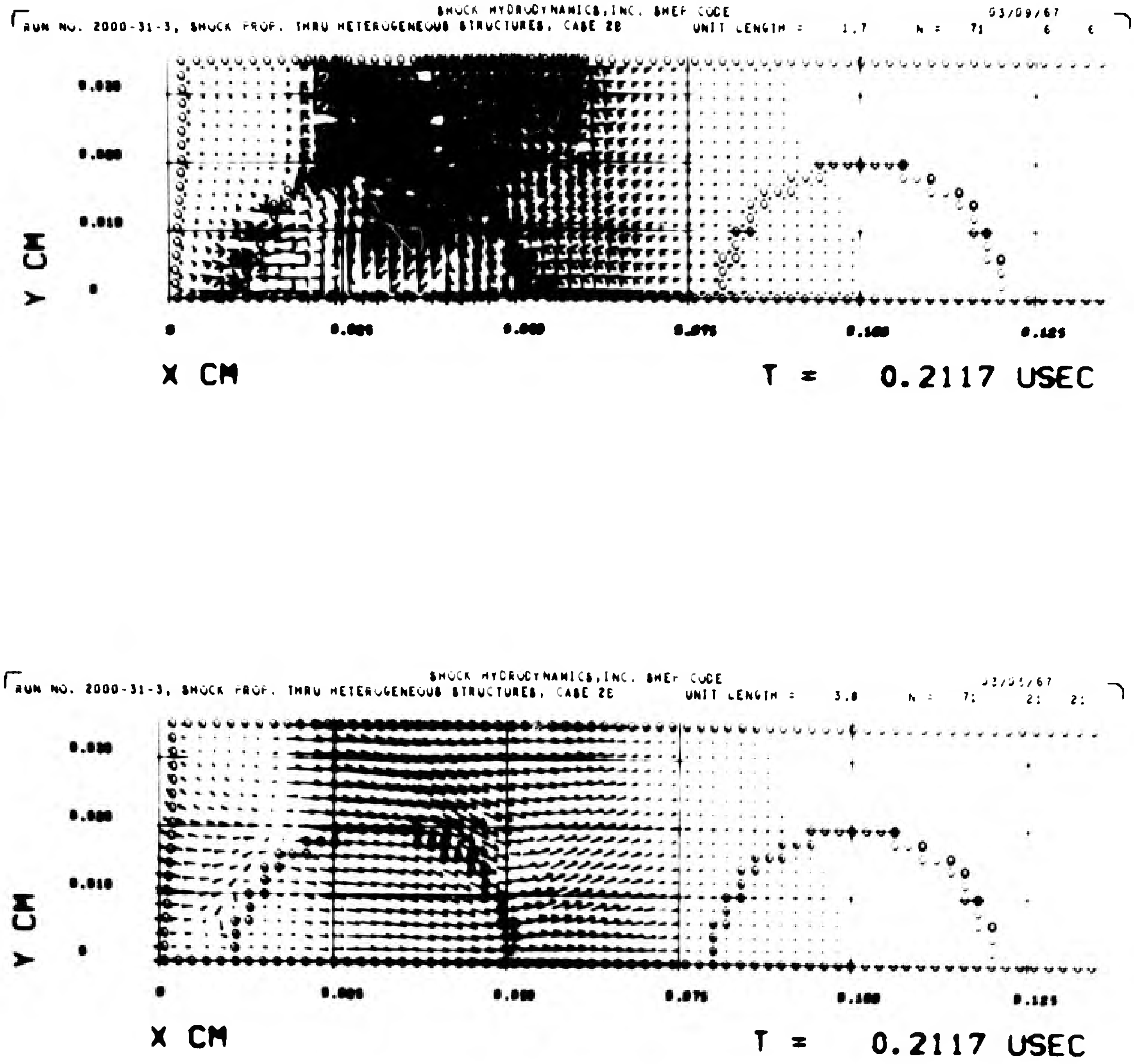

FIGURE 3-39. PRINCIPAL STRESS AND PARTICLE VELOCITY FIELDS, CASE 2B, t = .2117 μsec.

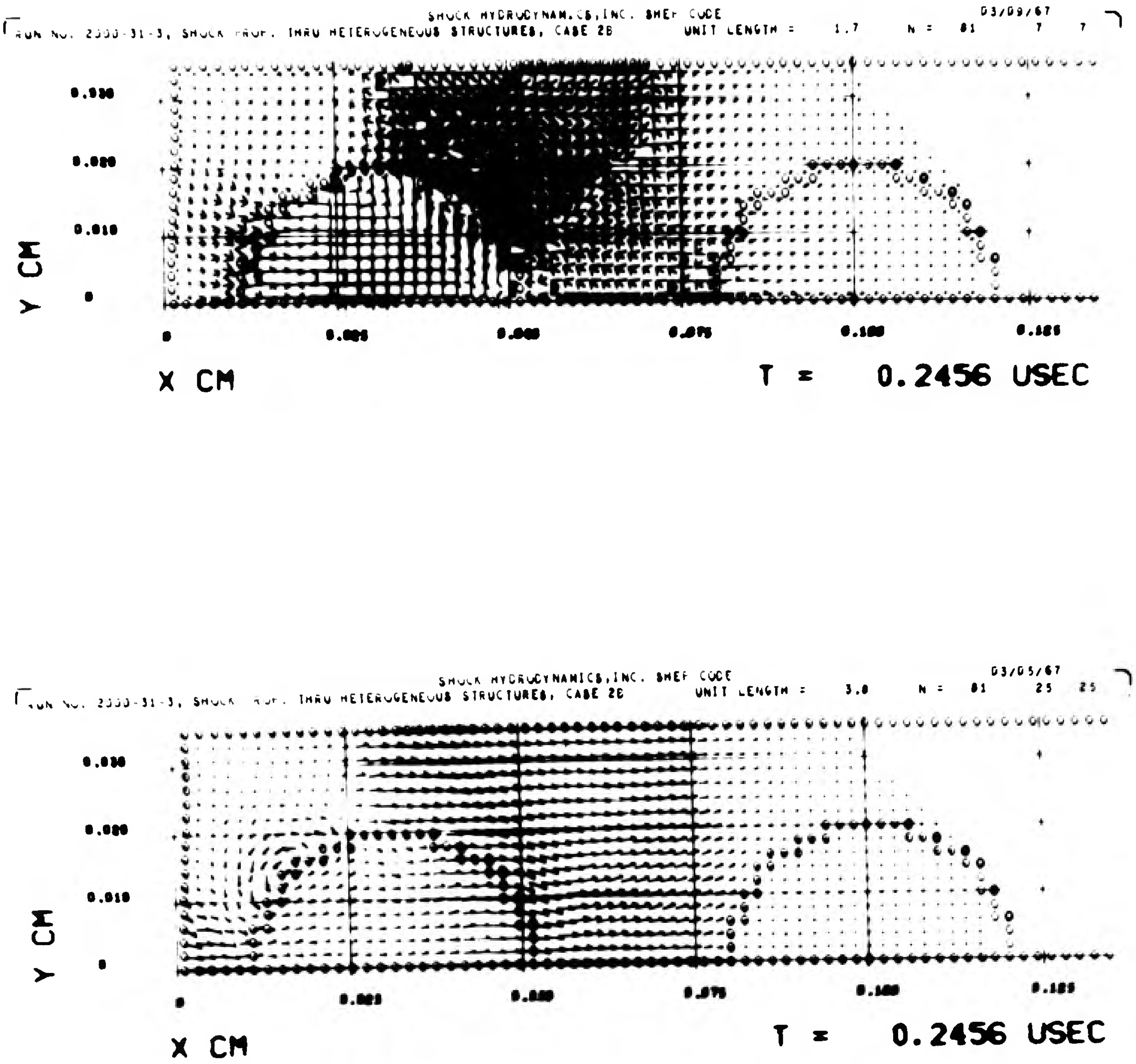

FIGURE 3-40. PRINCIPAL STRESS AND PARTICLE VELOCITY FIELDS, CASE 2B, t = .2456 μ sec.

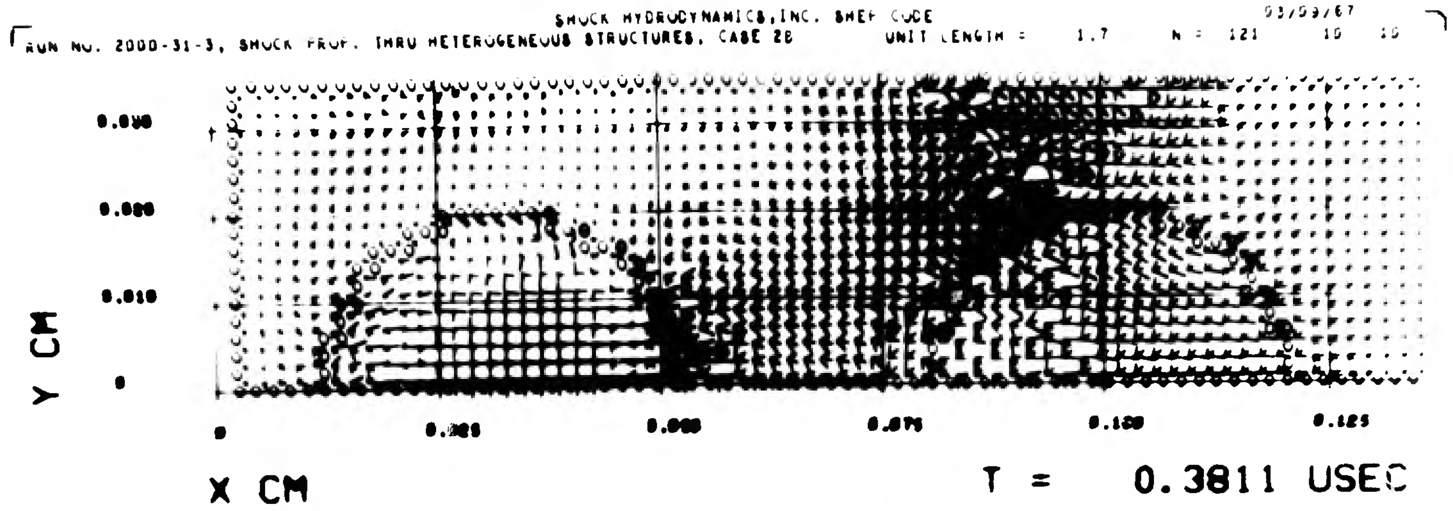

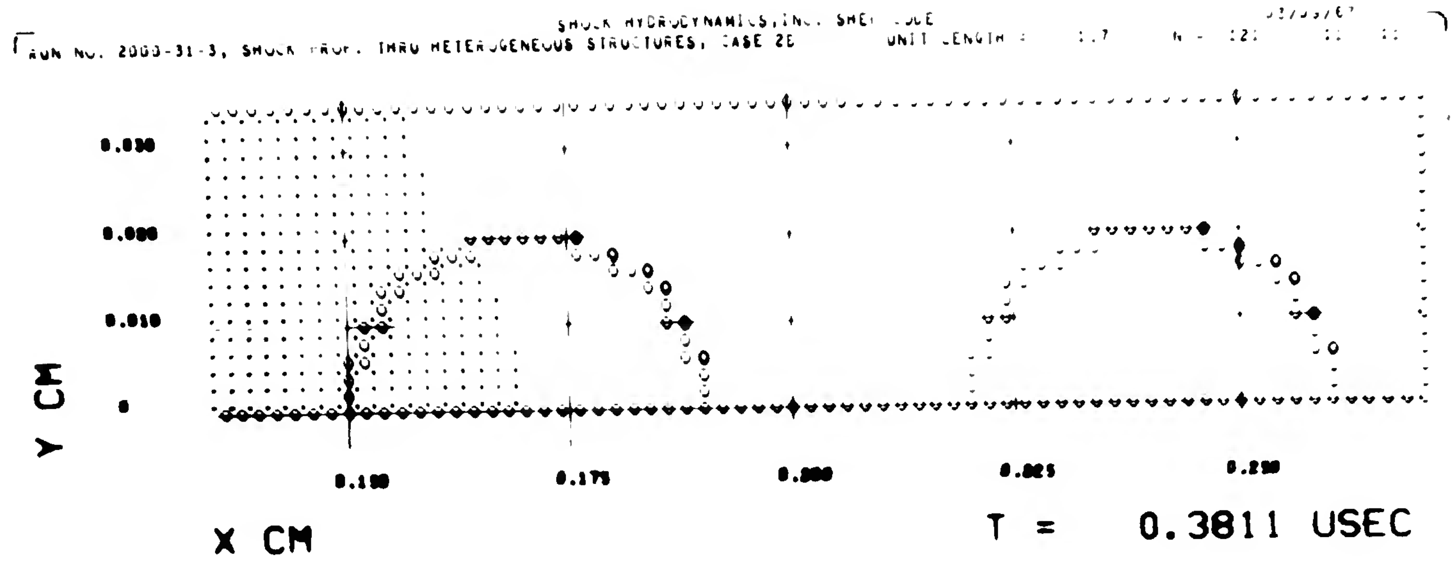

FIGURE 3-41. PRINCIPAL STRESS FIELD, CASE 2B, t = .3811 μ sec.

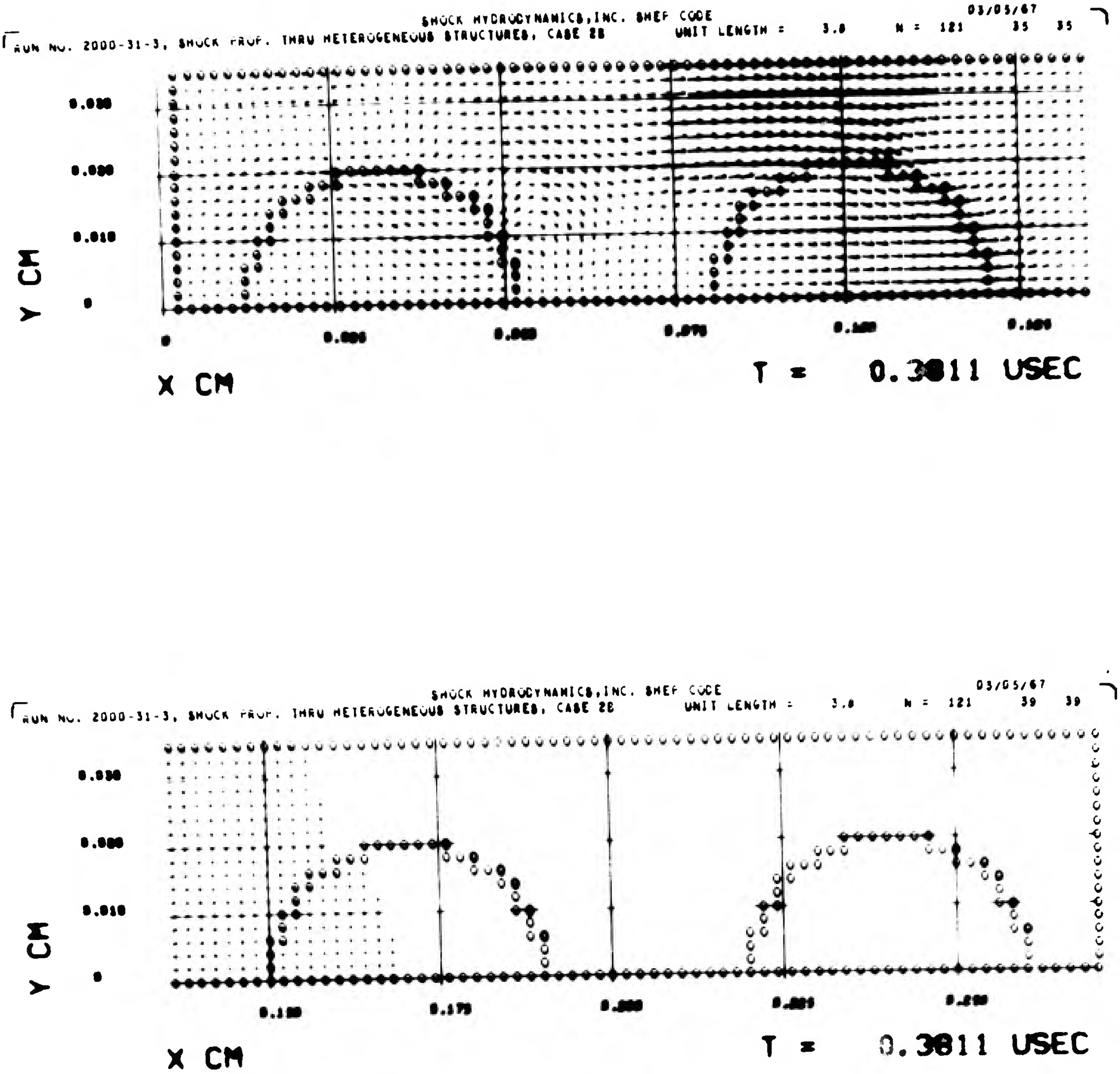

FIGURE 3-42. PARTICLE VELOCITY FIELD, CASE 2B, t = .3811 μ sec.

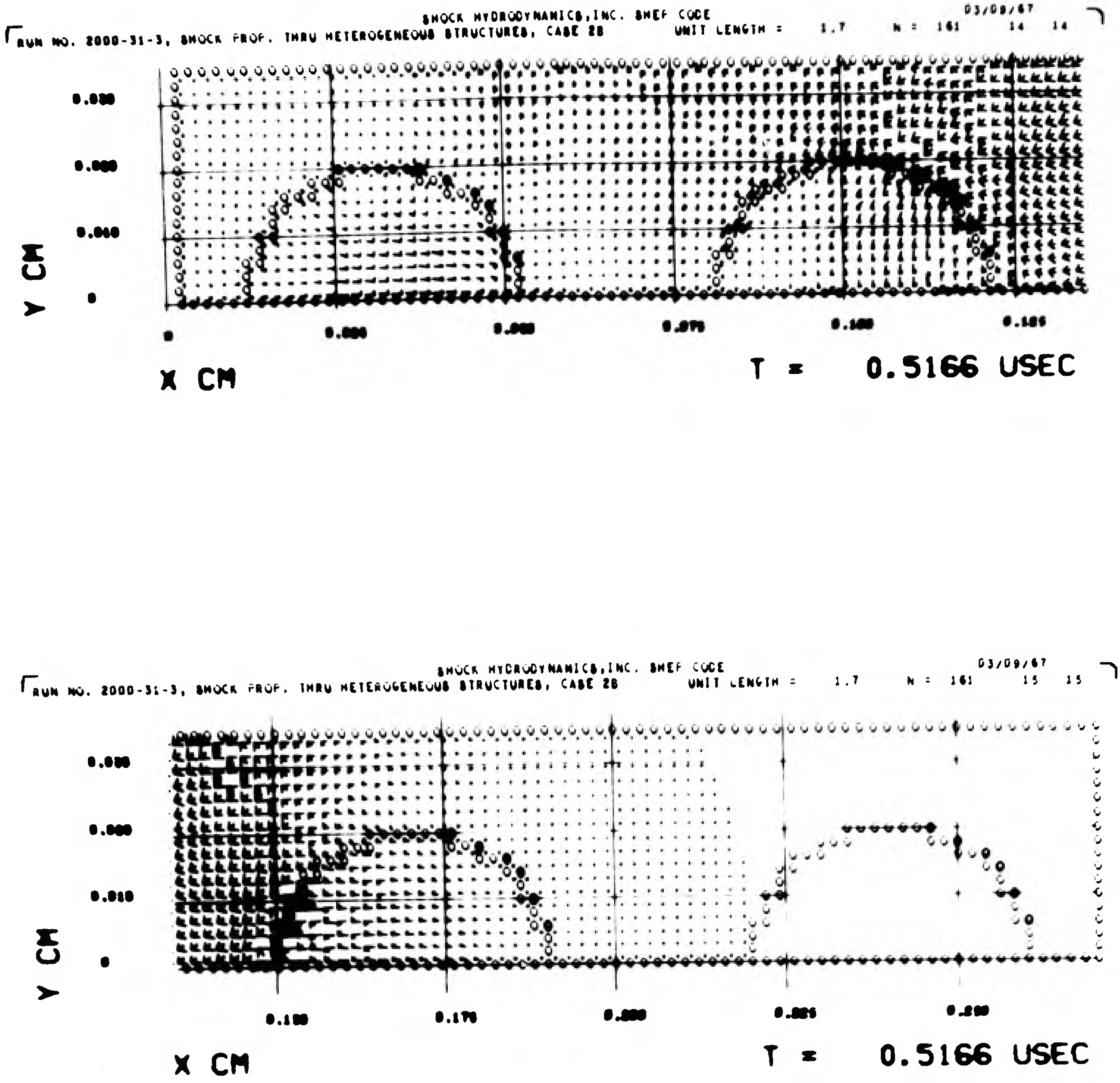

FIGURE 3-43. PRINCIPAL STRESS FIELD, CASE 2B, t = .5166 μ sec.

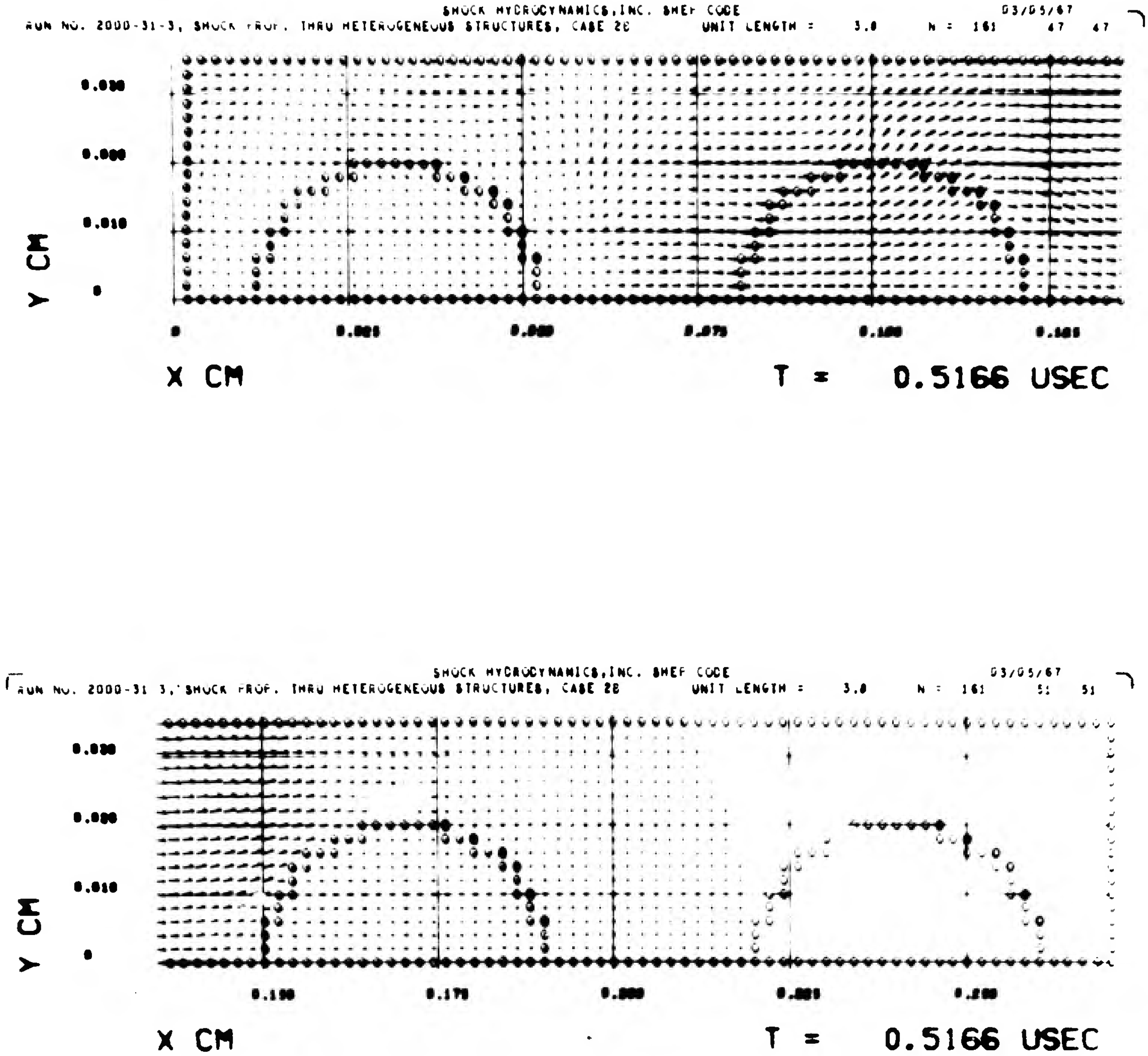

FIGURE 3-44. PARTICLE VELOCITY FIELD, CASE 2B, t = .5166 μ sec.

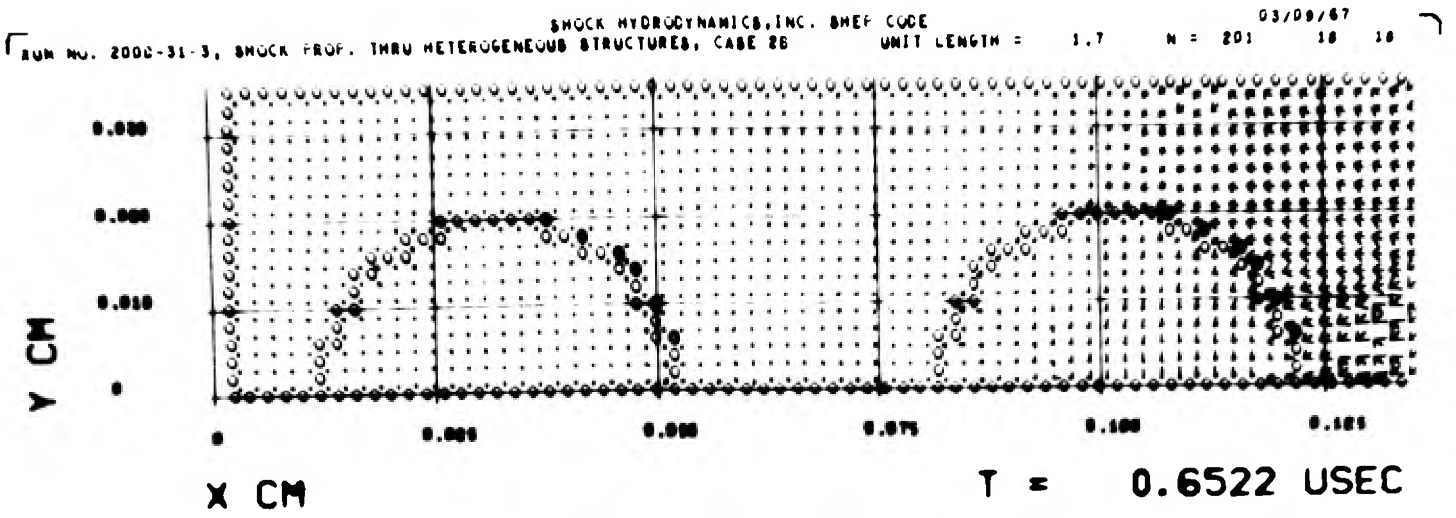

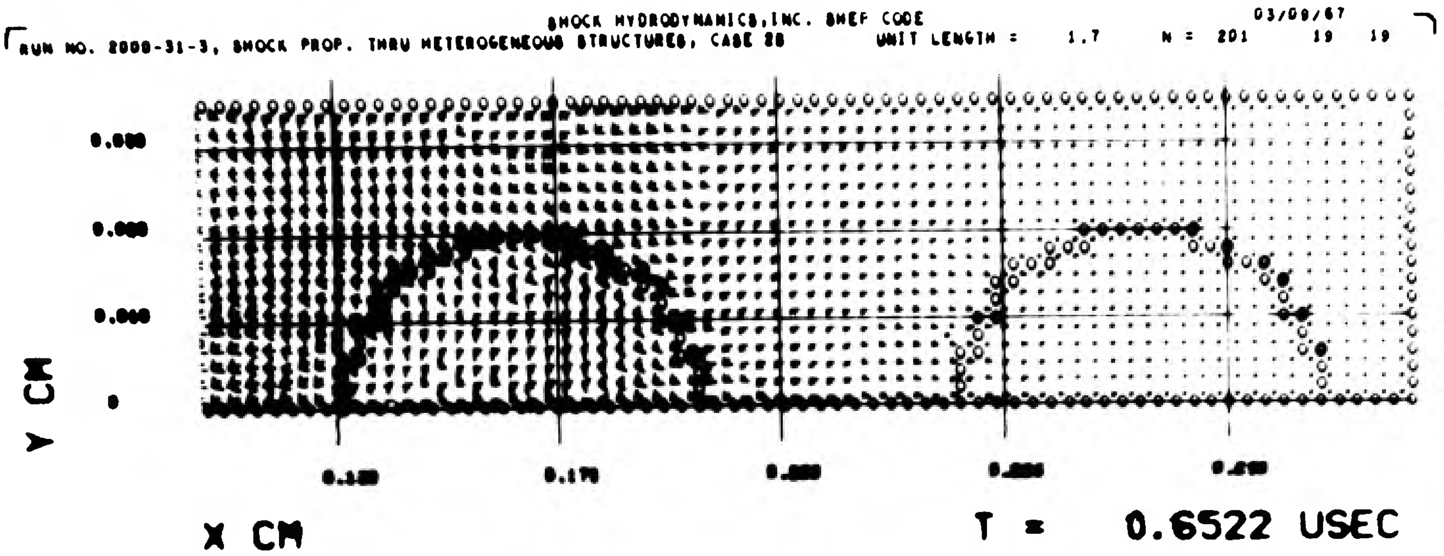

FIGURE 3-45. PRINCIPAL STRESS FIELD, CASE 2B, t = .6522μsec.

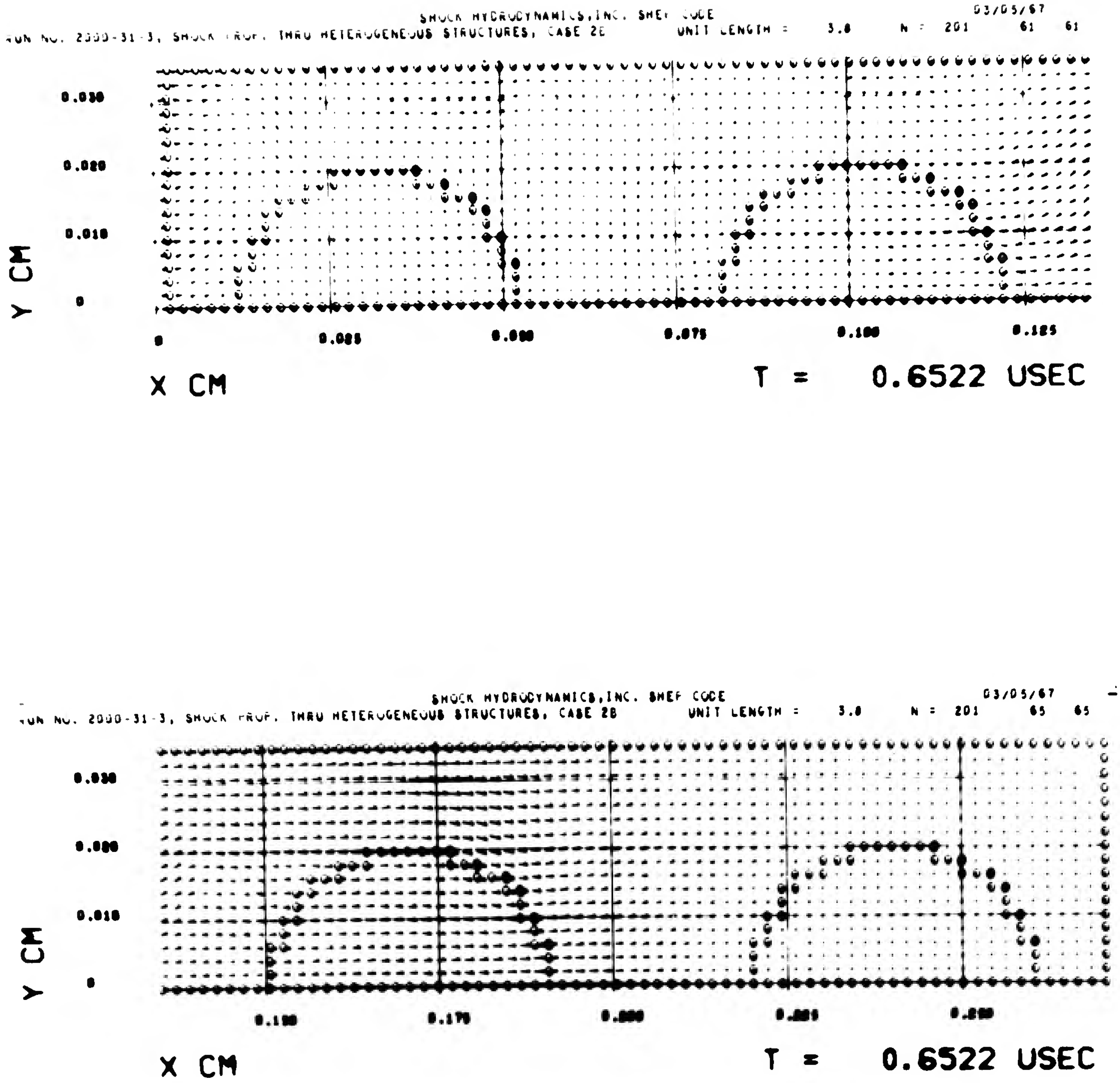

FIGURE 3-46. PARTICLE VELOCITY FIELD, CASE 2B, t = .6522 μ sec.

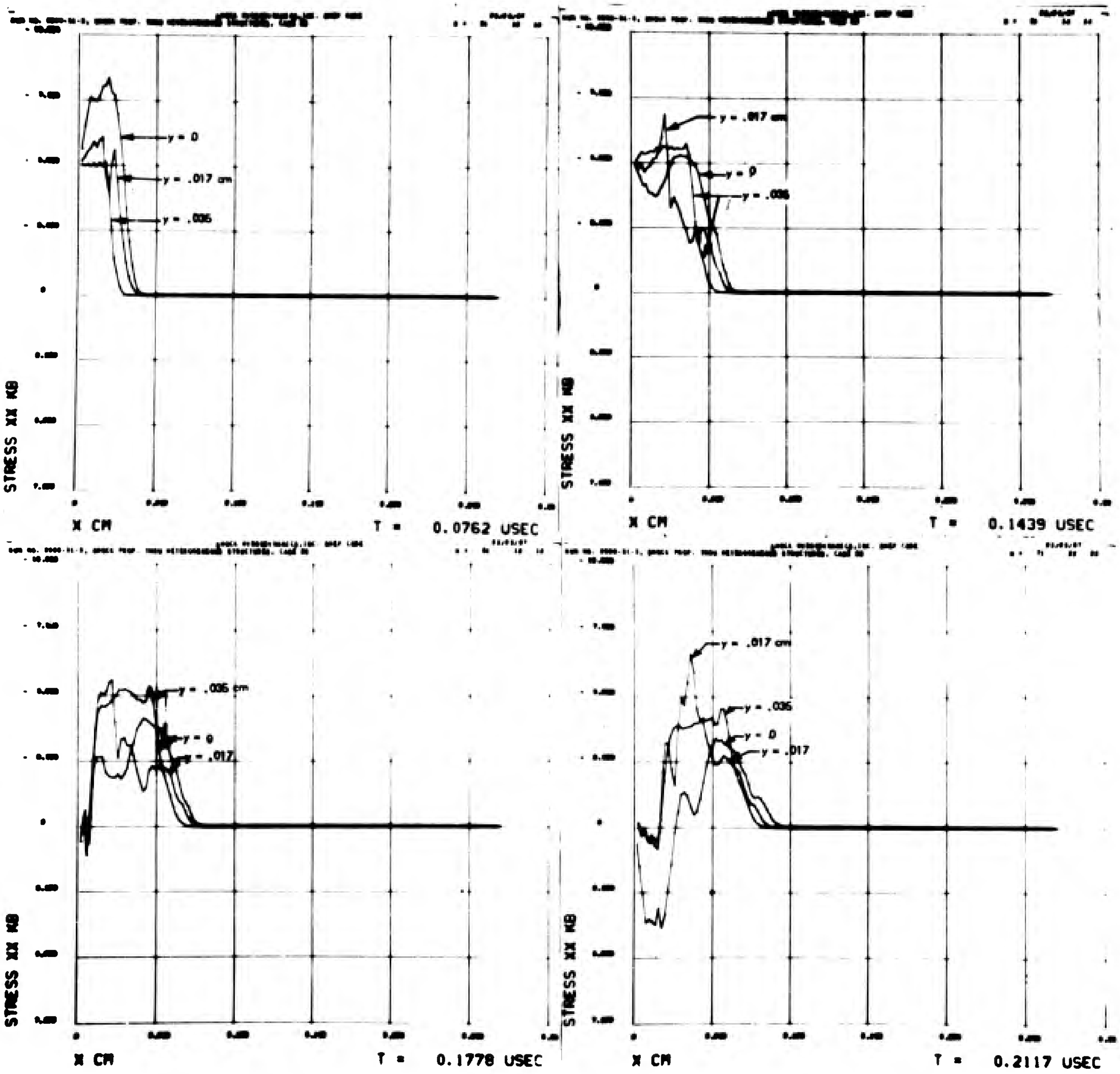

FIGURE 3-47. σ_x vs x AT THREE LATERAL POSITIONS, CASE 2B.

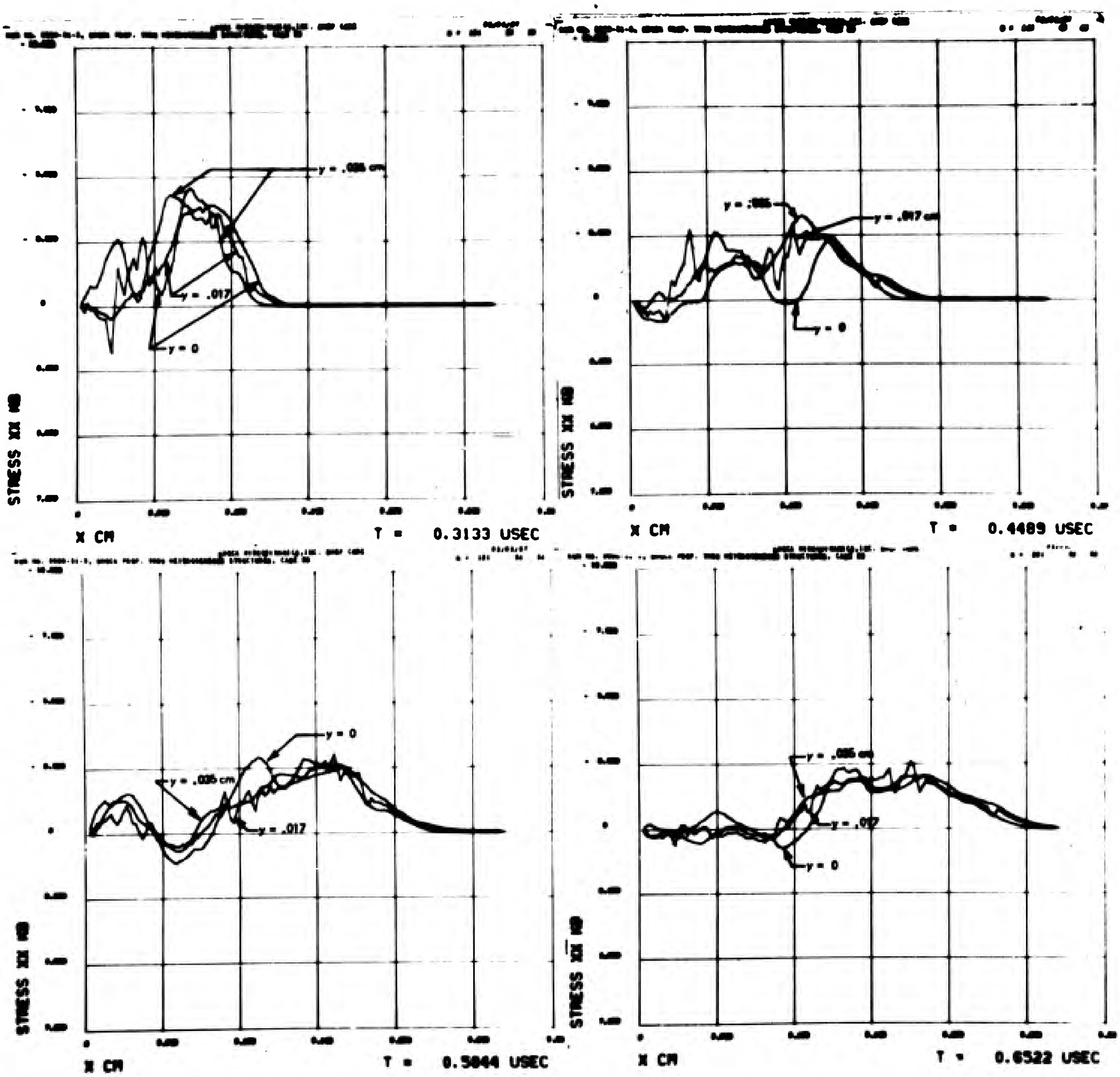

FIGURE 3-47 (cont'd). σ_x vs x AT THREE LATERAL POSITIONS, CASE 2B.

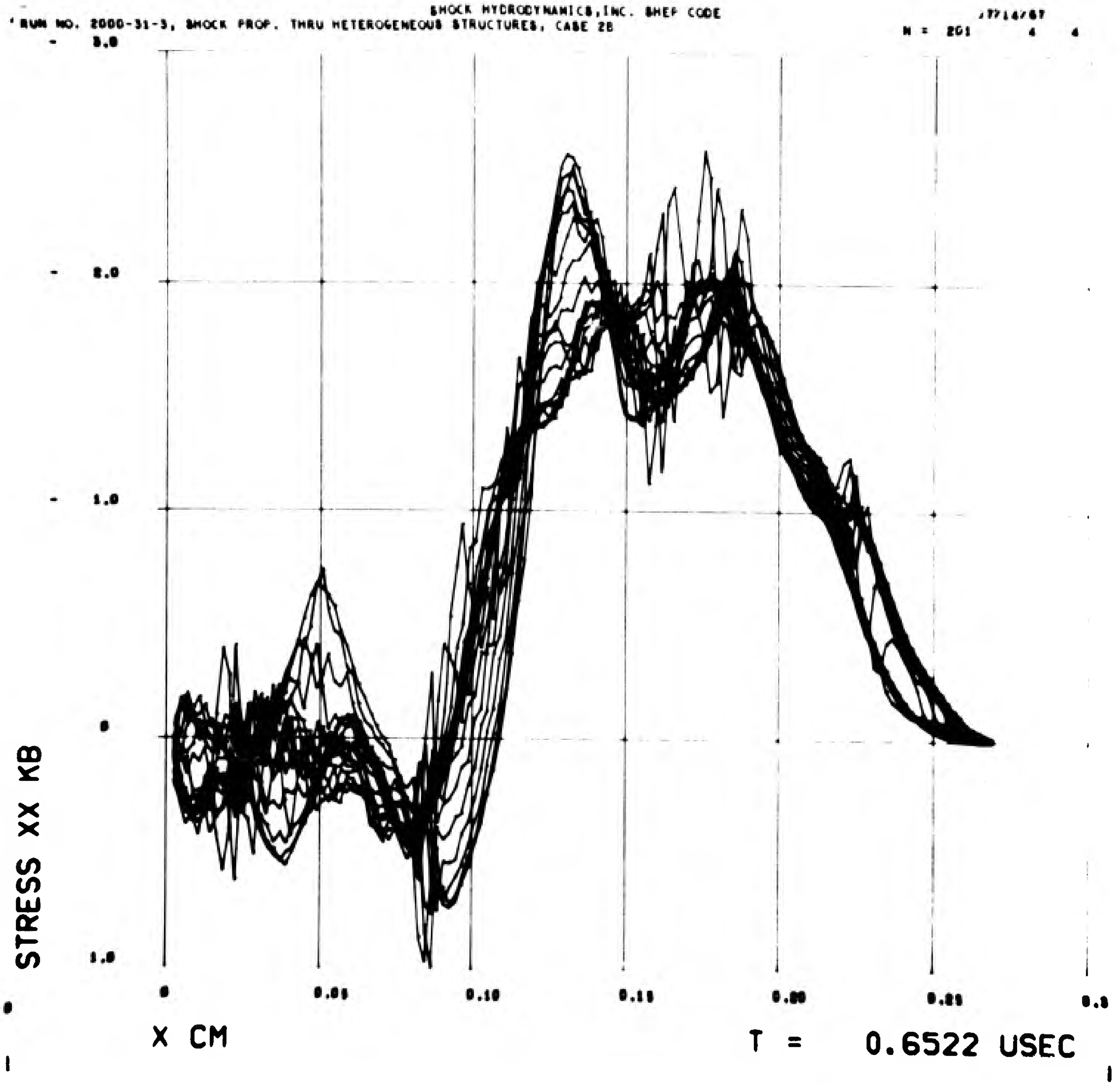

FIGURE 3-48. σ_x vs x AT ALL LATERAL MESH POSITIONS, CASE 2B.

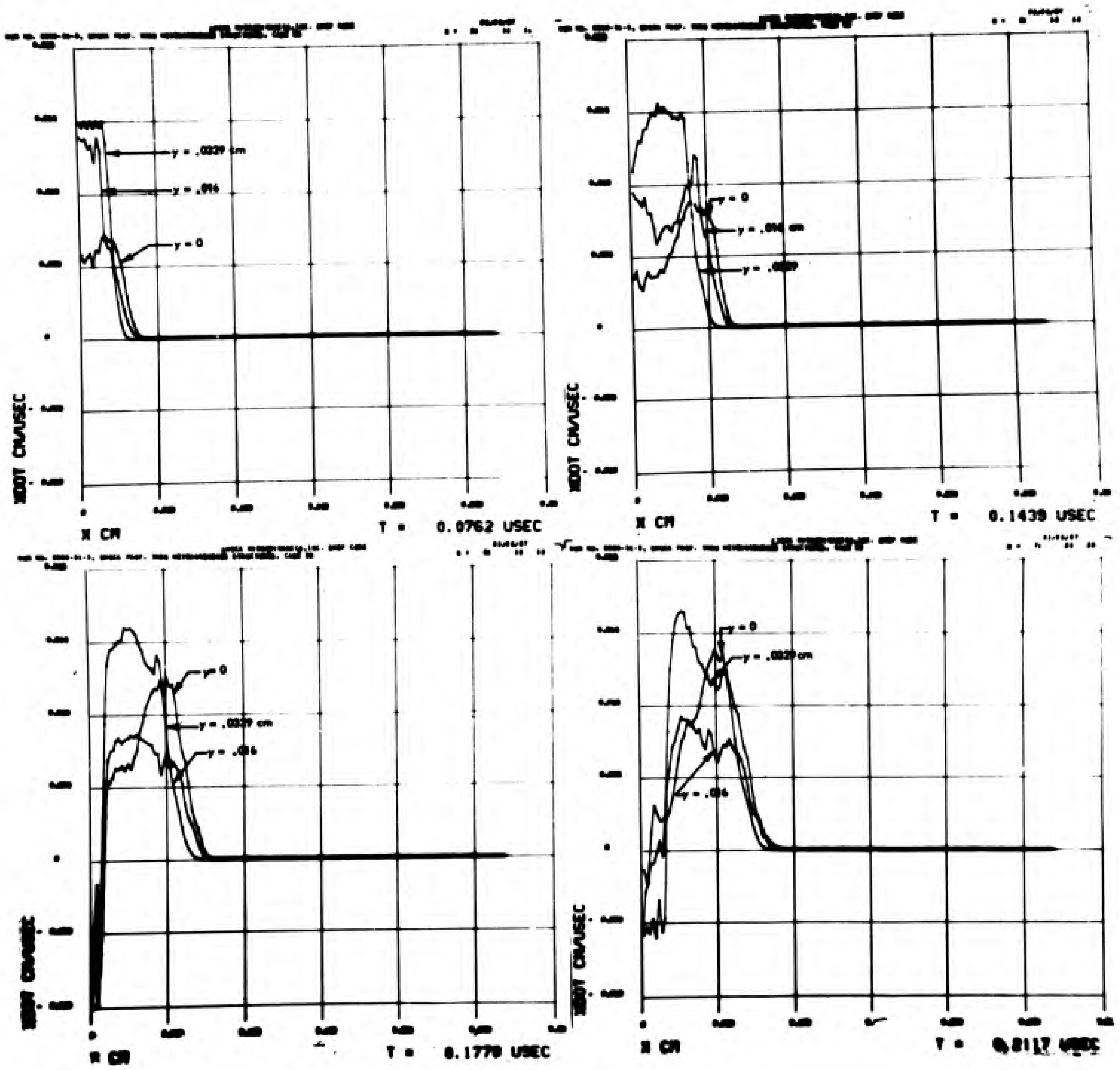

FIGURE 3-49. $\dot{x}$ vs x AT THREE LATERAL POSITIONS, CASE 2B.

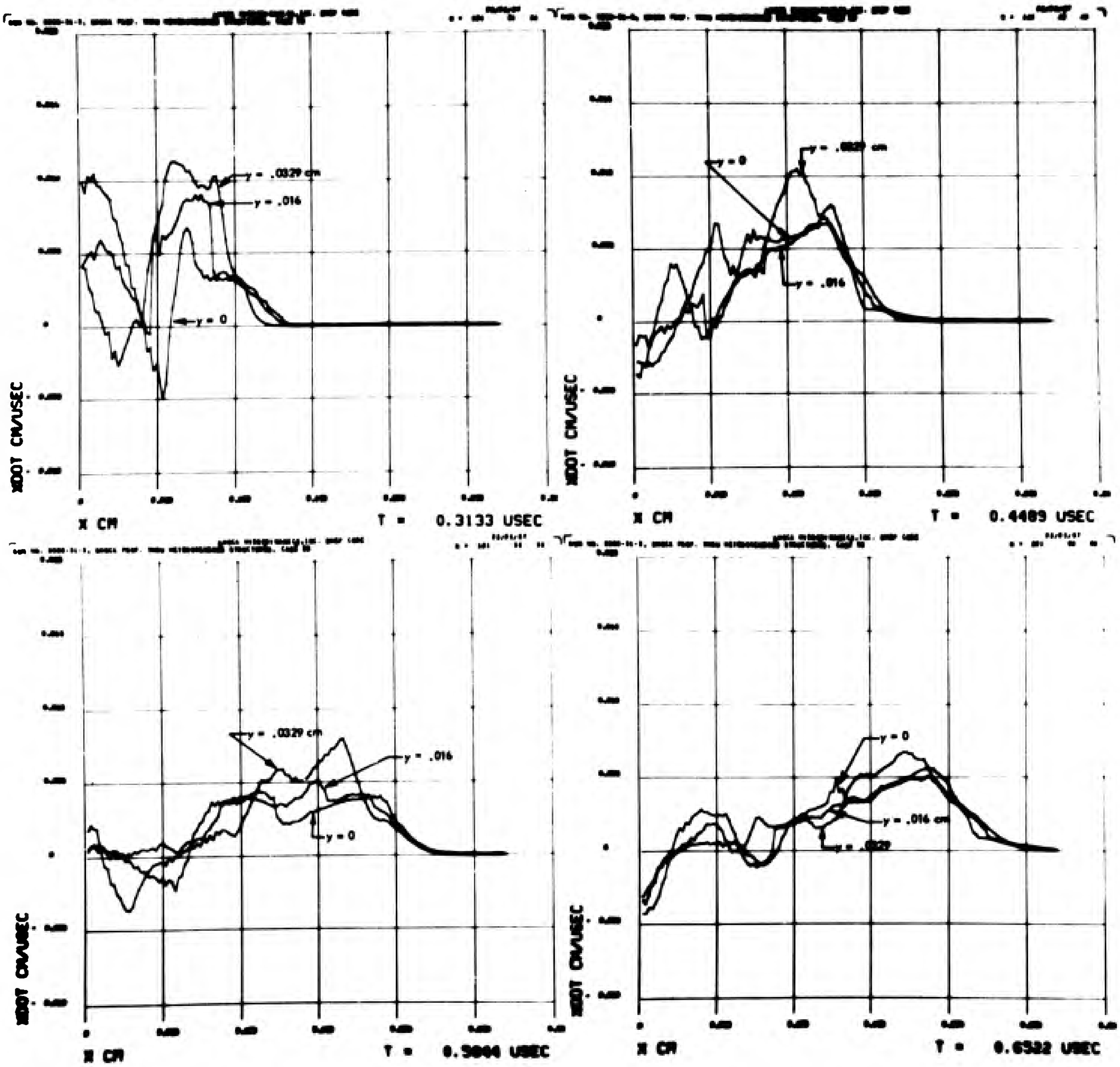

FIGURE 3-49 (cont'd). $\dot{x}$ vs x AT THREE LATERAL POSITIONS, CASE 2B.

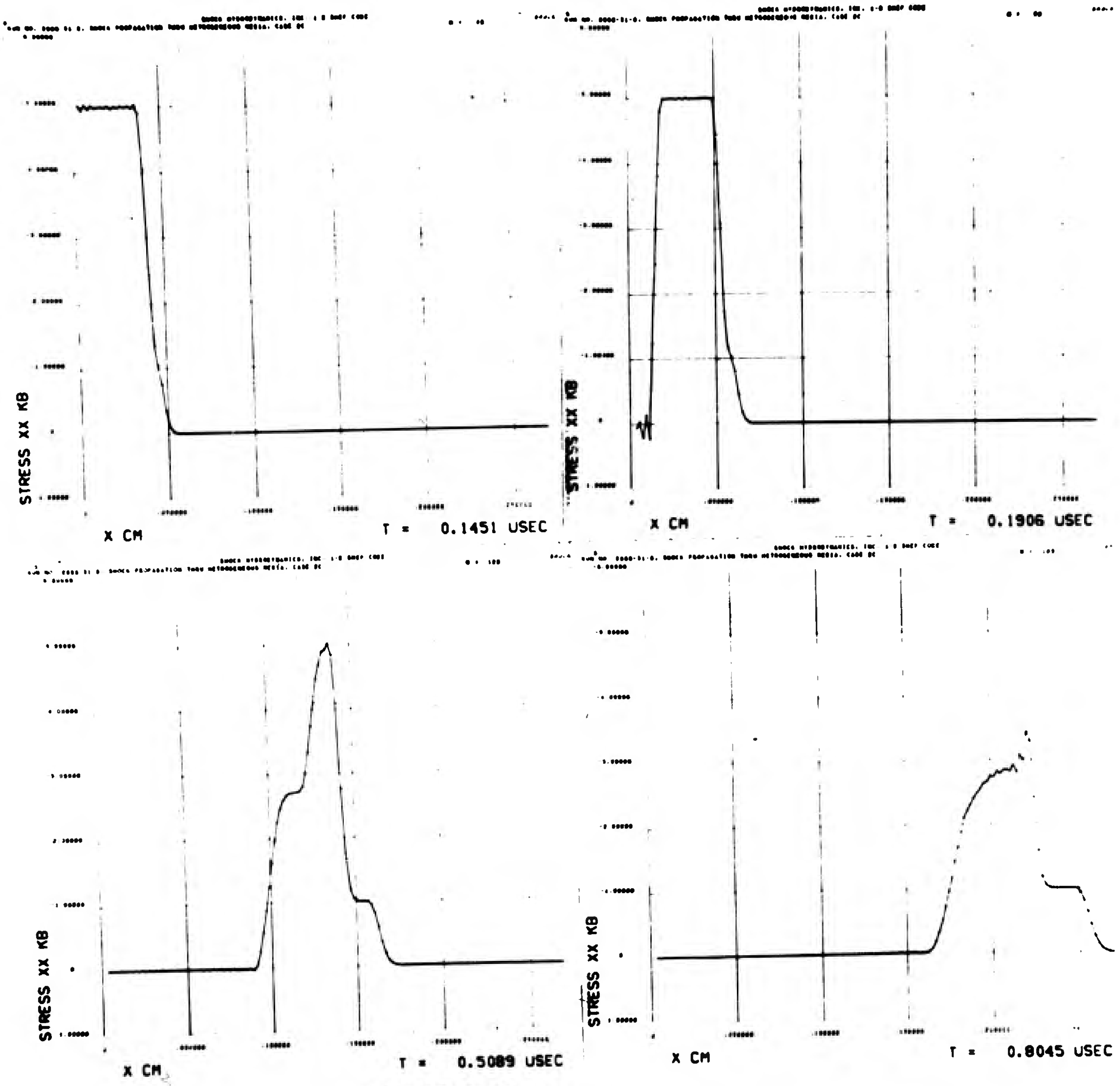

FIGURE 3-50. σ_x vs x, CASE 2C.

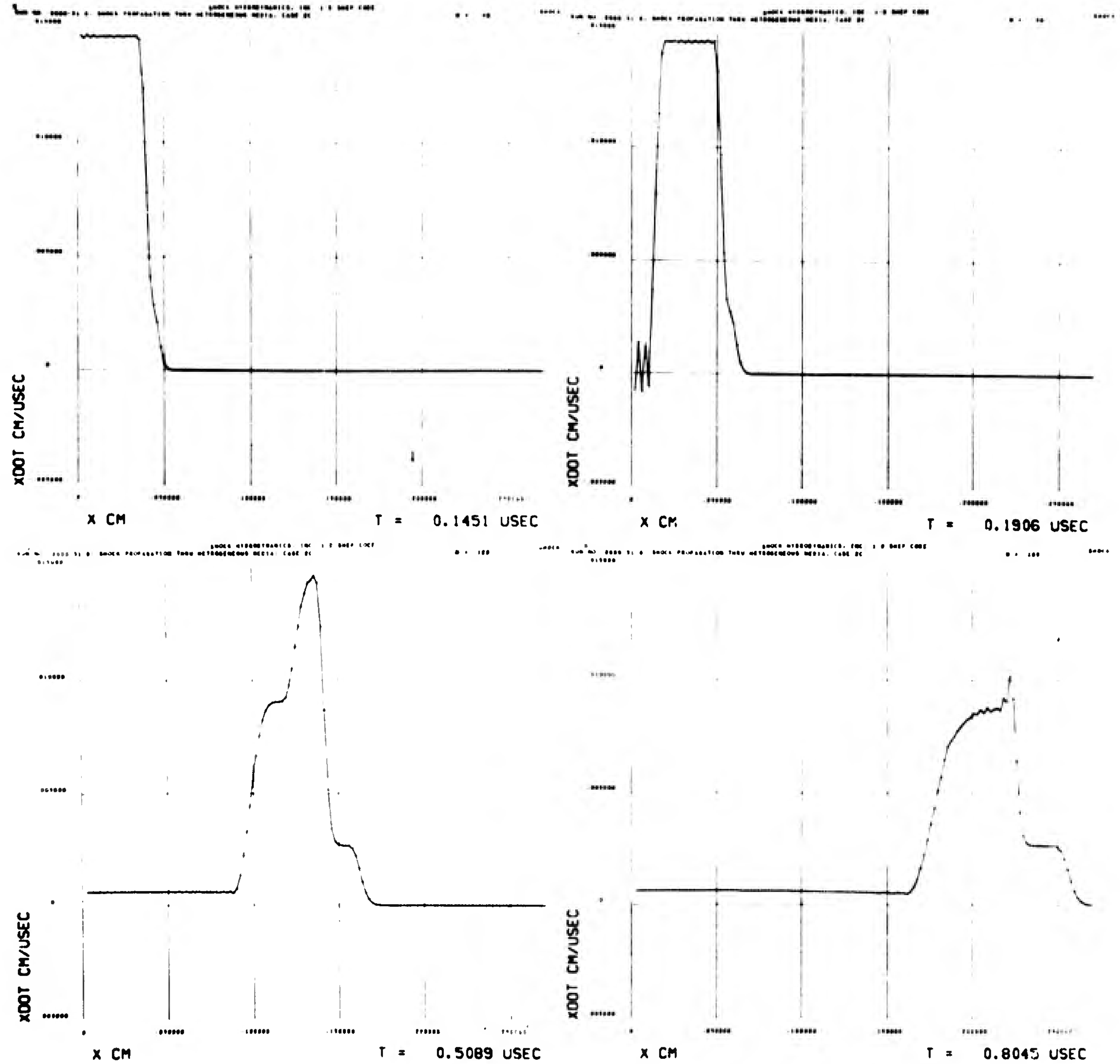

FIGURE 3-51. $\dot{x}$ vs x, CASE 2C.

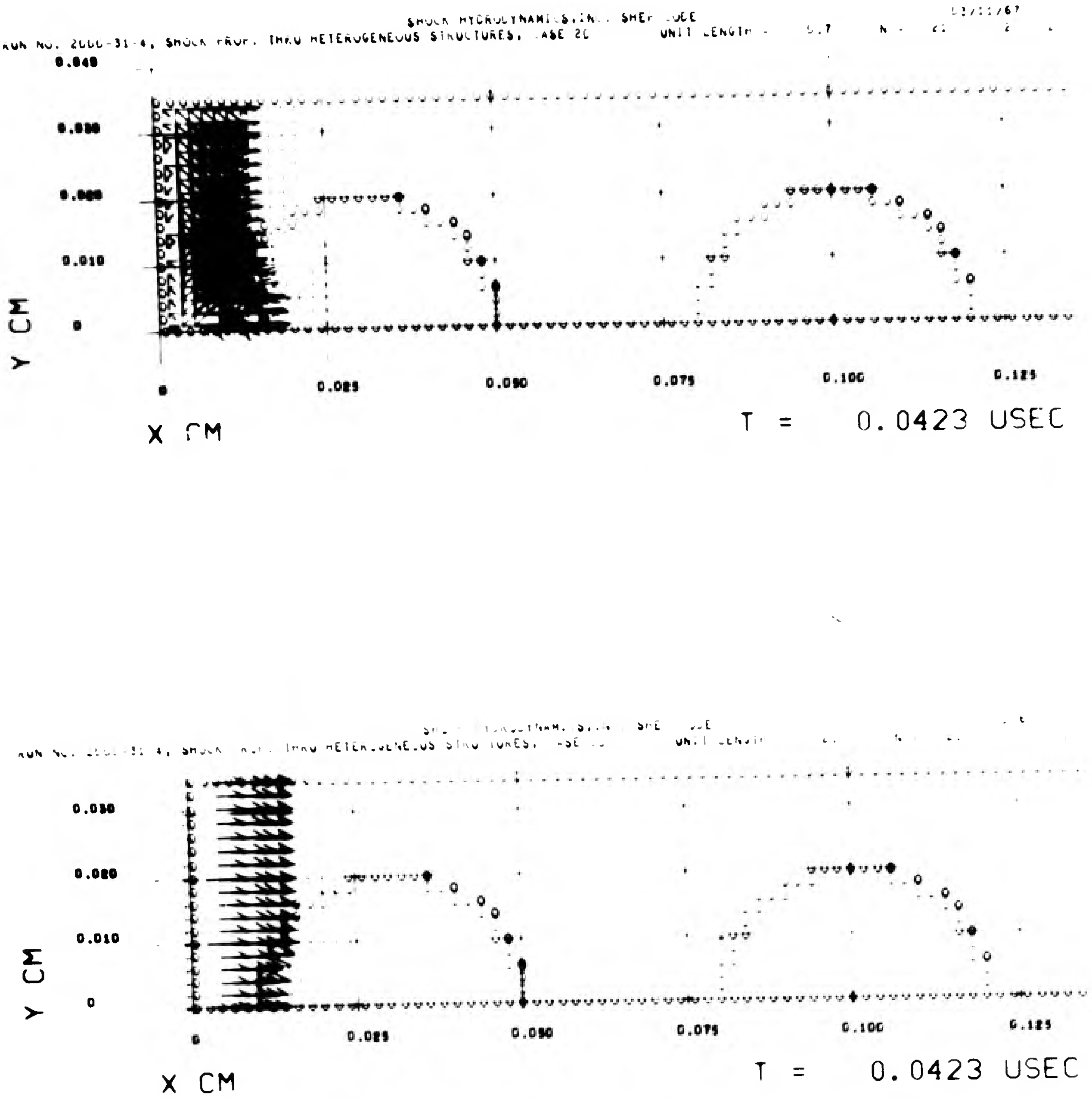

FIGURE 3-52. PRINCIPAL STRESS AND PARTICLE VELOCITY FIELDS, CASE 2D, t = .0423 μ sec.

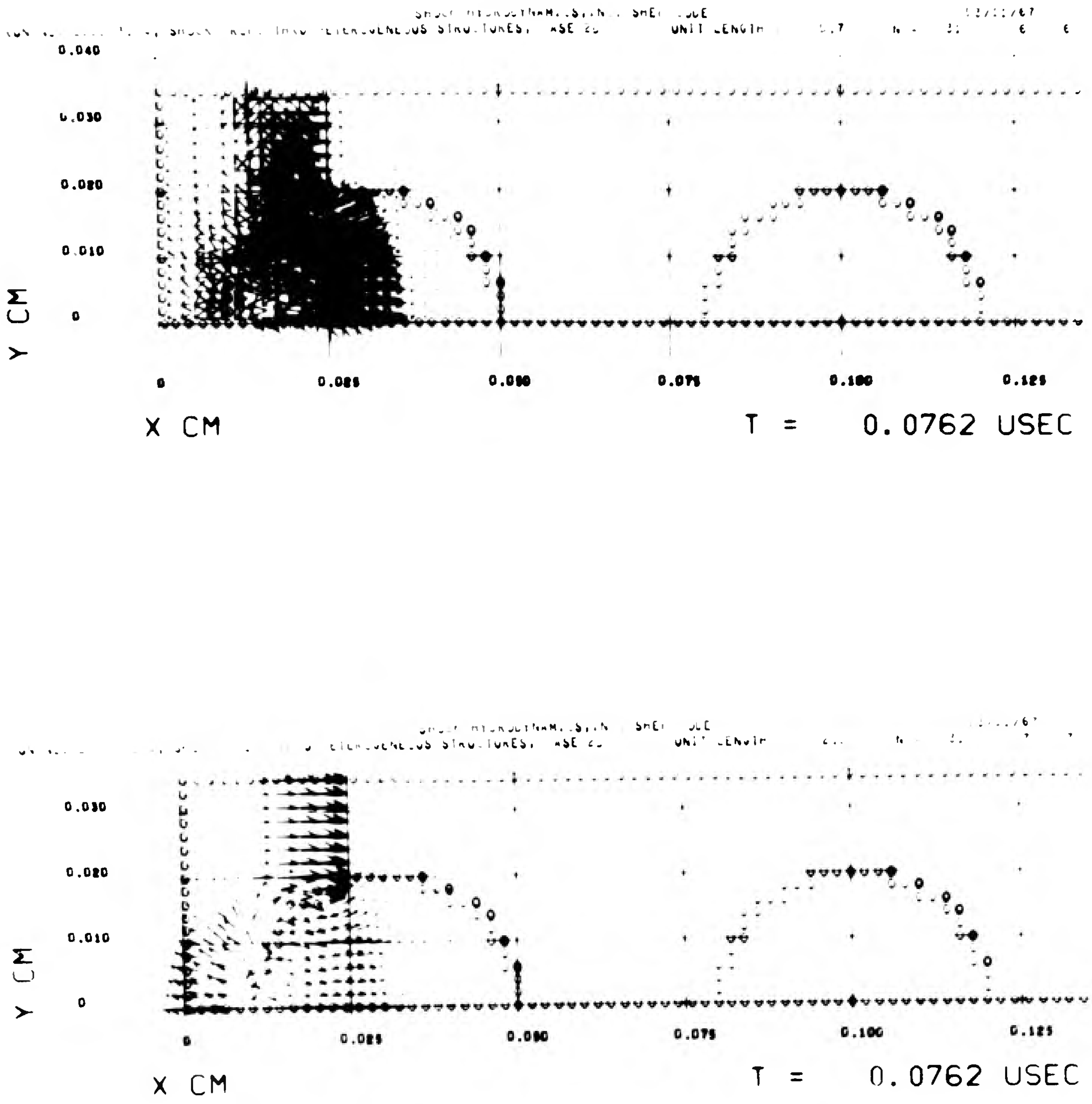

FIGURE 3-53. PRINCIPAL STRESS AND PARTICLE VELOCITY FIELDS, CASE 2D, t = .0762μ sec.

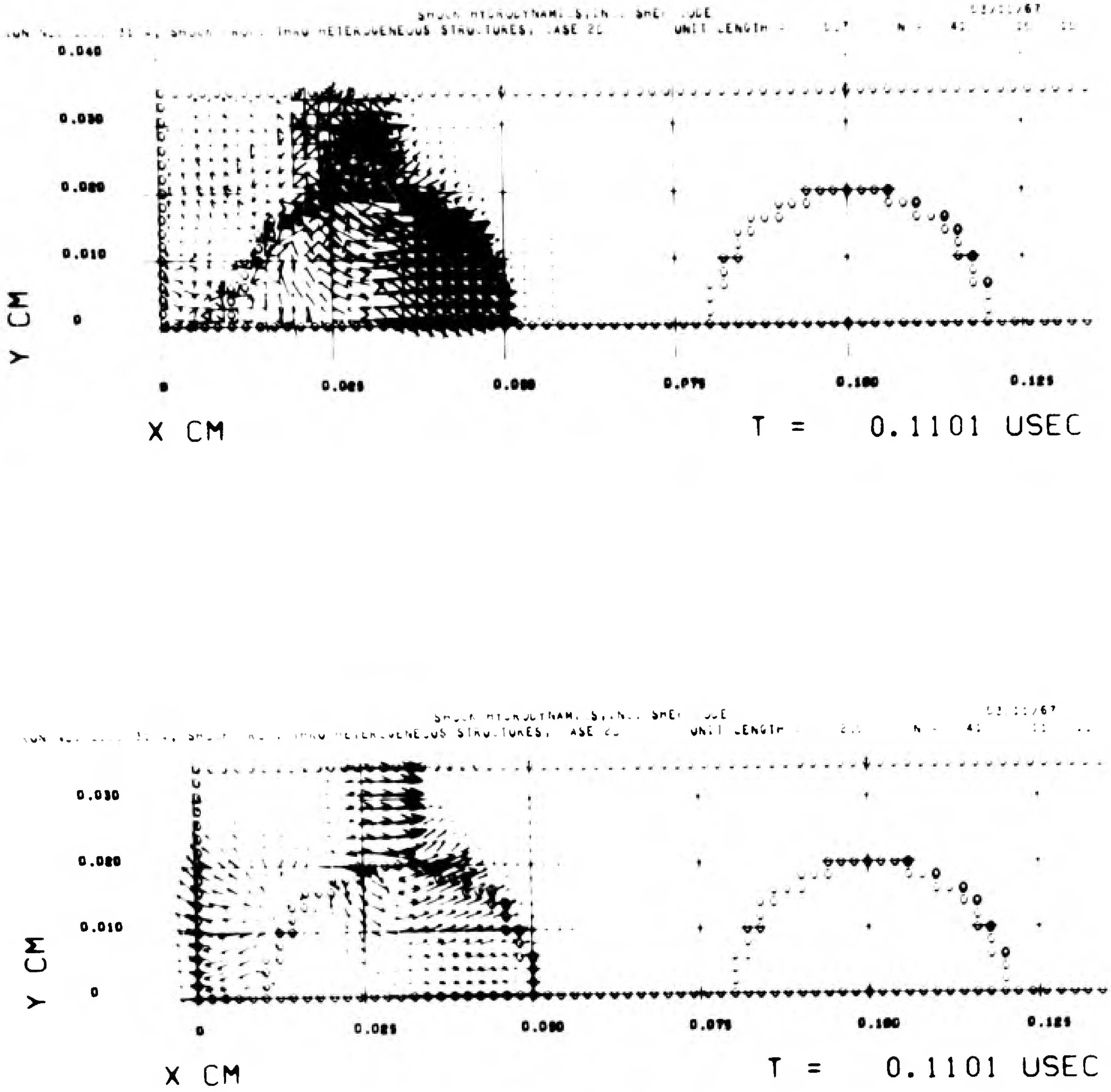

FIGURE 3-54. PRINCIPAL STRESS AND PARTICLE VELOCITY FIELDS, CASE 2D, t = .1101 μsec.

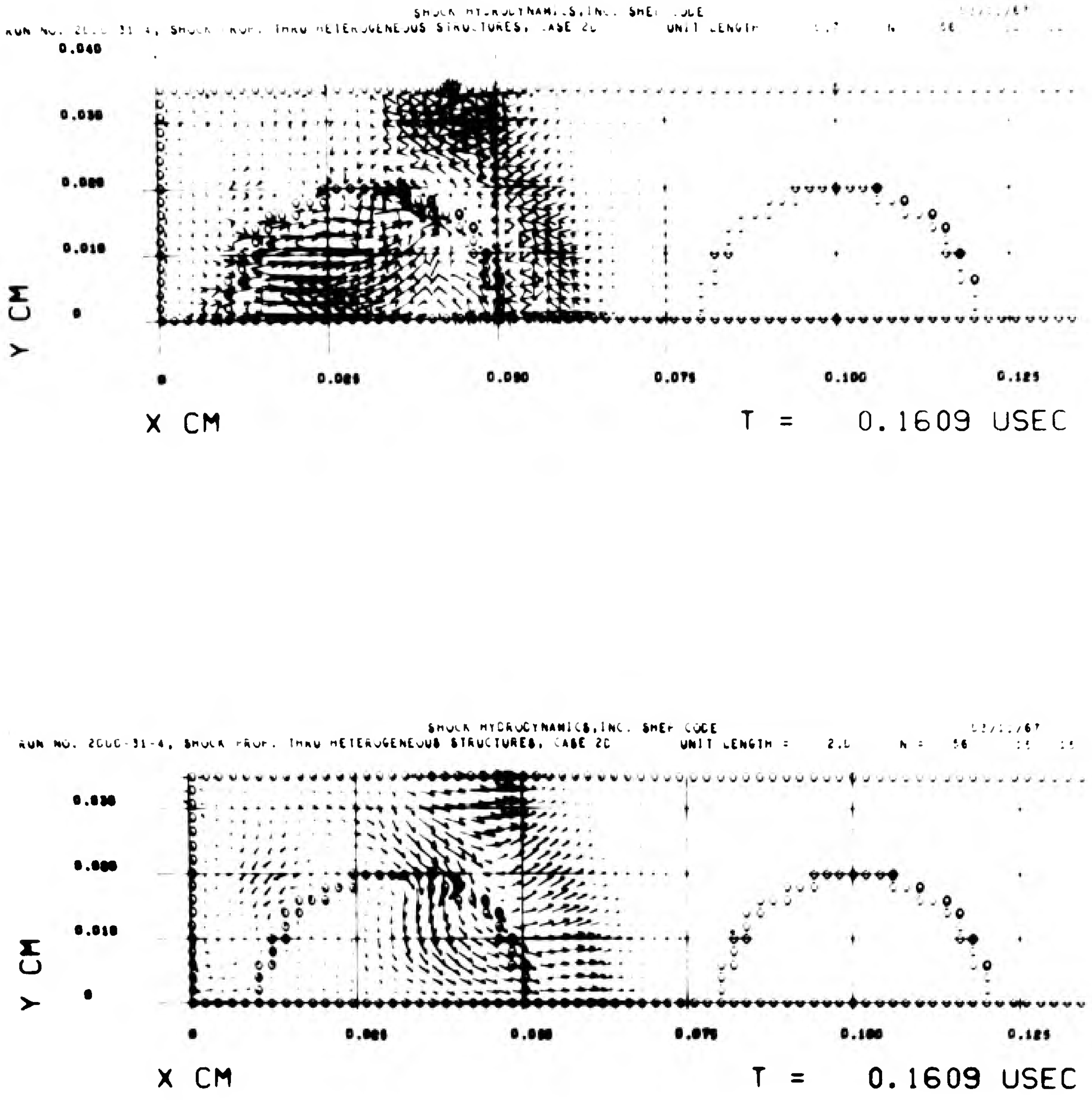

FIGURE 3-55. PRINCIPAL STRESS AND PARTICLE VELOCITY FIELDS, CASE 2D, t = .1609μ sec.

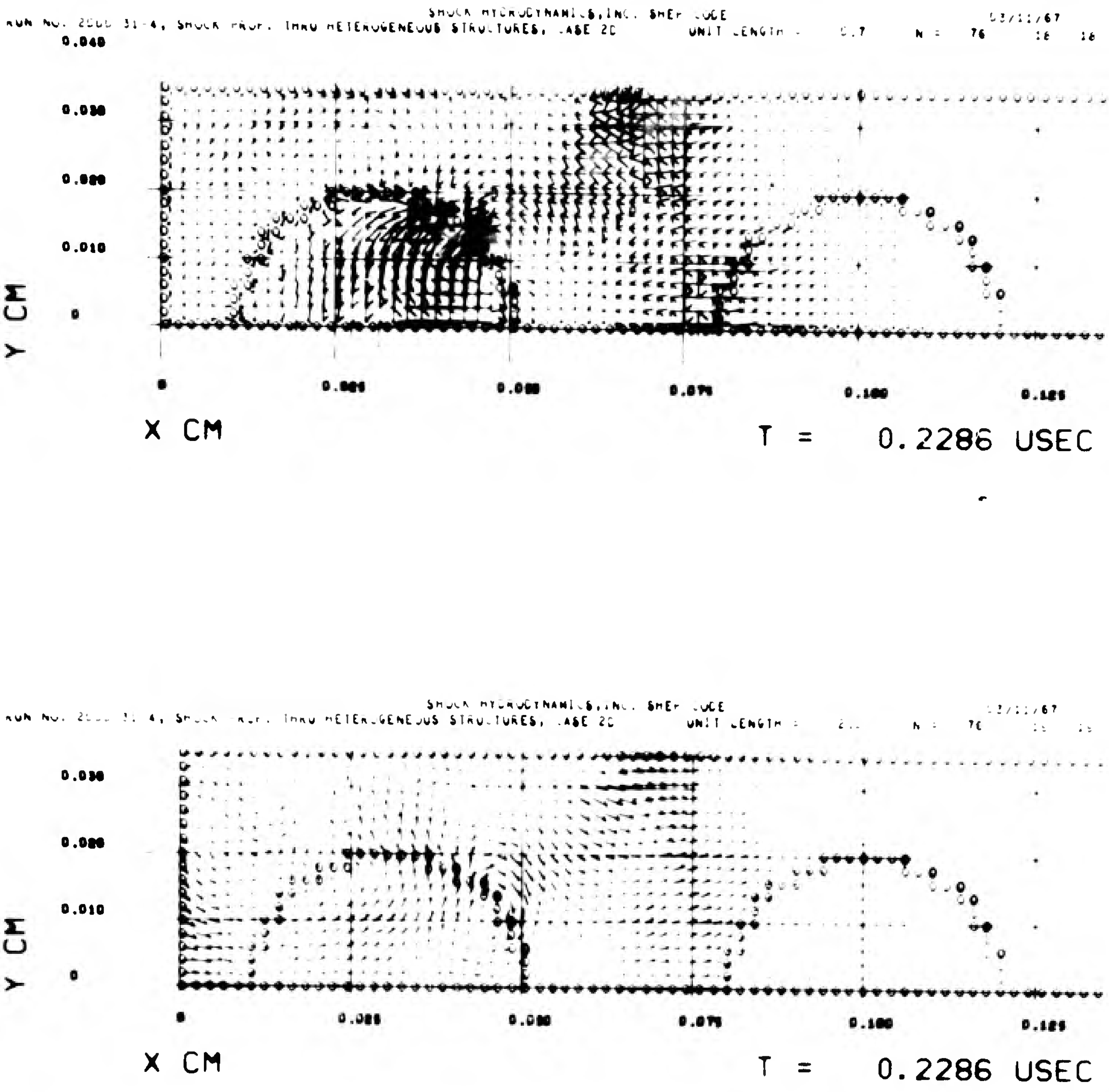

FIGURE 3-56. PRINCIPAL STRESS AND PARTICLE VELOCITY FIELDS, CASE 2D, t = .2286 μ sec.

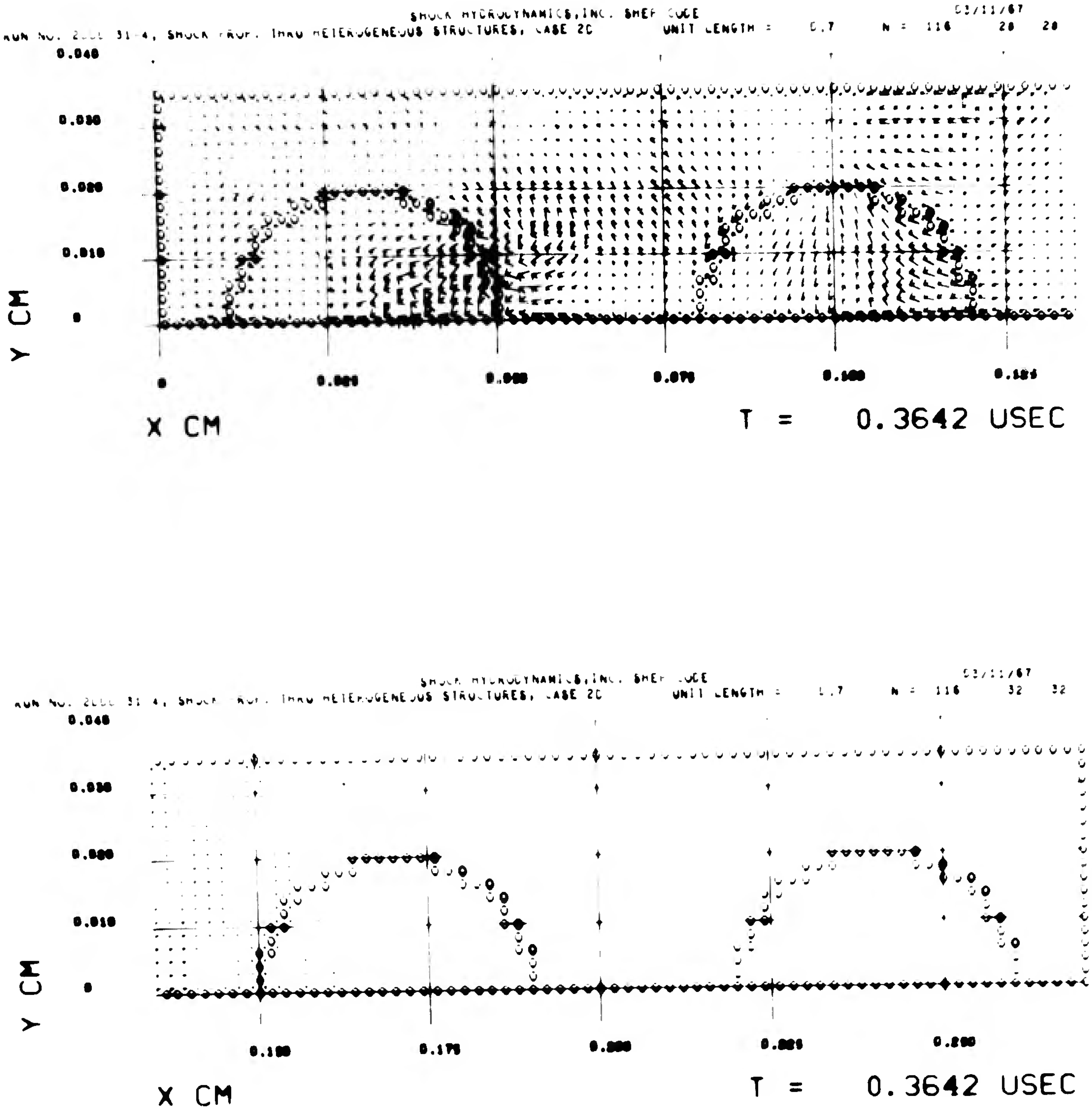

FIGURE 3-57. PRINCIPAL STRESS FIELD, CASE 2D, t = .3642 μsec.

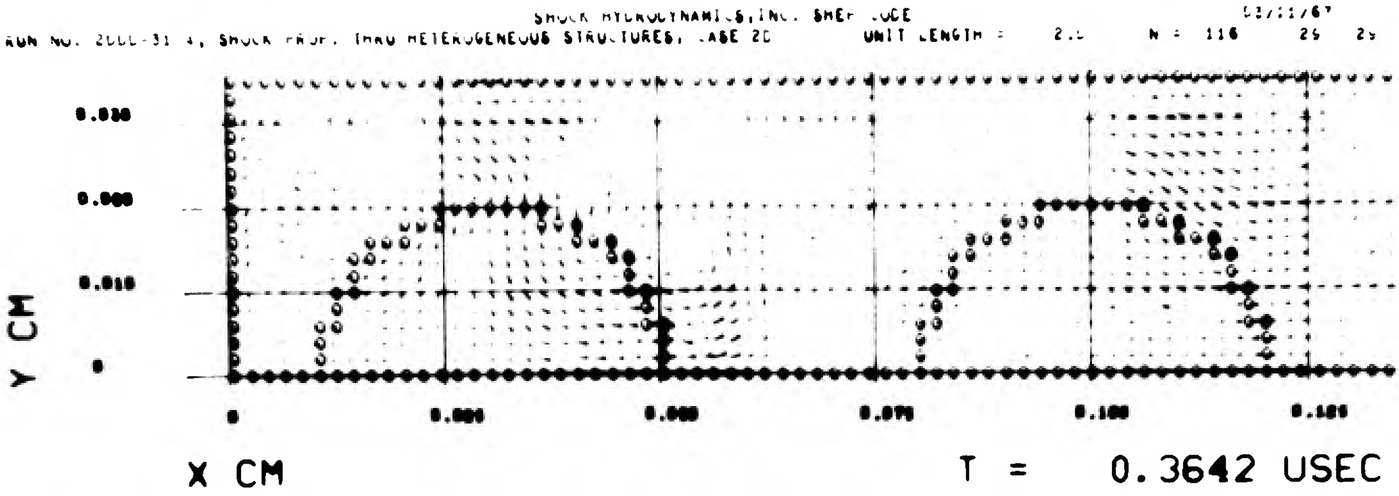

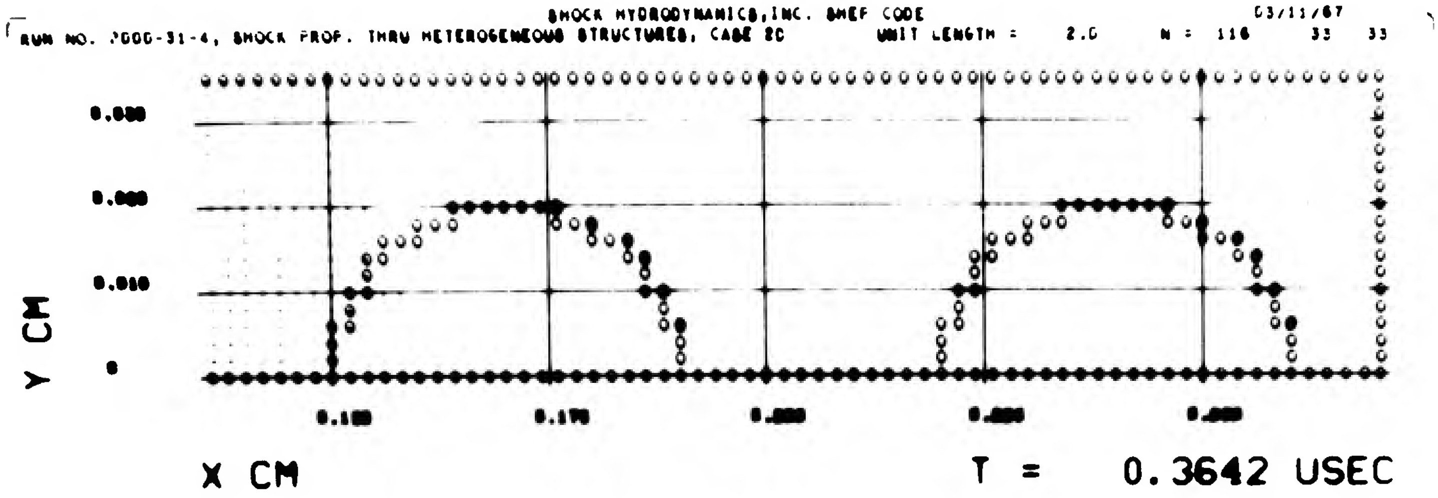

FIGURE 3-58. PARTICLE VELOCITY FIELD, CASE 2D, $t = .3642 \mu$ sec.

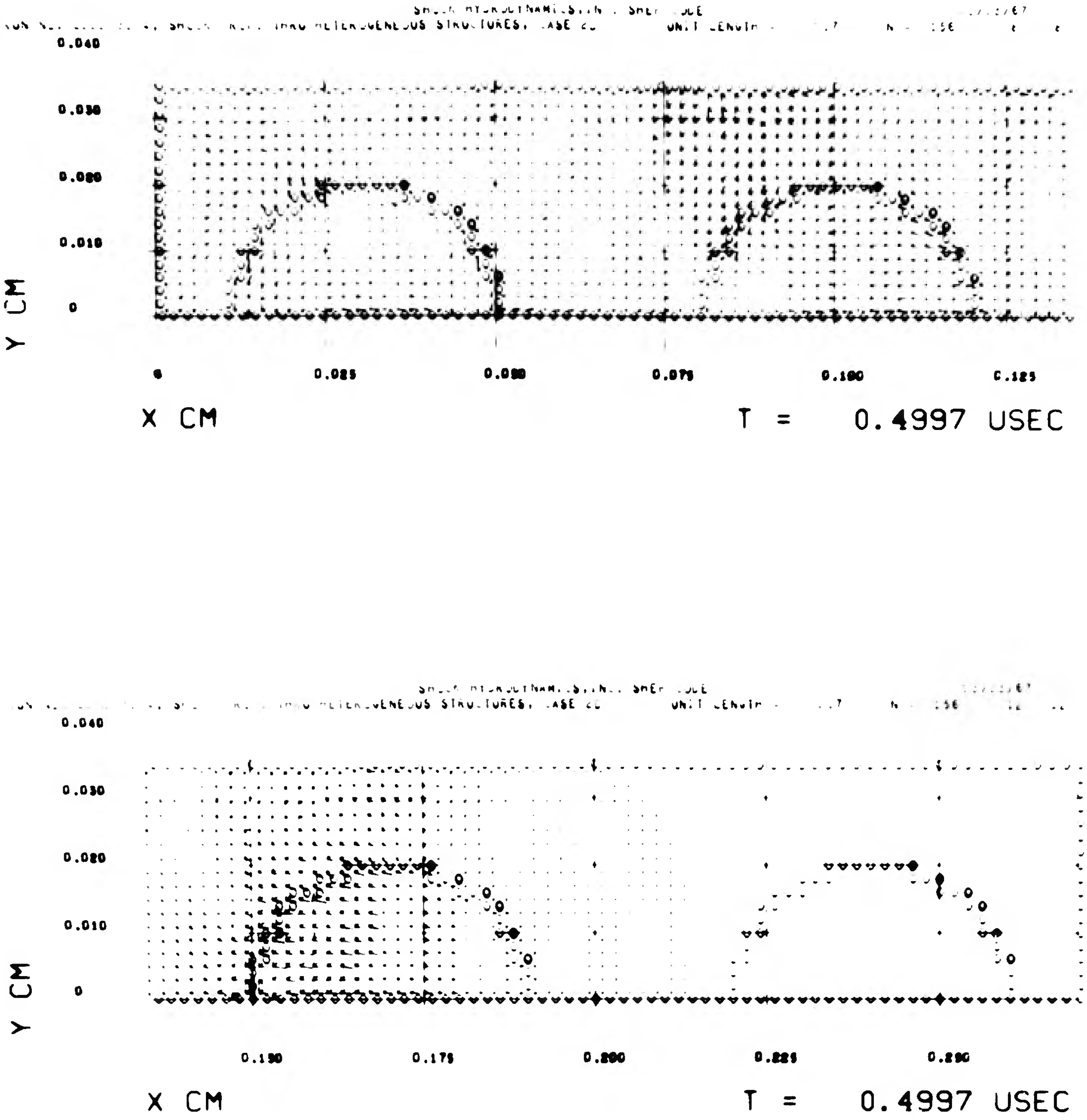

FIGURE 3-59. PRINCIPAL STRESS FIELD, CASE 2D, t = .4997 μ sec.

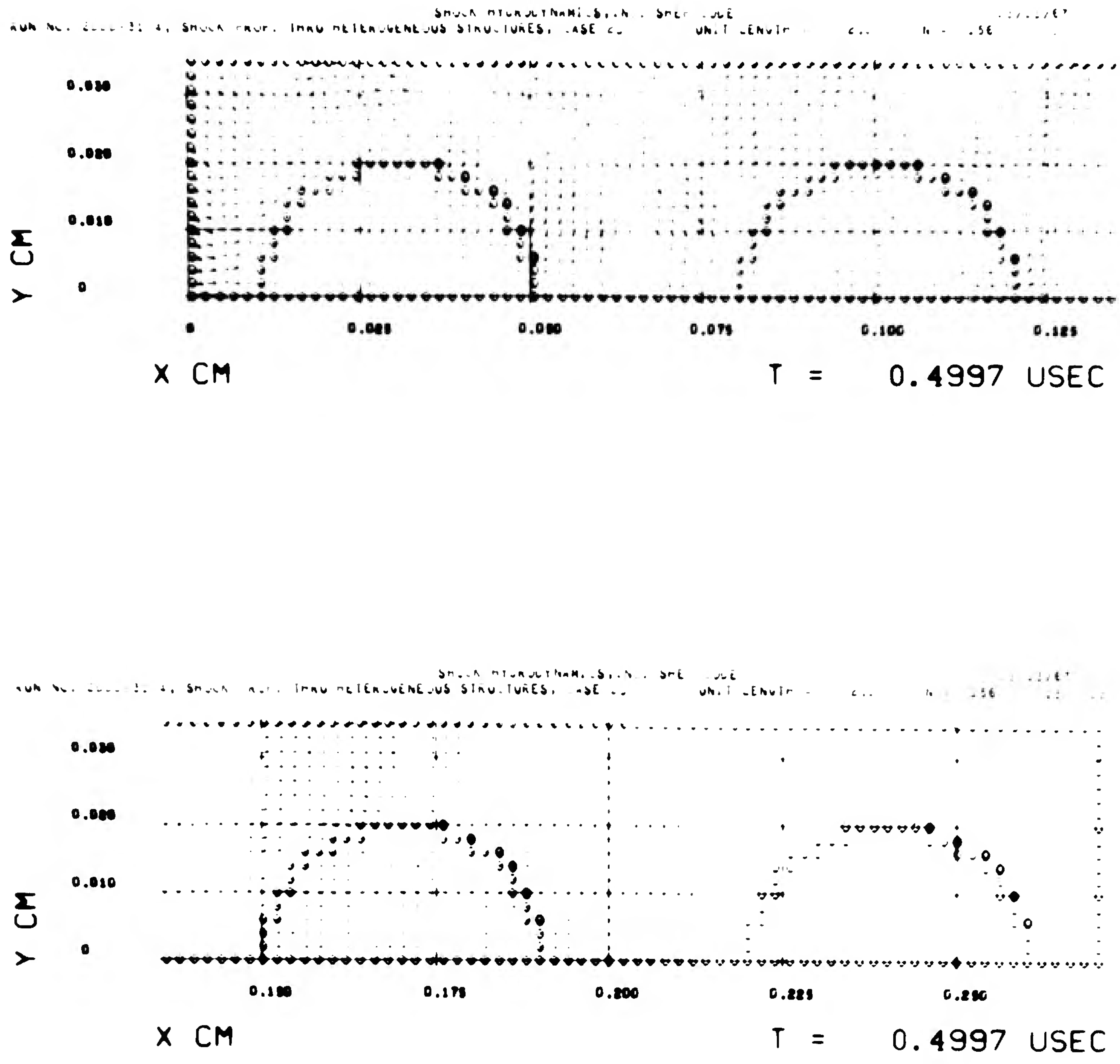

FIGURE 3-60. PARTICLE VELOCITY FIELD, CASE 2D, t = .4997μsec.

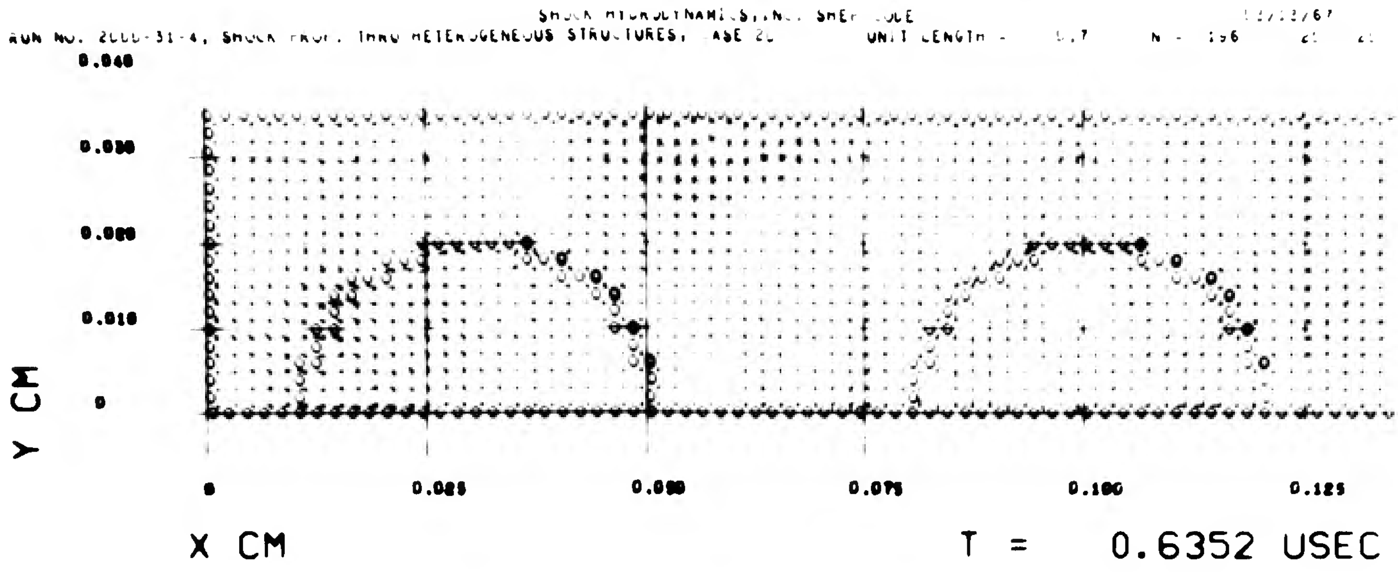

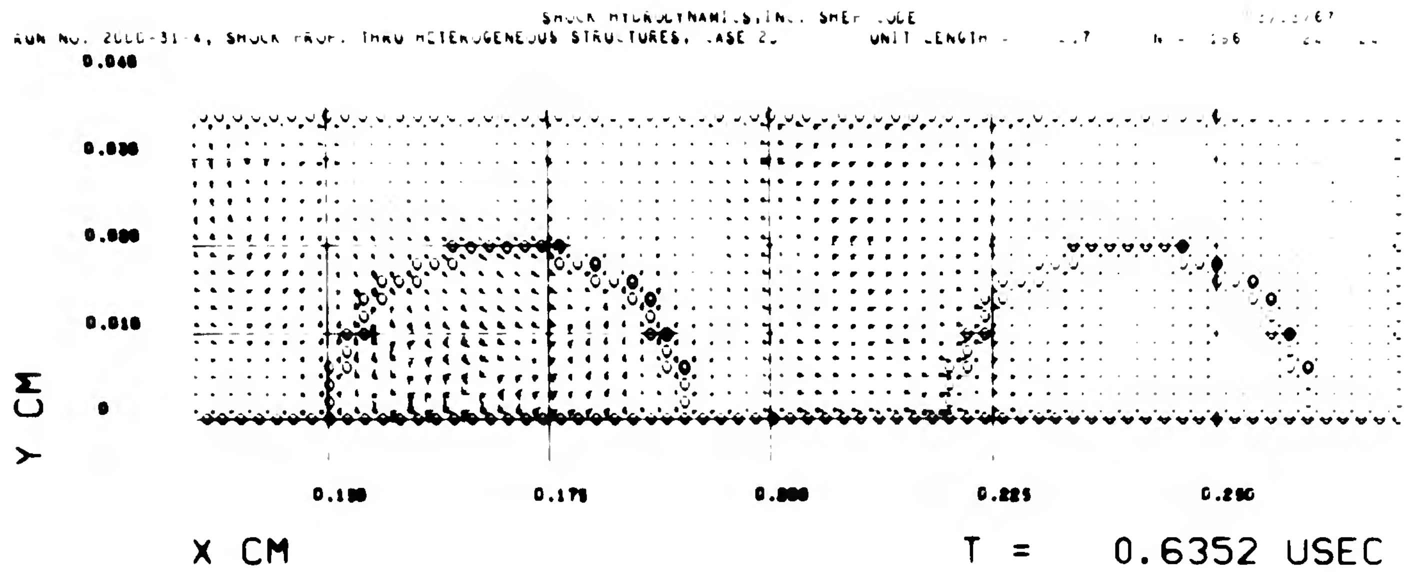

FIGURE 3-61. PRINCIPAL STRESS FIELD, CASE 2D, t = .6352μsec.

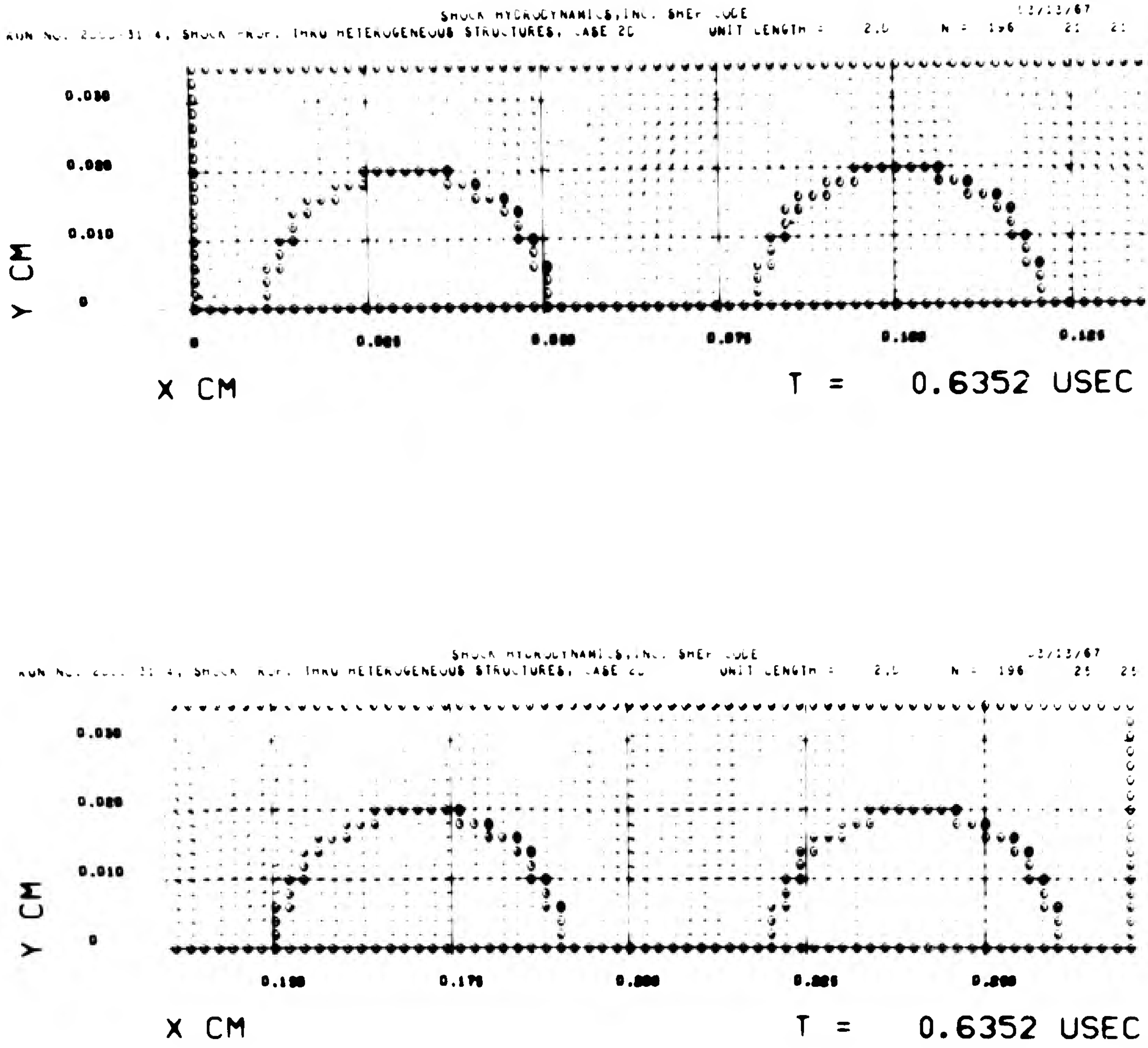

FIGURE 3-62. PARTICLE VELOCITY FIELD, CASE 2D, t = .6352μsec.

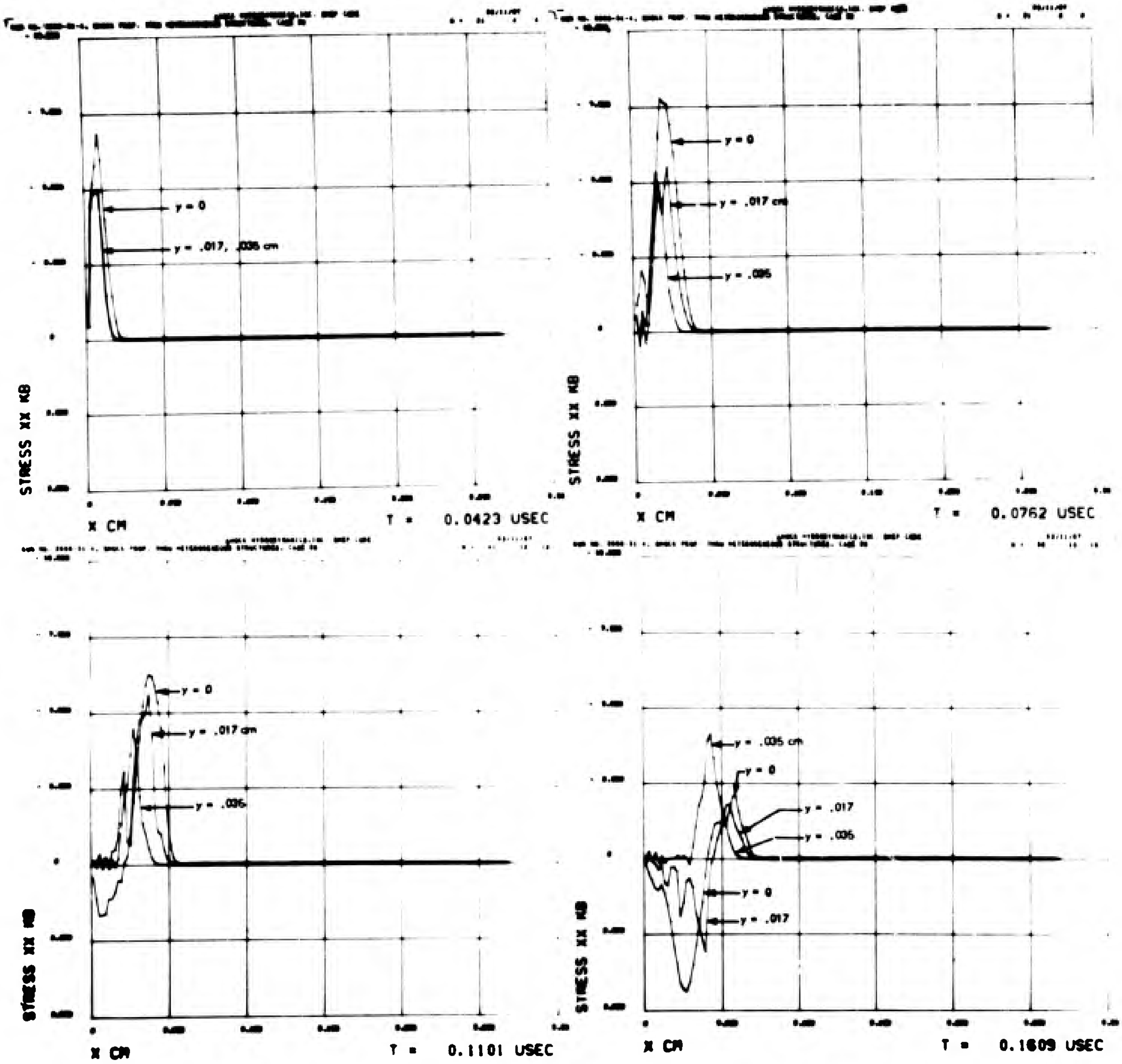

FIGURE 3-63. σ_x vs x AT THREE LATERAL POSITIONS, CASE 2D.

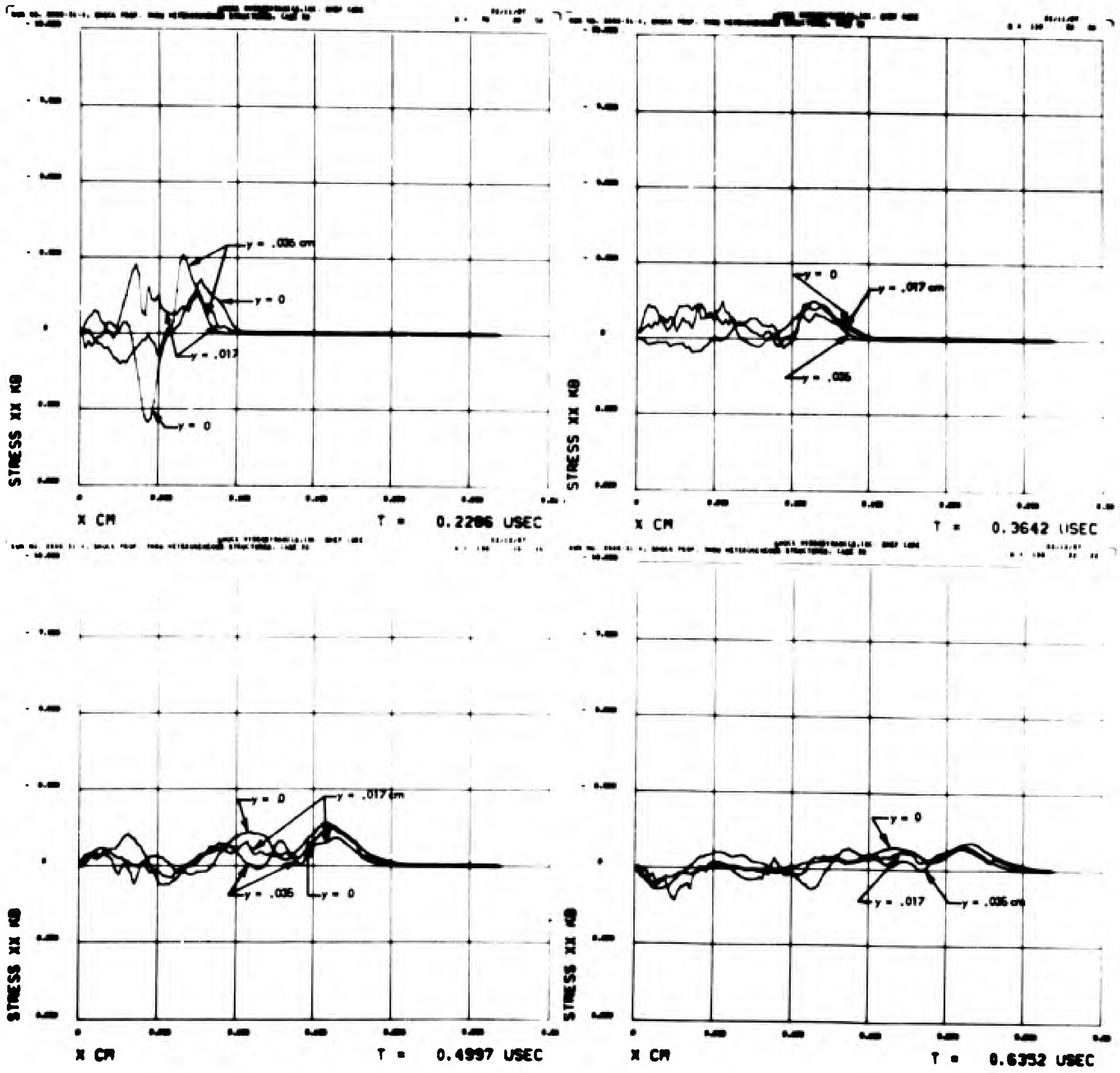

FIGURE 3-63 (cont'd). σ_x vs x AT THREE LATERAL POSITIONS, CASE 2D.

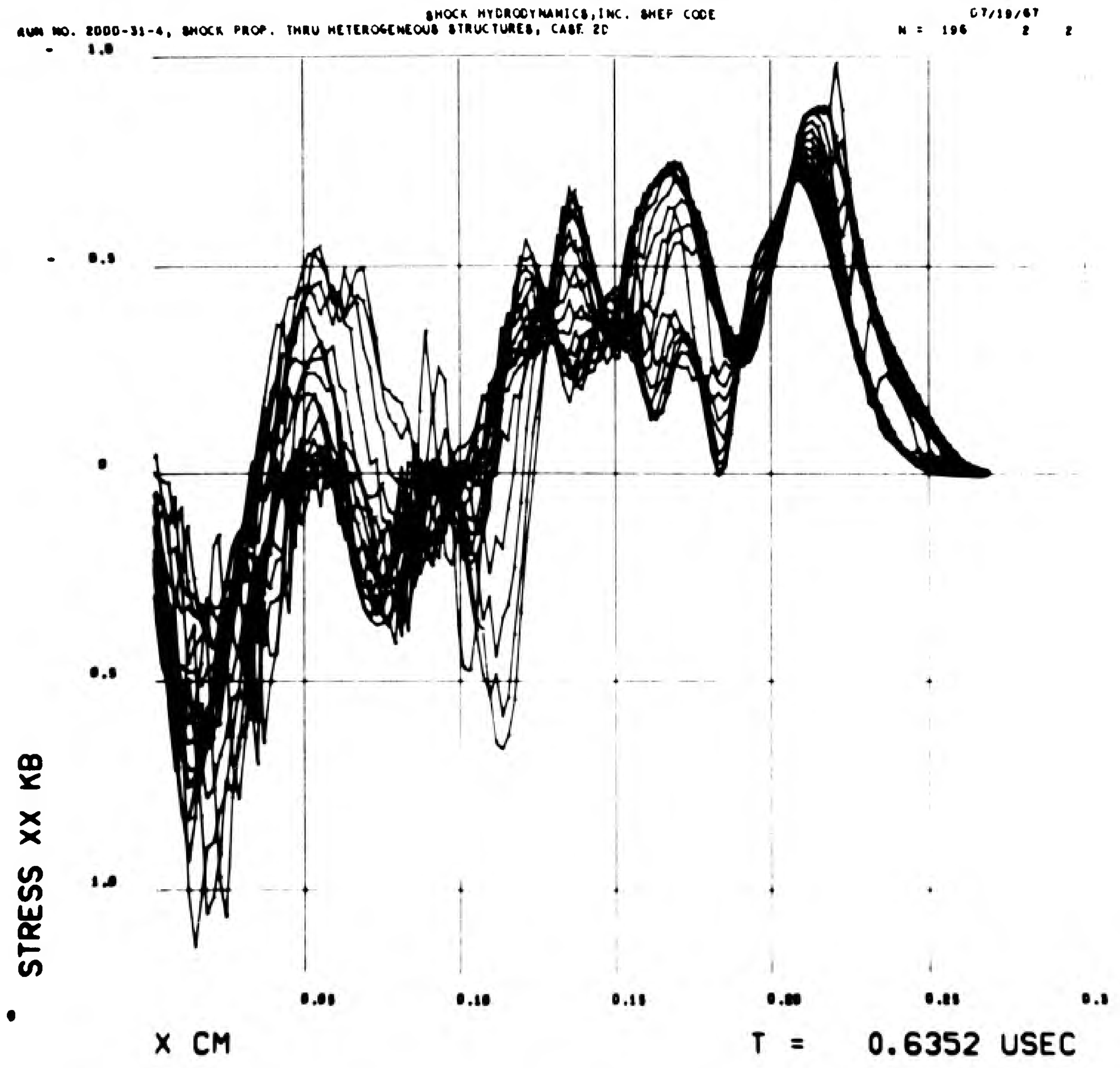

FIGURE 3-64. σ_x vs x AT ALL LATERAL MESH POSITIONS, CASE 2 D.

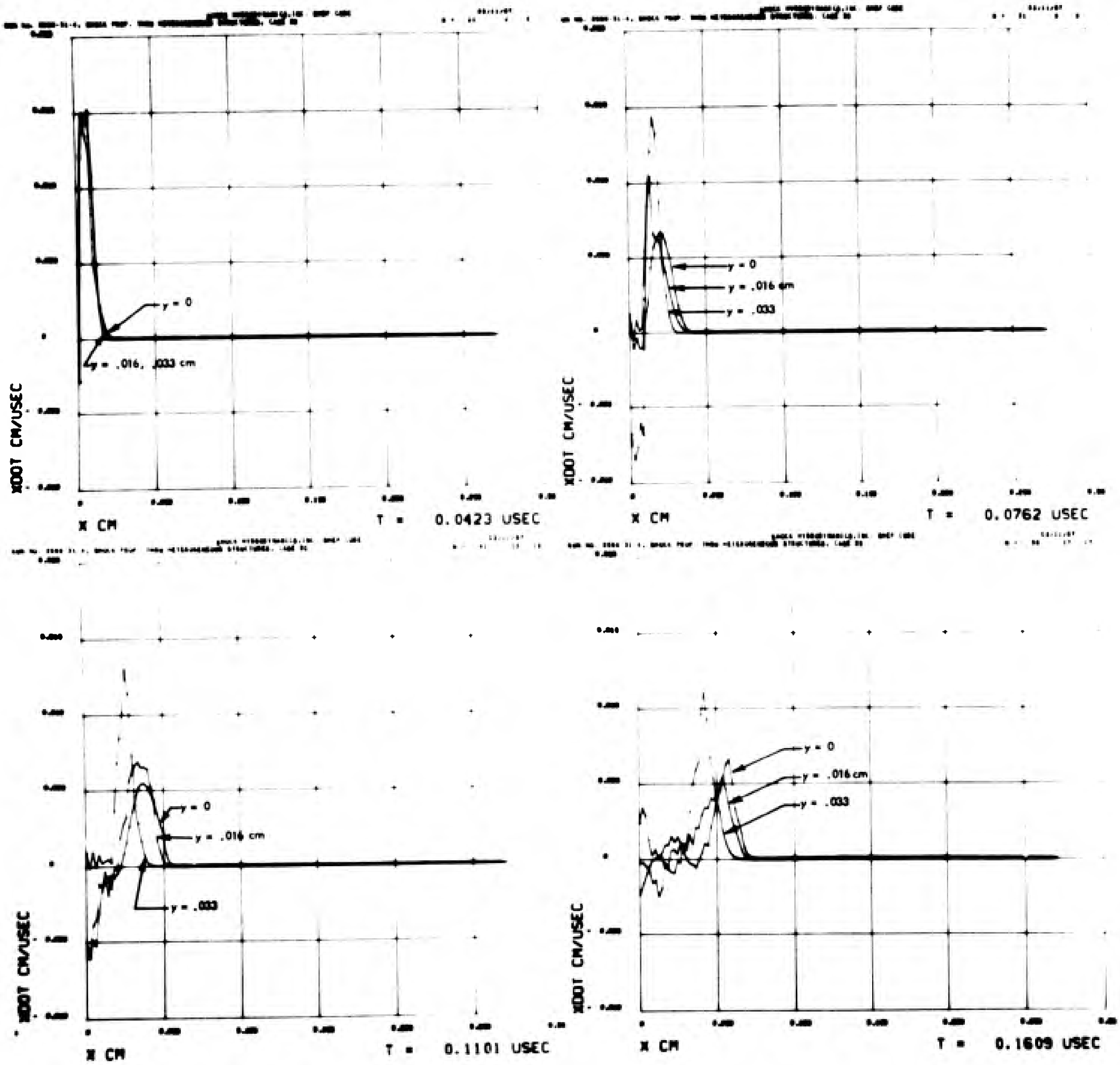

FIGURE 3-65. $\dot{x}$ vs x AT THREE LATERAL POSITIONS, CASE 2D.

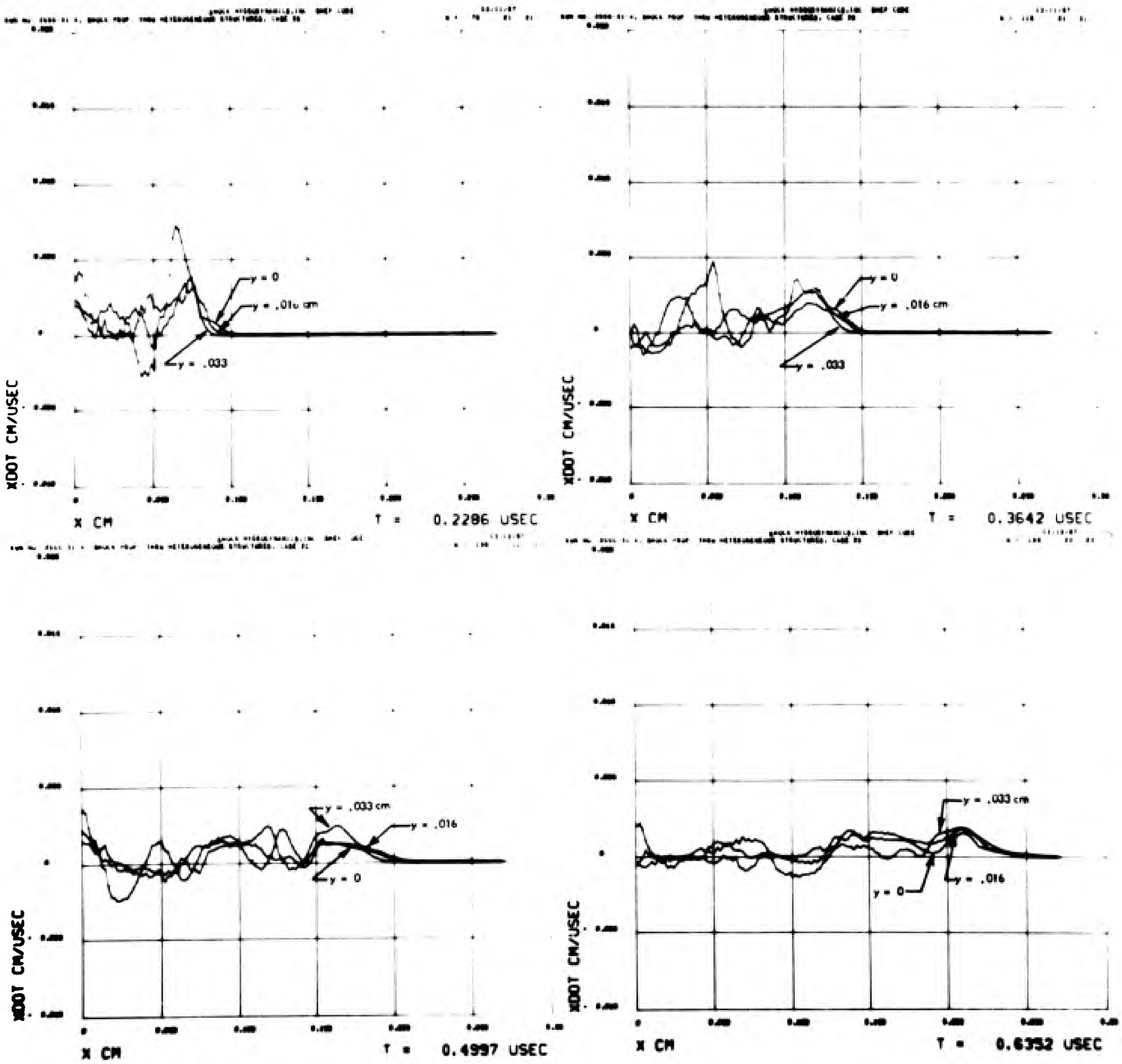

FIGURE 3-65 (cont'd). $\dot{x}$ vs x AT THREE LATERAL POSITIONS, CASE 2D.

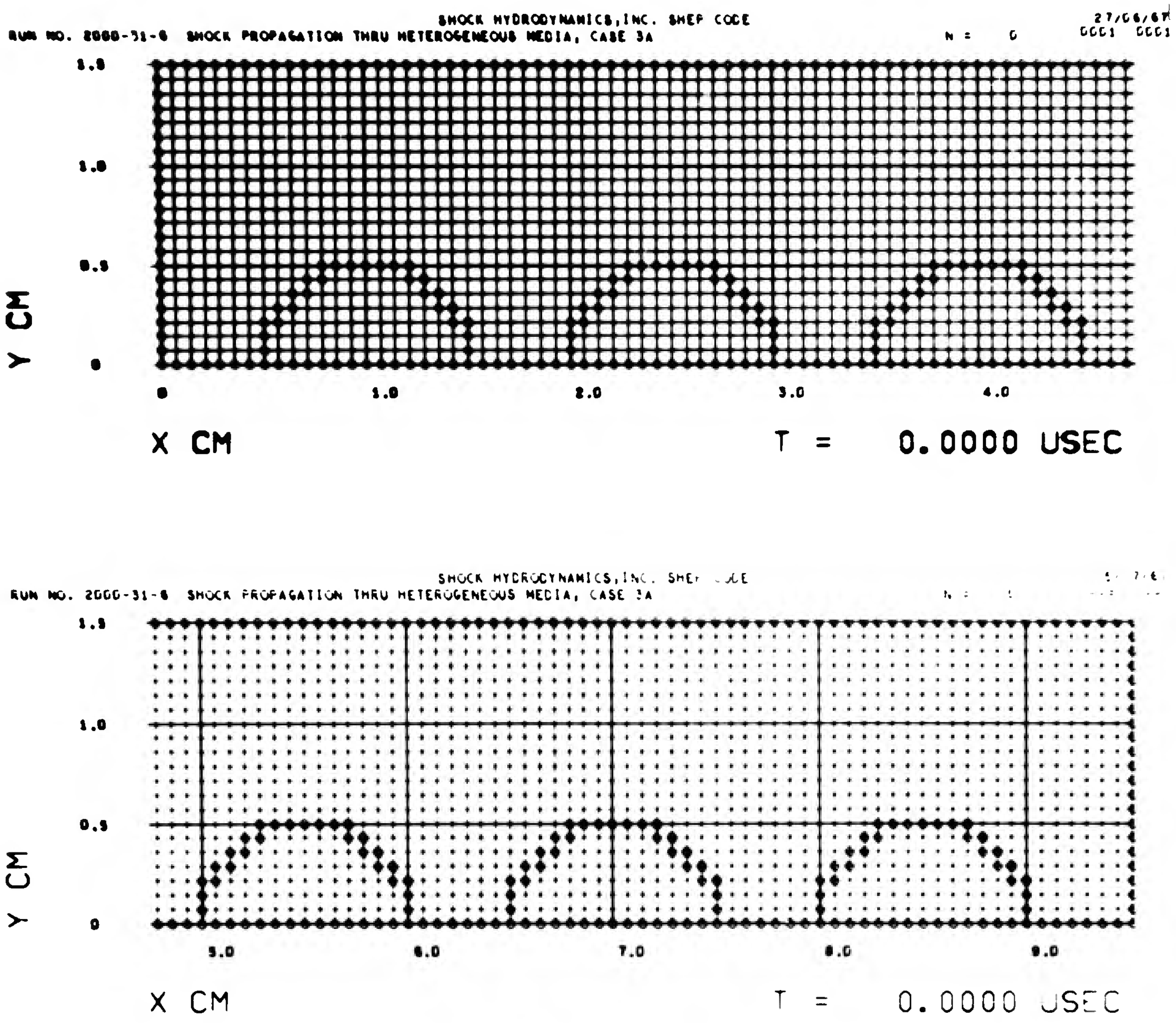

FIGURE 3-66. LAGRANGIAN MESH, CASE 3A.

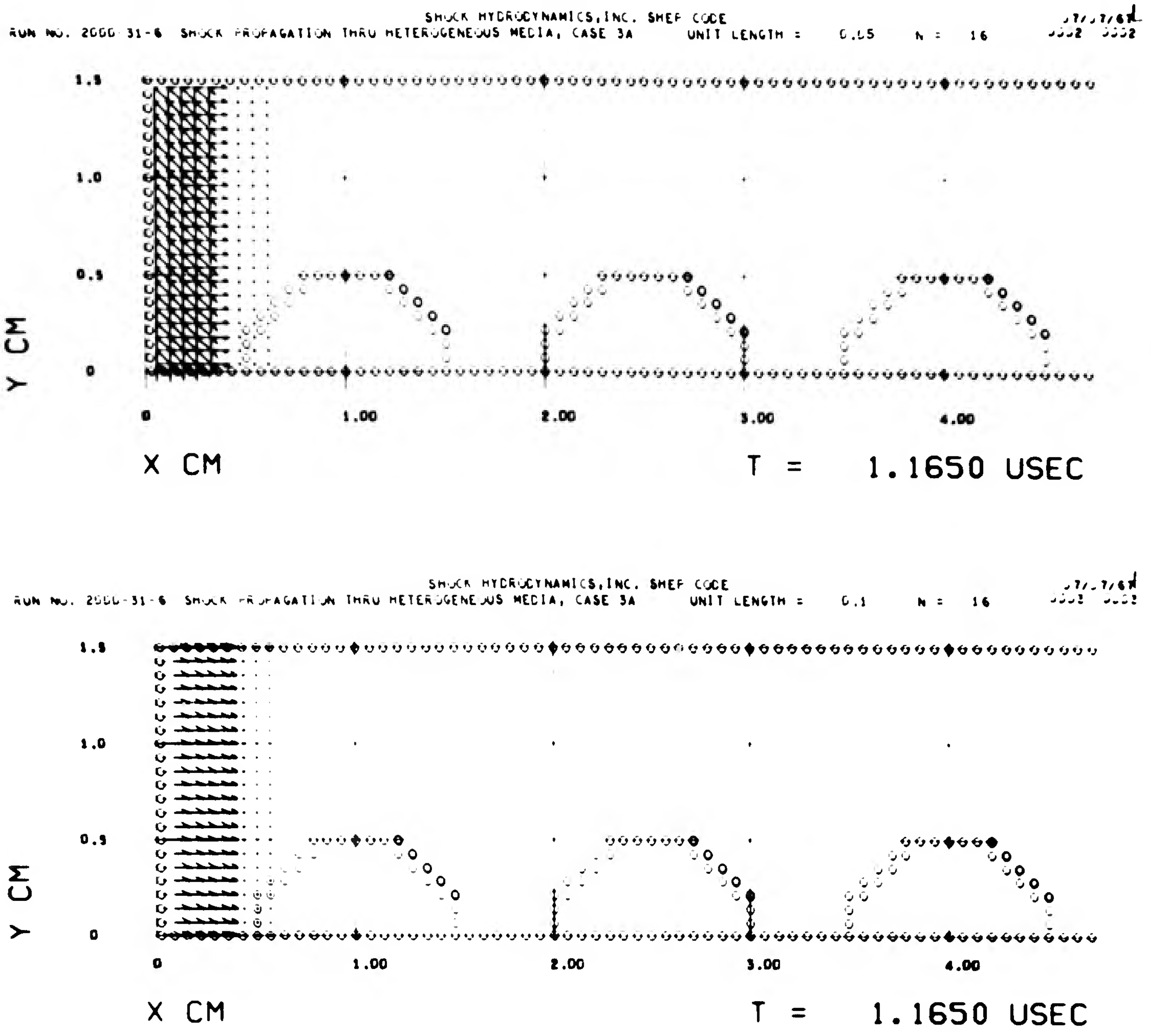

FIGURE 3-67. PRINCIPAL STRESS AND PARTICLE VELOCITY FIELDS, CASE 3A, $t = 1.165 \mu$ sec.

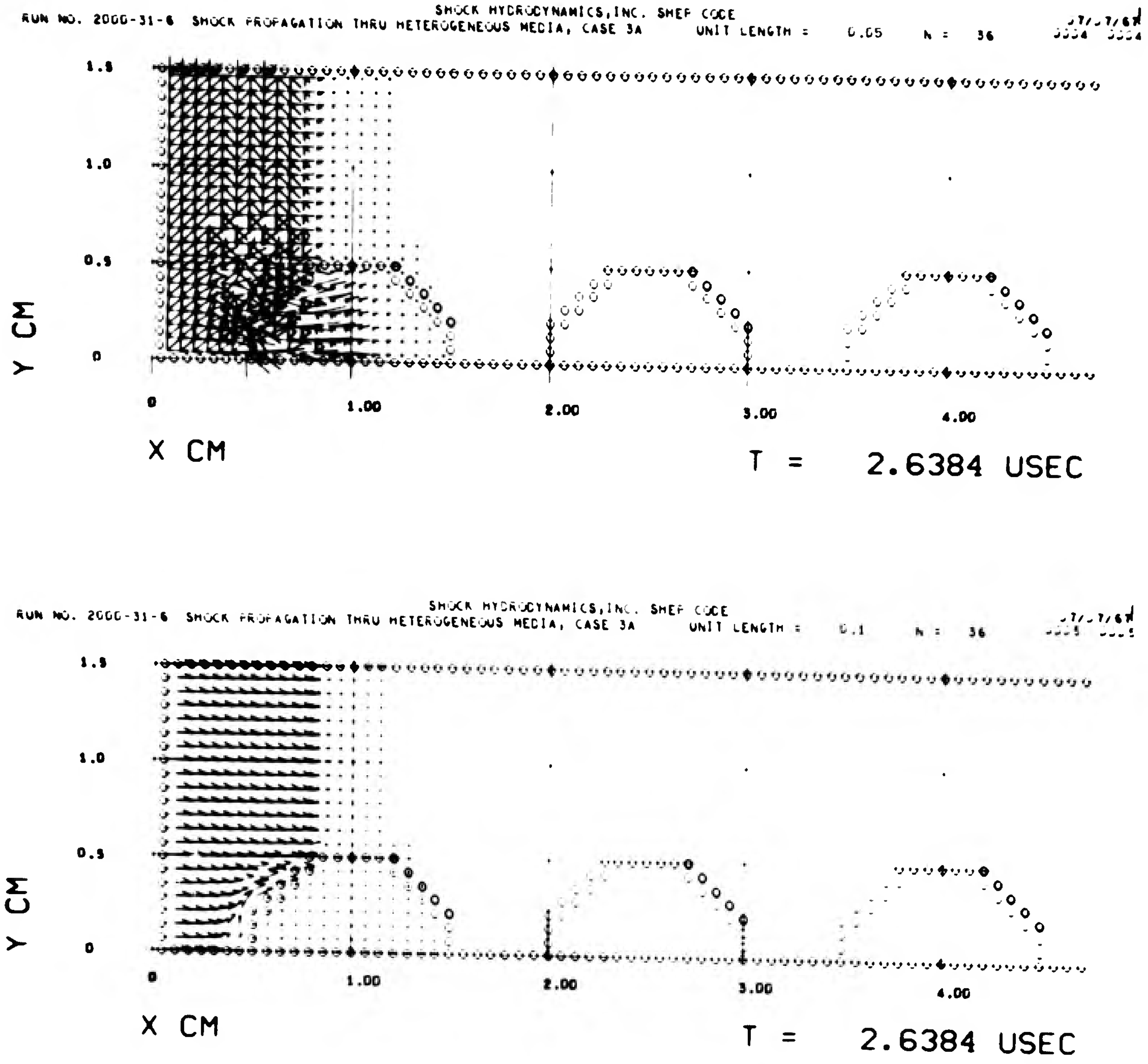

FIGURE 3-68. PRINCIPAL STRESS AND PARTICLE VELOCITY FIELDS, CASE 3A, $t = 2.638 \mu$ sec.

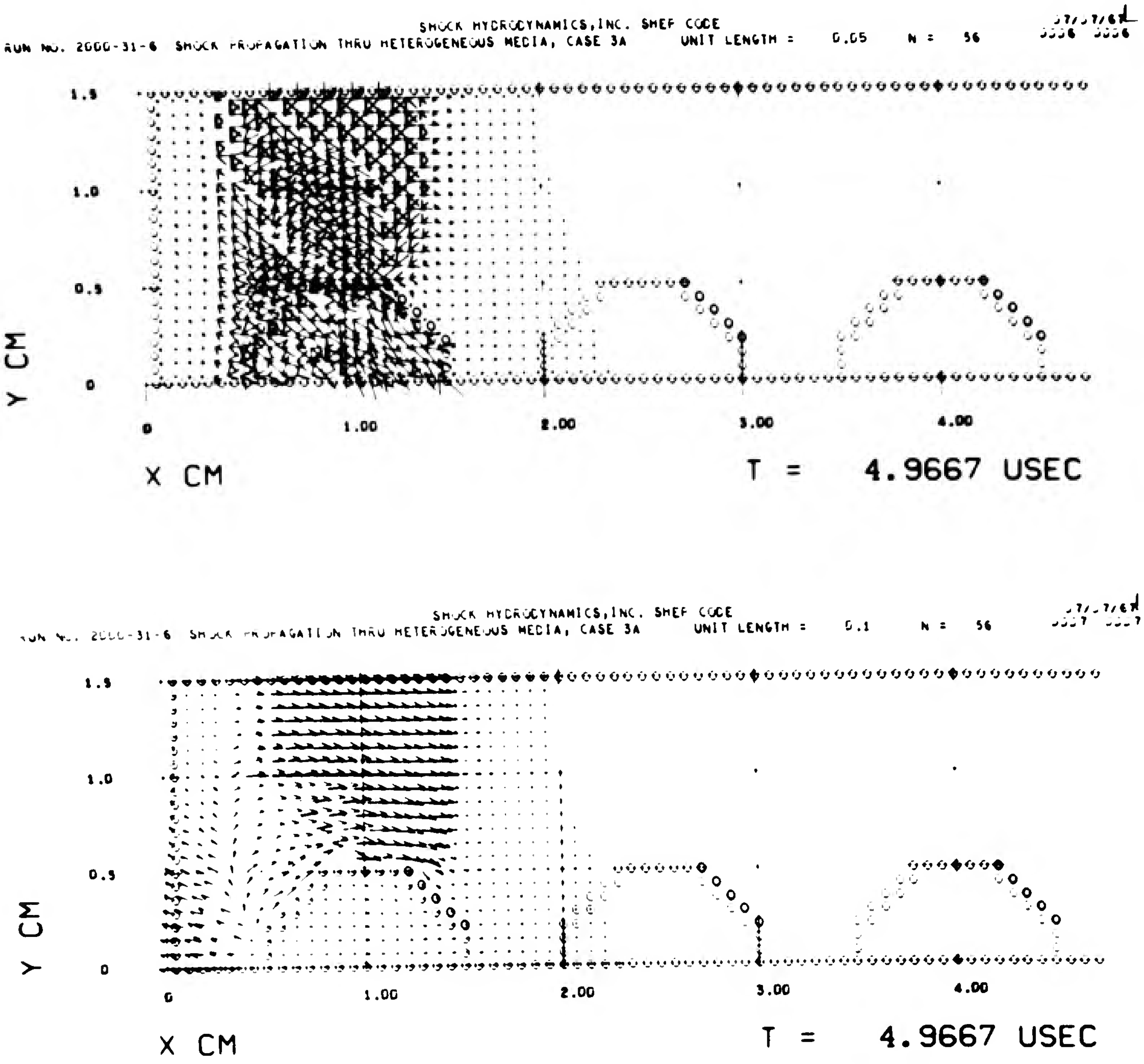

FIGURE 3-69. PRINCIPAL STRESS AND PARTICLE VELOCITY FIELDS, CASE 3A, t = 4.967μ sec.

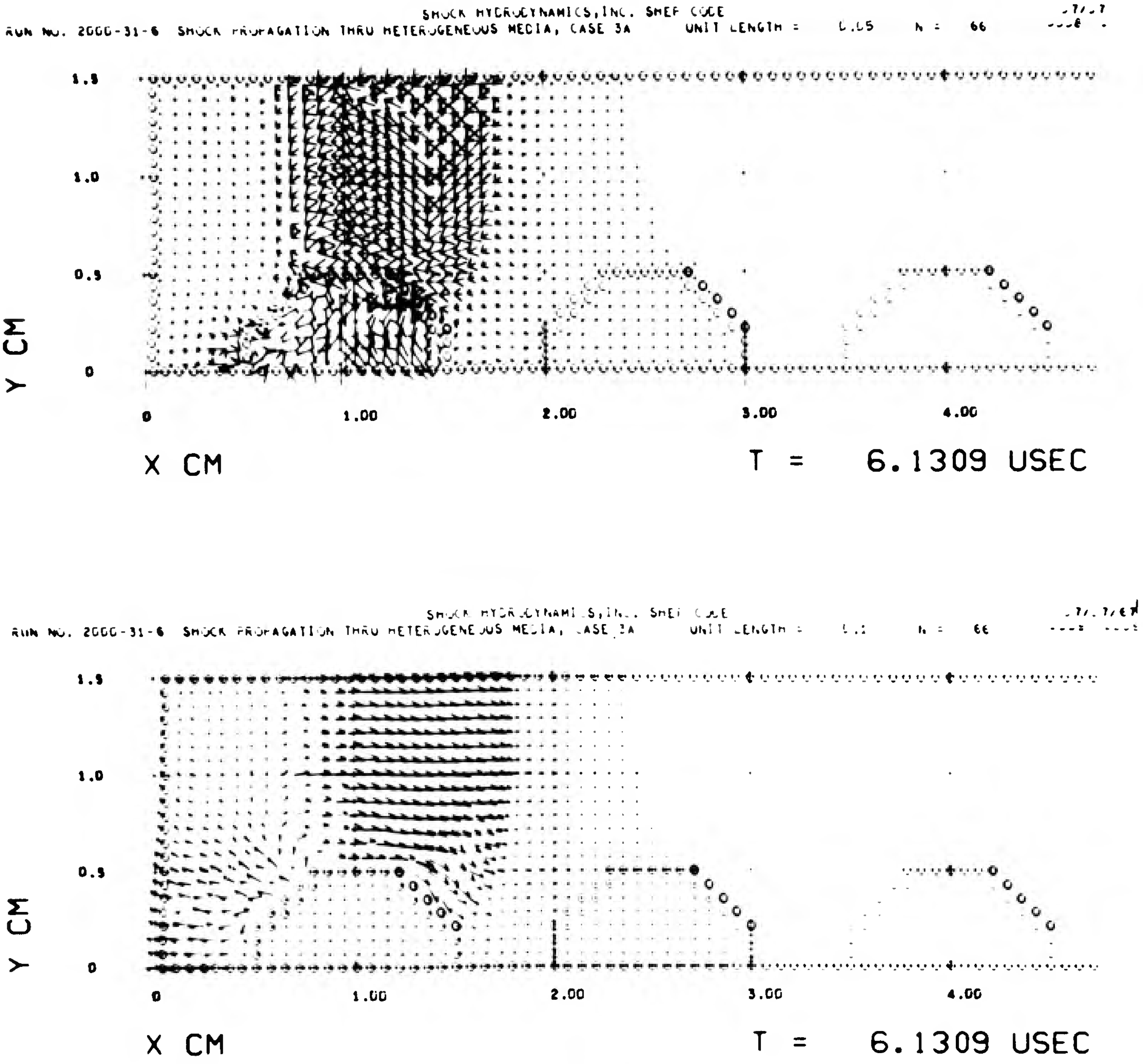

FIGURE 3-70. PRINCIPAL STRESS AND PARTICLE VELOCITY FIELDS, CASE 3A, t = 6.131 μ sec.

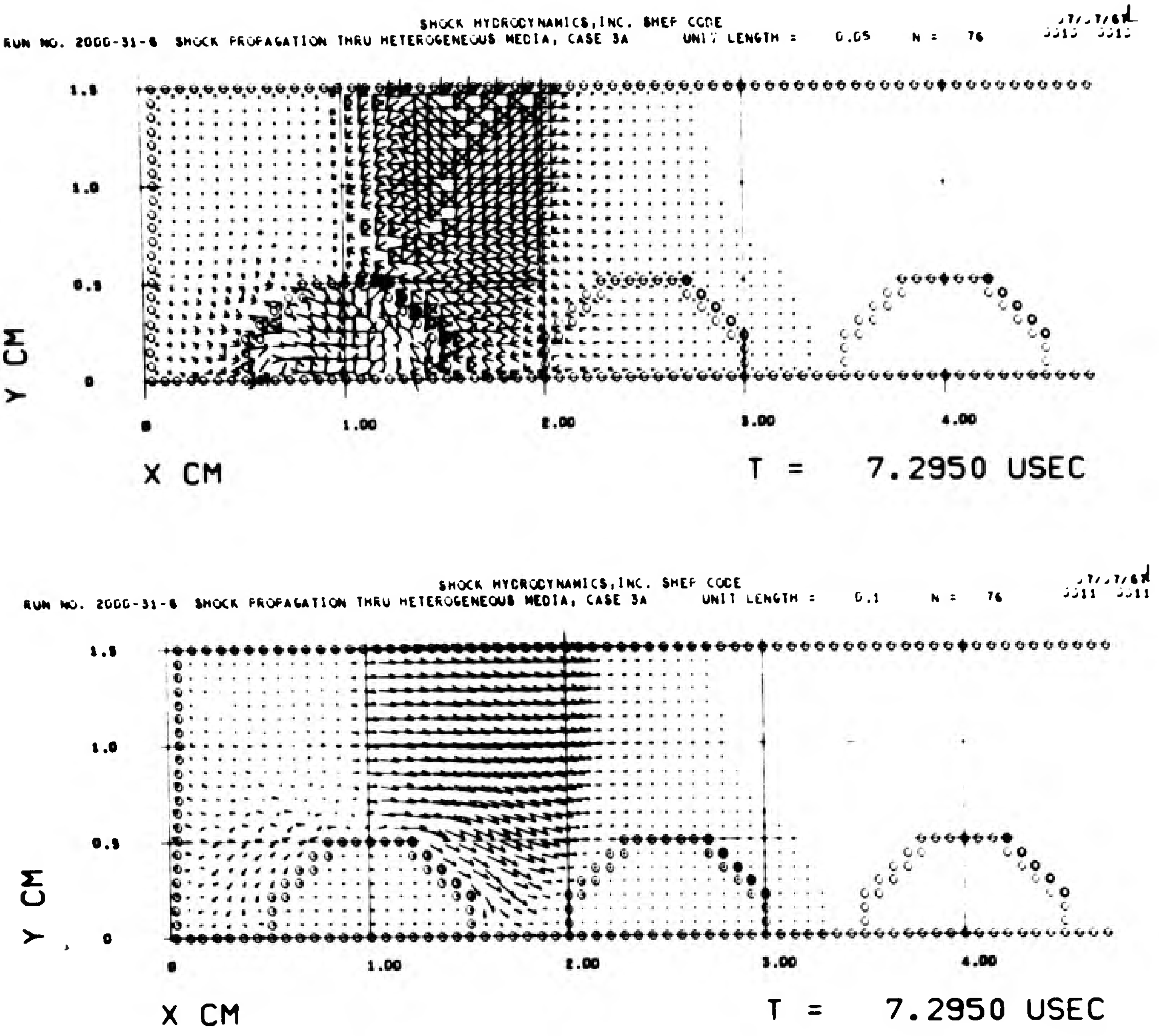

FIGURE 3-71. PRINCIPAL STRESS AND PARTICLE VELOCITY FIELDS, CASE 3A, $t = 7.295 \mu$ sec.

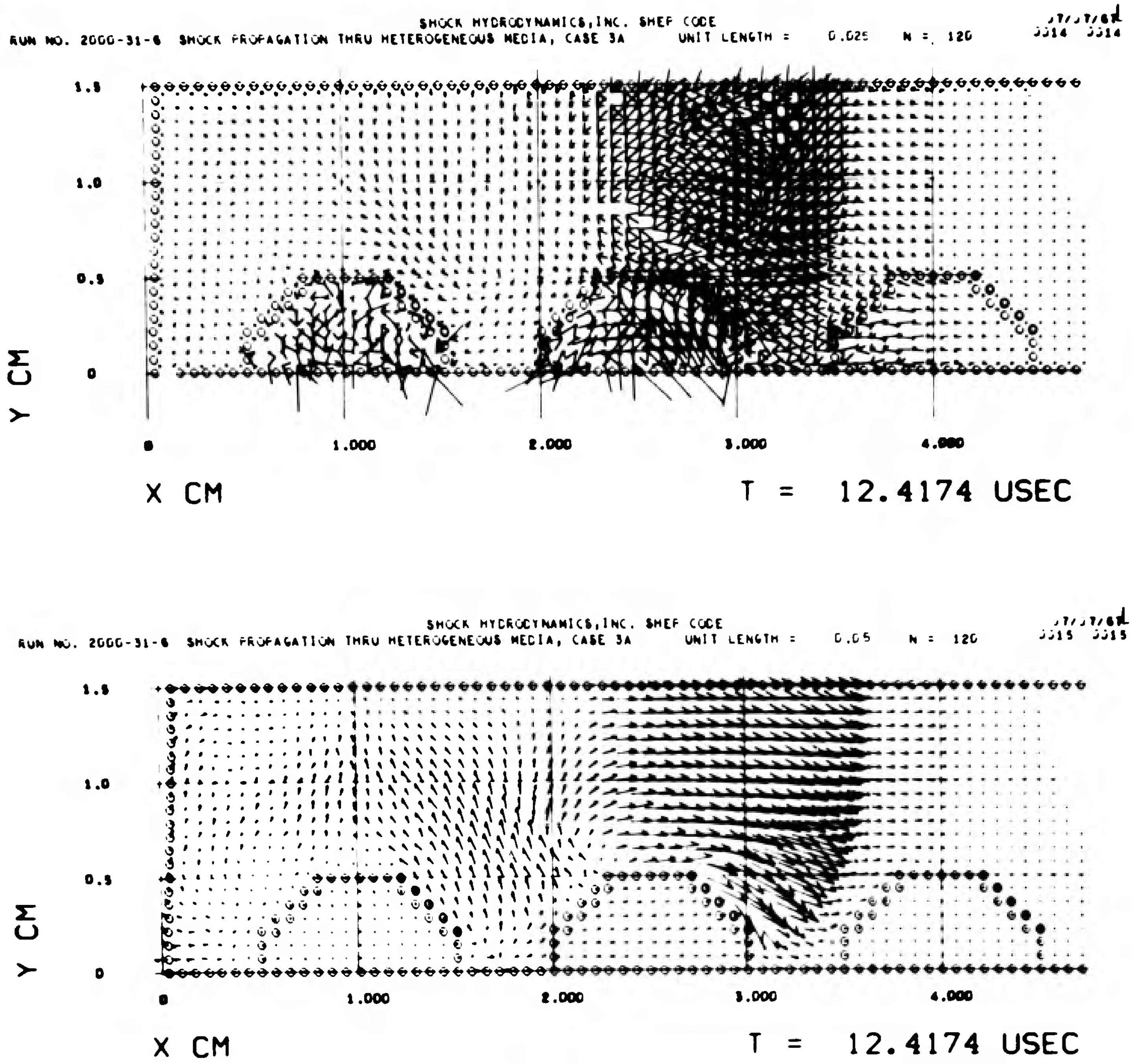

FIGURE 3-72. PRINCIPAL STRESS AND PARTICLE VELOCITY FIELDS, CASE 3A, t = 12.42 μ sec.

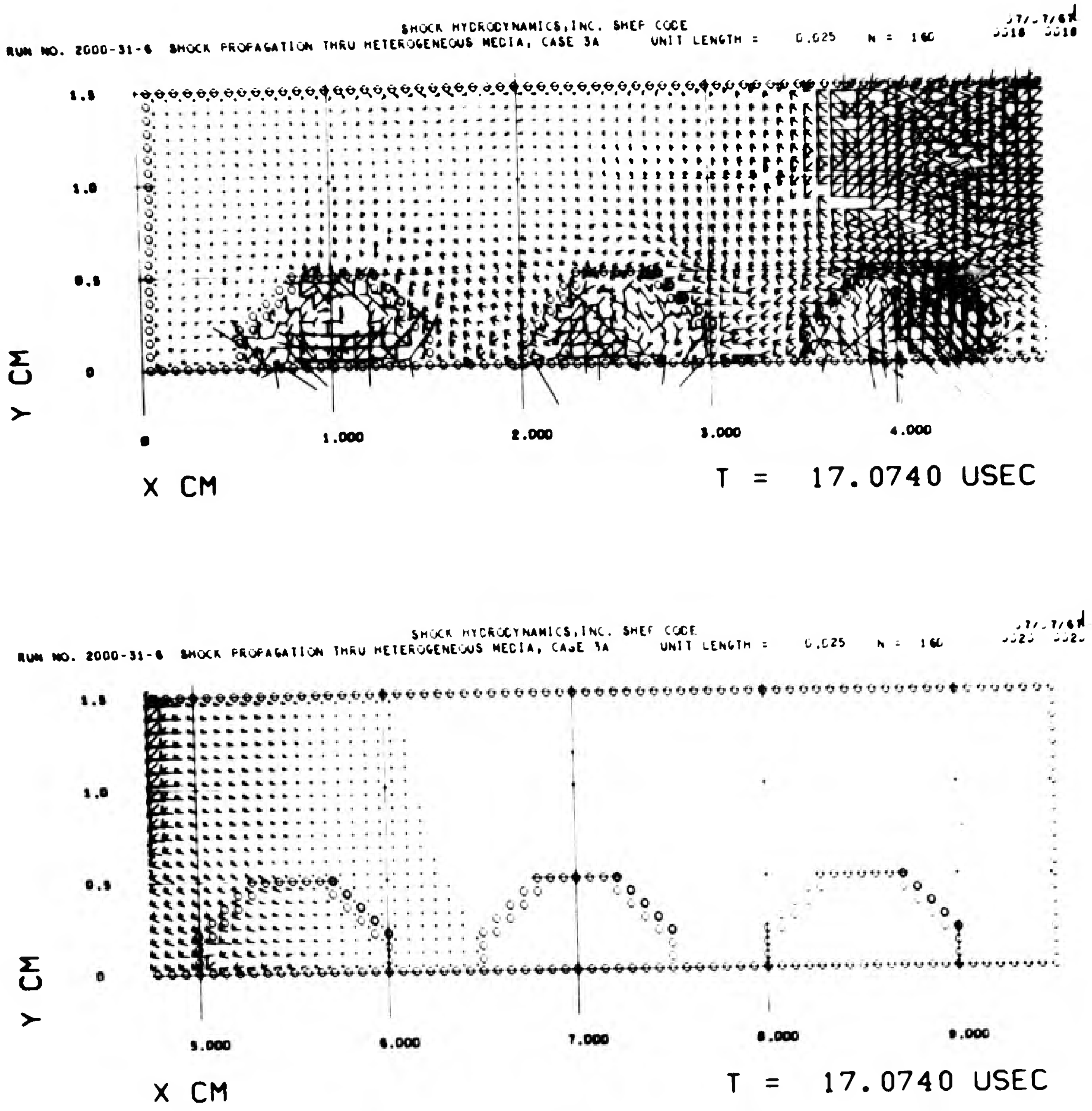

FIGURE 3-73. PRINCIPAL STRESS FIELD, CASE 3A, t = 17.07μ sec.

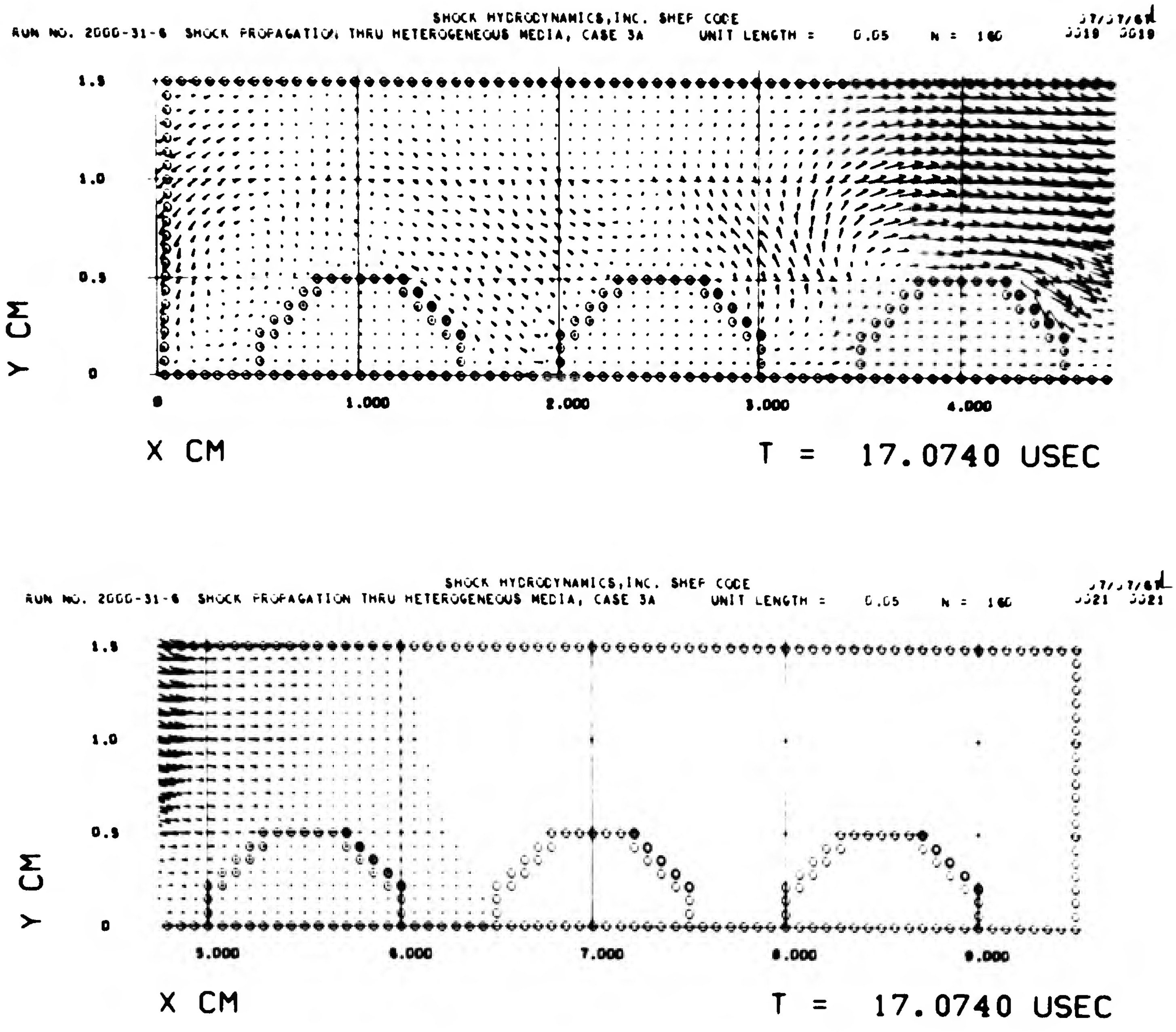

FIGURE 3-74. PARTICLE VELOCITY FIELD, CASE 3A, t = 17.07μ sec.

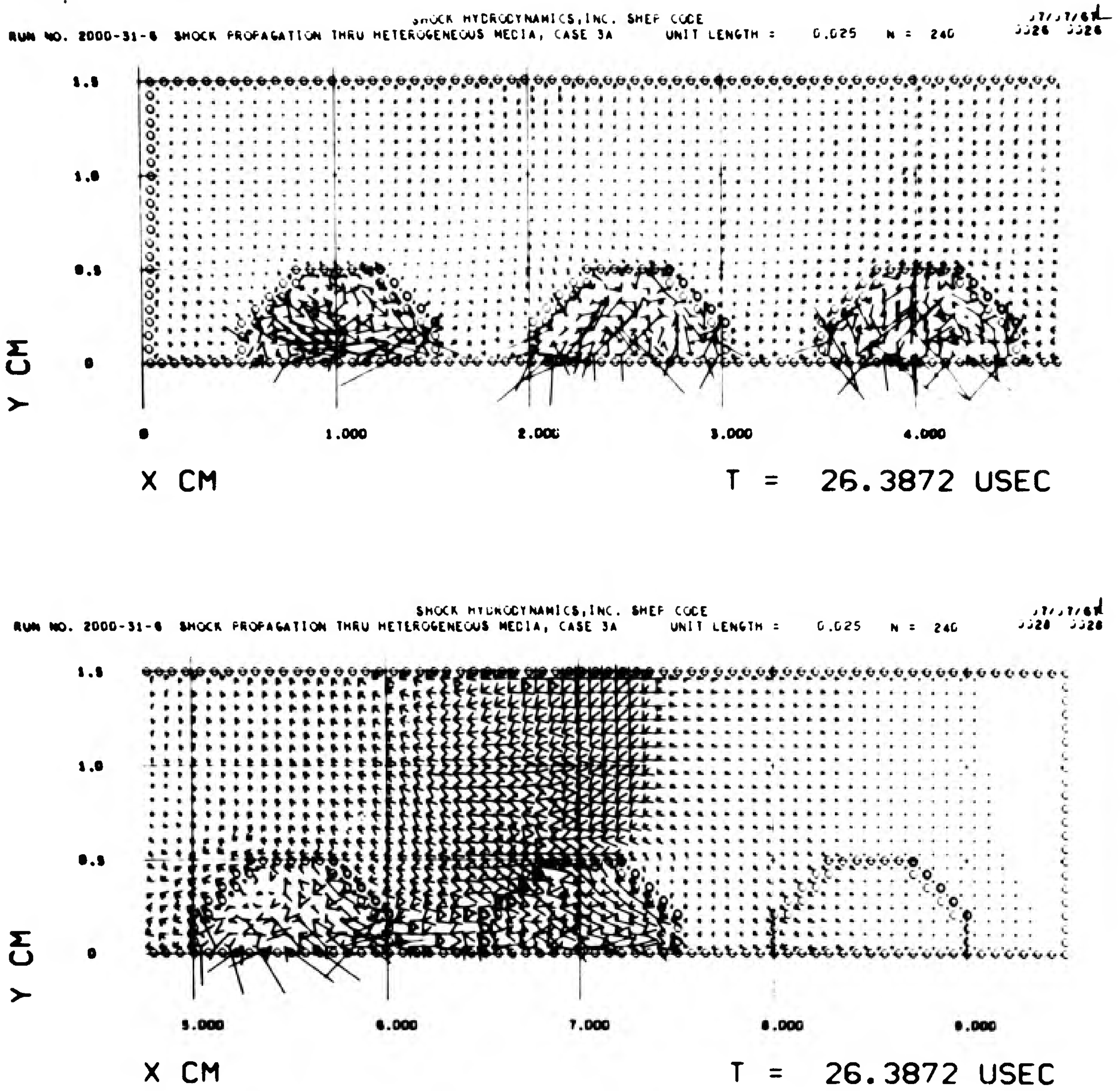

FIGURE 3-75. PRINCIPAL STRESS FIELD, CASE 3A, $t = 26.39 \mu$ sec.

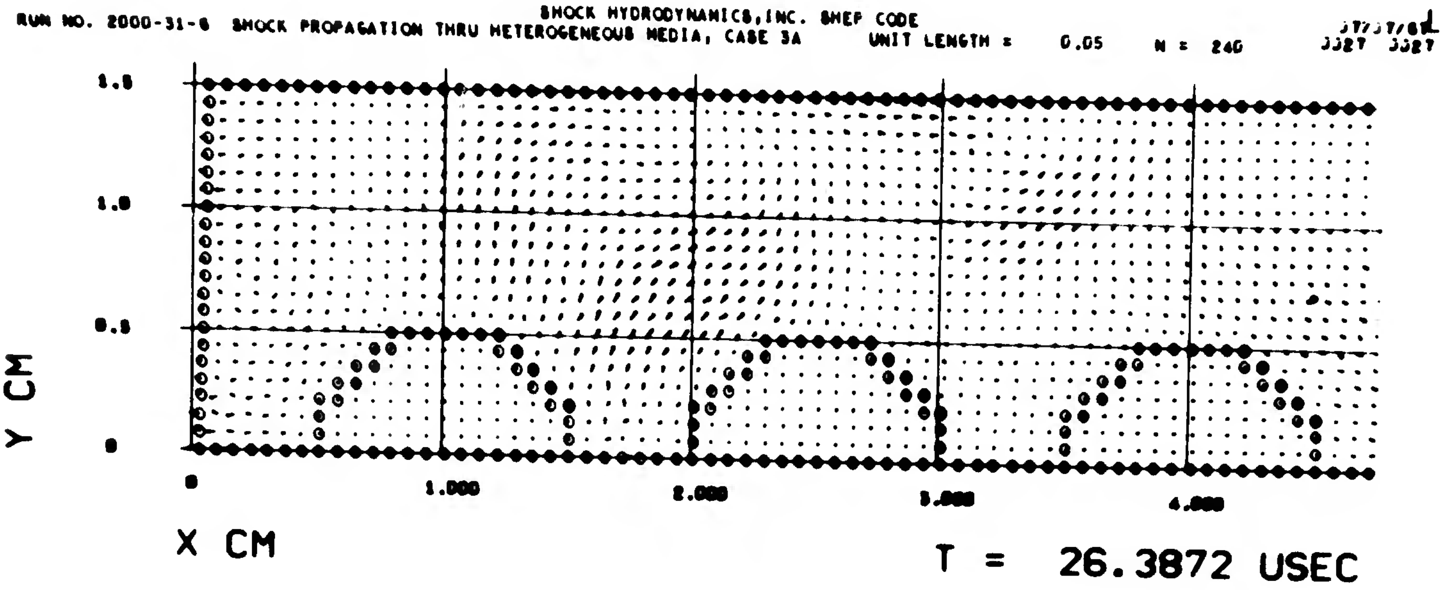

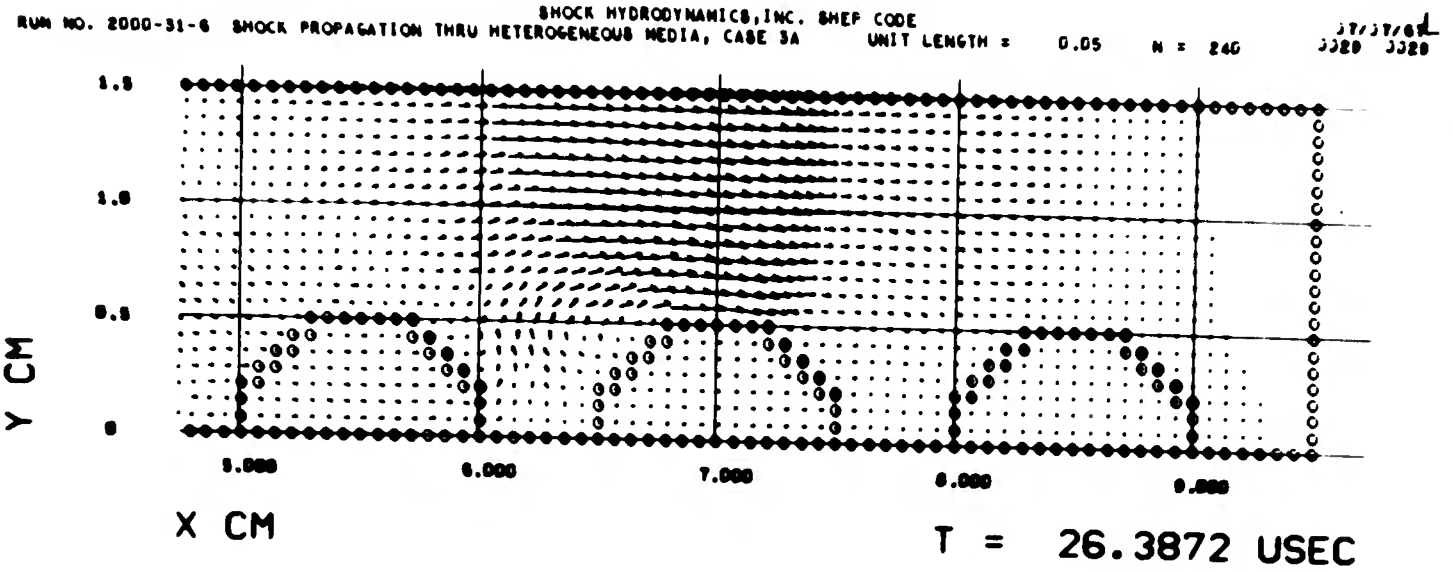

FIGURE 3-76. PARTICLE VELOCITY FIELD, CASE 3A, t = 26.39μ sec.

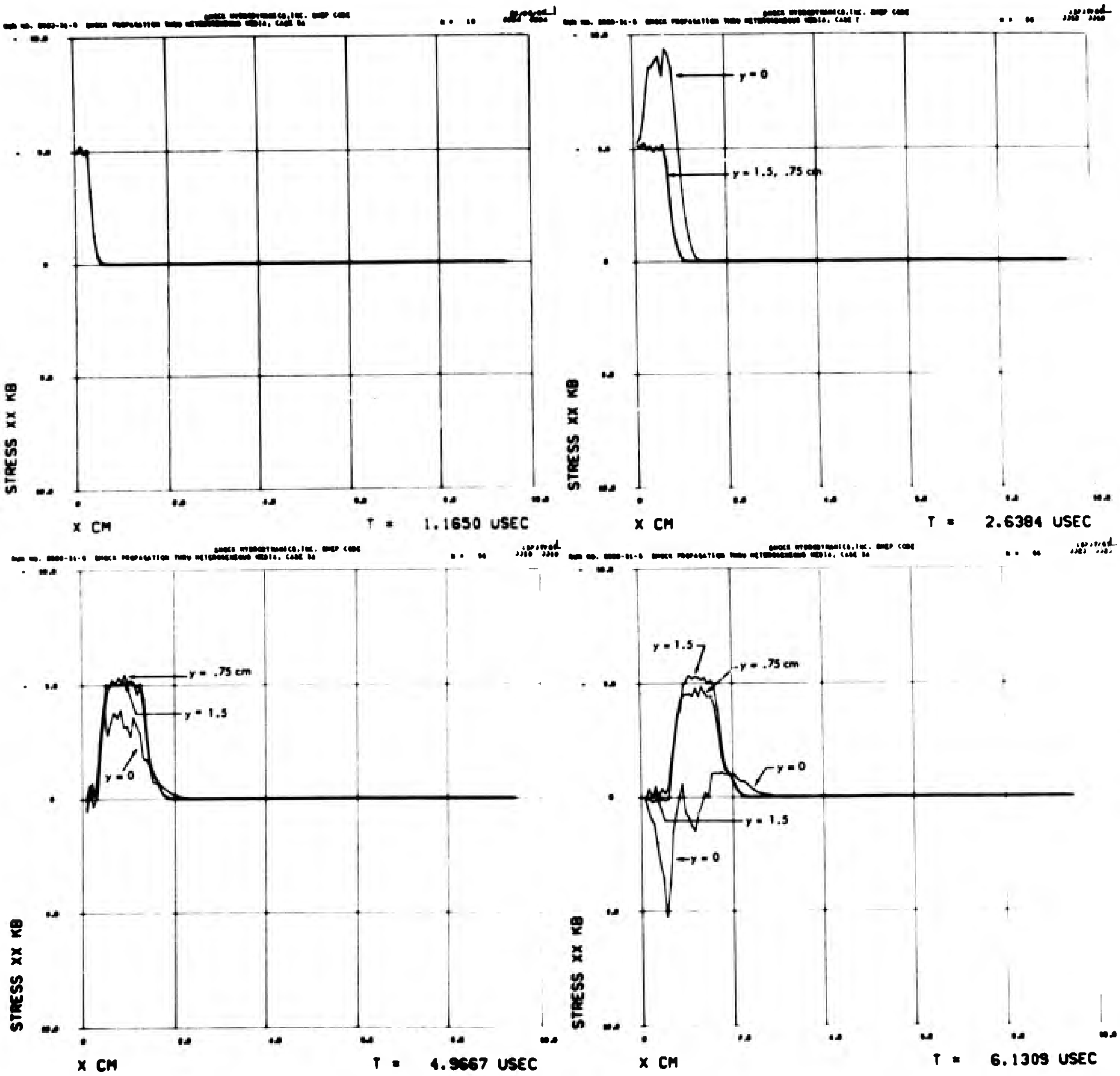

FIGURE 3-77. σ_x vs x AT THREE RADIAL POSITIONS,
CASE 3A.

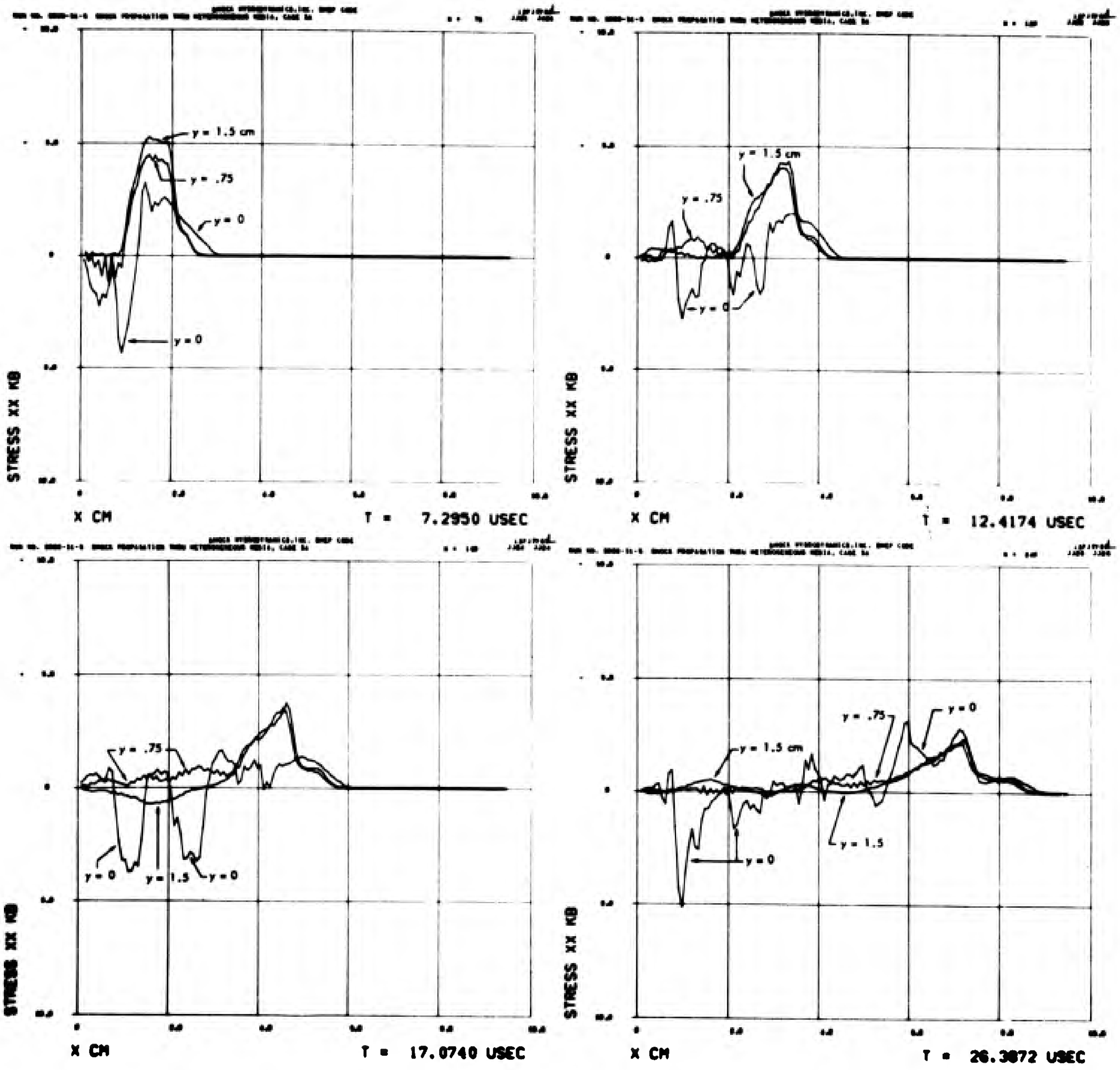

FIGURE 3-77 (cont'd). σ_x vs x AT THREE RADIAL POSITIONS, CASE 3A.

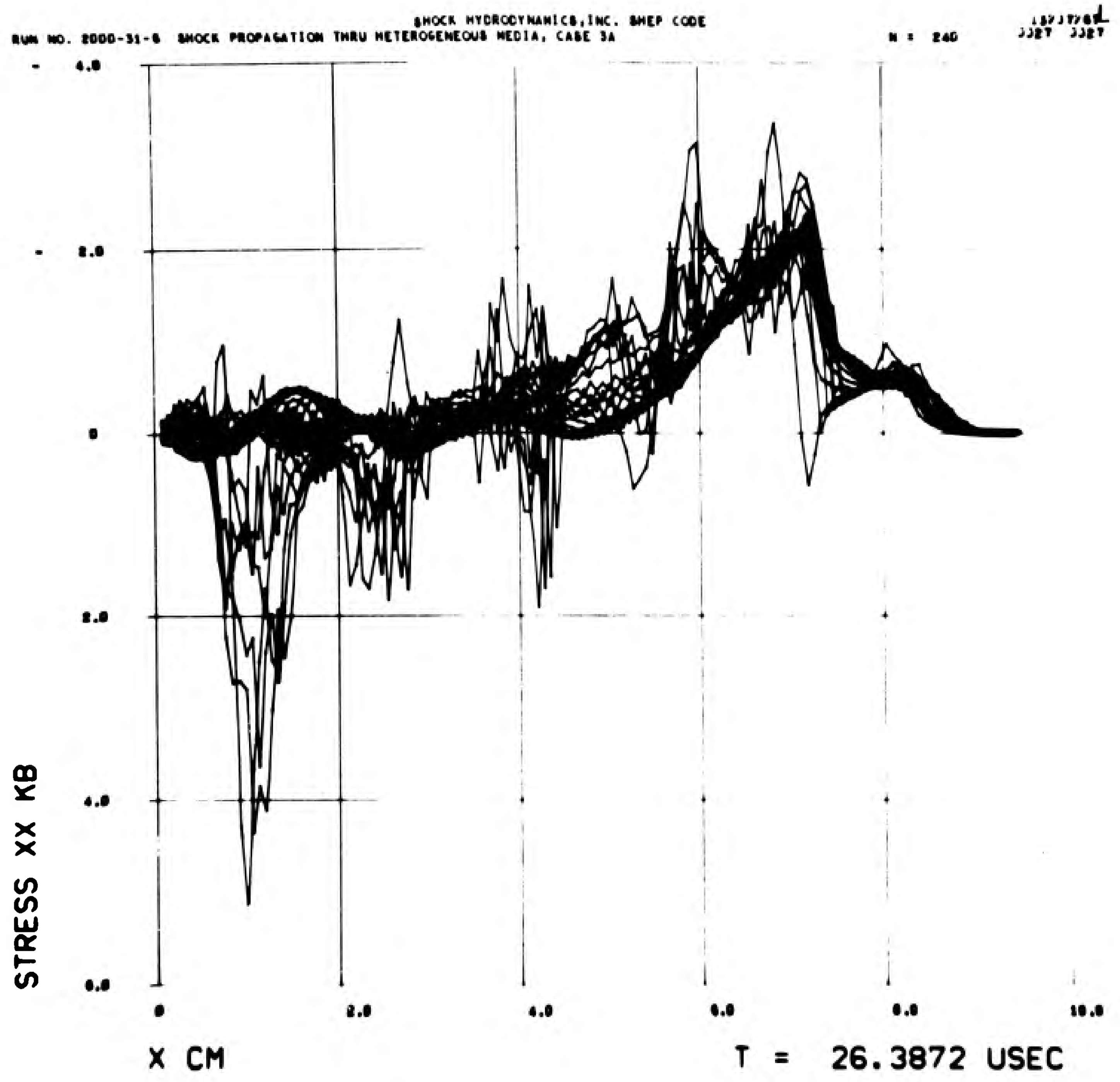

FIGURE 3-78. σ_x vs x AT ALL RADIAL MESH POSITIONS, CASE 3A.

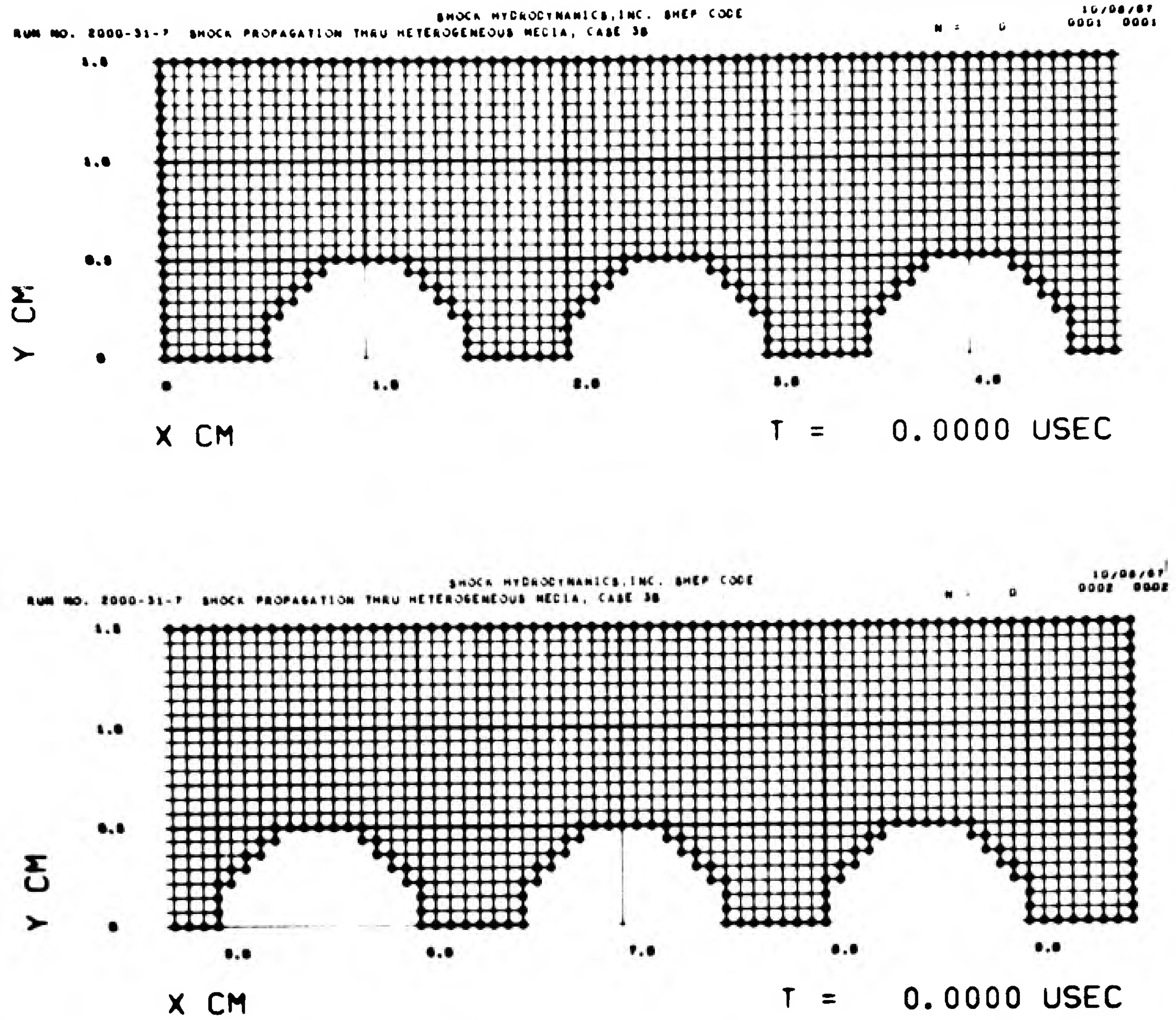

FIGURE 3-79. LAGRANGIAN MESH, CASE 3B.

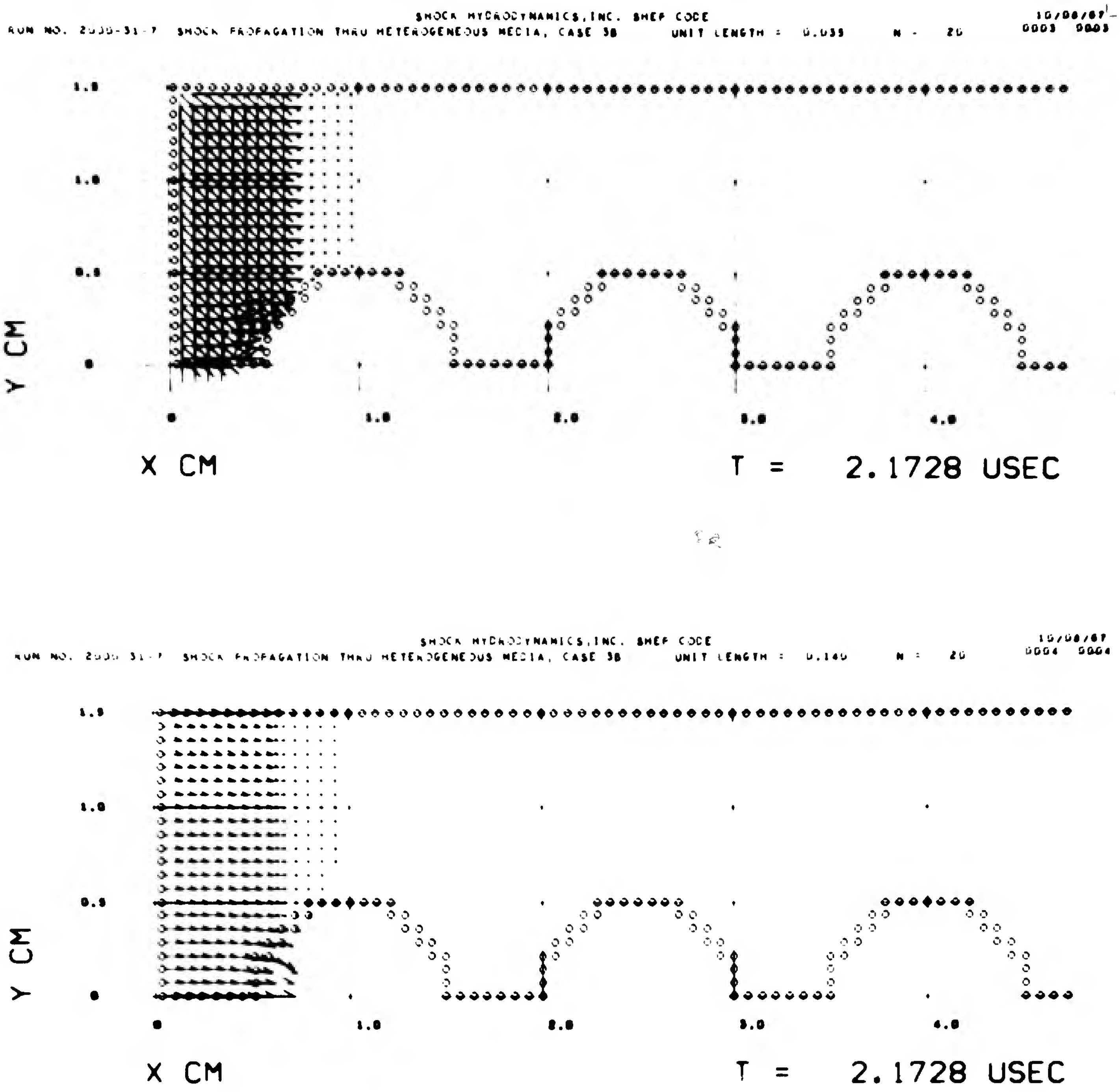

FIGURE 3-80. PRINCIPAL STRESS AND PARTICLE VELOCITY FIELDS, CASE 3B, t = 2.173μ sec.

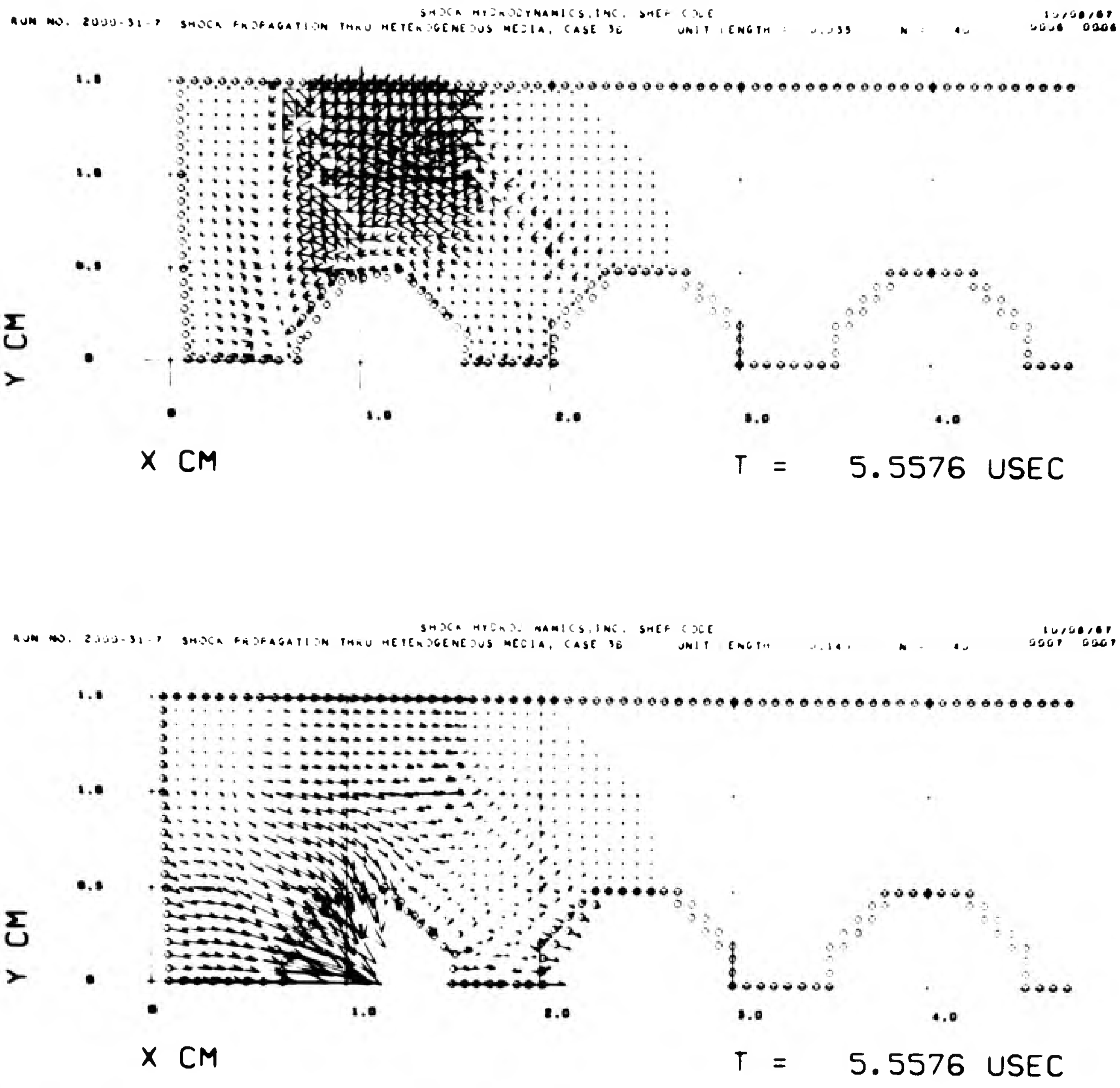

FIGURE 3-81. PRINCIPAL STRESS AND PARTICLE VELOCITY FIELDS, CASE 3B, t = 5.558 μ sec.

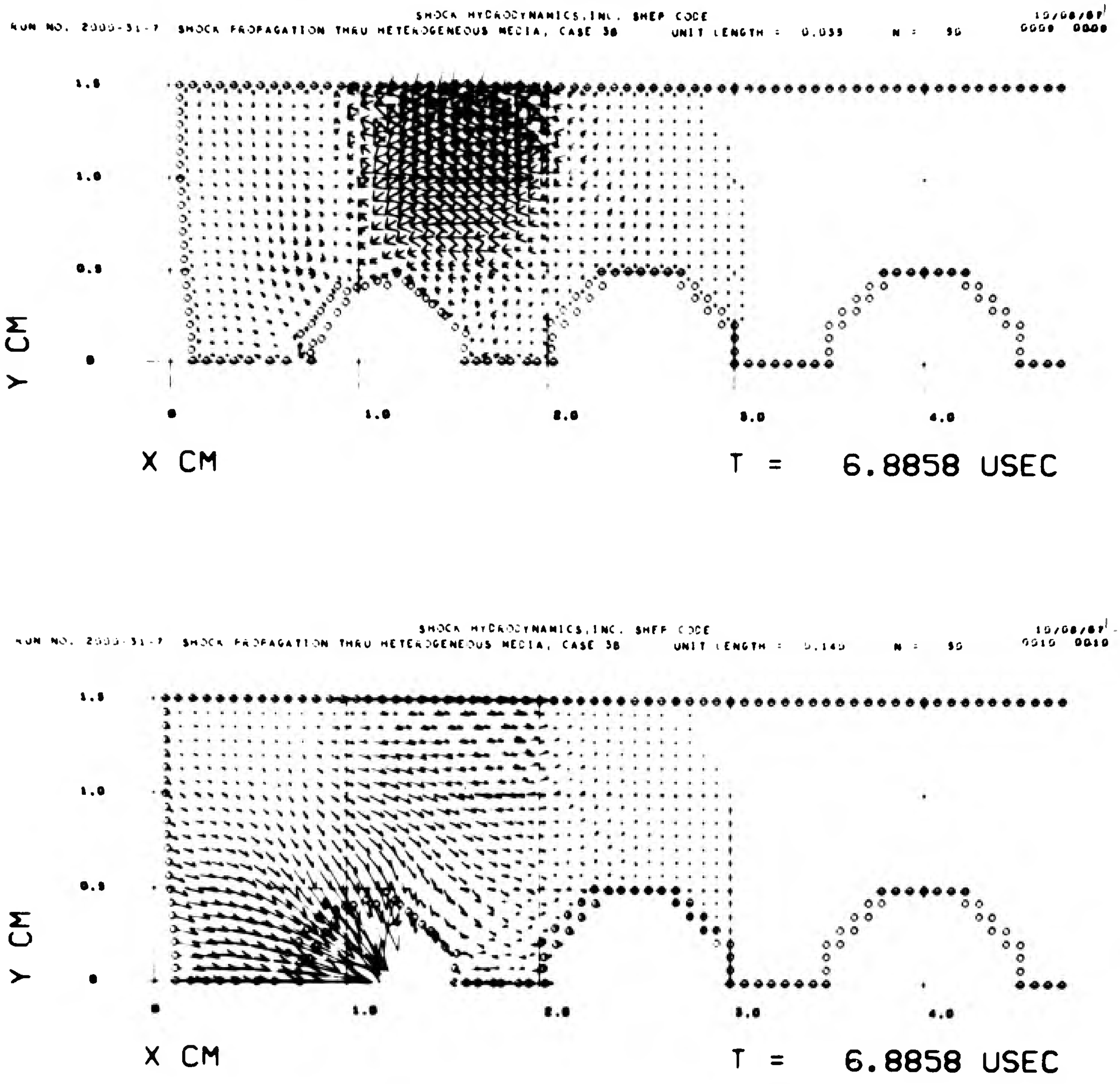

FIGURE 3-82. PRINCIPAL STRESS AND PARTICLE VELOCITY FIELDS, CASE 3B., t = 6.886μ sec.

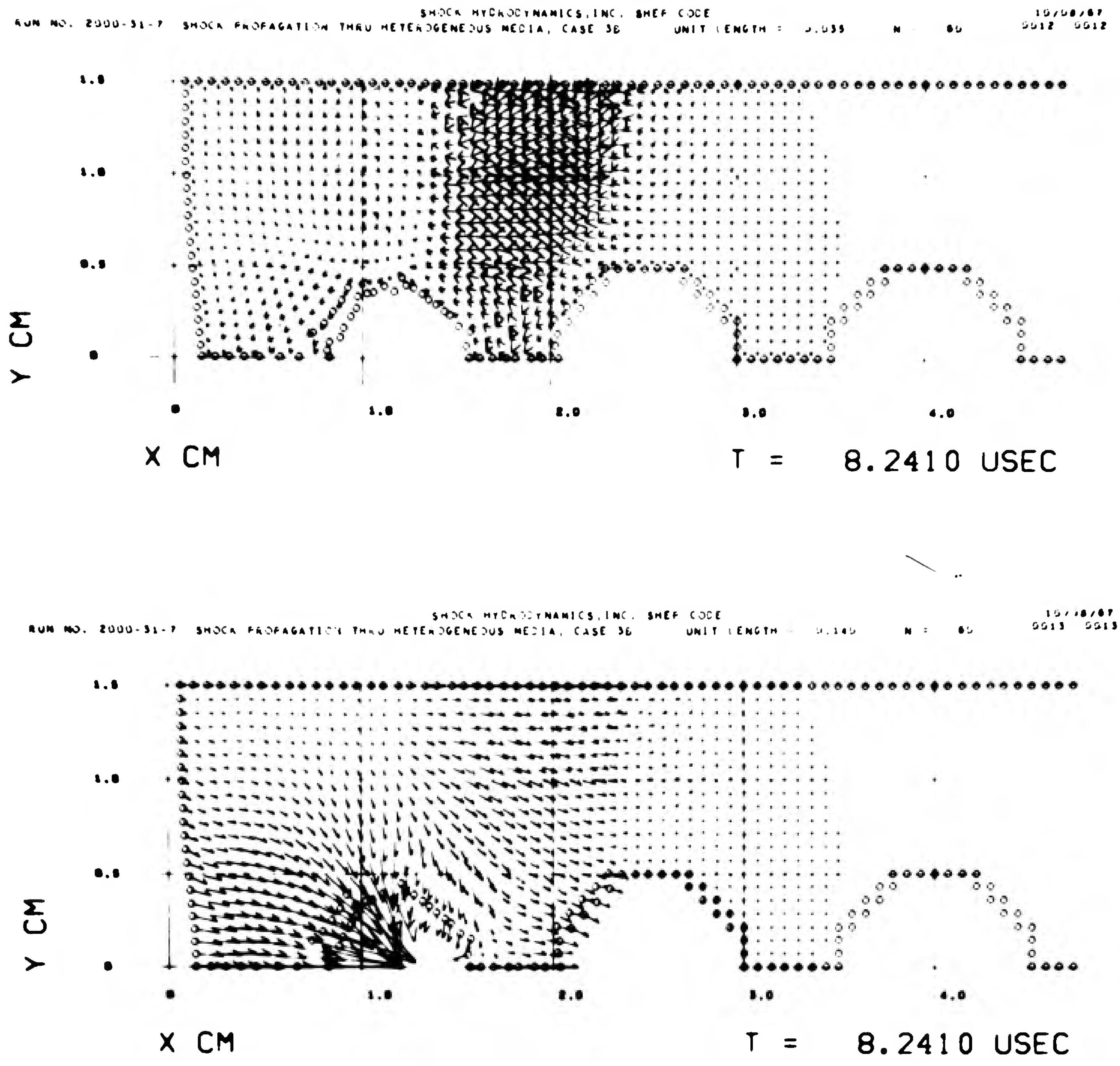

FIGURE 3-83. PRINCIPAL STRESS AND PARTICLE VELOCITY FIELDS, CASE 3B, $t = 8.241 \mu sec$.

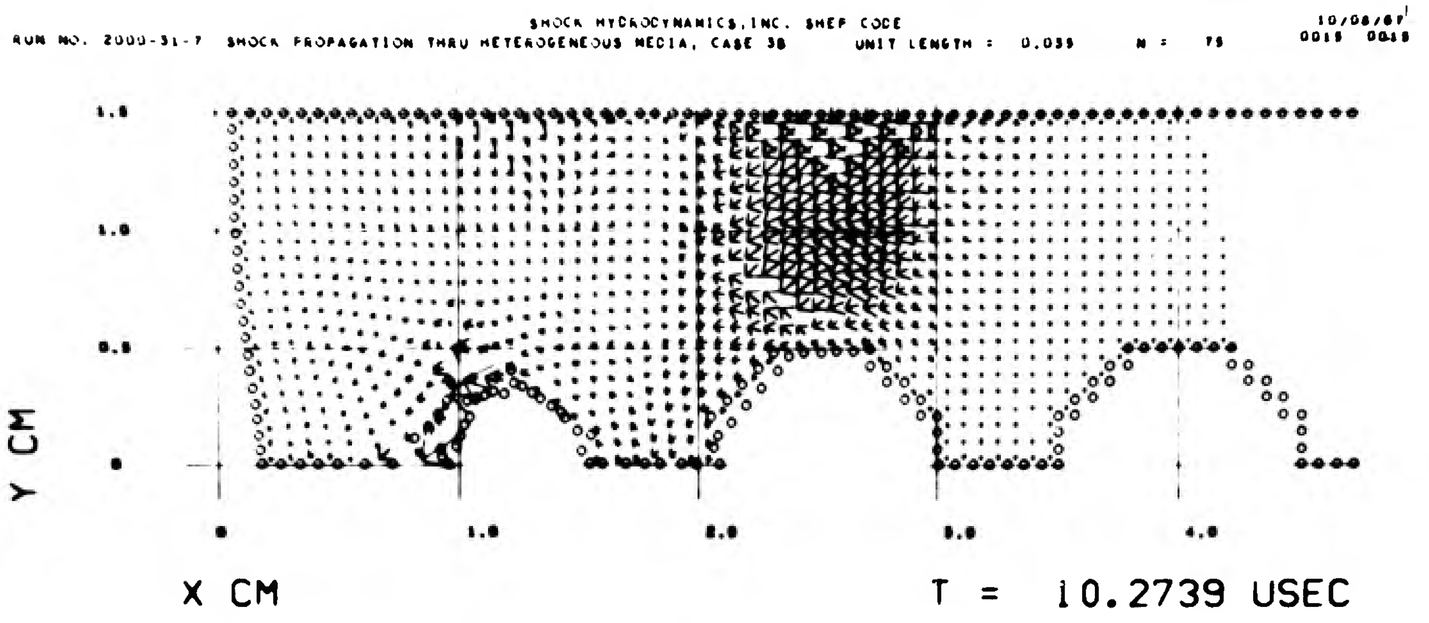

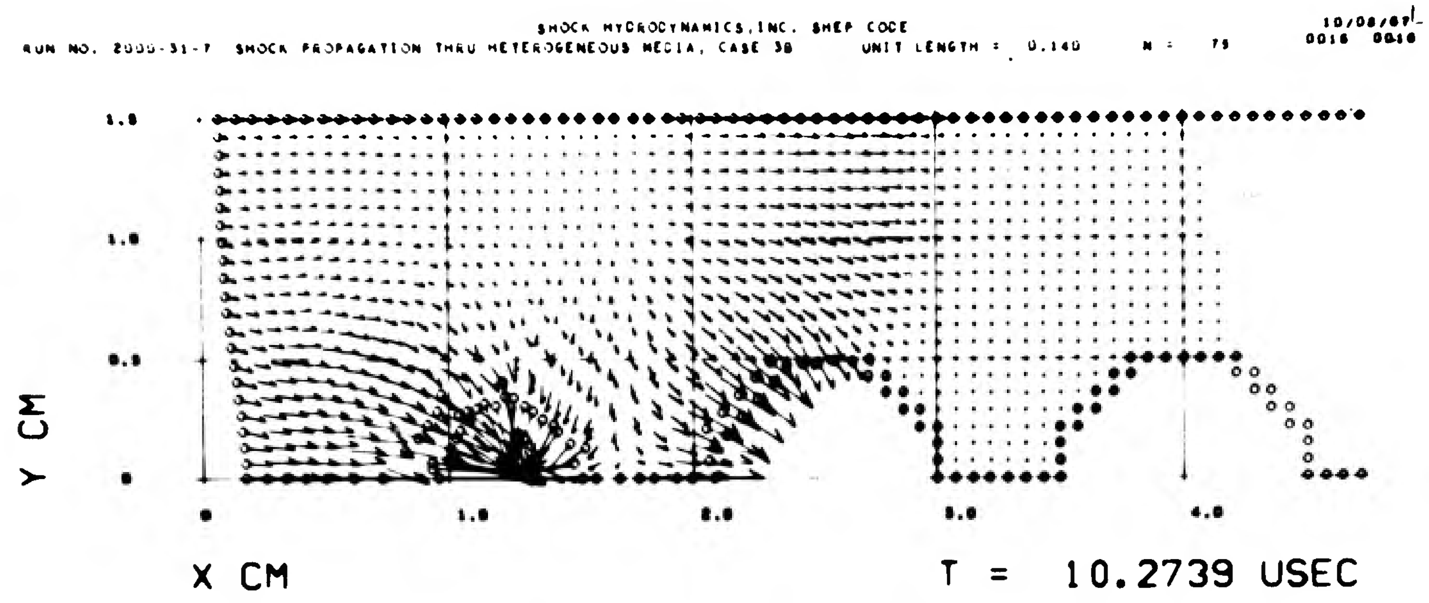

FIGURE 3-84. PRINCIPAL STRESS AND PARTICLE VELOCITY FIELDS, CASE 3B, t = 10.27 μsec.

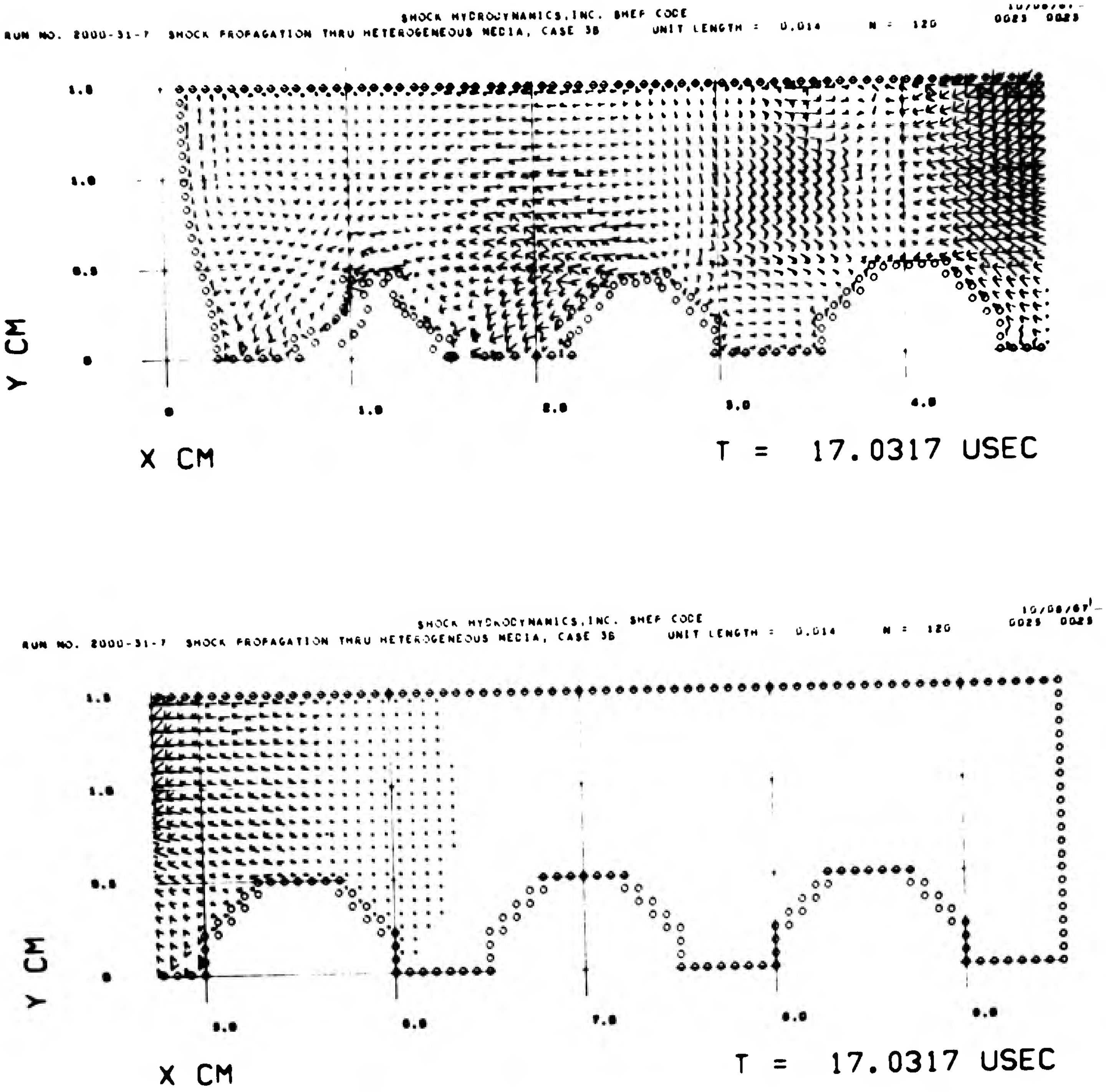

FIGURE 3-85. PRINCIPAL STRESS FIELD, CASE 3B, t = 17.03μ sec.

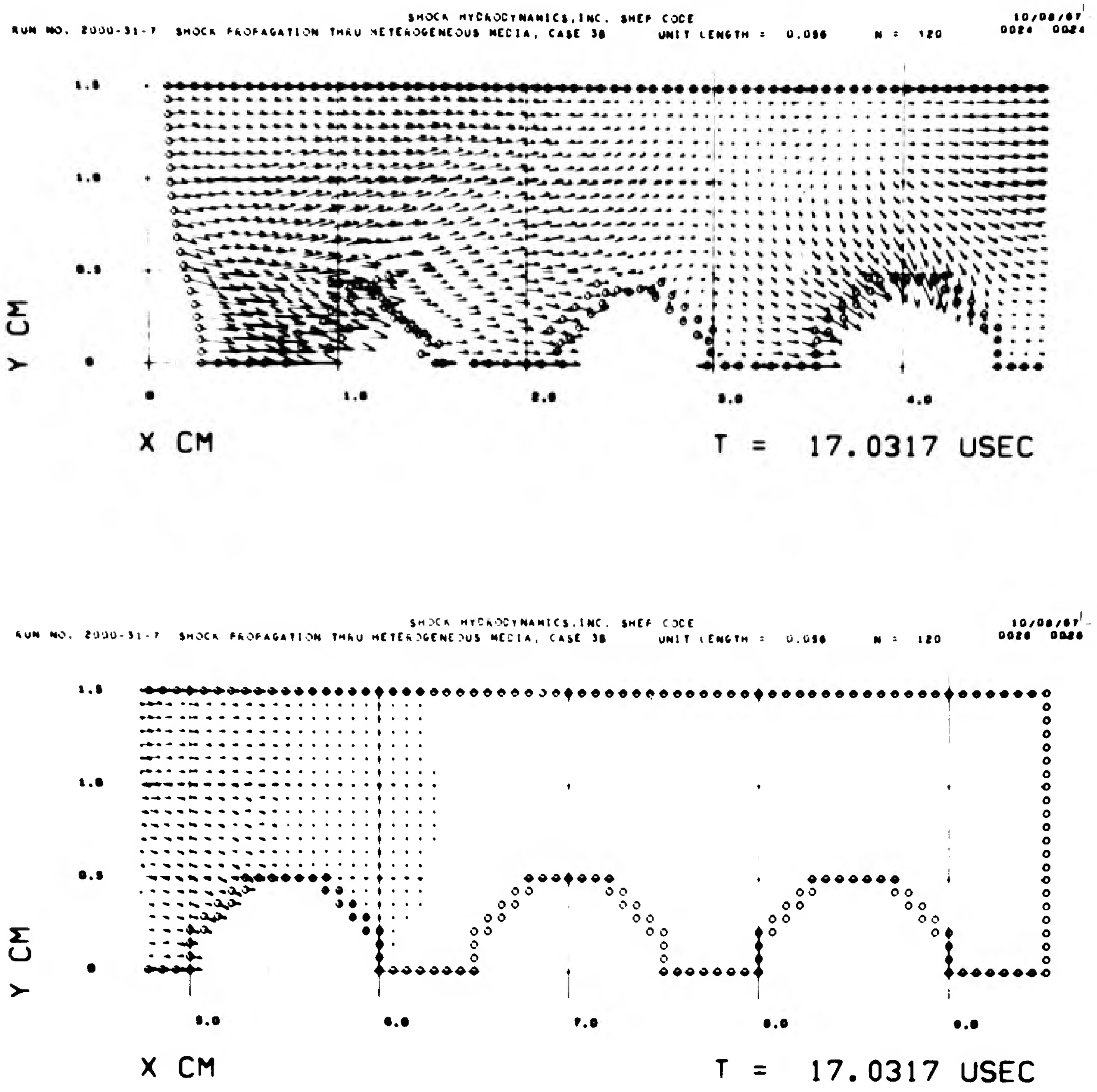

FIGURE 3-86. PARTICLE VELOCITY FIELD, CASE 3B, t = 17.03μ sec.

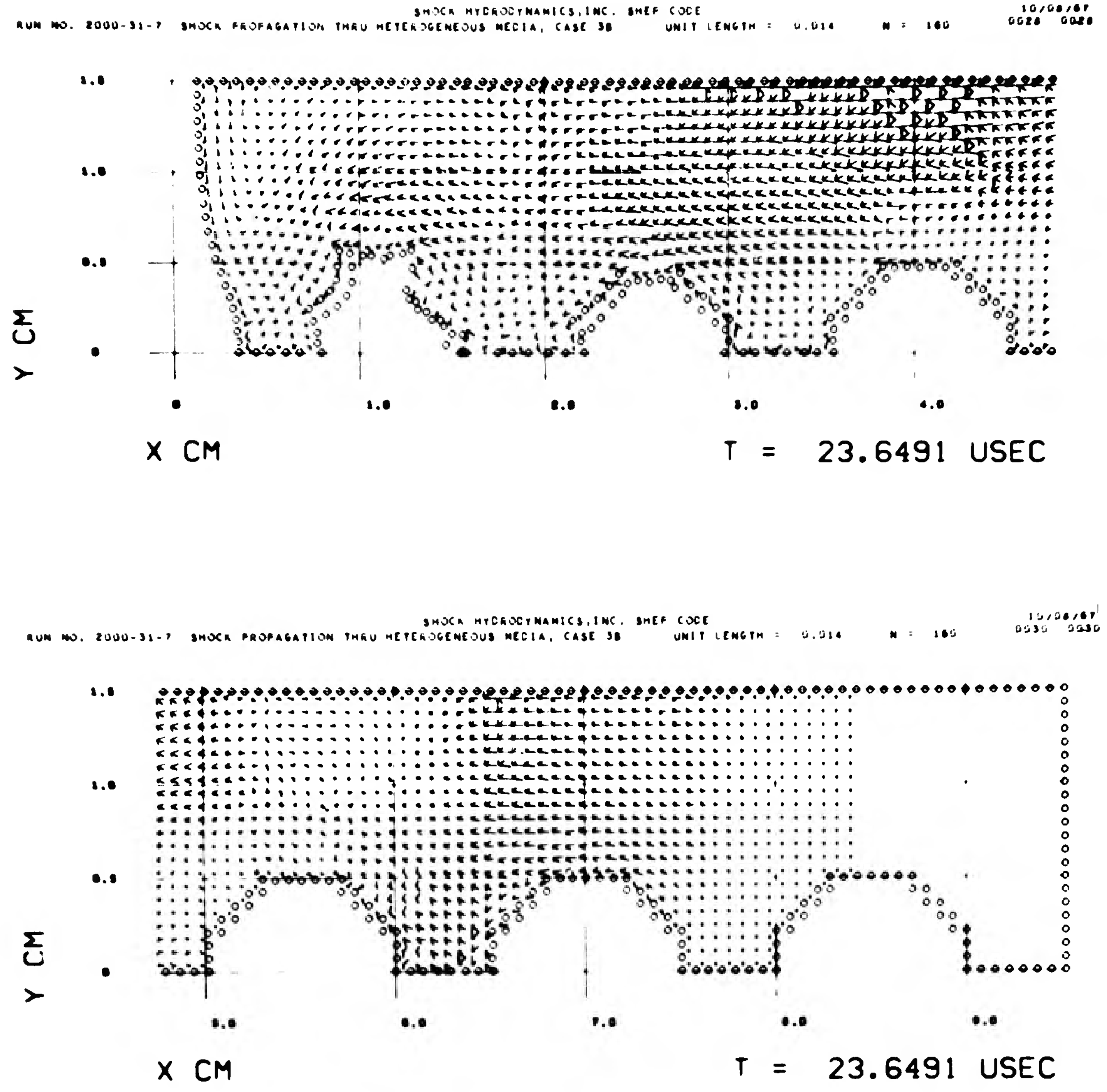

FIGURE 3-87. PRINCIPAL STRESS FIELD, CASE 3B, t = 23.65μ sec.

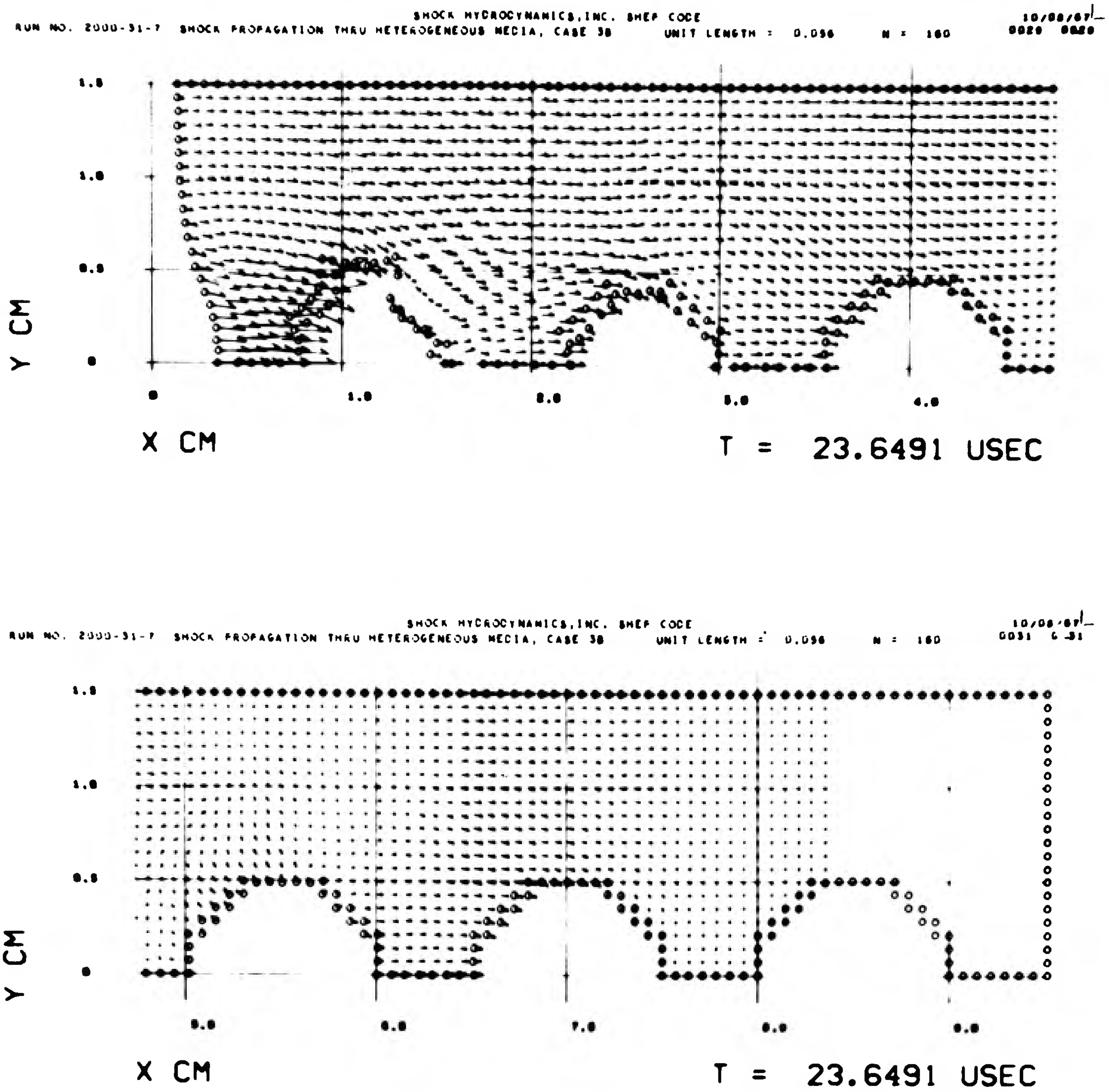

FIGURE 3-88. PARTICLE VELOCITY FIELD, CASE 3B, t = 23.65 μ sec.

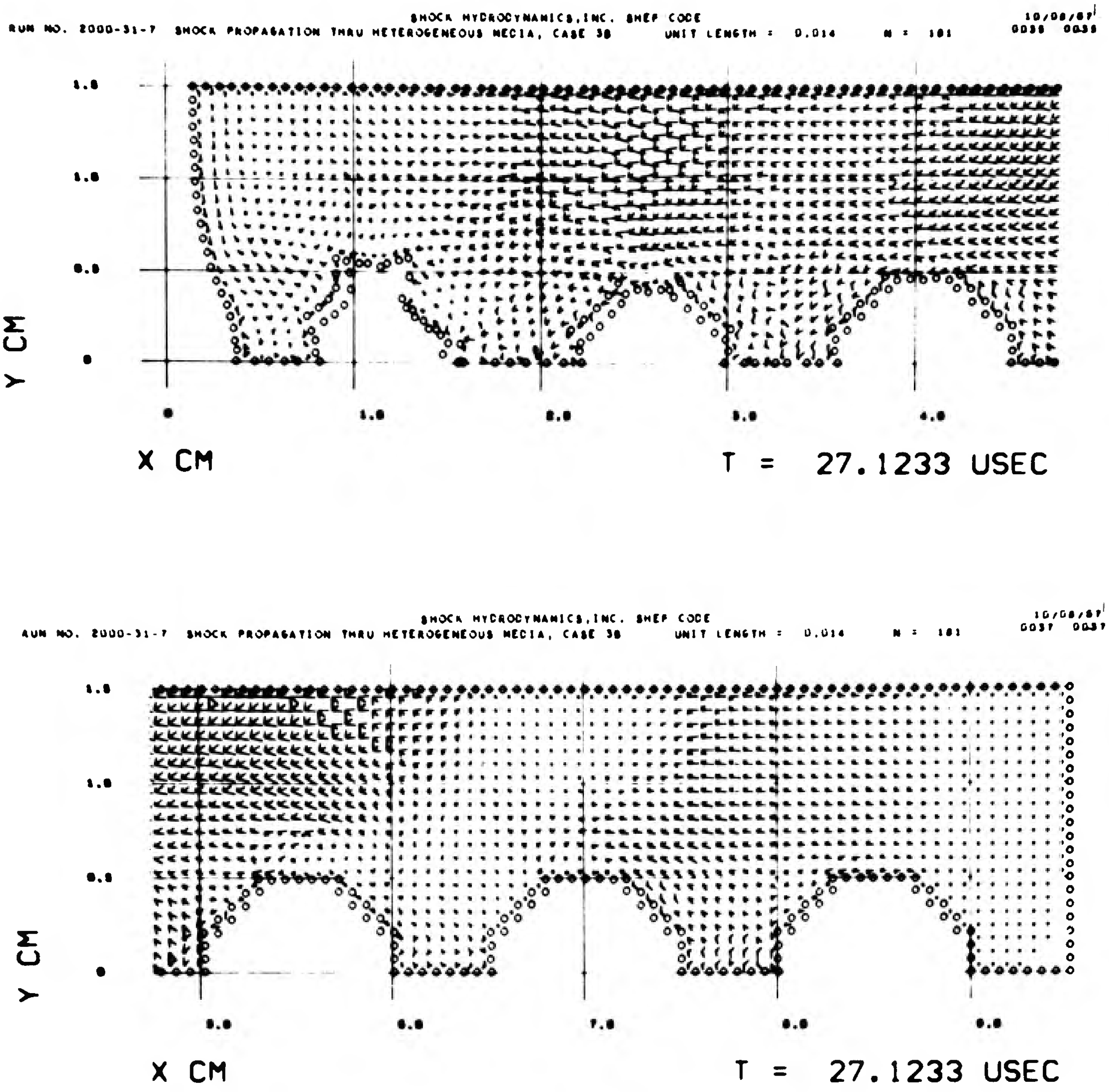

FIGURE 3-89. PRINCIPAL STRESS FIELD, CASE 3B, $t = 27.12\mu$ sec.

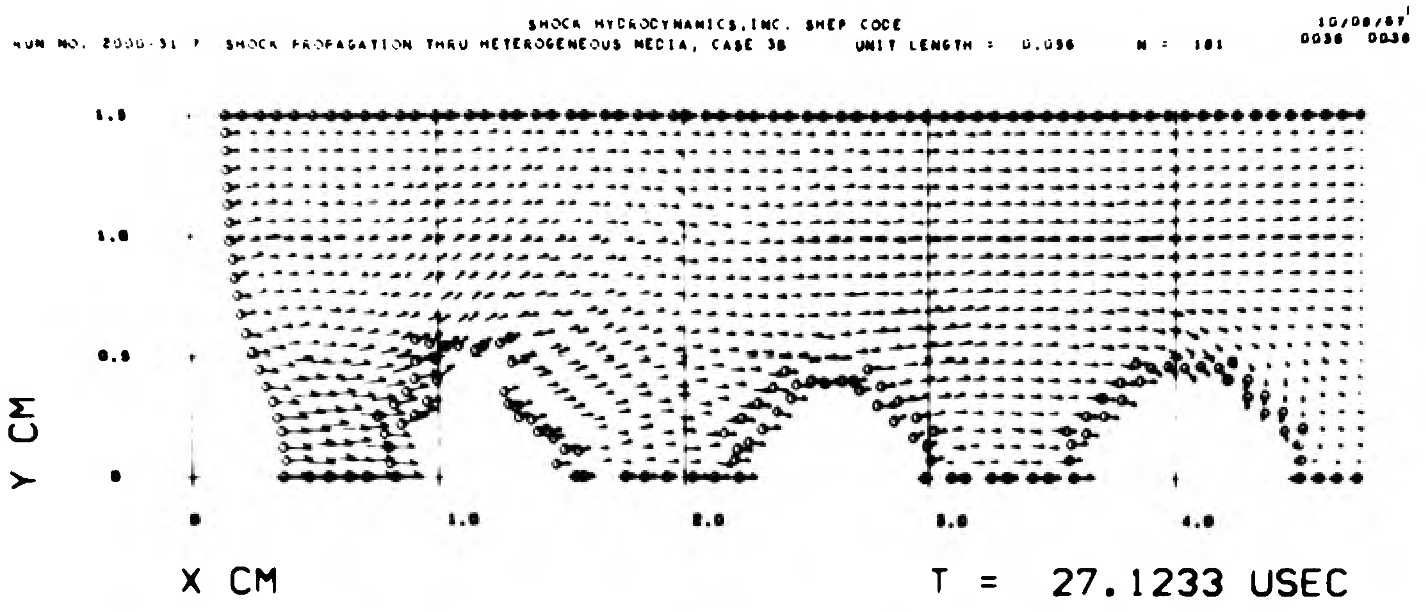

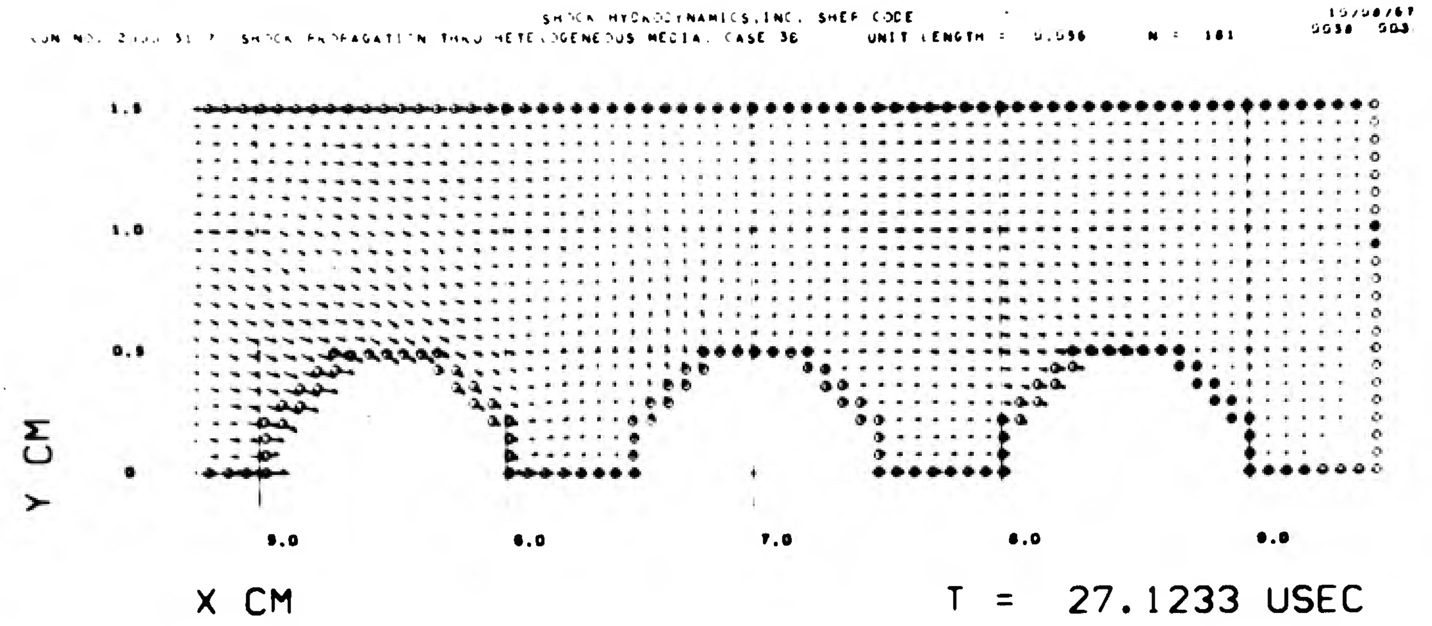

FIGURE 3-90. PARTICLE VELOCITY FIELD, CASE 3B, t = 27.12μ sec.

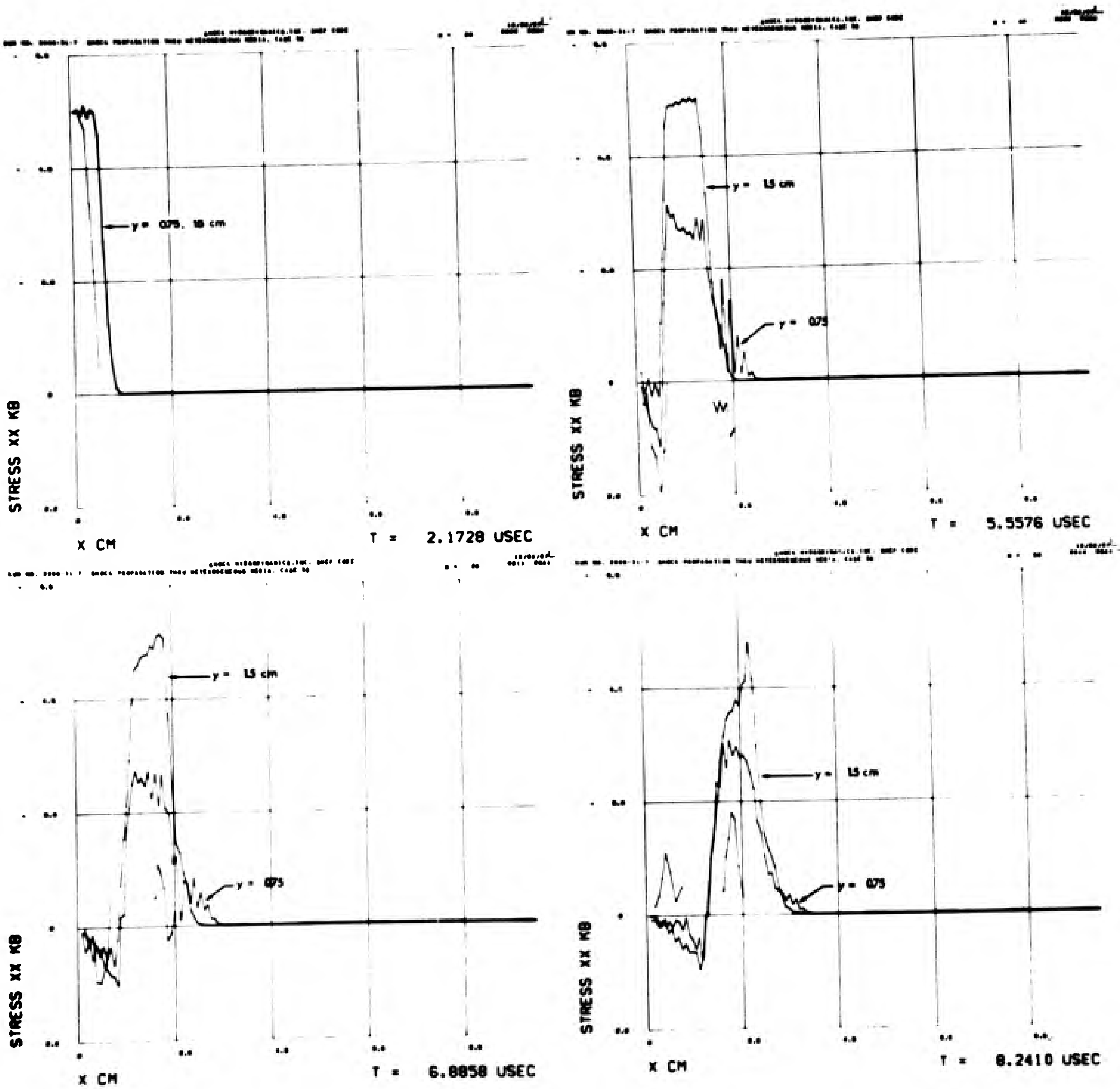

FIGURE 3-91. σ_x vs x AT THREE RADIAL POSITIONS, CASE 3B.

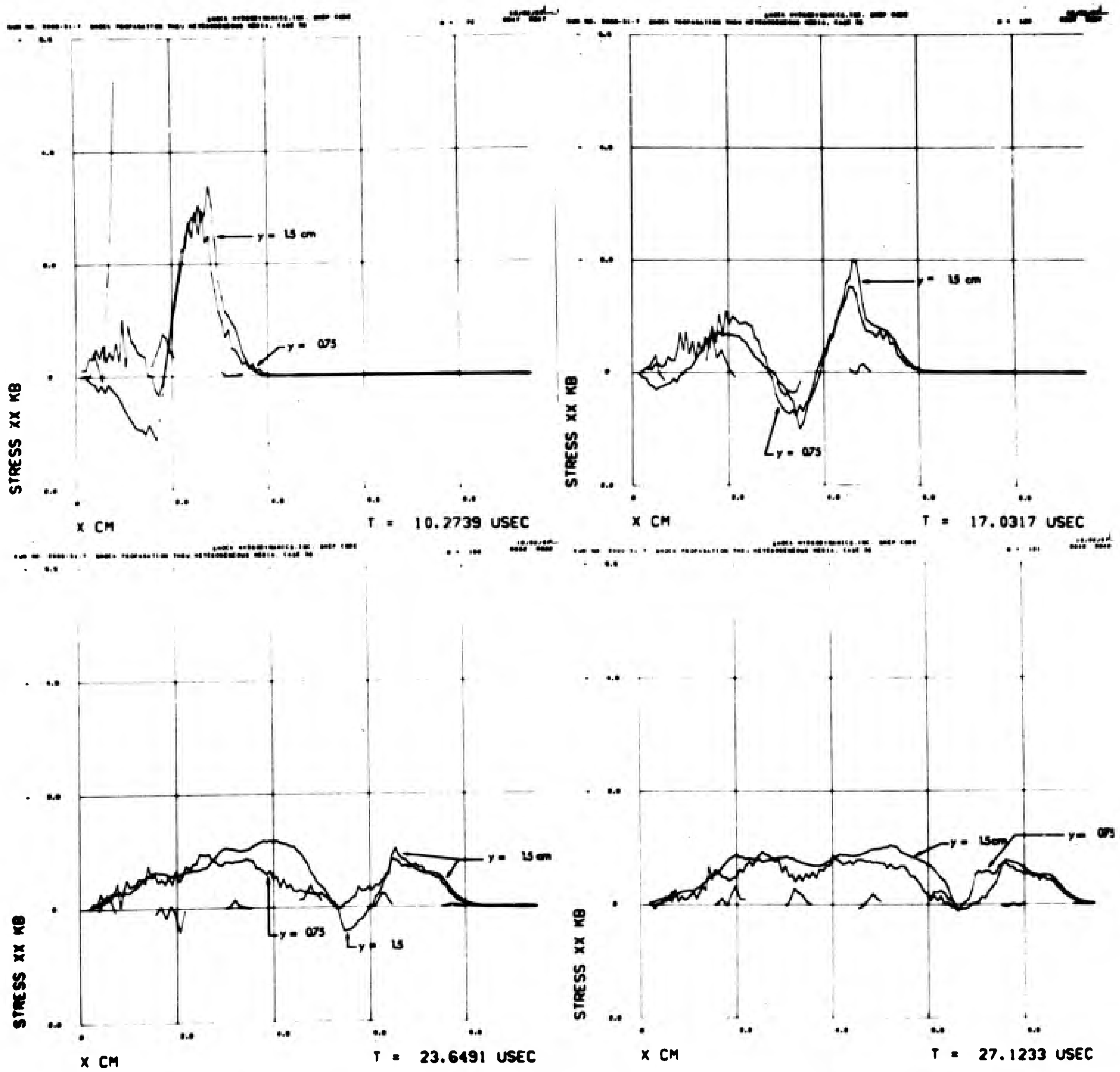

FIGURE 3-91 (cont'd). σ_x vs x AT THREE RADIAL POSITIONS, CASE 3B.

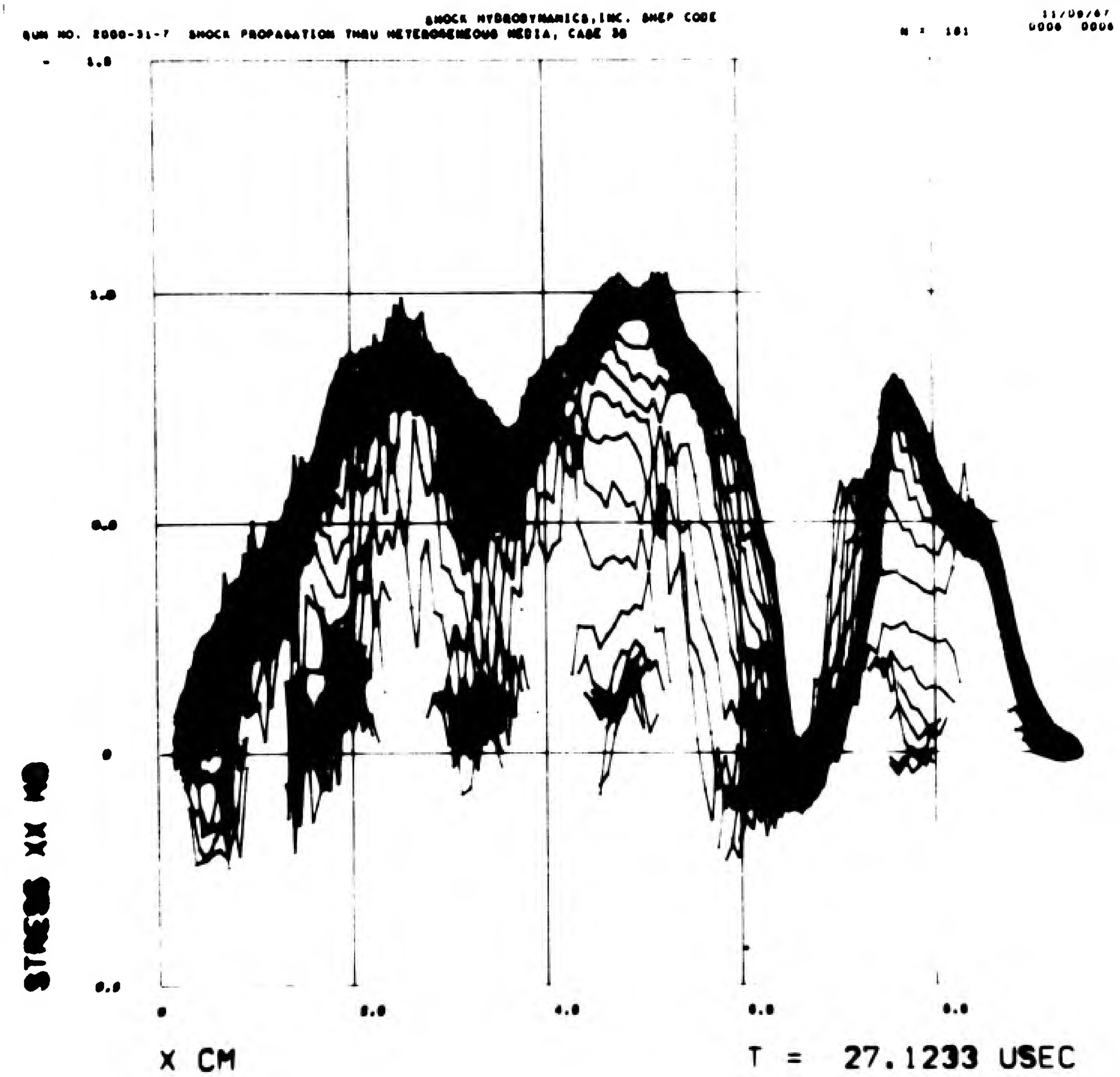

FIGURE 3-92. σ_x vs x AT ALL RADIAL MESH POSITIONS, CASE 3B.

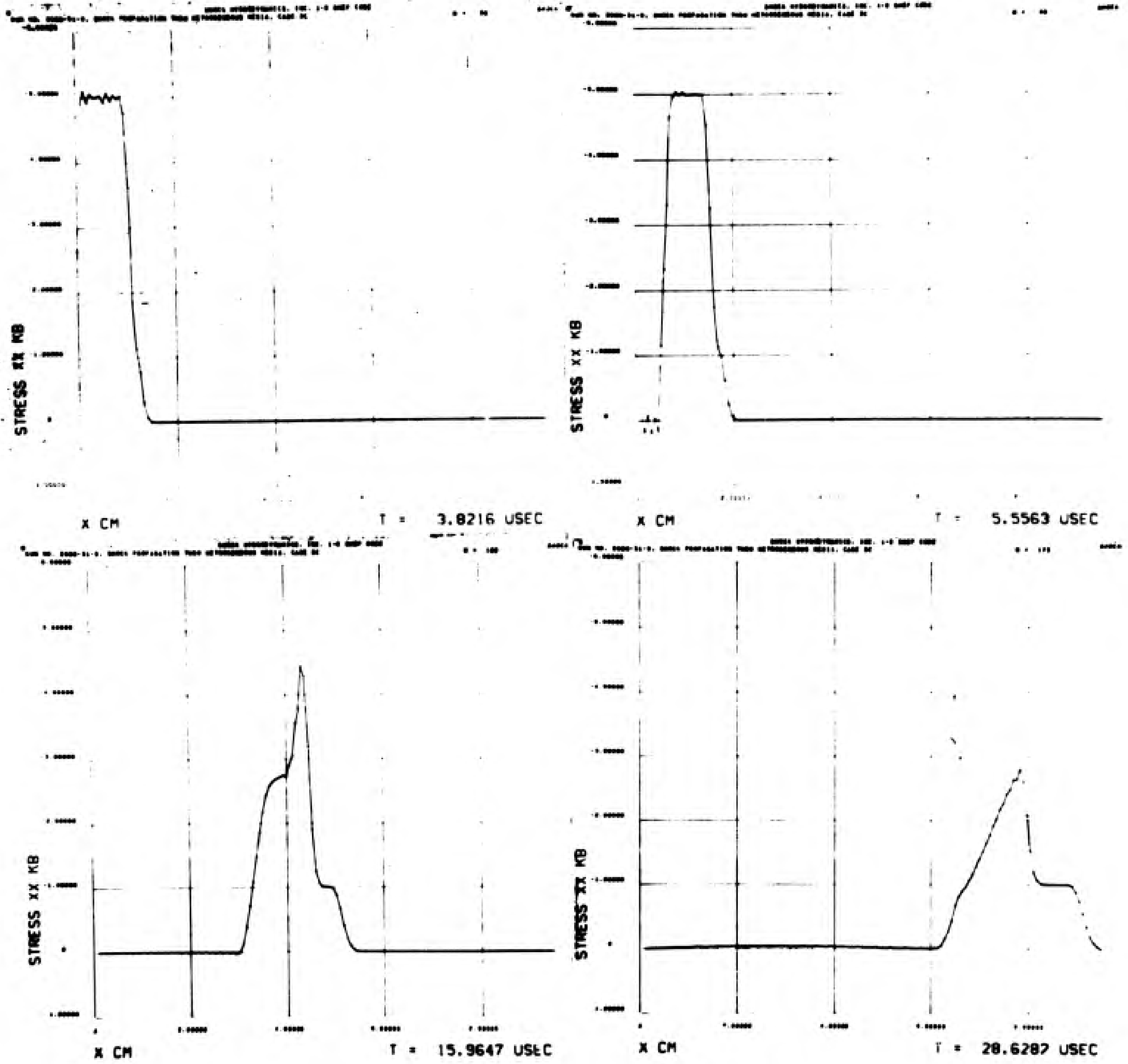

FIGURE 3-93. σ_x vs x, CASE 3C.

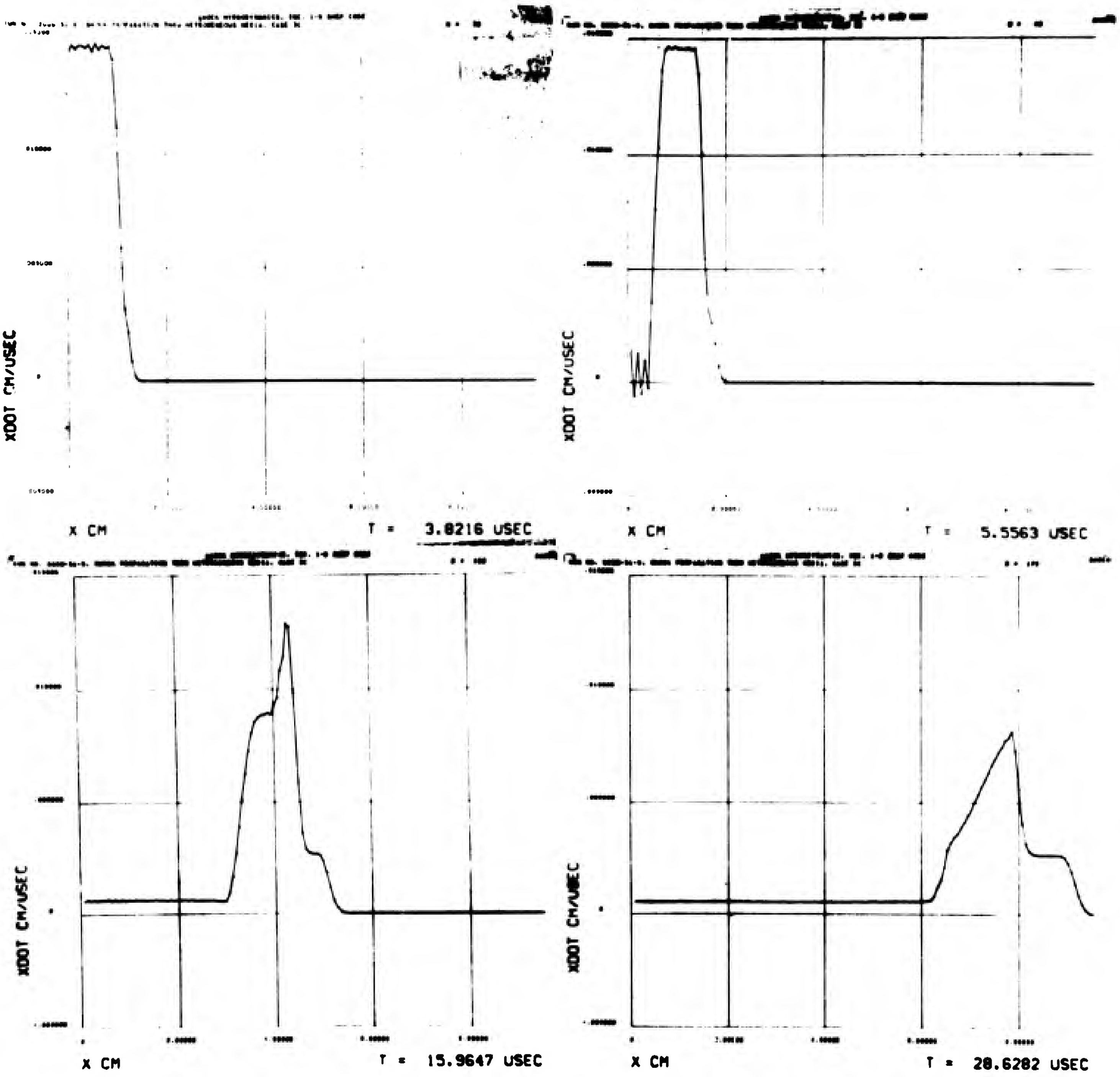

FIGURE 3-94. $\dot{x}$ vs x, CASE 3C.

REFERENCES

1. Hardening Technology Studies, Final Report LMSC-B130200, Vol. IV, 30 September 1965.
2. Averell, J. P., et al, "Simulation Test Techniques," Radiation Damage Study - Phase II, Vol. IX, AVMSD-0852-67-RR (November 1967) S/RD.
3. S. G. Lekhnitskii, "Theory of Elasticity of an Anisotropic Elastic Body," Holden-Day, Inc., San Francisco (1963).
4. R. S. Hearmon, "An Introduction to Applied Anisotropic Elasticity," Oxford University Press (1961).
5. Hardening Technology Studies, Contract AF 04(694)-655, Lockheed Missiles and Space Company, B130200, Vol. V, September 1965; Hardening Technology Studies-II, Contract AF04(694)-814, Ballistic Systems Division, TR-66-250, Vol. VI, September 1966.
6. Personal Communication, S. G. Oston, Avco Corp.
7. Radiation Damage Study, Contract AF 04(694)-824, Ballistic Systems Division, TR-66-372, Vol. XI, September 1966.
8. J. Wackerle, J. Appl. Phys. 33, 922 (1962).

Unclassified
Security Classification

DOCUMENT CONTROL DATA - R & D

(Security classification of title, body of abstract and indexing annotation must be entered when the overall report is classified)

1. ORIGINATING ACTIVITY *(Corporate author)* Avco Government Products Group Missile Systems Division 201 Lowell Street, Wilmington, Mass. 01887	2a. REPORT SECURITY CLASSIFICATION N/A 2b. GROUP N/A

3. REPORT TITLE
Radiation Damage Study - Phase II (RADS II)
Volume VI -- Shock Propagation in Heterogeneous Materials
Book Two of Two Books

4. DESCRIPTIVE NOTES *(Type of report and inclusive dates)*
Final Report

5. AUTHOR(S) *(First name, middle initial, last name)*
R. L. Bjork
M. H. Wagner
H. A. Lang

6. REPORT DATE September 1967	7a. TOTAL NO. OF PAGES 188	7b. NO. OF REFS 8

8a. CONTRACT OR GRANT NO. AF04(694)-990	9a. ORIGINATOR'S REPORT NUMBER(S) AVMSD-0852-67-RR-Vol VI Book 2 of 2 Books
b. PROJECT NO.	
c.	9b. OTHER REPORT NO(S) *(Any other numbers that may be assigned this report)*
d.	SAMSO TR 67-121

10. DISTRIBUTION STATEMENT
~~EACH TRANSMITTAL OF THIS DOCUMENT OUTSIDE THE DEPARTMENT OF DEFENSE MUST HAVE PRIOR APPROVAL OF HEADQUARTERS, SPACE AND MISSILE SYSTEMS ORGANIZATION, NORTON AFB, CALIFORNIA 92409 (SMYSE).~~

11. SUPPLEMENTARY NOTES	12. SPONSORING MILITARY ACTIVITY Space and Missile Systems Organization Air Force Systems Command Norton Air Force Base, California 92409

13. ABSTRACT

Numerical studies of shock propagation in anisotropic and in heterogeneous materials are reported. This work was performed by Shock Hydrodynamics, Inc., using the SHAN and SHEP computer codes.

DD FORM 1 NOV 65 1473

Unclassified
Security Classification

Unclassified

Security Classification

14 KEY WORDS	LINK A		LINK B		LINK C	
	ROLE	WT	ROLE	WT	ROLE	WT
SHAN						
SHEP						
Method of Characteristics						
Stress Profiles						
X-Ray Loading						

Unclassified

Security Classification